Electronic Characterisation and Computer Modelling of Thin Film Materials and Devices for Optoelectronic Applications

A thesis
presented by
Jens-Hendrik Zollondz

to the University of Abertay, Dundee
in partial fulfilment of the requirements
for the degree of Doctor of Philosophy

December 2001

I certify that this thesis is the true and accurate version of the thesis approved by the examiners.

Signed [redacted] Date 21/03/02

(Director of Studies)

Declaration

I declare that while registered as a candidate for the degree for which this thesis is presented I have not been a candidate for any other award. I further declare that except where stated the work contains in this thesis is original and was performed by the author.

Signed 

Jens-Hendrik Zollondz

Acknowledgements

I would like to thank my supervisors Dr. Charlie Main and Dr. Steve Reynolds for their support and advice. I found in their office always an open ear to discuss newest results and problems with coffee or red tea.

Further I would like to thank the University of Abertay for providing the M.Ph./Ph.D. position.

Thanks to Dr. Mervyn J. Rose, David McGuigan and Stuart Anthony from the "Jute shed" at Dundee University for deposition and provision of thick p-i-n samples that must have caused headaches because of the long deposition times needed.

Prof. Dr. Jürgen H. Werner and his group at IPE Stuttgart I would like to thank for one set of samples. Especially I'd like to thank Dr. Thomas Neidlinger, who was the contact person and who deposited the very thick samples.

A big thank you to Professor Dr. Martha Lux-Steiner from the Hahn-Meitner-Institut, Berlin, who made writing up possible by providing a part time vacancy after a sudden move from Scotland to Berlin after an early knock from Anton.

Thank you to Dr. Rudi Brüggemann, who introduced me to the University of Abertay Dundee group. Discussions during his visits in Dundee and via the internet were always helpful. Later his questions about progress of writing up was very important to keep me going.

Although the program was not used in this thesis many thanks to Harald Cordes for repeated advice and help on adapting his simulation program to the needed specifications.

From the old work-place I want to thank especially Mox Rösch for his help on providing and adapting the *i-v* measurement program to the Abertay set-up and for helpful hints on programming new routines.

It seems strange to thank one's landlord Colin Cartwright and landlady Alison Cartwright, but since the landlord was a colleague as well and the fact that there was always an open door for staying in the guest room when visiting Dundee in the writing up process, makes it a big thank you.

I want to thank Professor Dr. Allan Gillespie, who organised an extension for writing up that I couldn't make use of, because of Anton's heavy knocking.

Further I want to thank Dr. Allan MacLeod who always helped with any computer problems, even after repeated password reset after too many login tries with the wrong password...

I want to thank my big number of colleagues during my Ph.D. program and after: First of all Mr. Dr. Nick Cook and Mr. Dr. Justin(o) Shepherd I want to thank for repeated "reconversions".

As colleagues in the EPICentre I want to thank Dr. Hui Zhang and Dr. Maisong Ding and as colleague in the group Ivica Zrinscak. Mariana Gueorguieva I like to thank as flat mate for countless discussions about semiconductors in the small kitchen and for as many cookie breaks at work.

As a colleague who shared the office at my "writing up time" at the HMI in Berlin I like to thank Susanne von Aichberger for sharing discussions, Haribos and Apfeltee.

I want to thank Chris Murrell for proof reading and helping me to put the sentences into the right order.

Thank you to my mother who supported me throughout the whole time of my studies of physics.

Anton I want to thank for oh so many breaks to change nappies during the writing up process and for waking me up in cases when I had fallen asleep over books and papers in long nights of writing up.

Finally I want to thank my wife Priska. Her help and support during the last year provided the space I needed to write up this thesis.

Abstract

Double beam collection efficiency measurements have been carried out on hydrogenated amorphous silicon p-i-n devices. Apparent collection efficiencies higher than unity were observed, and explained by a process identified as photogating, in which a low intensity weakly absorbed probe beam *modulates* the photocurrent produced by a high intensity strongly absorbed bias beam.

Computer simulations were used to gain insight into the photogating phenomenon. It was found that the gating effect operates by the modulation of the internal field profile in a device, via deeply trapped space charge introduced by the probe beam. Conditions for high collection efficiencies were identified by modelling and by experiment. Collection efficiencies of 100 or greater could be achieved, much higher than any previously reported in the literature. The effects of external parameters including bias and probe beam wavelength and intensity, and applied voltage were studied. Additionally, the effects of internal parameters, such as the density and spatial distribution of defects, were investigated. The photogating phenomenon proved a sensitive and potentially useful indicator of defect density.

The time response of the photogating effect revealed slow components to the response, associated with the need to involve deeply trapped space charge in the effect. Measurements of this time response explain in part the much lower values of collection efficiency reported earlier, which were made using ac lock-in techniques.

A comparison was made of the two-beam photogating experiment, with a single beam current-voltage measurement, which is also influenced by trapped space charge, as indicators of defect distributions. It was found that the photogating measurement is a more accurate indicator of the distribution of space charge, and hence defects, within a

device.

Application of the photogating effect in a colour detector is introduced and a detector structure proposed. The simple structure and the thin film technique of a-Si:H deposition suggests the possibility of a low cost photodetector with high colour resolution.

Contents

Symbol and abbreviation list

A	area
d	sample thickness
D^+	unoccupied defect state
D^0	defect state occupied with one electron
D^-	defect state occupied with two electrons
$D^{+/0}$	recombination path *via* D^+ and D^0
$D^{0/-}$	recombination path *via* D^0 and D^-
D_n	electron diffusion constant
D_p	hole diffusion constant
E	energy
E	internal electric field
ΔE	energy of the defect in relation to the conduction band
E_C	conduction band energy
E_{eff}	effective internal electric field
E_F	Fermi energy
E_g	optical band gap
$E^{+/0}$	$D^{+/0}$ energy
$e_n^{(.)}$	electron reemission coefficient
$e_p^{(.)}$	hole reemission coefficient
E_V	valence band energy
G	generation rate
$g(E_C)$	conduction band edge density of states
$g(E_V)$	valence band edge density of states
η	Planck's constant
i	current
i_b	current under bias illumination only
i_{bp}	current under bias and probe illumination
i_d	dark current
i_{ph}	photo current
j	current density
j_b	current density under bias illumination only
j_{bp}	current density under bias and probe illumination

j_{diffi}	diffusion partial current
j_{drift}	drift partial current
j_n	electron partial current density
j_p	hole partial current density
k	Boltzmann's constant
$\boldsymbol{k}$	wave vector
n	electron density
N_D	number of defects
p	hole density
q	electric charge
$R(\lambda)$	wavelength dependent reflectivity
R_n	recombination rate of electrons
R_p	recombination rate of holes
s	cross section
T	temperature
t	time
t_n	n layer thickness
t_p	p layer thickness
t_{trans}	response time
U	defect correlation energy
v	thermal velocity
V	applied voltage
V	volume
v_{drift}	drift velocity of charge carriers
α	absorption coefficient
ε	dielectric constant
ε_0	dielectric constant in vacuum
η	collection efficiency
λ	wavelength
λ_b	bias beam wavelength
λ_p	probe beam wavelength
μ_n	electron mobility
μ_p	hole mobility

ν	attempt-to-escape-frequency
φ	electric potential
Φ	photon flux
Φ_b	bias beam photon flux
Φ_p	probe beam photon flux
ρ	electric charge
σ_n^+, σ_n^-	capture coefficient of charged defects
σ_n^0, σ_p^0	capture coefficient of neutral defects
τ_{on}	50 % rise-time
ω	frequency

1. Introduction

1.1. An historic view on hydrogenated amorphous silicon

Hydrogenated amorphous silicon (a-Si:H) took its time to become a part of research on amorphous semiconductors. In the late 1960's research on a-Si:H took over from research on amorphous silicon, which was prepared from sputtering or thermal evaporation. The unhydrogenated material is a poor semicondutor with a very high defect density, which prevents doping and resulted in poor photoconductivity.

When Chittick et al. (Chittick et al., 1969) deposited a-Si:H by using glow discharge as the deposition technique they were using basic but similar equipment as it is used today. The first results revealed that the deposited films lacked conduction in defect states which implied a low defect density and increased conduction due to impurities (Chittick et al., 1969, Chittick and Sterling, 1985). Although the infra-red vibrations of silicon-hydrogen bonds were observed they were not recognised as such and further research was terminated.

Spear, interested in the new method of making amorphous silicon managed to take over Chittick's reactor and was further on working on characterisation of this new material in Dundee. In the following years the Dundee group around Spear showed that a-Si:H had good electrical transport properties: fairly high carrier mobility and because of a low defect density strong photoconductivity (LeComber and Spear, 1970, Spear, 1974, Spear et al., 1974). But the initial spark of research on a-Si:H was the p- and n-type doping of the material (Spear and LeComber, 1975). Substitutional doping was known and understood for crystalline semiconductors, whereas in amorphous materials it was thought impossible. The argument follows from the 8-N rule (Mott, 1969) for the chemical bonding. In crystalline silicon the dopants substituted a site in the silicon grating, intending to obey the 4-fold coordination. Both dopants, phosphorus and boron

are expected to have a 3-fold coordination in an amorphous material. The fact that doping efficiency is quite low in a-Si:H suggests that the majority of dopants are really 3-fold rather than 4-fold coordinated, where the active coordination is the 4-fold one, as in crystalline silicon (Boyce and Ready, 1988).

A second problem was expected from the hydrogen involved. For crystalline silicon hydrogen passivates the acceptor and donor states (Pankove et al., 1983, Johnson et al., 1986). But since hydrogen has a higher chemical affinity for silicon than for boron or phosphorus (Boyce and Ready, 1988) some dopants remain active. That this number of *active* dopants suffices is founded in the incorporation of hydrogen. Because hydrogen satisfies open (dangling) bonds (of the Si- atoms) the number of midgap states are reduced and the dopants can shift the Fermi level either towards the conduction band (phosphorus) or to the valence band (boron). In amorphous silicon without hydrogen the electrical transport is mainly carried by the high density of these midgap dangling bond states and the high number of these states pinned the Fermi level to the middle of the band gap.

Low cost, because of deposition at low temperatures and thin film technology (making use of high optical absorption) and the possibility of doping opened wide the field for research and industry. Additional alloying of a-Si:H with nitrogen, carbon and germanium, and hence gap engineering, opened the possibilities even wider. Solar cells, driving circuits for liquid crystals displays and thin film transistor displays are applications that were developed since then.

Carlson and Wronski (Carlson and Wronski, 1976) started with a photovoltaic device and initially reached with an a-Si:H solar cell, 2-3 % of collection efficiency. Subsequent research by many groups has increased the efficiency of solar cells up to 12-14 %. Multilayer structures and heterojunctions, subject to recent research are supposed

to reach higher values. Amorphous silicon solar cell technology held a market share of 9.6 % in 2000 (12.3 % in 1999), which is still the highest in the area of thin film technology (Schmela and Kreutzmann, 2001, Fuhs, 1999) but is due to lose this leadership to $CuInSe_2$ (0.2 % in 2000) as the coming thin film technology (Kreutzmann, 2000). That is mainly because of the degradation effect of a-Si:H under solar exposure (Staebler and Wronski, 1977). The stabilised conversion efficiency after one year outdoor operation has only stayed at approximately 5 %. Instead a-Si:H "solar" cells captured the market in domestic appliances because of their better power conversion under fluorescent light sources, as for handheld calculators, watches or similar products.

Research on large area electronic arrays of a-Si:H devices started a few years later after the first field effect transistors were reported (Snell et al., 1981). Applications like liquid crystal displays, optical scanners and radiation imagers on large areas were developed. Recent interest of research is on thin film transistor technology for flat panel displays.

Additionally a numerous variety of applications lie in the field of sensors and detectors.

1.2. Measurement and simulation: state of equilibrium

The complexity of hydrogenated amorphous silicon has made necessary work of over 30 years on this material up to today. Although the basic principles on which amorphous silicon is working are known and understood, work is still needed about this complex material to adapt to new applications. Over the years the application emphasis has shifted from solar cell power conversion to thin film transistors.

With this shift not only the application but also the knowledge of the material had to be adapted to the new requirements. For example layers of a few nanometers are used in

thin film transistor technology, whose electronic properties only can be understood and enhanced with as much knowledge about the material as possible. Also, although the main focus of a-Si:H is on thin film transistors, the application as solar cells, sensors and detectors are still in the field of interest.

The understanding of devices has been hindered because detailed structural information is lacking. E.g. for a p-i-n structure the interfaces are sensitive to fabrication steps and the equations that govern the electrical characteristics of the devices are difficult to solve. These equations must be solved numerically. Computer simulation programs and powerful computers open the direct view on internal parameters of the material. The properties of the i-layer have importance for collection, and information could be obtained by analysis of a dummy layer. This dummy layer is deposited simultaneous with the i-layer (which is important for the photogeneration) to examine there the density of states, mobility and lifetimes of photocarriers or the defect densities with standard procedures as e. g. photoconductivity measurements, moving grating, or constant photocurrent measurements.

An alternative, such as a knowledge of these parameters in the *ready made* p-i-n device would be ideal, because the interfaces are very sensitive for the behaviour of the sample as mentioned earlier. Here a measurement of these internal parameters on the ready made p-i-n structure would be best but the variety of measurement techniques as used for films to reveal these internal parameters are difficult to perform because of the complexity of the system. However, some techniques like time-of-flight (TOF) or *i-v* analysis give some information of internal parameters of the ready made p-i-n devices.

Since simulation programs and the calculating power of even personal computers are far advanced today, such information can be revealed from *simulating* the device. In a later chapter the simulation program used for calculations in this thesis is introduced

and explained (chapter 4). Output files with information about band structure, current densities, electric potential, internal electric field, drift and diffusion length and densities of charge carriers, recombination and life times give a view on internal parameters. Also the *i-v* characteristic or more complex measurement output information (like the dual beam collection efficiency) is available.

But since these last mentioned simulated data such as *i-v* characteristics can also be measured a comparison and fitting of the simulation to measured data can be realised. With the knowledge of the danger of varying 10's of parameters and maybe altering the wrong parameters, measurement should always give a feedback to simulation. The more aspects of one measurement are examined or the more complex the measurement the less degrees of freedom in variation of input parameters. That means if a simple *i-v* measurement with one sided illumination can be simulated with a good fit of simulation for the experiment *and* simulation (with the same input parameters) then the same sample should show well fitted results of the *i-v* characteristics under illumination from the other side or for a second more complex measurement, for which both sides are illuminated.

This applies especially for simple input parameters that should be used first for any simulation. E.g. if first results fit with a simple defect model as a single energy level the step to a Gaussian distribution or even to the defect pool model should be avoided. This 'rule of economy' is because for further fitting under the additional parameters more degrees of variation are left open.

Using this procedure should be seen only as a rough instruction for processing of simulation and measurement fitting. The wide spread argument that anything can be fitted to anything, with a sufficient number of parameters should be reconsidered. Because the interaction between measurement and simulation allows a fine iteration

process to match the two, and can result in a good understanding of internal parameters, which consequently will result in an enhancement of the device.

1.3. Photogating

Quantum efficiencies greater than unity, or photogating, is a phenomenon that was first observed by Maruska et al. in 1984 (Maruska et al., 1984). Publications of other groups followed and the effect was found for a variety of devices (Hou and Fonash, 1992, Rubinelli, 1994, Chatterjee, 1994).

In all cases the collection efficiency is calculated due to a weak probe beam under a strong bias illumination. The exceeding of unity is due to a field enhancement by the probe-beam-generated photocarriers, at the internal field minimum that is created by the strong generation of the bias beam in that area (refer to chapter 2.9). This concept results in further specifications on the beam to achieve high gains. The bias beam should be absorbed strongly at one side of the device, so that a pronounced field minimum is observed close to the incident bias beam side, while the probe beam is supposed to be homogeneously absorbed (hence independent of the side), with the result that the field enhancement is in an area where bias beam generation is highest. Here the gating term originates, because the collection of the bias beam is enhanced by addition of the probe beam. But by taking only the *changed* parameter, i.e. additional probe beam illumination (hence additional photons), into account, collection associated with the low photon flux of the probe beam results in high collection efficiencies of the probe by extra release of bias beam originated photo carriers, and what is termed, because of the great number of these photocarriers, *gating*.

1.4. Aim of this thesis

One of the scopes of this thesis is to explain the above process of photogating and to have a critical look at measurements in the literature and reveal problems that could occur from measurement techniques. This study includes steady state measurements and time dependent measurements and steady state simulation.

With the deeper understanding of the effect resulting from this work, possible applications are proposed. These applications are as follows:

- An opto-electric amplifier
- Defect analysis in ready made a-Si:H p-i-n diodes
- Colour detecting device

Whereas the opto-electric amplifier results from the nature of the set-up and explains itself: the input parameters are the optical part while the read out is in a current signal. Subject of investigation are here gain and problems of such an amplifier. The defect analysis is studied in a degradation series to prove the sensitivity of the experiments to an increased defect density. Finally the colour sensitivity and the time response are studied of a possible detector.

2. General background of hydrogenated amorphous silicon (a-Si:H)

This chapter will introduce the reader to the material of hydrogenated amorphous silicon.

In section 2.1 the physical structure of a-Si:H will be explained in comparison to crystalline silicon. The resulting density of states (DOS) will be shown and explained in section 2.2. Optical absorption (section 2.3) and electronic properties (section 2.4) are the subjects of following sections in which the generation, transport, trapping and recombination of the material are introduced. The metastability of a-Si:H, hence the Staebler-Wronski-effect is discussed in section 2.5.

Section 2.6 introduces the reader to the device structure of a p-i-n by explaining the difference to a p-n junction on the basis of the electric potential (section 2.6.1), and the electric field (section 2.6.2). In section 2.7 and 2.8 the *i-v* characteristics with and without illumination are explained.

A literature review of collection efficiency measurements greater than unity is given in section 2.9 and the separation of electron and hole gating are subject of subsections 2.9.1 and 2.9.2. A motivation for measurements on the transient response (section 2.10) concludes the chapter.

2.1. Structure

The geometric structure of (hydrogenated) amorphous silicon is locally as for crystalline silicon i.e. tetrahedral. The covalent bonds between the silicon atoms are much the same in the amorphous material but the bonding angles and lengths show variations from the ideal as found in crystalline silicon (Figure 2.1). Average bond

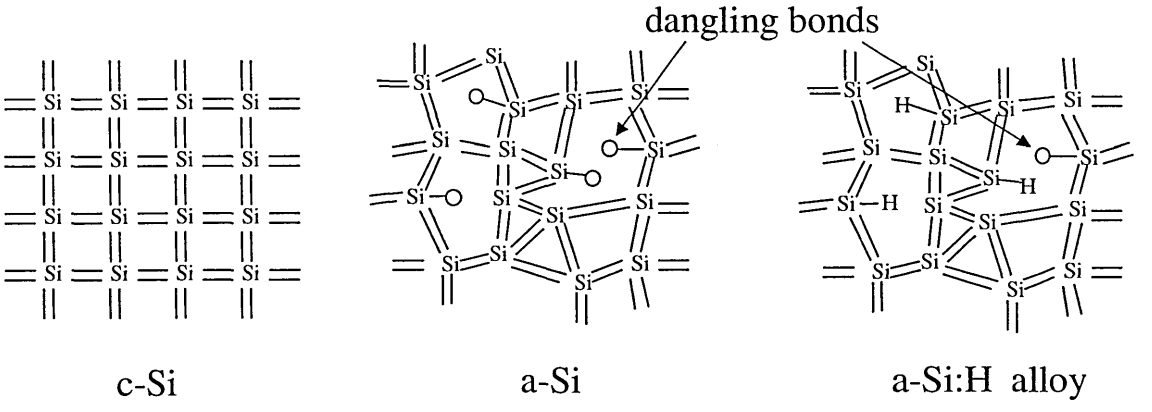

Figure 2.1: Different structural types of silicon (Si).

length and average bond angle are conserved but amorphous material has the same short range order as the crystal but lacks the long range order. Figure 2.2 shows the radial distribution function of amorphous and crystalline silicon. Here the first and second neighbour show the same distances whereas the information on the distances of third neighbours is lost in the amorphous structure. Because of the disordered structure, bonds without a bonding partner (dangling bonds) are found in the amorphous material. Incorporation of hydrogen satisfies most of these dangling bonds and leads to better material properties (compare Figure 2.1).

Since the periodicity of the atomic structure is central to the description of the semiconductor, using Bloch's theorem, in a disordered semiconductor optical and electronic properties are influenced by disorder and in contrast to the crystalline counterpart with its sharp band-edges amorphous silicon shows a sloping decay of states that reach into the band gap, the so called band tails, and deep level defect states related to dangling bonds.

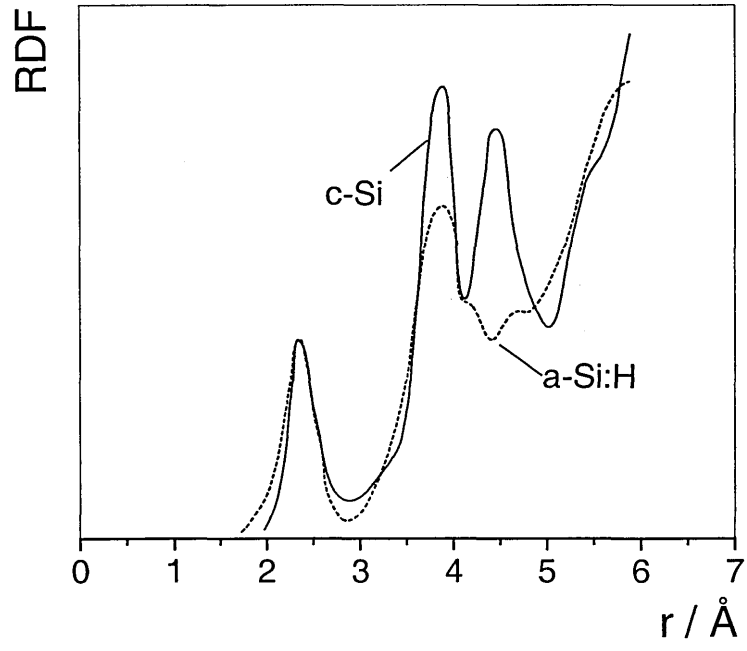

Figure 2.2: Radial density function of hydrogenated amorphous silicon (a-Si:H) and crystalline (c-Si) from x-ray deflection experiments, from Abel (Abel, 1993).

2.2. Density of states

For crystalline silicon with its strict tetrahedral structure the band structure results directly from the Bloch theorem and the wave vector ***k*** is a conserved quantum number.

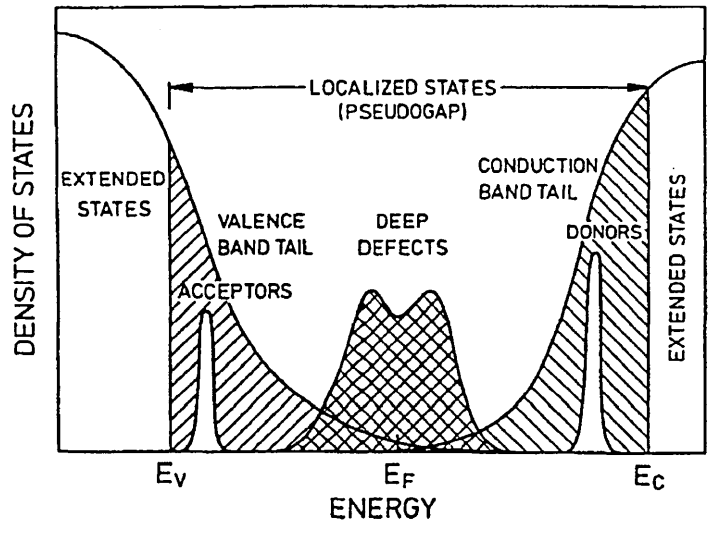

Figure 2.3: Schematic illustration of the density of states (DOS) in amorphous semiconductors, from Overhof and Thomas (Overhof and Thomas, 1989).

Since the amorphous material lacks the long range order the description with a ***k*** vector is not reasonable. Variation of the bond angles of up to 10 % and bond length variations are described by Anderson's model with potential wells

that vary in depth (P. W. Anderson, 1958). The consequences of the loss of ***k***-conservation and description of amorphous silicon with the Anderson model are that the energy bands are no longer described by a well defined *E(**k**)* dispersion relation, but instead we must rely on a density of states (DOS) distribution *N(E)*. Furthermore the conversation of momentum selection rules do not apply to optical transitions. By overlap of states in *real space* for the amorphous material the indirect semiconductor of crystalline silicon becomes a 'quasi-direct' semiconductor. But the disorder of the amorphous material results also in a reduced carrier mobility because of frequent scattering. The consequences in the DOS are localised states resulting in band tails.

The term of *mobility edges* is introduced instead of *band edges*, and *mobility gap* instead of *band gap*.[1] Figure 2.3 shows the schematic DOS of amorphous silicon. In the outermost (not hatched) areas the extended states are shown which are the analogous to the extended Bloch states in crystalline silicon. In the mobility gap, that is defined by the mobility edges, localised states are found, which are band tail states and deep defect states.

2.2.1. Band tail states

The prediction of localised states is established by a number of measurements showing how they influence electric transport, dopeability and recombination of free charge carriers. A big influence is to be seen in band tail states.

The band tail states originate from bond angle and length variations and show their character in their slope. The valence band tail is more influenced by these bond variations in that the exponential gradient is lower and the band tail reaches deeper in

[1] Although *mobility gap* is the correct term for amorphous silicon the term of a *band gap* is used and accepted. *Mobility edge* is mainly used only to show the difference in the band structure to crystalline silicon.

the band gap in comparison to the conduction band tail (Overhof and Thomas, 1989). The gradient of the valence band is determined from the exponential energy dependence of the optical absorption (Urbach, 1953) and is typically at 45–55 meV, while the conduction band tail is steeper with a gradient of 20-30 meV.

2.2.2. Dangling bonds

Because not all silicon bonds of the amorphous structure are saturated, this results in open (dangling) bonds, which form deep level defect states. These dangling bonds form localised energy states close to the middle of the mobility gap and exist in spite of additional hydrogen during the deposition process in amorphous hydrogenated silicon. Although the hydrogen satisfies most of the open bonds of the amorphous structure a non-negligible number remains unsatisfied (hence "dangling"). The occupation of these dangling bonds depends on the position of the Fermi energy (E_F), and hence also on quasi-Fermi levels. The positively charged unoccupied state (D^+) and the neutral with one electron occupied state (D^0) are positioned close under the middle of the mobility gap, while the double occupied state (D^-) is found, because of its positive correlation energy, higher (above the mid gap) (Elliot, 1983). The correlation energy is defined as

$$U = q^2 / 4\pi\varepsilon\varepsilon_0 r - W, \tag{2.1}$$

where q is the elementary charge r the effective separation of the two electrons that the first term is the Coulomb interaction. The second term is due to lattice relaxation: addition of an electron to a localised state lowers the electronic energy by the amount W. (Street, 1991)

2.3. Optical absorption in amorphous silicon

Absorption in hydrogenated amorphous silicon is one order of magnitude higher than in its crystalline counterpart. Because of the structure with its bond angle and lengths variations an overlap of bond states in real space is found (compare section 2.1). This results in a quasi-direct semiconductor with high absorption whereas crystalline silicon shows properties of an indirect semiconductor, i.e. lower absorption. In Figure 2.4 the absorption coefficients of amorphous and crystalline silicon are shown as a function of energy. The good absorption properties of a-Si:H allow layer thicknesses of 1 μm to collect nearly the whole solar spectrum.

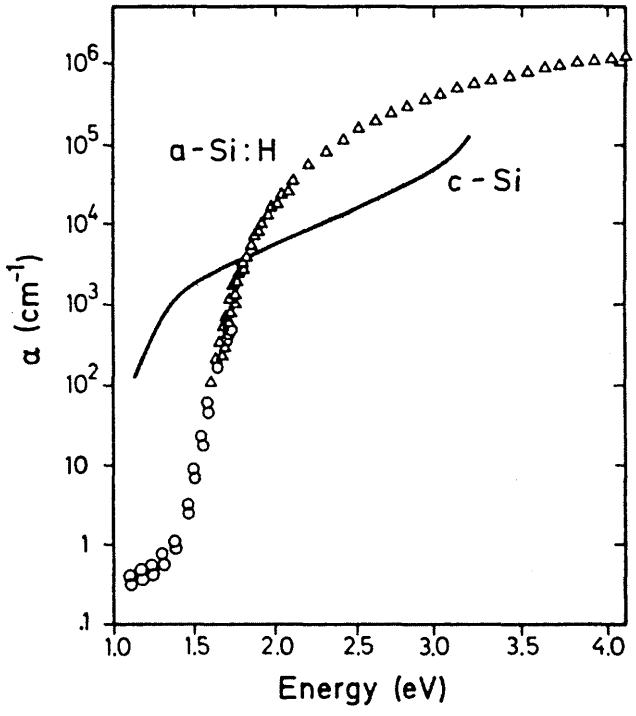

Figure 2.4: Absorption in hydrogenated amorphous silicon (a-Si:H) and crystalline silicon (c-Si), from Cody et al. (Cody et al., 1980).

For applications of a-Si:H in optoelectronic devices the position and shape of the absorption edge are of particular interest. Various methods have been used to measure the absorption constant α. In the range $\alpha > 10^3$ cm^{-1} by optical transmission and at lower values of α by primary and secondary photoconductivity (Cody et al., 1980, Vanecek et al., 1984, Pierz et al., 1987) or photothermal deflection spectroscopy (Jackson and Amer, 1982).

The absorption spectrum as it is shown in Figure 2.4 contains implicit information on the density of states. After the sudden increase in α (especially for c-Si) at the band

gap (for c-Si at 1.1 eV and for a-Si:H at approximately 1.8 eV) follows the high energy part corresponding to band to band conversion. For a-Si:H and the high number of band gap states the sudden increase in absorption is not as abrupt as for c-Si – mainly because of the tail states. Transitions from the valence band tail into the conduction band are possible and influence the optical absorption. The slope of the exponential decay in a logarithmic scale is called the Urbach energy (Urbach, 1953). Furthermore the slight increase for low energies (below 1.4 eV) shows the character of midgap states. The shoulder for the lowest energy values in Figure 2.4 originates from defect-band-transitions. These deep defect states depend on deposition parameters and on defect densities. The fact that the curve is increasing gives an indication of a distribution of midgap states.

2.3.1. Mobility gap

The optical band gap E_g is an important parameter of interest for semiconductors. Since in amorphous silicon the band tails decay continuously with energy, a band gap only can be defined in terms of an extrapolation of the bands. An assumption sometimes used is that for absorption $\alpha > 10^4$ cm^{-1} that absorption takes place between extended states. A second approach is to see the band gap E_g as an extrapolation of the bands and parabolic band edges, described by Tauc expression (Tauc et al., 1966, Tauc, 1974).

$$(\alpha\eta\omega)^{1/2} = B(\eta\omega - E_g) \tag{2.2}$$

where η is Plank's constant, ω the frequency, B a proportional constant and E_g is the band gap. The linear extrapolation of the plot of $(\alpha\eta\omega)^{1/2}$ versus the photon energy to the abscissa (Tauc plot) yields a value of an efficient optical gap E_g or Tauc gap.

2.4. Electronic properties

The band structure of hydrogenated amorphous silicon determines the electronic properties of the material. Transport, trapping and recombination is affected by gap states - dangling bonds and band tails.

2.4.1. Transport

At temperatures higher than 100 K transport is dominated by free electrons and holes beyond the mobility edges. Because of the higher mobility of electrons transport is mainly dominated by electrons in intrinsic a-Si:H. The number of free charge carriers is controlled by trapping and thermal emission in and from band tail states. According to Boltzmann's distribution the re-emission decreases exponentially the lower the energetic level. Additionally the number of states decreases the deeper these are in the gap. This results in a rapidly decreasing exchange speed from the band edges. The process described is known as *multiple trapping* (Tiedje and Rose, 1980, Orenstein and Kastner, 1981). The effective carrier mobility is therefore lower than the actual mobility of the conducting states and is temperature dependent because of the thermal activation. For temperatures below 100 K tunnelling between localised states is observed (Baranovskii et al., 1995).

In the steady state the continuity equations for electrons *(n)* and holes *(p)* describe the electrical transport mechanism in amorphous materials:

$$div\ j_n = q(R_n - G) \tag{2.3}$$

$$-div\ j_p = q(R_p - G)\,. \tag{2.4}$$

Here, R_n and R_p are the recombination rates of electrons and holes, G the stationary generation rate, j_n and j_p the electron and hole current densities, and q is the electronic charge.

The electron and hole current density is composed of the partial current densities of drift (j_{drift}) and diffusion (j_{diff}):

$$j = j_{drift} + j_{diff} . \tag{2.5}$$

The diffusion current density for electrons results from the undirected thermal movement of the charge carriers

$$j_{diff} = qD_n \frac{\partial n}{\partial x}, \tag{2.6}$$

where D_n is the diffusion constant for electrons.

The drift partial current density of electrons results from the directed velocity (v_{drift}) of the charge carriers, which depends on the electric field E and their mobility μ_n:

$$j_{drift} = qnv_{drift} = qn\mu_n E .$$

Substitution of electrons by holes and the diffusion constant for electrons with that for holes leads to the analogue equations of the hole partial current densities for drift and diffusion. The electron partial current density is described by

$$j_n = q(n\mu_n E + D_n \frac{\partial n}{\partial x}) \tag{2.7}$$

and the hole partial current density by

$$j_p = q(p\mu_p E + D_p \frac{\partial p}{\partial x}) . \tag{2.8}$$

The relation between drift and diffusion current is given by the Einstein relation:

$$D = \frac{kT}{q}\mu . \tag{2.9}$$

The relation between potential φ, hence electric field E and charge ρ is given by Poisson's equation:

$$\Delta\varphi = \frac{dE}{dx} = -\frac{\rho}{\varepsilon\varepsilon_0}, \tag{2.10}$$

where ε is the relative permittivity constant of the material and ε_0 is the permittivity of free space.

2.4.2. Trapping

Trapping describes the process of capture of free charge carriers into localised states in the band gap. Due to the density of states distribution two trapping processes are possible: trapping into the band tail states and trapping into dangling bond states. The process is important for electrical properties of hydrogenated amorphous silicon because trapped charge influences the internal electric field in the device by screening or enhancing it. Additionally trapped charge can form recombination centres for other charge carriers.

As described above in the last section 2.4.1 the process of conduction of electrons and holes occurs by a frequent process of trapping in band tail states followed by excitation to the higher energy conducting states. The deeper the trap is in the band gap the lower is the emission probability, i.e. band tail states deep in the gap form recombination centres and contribute to localised charge that influence the electric field. Since the valence band tail is broader than the conduction band tail, trapping of holes in the valence band tail is more likely than trapping of electrons in the conduction band tail. The distinction between states that contribute to transport by thermal activation and by trapped charge contributing as recombination centres is defined by the demarcation energies. The demarcation energy, e.g. for electrons, is defined as the energy of a gap state with the same probability of emission and recombination of the trapped charge. In states above this demarcation energy trapped charge has a higher probability of emission above the mobility edge and states below this energy have a higher probability of recombination.

A very high number of defects (dangling bond states), as for amorphous silicon (without hydrogen), could result in hopping conduction at the Fermi level. But since the number of dangling bond states is drastically reduced in amorphous hydrogenated silicon hopping transport at the Fermi level is almost completely suppressed (Street, 1991). Thus in hydrogenated amorphous silicon, dangling bonds are mainly trapping or recombination centres. Figure 2.5 shows the possible transition from and to the dangling bond states. There are three dangling bond states, that depend on the occupation of electrons and holes, found in amorphous silicon: the uncharged state D^0 occupied by one electron, the negatively charged state D^- occupied by two electrons and the unoccupied positively charged state D^+.

Release of an electron (e.g. thermal emission) from the single occupied neutral state (D^0) results in a positive, electron-attractive localised state (D^+). Trapping of an electron in the original state (D^0) results in a localised negative charge occupied by an electron pair (D^-). Transitions are possible via conduction band *and* valence band.

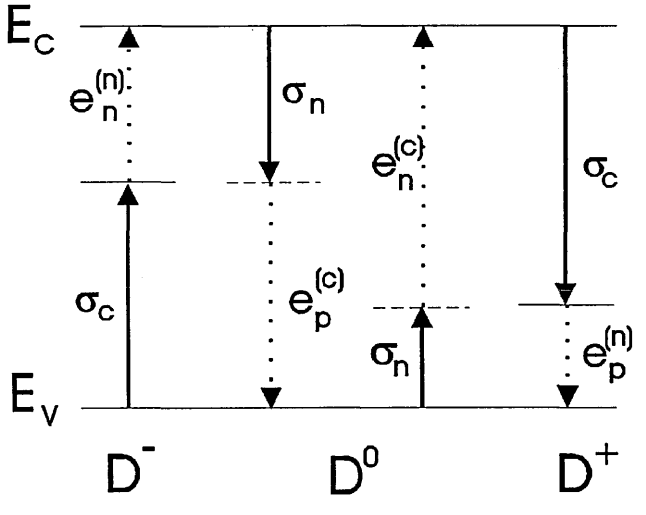

Figure 2.5: Capture and emission paths of the three dangling bond states.

Trapping in a localised state is described by capture coefficients σ_n and σ_c or by capture cross sections that are related as

$$\sigma = vs, \qquad (2.11)$$

where v is the thermal velocity and s the cross section.

σ_n describes the capture coefficient of the uncharged

state and σ_c gives the capture coefficient of a charged state. Because of the Coulomb interaction of charged states, $\sigma_c > \sigma_n$.

Thermal release describes the inverse processes of the capture and reemission probabilities ($e_p^{(..)}$, $e_n^{(..)}$). The lower index states the charge carrier type that is excited and the upper index states the related capture process.

2.4.3. Recombination

Recombination means the loss of two complementary charge carriers by physical contact. Because of the high number of gap states, which function as trapping centres, recombination in amorphous silicon is more likely to proceed *via* gap states (Hall, 1951, 1952, Shockley and Read jr., 1952) than direct recombination of two free charge carriers, which is negligible. The recombination can be radiative between band tail states and non-radiative from the band edges to defect states. While at low temperatures the radiative band tail mechanism dominates recombination, above 100 K the non-radiative path takes over.

In hydrogenated amorphous silicon the main recombination centres are dangling bonds. The low probability of thermal emission of trapped charge out of deep gap states results in high probabilities of the complementary charge carrier to be trapped in the same state that results in recombination.

The nett recombination rate results from the capture rate and the thermal emission rate of all gap states involved. Under illumination a positive nett recombination rate is observed while in the dark or under certain circumstances of illumination a negative nett recombination rate can be observed, which means the thermal emission rate from theses states is greater than the recombination rate *via* these states.

2.5. Staebler–Wronski-effect

When amorphous hydrogenated silicon is exposed to prolonged absorbing light at sufficient intensity and temperature (300 K) a decrease in the photoconductivity during the illumination and a drop in the dark photoconductivity is observed. (Staebler and Wronski, 1977)

Staebler and Wronski suggested that both observations were due to creation of additional localised gap states. This effect is observed to be metastable and can be annealed by tempering at temperatures of $T \geq 160°$ C resulting in dark- and photo - conductivities returning substantially to original values.

The shift of the Fermi-level in direction to a mid gap position under illumination is due to an increased number of dangling bonds (Hirabayashi et al., 1980, Dersch et al., 1981). These metastable defects can be generated with different methods, i.e. light induced, by current injection (Krühler et al., 1984) or irradiation by keV energy electrons (Schade and Pankove, 1981).

The microscopic breaking of weak silicon-silicon bonds (Stutzmann et al., 1985) to dangling bonds is discussed in detail in the literature. In the theory of the *weak-bond model* defects are seen in disorder, which results from breaking of Si-Si bonds starting with the weakest bonds.

2.6. p-i-n diode

Since all experiments in this thesis are on a-Si:H p-i-n samples this section will give an overview over the structure and basic properties of this kind of device. The description is in the context of a p-n device as it is more familiar from crystalline silicon.

Due to the property of a-Si:H to be 'dopable' by adding Diborane (B_2H_6) or Phosphine (PH_3) to Silane (SiH_4) in the deposition process produces p- or n- character while the undoped layer is 'intrinsic'[2]. Incorporation of Boron results in p-doping, hence oversupply of holes, whereas the incorporation of phosphorus results in n-doping because of excess electron supply. Due to the 8-N rule (Mott, 1969) a low number is in the dopant active 4-fold state most dopants are, following the 8-N rule, in the dopant inactive 3-fold state (compare chapter 1). The absorption in low field regions and diffusion in the space charge region as it is observed in crystalline silicon is due to a low mobility of both charge carriers in a-Si:H not possible. While even in intrinsic (undoped) a-Si:H low mobilities are observed because of the structural disorder and hence scattering, crystalline silicon shows far higher mobilities. This has the effect that the diffusion lengths in a-Si:H are too short to allow charge carriers to leave areas of low fields, requiring a different device structure, introduced in section 2.6.2. But since this device structure has its basis in a p-n structure as it is used for crystalline silicon devices the following section introduces this type of device first, to then proceed by observing and adapting the electric field for the use of a material with poor charge carrier mobilities as amorphous silicon.

[2] Although undoped amorphous hydrogenated silicon shows slight n-character. (Street, 1991).

2.6.1. The electric potential of a p-n interface

At a p-n junction Figure 2.6a) a space charge region builds up by diffusion of the majority charge carriers that leads to the space charge distribution $\rho(x)$ and potential $\varphi(x)$ shown in Figure 2.6b) and c).

For normal doping all doping atoms in p- as well as the n- region are ionised, i.e. acceptors (N_a) in the p-region and a constant number of holes outside the space charge region, and respectively donors (N_d) in the n-region and a constant number of electrons outside the space charge region. By diffusion of the (mobile) majority charge carriers and recombination in the opposing layer the remaining (localised) ionised doping atoms build up the space charged areas as shown in Figure 2.6. In equilibrium a drift current compensates the diffusion current of the majority carriers.

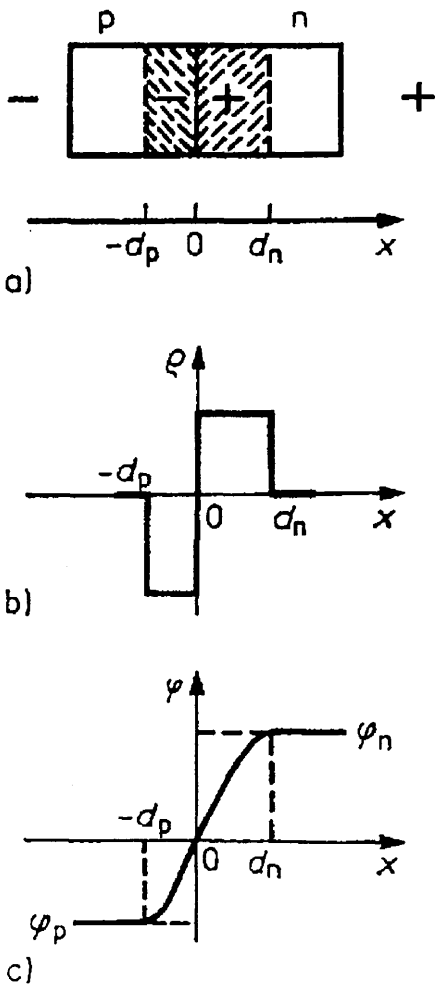

Figure 2.6: Space charge ρ and electric potential φ of an p-n junction (idealised), from Bonc and Kalasnikov (Bonc and Kalasnikov, 1982).

The relation between charge distribution $\rho(x)$ and potential $\varphi(x)$ is given by Poisson's equation (section 2.4.1)

$$\Delta\varphi = -\frac{\rho}{\varepsilon\varepsilon_0}.$$

Assumption of boundary conditions and integration of the charge distribution $\rho(x)$ results in the potential $\varphi(x)$.

2.6.2. The electric field of a p-n junction and of a p-i-n diode

The charge distribution and the resulting potential shown in the last section (Figure 2.6) result in an idealised electric field distribution as shown in Figure 2.7.

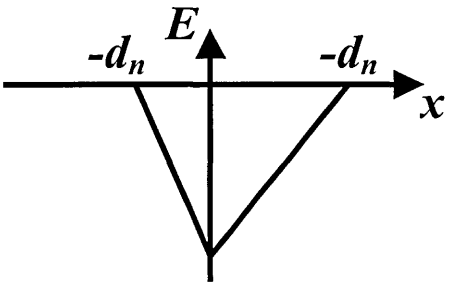

Figure 2.7: Electric field of a p-n junction (idealised).

Resulting from the Poisson's equation is

$$E(x) = -\frac{d\varphi}{dx}.$$

Diffusion and collection of charge which occurs readily in a crystalline silicon p-n junction, is not so easy in amorphous silicon because of the lower mobility of the charge carriers, and the increased probability of recombination brought about by defects. In a-Si:H the mobility is between 10-20 $cm^2V^{-1}s^{-1}$ (Street, 1991) (in the intrinsic material) in comparison to 100-2000 $cm^2V^{-1}s^{-1}$ (Wolf, 1969) in c-Si. Hence diffusion lengths in a-Si:H are normally too short for charge carriers to leave low field regions.

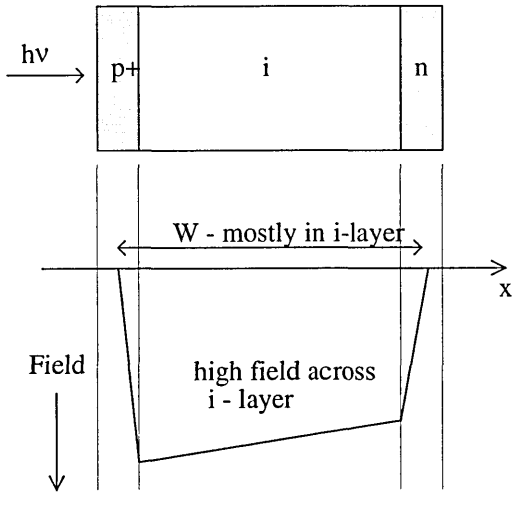

Figure 2.8: Idealised electric field of a p-i-n diode.

Adding a third *intrinsic 'i'* layer

between the two doped layers (Figure 2.8) results in a extended space charge area in which there should be a raised electric field. The idea is that in this intrinsic layer the electric field can separate the charge carriers at the position of generation and leads to drift of the charge carries to their contacts, resulting in improved collection efficiency.

But in a realistic amorphous silicon p-i-n diode the electric field 'sags' through the i-layer. This decline in the electric field is dependent on the thickness of the i-layer. For very thick p-i-n diodes the field is approaching *zero* over a wide range as revealed in Figure 2.9 and Figure 2.10 demonstrated using the computer simulation employed in this work. A low field results in poor opto-electronic properties. Thick solar cells would be very inefficient, so that applications of thick p-i-n diodes are restricted to the application of detectors operated with field-enhancing reverse voltages.

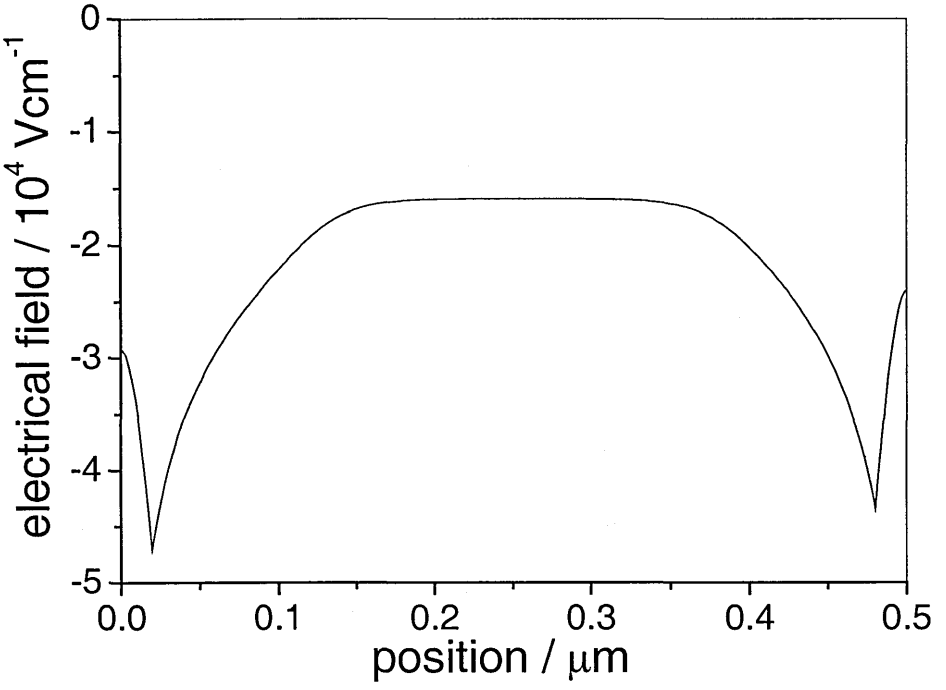

Figure 2.9: Simulated electric field for a 0.5 μm thick a-Si:H diode.

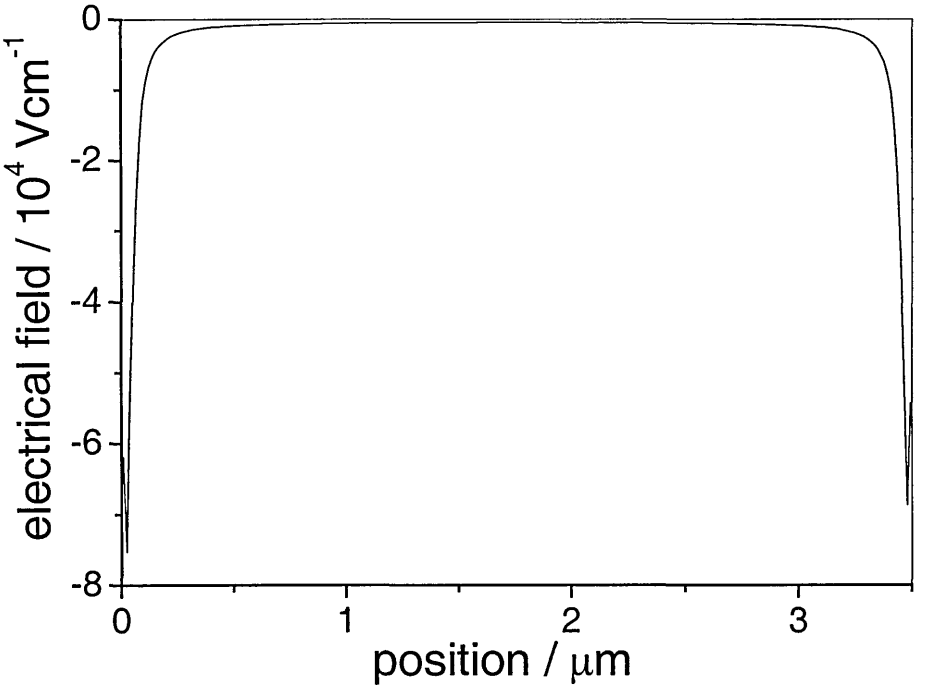

Figure 2.10: Simulated electric field for a 3.5 μm thick a-Si:H diode.

2.6.3. Comparison of c-Si p-i-n and a-Si:H p-i-n

Although crystalline solar cells are made in form of p-n structures other applications as detectors like photodiodes are produced in a p-i-n structure. Fast response times, high photosensitivity and stability are properties of this kind of detector.

Because of the lower mobility of charge carriers solar cells made of hydrogenated amorphous silicon are made in a p-i-n structure. To compare these two similar made structures is difficult because the applications are different in that a restriction to a detector of both materials in this section has to be made.

Crystalline silicon in either form, p-n or p-i-n, has to be made from an energy consuming crystal drawing process to a c-Si rod or similar procedures that imply a high temperature silicon melt (approx. 1400°C) followed by a cutting procedure. Losses of the cutting or sawing process of the solid c-Si rod are very high that the whole process can be seen as very expensive. Furthermore thicker absorber layers are needed than for the amorphous material since the absorbency of the crystalline material is lower (see section 2.3).

Amorphous silicon can be deposited at relative low temperatures (approx. 250°C). Different techniques are used as PECVD, photo-CVD, reactive sputtering or hot wire deposition but always at these low temperatures. Cutting is not needed since the material can be deposited directly onto the substrate. The shape or form of the substrate is not important and even moderate bendable materials are usable.

A p-i-n sensor requires that the undoped layer has to be as thick as possible to absorb the maximum flux of photons. On the other hand the intrinsic layer cannot be thicker than the depletion width, without losing collection efficiency (compare field distribution in the last section 2.6.2). But by applying a reverse voltage the depletion

width can be increased up to 50 μm (Perez Mendez et al., 1989). But for solar cells an i-layer thickness of 0.5 μm is enough to absorb nearly the whole solar spectrum that for solar cells this problem does not occur.

Although the structure for the amorphous material is restricted to p-i-n structures the properties of the material holds the advantage of alloying to vary the band gap. The band gap of a device made of a Silicon-Germanium alloy can be varied continuously about 1.65 to 0.95 eV (Chevallier et al., 1977), i. e. lower band gaps than for "pure" a-Si:H, while an alloy of silicon-carbon ($Si_{1-x}C_x$) results in a band gap increase with a variation range between 1.7 to 3.0 eV (D. A. Anderson and Spear, 1977, Munekata et al., 1981, Mui et al., 1987). Even higher band gaps can be observed for silicon-nitride alloys with band gaps of up to 5 eV. (Searle et al., 1987, Robertson, 1991, Maeda and Umezu, 1991) Having the freedom of varying the band gap offers the possibility of designing double (Hamakawa, 1980) or triple cells.

For an application as solar cell these stacked cells reach higher theoretical collection efficiency values since the single layers can be adapted to a wavelength range and losses are minimised. But problems are associated with high defect densities especially for the lower band gap materials of $Si_{1-x}Ge_x$ and even degradation with germanium contents (Hauschildt et al., 1980) and matching of the in-series working tandem or triple cells (Goetzberger et al., 1994). The different absorption properties of a band gap engineered multilayer cell can also be used to detect and distinguish colours. (Stiebig et al., 1996, Caputo et al., 1996, Topic et al., 1998, Neidlinger et al., 1997, Knipp et al., 1998, Stiebig et al., 1998, Stannowski et al., 1999, Zimmer et al., 1999)

2.7. Steady state dark current

A typical *i-v* dark characteristic of a p-i-n a-Si:H device is shown in Figure 2.11. Three different regions can be distinguished: the reverse region (1), the exponential region (2) and the far forward bias region, where the current is controlled by the series resistance (3). In the reverse region, i.e. for reverse applied voltages, the current in most

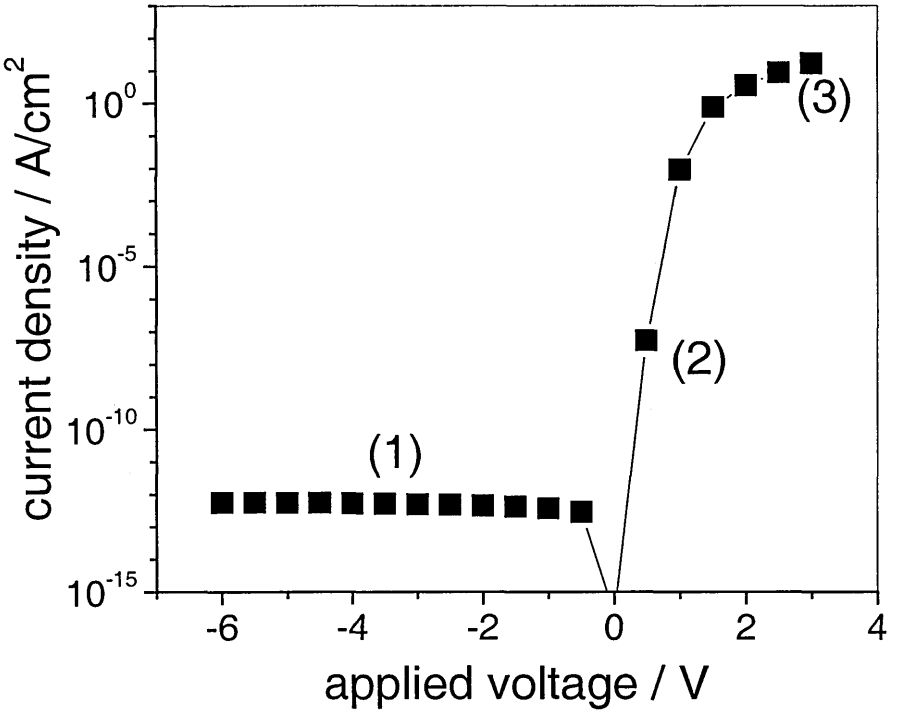

Figure 2.11: Dark *i-v* characteristics (d = 1.0 μm).

cases is dominated by shunt resistance. This shunt resistance is related to pinholes propagating through the film causing an incomplete formation of the junction. (Fiorini and Mittiga, 1992). But when shunt resistance do not affect the performance of the solar cell or detector the reverse current of the device can be observed (McMahon et al., 1984).

The reverse current arises from generation in the depletion region and its value depends on the density of states in the band gap and their capture cross section (see section 5.2). The process is that electrons are excited from the valence band to empty gap states and from filled traps to the conduction band. These excitations generate electron-hole pairs, which are separated and collected by the internal electric field (Street, 1991).

In the second region the current is increasing exponentially to lead over to the third region where series resistance of the material and contacts show their influence and can be determined.

2.8. Steady state photo current

With illumination the generated electron-hole pairs have to be separated and then drift or diffuse to their contacts to contribute to the current measurable in the external electrical circuit.

2.8.1. Generation

Illumination with energy higher than the band gap excites excess charge carriers to contribute to the photocurrent. Because of the states in the band gap transitions from theses states can be also observed that energies smaller than the gap can generate free carriers. Absorption in a-Si:H is high and generation profiles follow an exponential decay on entering the sample. For short wavelengths the generation is very high in the front of the device. Losses in the front doped area are here very high. For moderate absorption the generation profile extents into the i-layer while for low generation with weakly absorbed light the generation is low over the whole i-layer and can be seen as roughly constant, so that the generation profile can be termed *homogeneous*.

2.8.2. Transport by drift and diffusion

After generation the charge carriers must be separated, and this is done by the internal electric field. Then the charge carriers have to reach the contacts to contribute to the current. The current for each carrier has two components - the diffusion current, caused by a gradient of carriers and the drift current caused by the electric field that dominates the i-layer as described in section 2.6.2.

High absorption results in high generation close to the incident side. Losses through absorption in the defect rich doped areas are observed but also a diffusion current back into the doped area against the electric field is found (Crandall, 1983).

2.9. Collection efficiencies higher than unity

Collection efficiency exceeding one is found in literature as collection efficiency greater than unity or is known as photogating in a two beam experiment. It describes the phenomenon of apparently higher collection of photocarriers than the light quantum input. In the literature these terms are used for electron gating since electron gating is the only gating experiment reported by other groups, to the author's knowledge. The author presented at ISCMP - Varna 1998 and MRS 1999 the work on hole gating experiments. (Zollondz et al., 1998, Zollondz et al., 1999)

2.9.1. Electron gating

Photoconductivity gains greater than unity are normaly associated with *secondary* photocurrents in devices with ohmic contacts, where carrier replenishment occurs. (Rose, 1963) Collection efficiency values exceeding unity in an a-Si:H based device were first observed by Maruska et al. (Maruska et al., 1984) who used a *m-i-n*$^+$ structure after prior AM1 illumination (400 h) and hence degradation. The authors incorrectly explained the effect as a series resistance associated with an inbuilt low field region at the *back* (the side furthest from the bias illumination) of the sample. This series resistance was said to control the strongly absorbed light of the bias beam and was modulated by the weakly absorbed probe beam. This effect was called *photogating* and could result in collection efficiencies greater than one. Subsequent work (Hou and

Fonash, 1992, Rubinelli, 1994, Chatterjee, 1994, Zollondz et al., 1996, Brüggemann et al., 1997, Zollondz et al., 1998, Main et al., 1999, Zollondz et al., 1999) has shown that a low field region is found at the *front* of the device, i.e. where the bias beam is strongly absorbed, rather than the back.

Computer modelling has helped to look into internal details of the phenomenon and to explain it. Hou and Fonash (Hou and Fonash, 1992) and Rubinelli (Rubinelli, 1994) pointed out that the strongly absorbed bias light creates a low field region in the front of the i-layer close to the p-i interface, while an increase of the electric field in the back of the sample is observed. The homogenous generation profile of a weakly absorbed illumination incident through the front of the device[3] generates charge carriers throughout the device. Trapping of photocarriers generated by the probe beam in the back of the device results in an increase of the field in the front low-field region, allowing the release of blue-bias-beam-produced photocarriers.

Chatterjee (Chatterjee, 1994) found collection efficiencies higher than one for a m-i-n structure for a complementary case. He found gating for a red bias beam under blue probe illumination. In this case the low field region is associated with a degraded layer near the front *m-i* interface. Bae and Fonash (Bae and Fonash, 1996) were also able to demonstrate gating of red bias photocarriers by blue probe illumination in heterojunction devices. None of the above work measured collection efficiencies much greater than 2.

Larger photocurrent gains (up to 1000) have been reported by Rubinelli et al. (Rubinelli et al., 1993) for a Schottky barrier and a n-i-n structure in forward bias beyond the flat band condition. In the dark a single carrier electron injection is observed and a low field virtual cathode region is found close to the injecting contact. The probe

[3] or through the back of the sample, hence homogenous absorption

beam (in absence of a bias beam) gates currents from the dark current by modulating the virtual cathode potential.

Resulting from the work presented in this thesis collection efficiencies are reported far higher than 1, without injecting contact but in reverse bias, hence requiring blocking contacts (Zollondz et al., 1996, Brüggemann et al., 1997, Zollondz et al., 1998, Zollondz et al., 1999). These experiments are on thick (d = 3.5 μm) a-Si:H p-i-n samples. Measured collection efficiencies up to 150 were observed.

2.9.2. Hole gating

For electron gating the bias beam is incident onto the p-side and the low field region is observed close to the p-i interface. Released carriers have to drift under an applied reverse bias voltage to the according contacts, i.e. released holes to the p-contact and released electrons to the n-contact.

By reversing the experiment the field minimum is observed at the n-i interface and the released holes out of the low field region have a longer distance, under reverse bias voltage, to be collected at their contact (p-contact). This work, by the author, gave rise to the term *hole gating* for gating experiments with this kind of beam arrangement. (Zollondz et al., 1998, Zollondz et al., 1999) By introducing this term and to stress the difference to electron gating the "normal gating" reported by other groups should be seen as *electron gating*.

2.10. Transient response of the gating phenomenon

Long settling times and the knowledge of the effect involving small field changes at low field regions gave reason to a study of the transient response of the photogating effect.

To the authors knowledge no results are presented on the transient response of the photogating effect. Very high collection efficiency results for *steady state measurements,* have been presented by the author at various conferences (Zollondz et al., 1996, Brüggemann et al., 1997, Zollondz et al., 1998, Main et al., 1999, Zollondz et al., 1999), and journals and in this thesis. This is in distinction to all other published work (Maruska et al., 1984, Hou and Fonash, 1992, Rubinelli, 1994, Chatterjee, 1994, Bae and Fonash, 1996, Binnewies, 1997, Unold et al., 1999) which was carried out with lock-in techniques. Because of this, and the possible effects of slow response times on the validity of ac – lock-in techniques, a study of the transient response was deemed necessary, and is reported in the present thesis.

3. Experimental facilities and techniques

In this chapter all the experimental configurations used are illustrated. Furthermore a number of experiments are described that were performed on these arrangements.

In section 3.1 the experimental arrangements for all steady state measurements are shown. This includes all *single beam* steady state experimental arrangements as for *i-v* measurements and regular collection efficiency measurements.

The dual beam set-up to measure gated collection efficiencies is described in subsections of section 3.2.

In section 3.3 the experimental dual beam set-up for measurements of the transient response of gated collection efficiencies is introduced and explained.

3.1. Steady state measurement

The steady state set-up was used for a number of measurements: not only for the dual beam gating experiment but also to record (dark-) *i-v* curves. It was also possible to measure collection efficiency data by analysing the *i-v* single beam results.

Although the set-up was modified and adapted for the different applications some parameters were used for all measurements, i.e. the main unit, an electrometer (Keithley 617) that was controlled by a personal computer. Furthermore the sample was contained always in a grounded diecast box to screen external fields. The contacts of the sample were made with silver paint and apertures were used on both illumination sides to restrict the illuminated area.

Due to steady state measurements that are very sensitive to background light, all measurements were taken with the room light switched off and additionally a black cloth shielded any light entrances from stray illumination.

3.1.1. Current-voltage characteristics

The set-up shown in Figure 3.1 was used for all current-voltage *(i-v)* characteristics. In order to measure the current i at an applied voltage V a computer-control program was used. For the dark *i-v* curve the personal computer ran a program that controlled an electrometer to apply a voltage for a given time interval. Then the program took the current value and saved the data set and proceeded to the next voltage value. In contrast to that the procedure was different for illuminated samples. Here the voltage was applied for a given time and a certain number of measurements was taken. After a double interval of time a second set of measurements were taken and the average values of both sets compared. For a deviation lower than a preset value the data

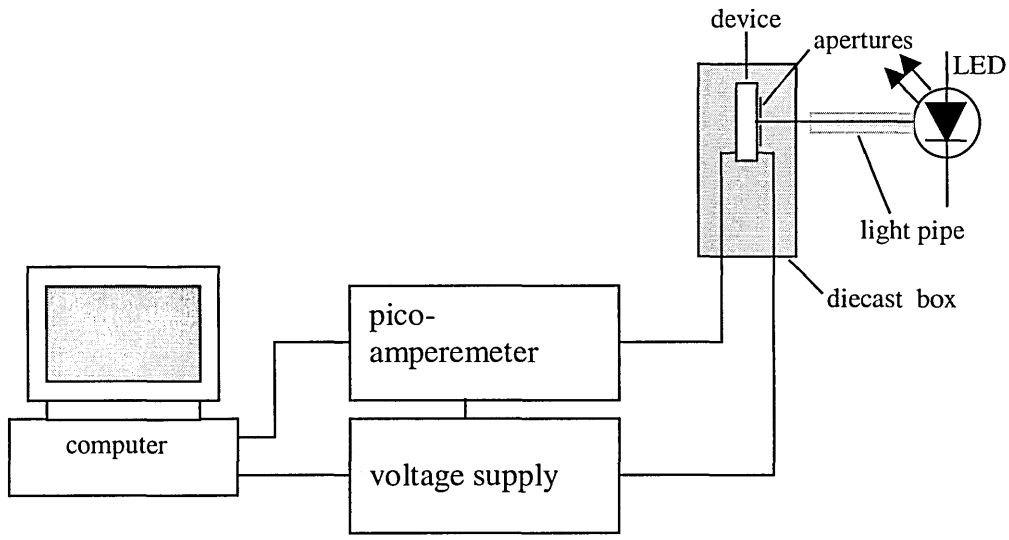

Figure 3.1: Experimental set-up for *i-v* characteristics.

were stored. Otherwise, after another doubled time delay, a third set of measurements was taken. The new average value was then compared with the last one until a satisfactorily small deviation was reached and the data set was stored.

With this procedure drifting currents were avoided and only settled values were measured and taken into account.

Dark *i-v* characteristics give direct information about the diode characteristic of the device and constitute an important measurement of the quality of solar cells. Detectors reveal much of their characteristics in a dark *i-v* curve.

The saturation current of a non-illuminated solar cell or detector can give approximate information on the number of defects in the sample:

When

$$G = \nu \exp(-\Delta E/kT) N_D \,, \tag{3.1}$$

where G is the (thermal) generation rate, ν is the attempt-to-escape-frequency, ΔE is the energy of the defect in relation to the conduction band and N_D the number of defects.

Furthermore

$$j_d = qGV \,, \tag{3.2}$$

where j_d is the measured dark current density, q the elementary charge and V the volume defined by the area of the sample contacts and its thickness.

From equation 3.1 and 3.2, it follows that

$$N_D = j_d/(\nu \exp(-\Delta E/kT) qV) \,. \tag{3.3}$$

N_D defines the number of defects in the sample. Of course this is an approximation in the assumption of a single energy level for ΔE but the result should be seen as an estimation of the defect number in the sample used for later photogating experiments.

3.1.2. Collection efficiency

For the single beam collection efficiency measurements two experimental arrangements and measurement techniques were used: one was an ordinary collection efficiency measurement with a set-up as shown in Figure 3.2 and the second one gave similar spectral information, with knowledge of the incident photon flux by analysing the measured *i-v* data which were obtained from measurements with the set-up described in the previous section (Figure 3.1).

The arrangement shown in Figure 3.2 had two light sources, a xenon-arc-lamp (Xe-lamp) for wavelengths $\lambda < 650$ nm and a halogen-lamp (Ha-lamp) for wavelengths above that. A single monochromator was used and also filters to block higher orders of the diffracted light. The light beam passed a chopper before entering the monochromator. Behind the monochromator a collimator and an aperture were used.

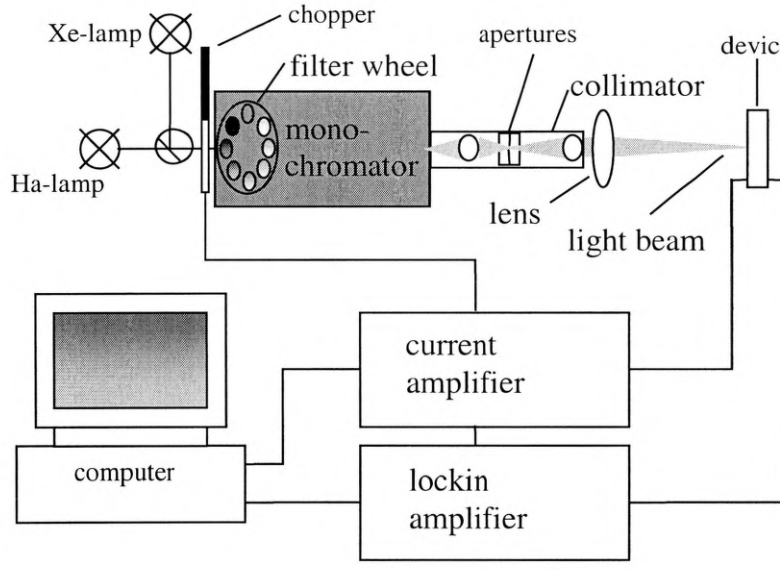

Figure 3.2: Experimental set-up for collection efficiency measurements.

The image of the aperture was imaged on the sample after passing the collimator and a lens. A calibrated photodiode (Hamamatzu) was used as a reference detector cell. On both the sample and the reference cell the illuminated area was chosen to be smaller than the respective device's contact. The signal was amplified by a current amplifier and read out by a lock-in-amplifier.

The measurement itself was done with a calibration run over the wavelength range of the actual measurement on the reference cell followed by the measurement on the sample.

The single beam collection efficiency is calculated as

$$\eta_{ext}(\lambda) = j(\lambda,V)/q\Phi(\lambda), \tag{3.4}$$

where $j(\lambda,V)$ is the measured current density in the sample examined and $\Phi(\lambda)$ is the incident photon flux at the wavelength λ. Taking no reflection and transmission into account equation 3.4 defines the external quantum efficiency. Since the absorption in a-Si:H is very high in the measured part of the spectrum and the samples are very thick, then neglecting transmission, the internal efficiency is defined as

$$\eta_{\text{int}}(\lambda) = \eta_{ext}(\lambda)/1 - R(\lambda), \tag{3.5}$$

where $R(\lambda)$ is the wavelength dependent reflectivity.

For the second method spectral information could be converted from the *i-v* measurements to collection efficiency data: with a knowledge of the incident photon flux $\Phi(\lambda)$ the collection efficiency η could be calculated from the current measurements i_{ph} of a defined illuminated area A:

$$\eta(\lambda) = i_{ph}/qA\Phi(\lambda). \tag{3.6}$$

Here, losses in the contacts were taken into account so that an internal collection efficiency is obtained.[4]

3.2. The dual beam experiment

Under certain circumstances the collection efficiency of a second, *probe* beam applied in addition to the bias illumination, can exceed unity. This effect is also termed as *gating* (Maruska et al., 1984). The principle of the dual beam collection efficiency measurement or gating involves a strongly absorbed bias beam and a weakly absorbed probe beam. For a-Si:H these specifications are satisfied for a bias wavelength of $\lambda_b \approx 470$ nm and a probe beam wavelength of $\lambda_p \approx 620$ nm. Further, the bias beam photon flux should be at least one order of magnitude higher than to the probe beam photon flux. The photogated collection is found for the probe beam.

The collection efficiency of the *probe* beam values under bias illumination are calculated as

$$QE = (i_{bp} - i_b)/(qA\Phi_p), \tag{3.7}$$

where A is the device cross-section area, q the electronic charge and Φ_p is the incident probe beam photon flux. i_{bp} and i_b are the measured currents. For the current densities j_{bp} under bias *and* probe illumination and j_b under bias *only* illumination:

$$QE = (j_{bp} - j_b)/q\Phi_p. \tag{3.8}$$

The resulting collection efficiency values for each voltage are therefore calculated from the differences between the two measured *i-v* curves with an applied bias *and* probe beam, and with an applied bias beam *only,* in relation to the incident photon flux (of the probe beam).

[4] Transmission of the contacts was taken into account using information from the institutes which made them. Furthermore on these samples full collection at high reverse voltages was verified (Zollondz, 1995).

In previous work, the p-i-n sample is illuminated with a bias beam from the p-side and a probe beam from the same side. (Maruska et al., 1984) This layout is not the only one to observe high collection efficiencies but is the only one published by other research groups. Due to the nearly homogenous absorption profile of the probe beam, a beam set-up with the bias beam from the p-side and the probe beam from the n-side results in even higher collection efficiency results, as the present author has reported (Zollondz et al., 1996, Brüggemann et al., 1997, Main et al., 1999). Reversing probe and bias beam to n-side bias and p-side probe (Zollondz et al., 1998, Zollondz et al., 1999) results is another possible beam situation that was investigated.

The arrangement used (Figure 3.3) is different in one crucial way from all other arrangements of measuring the photogating effect reported in the literature (Maruska et al., 1984, Hou and Fonash, 1992, Rubinelli, 1994, Chatterjee, 1994, Bae and Fonash, 1996, Binnewies, 1997, Unold et al., 1999). The experiment presented here is a two step *steady state* experiment with time intervals controlled by a computer program, so that

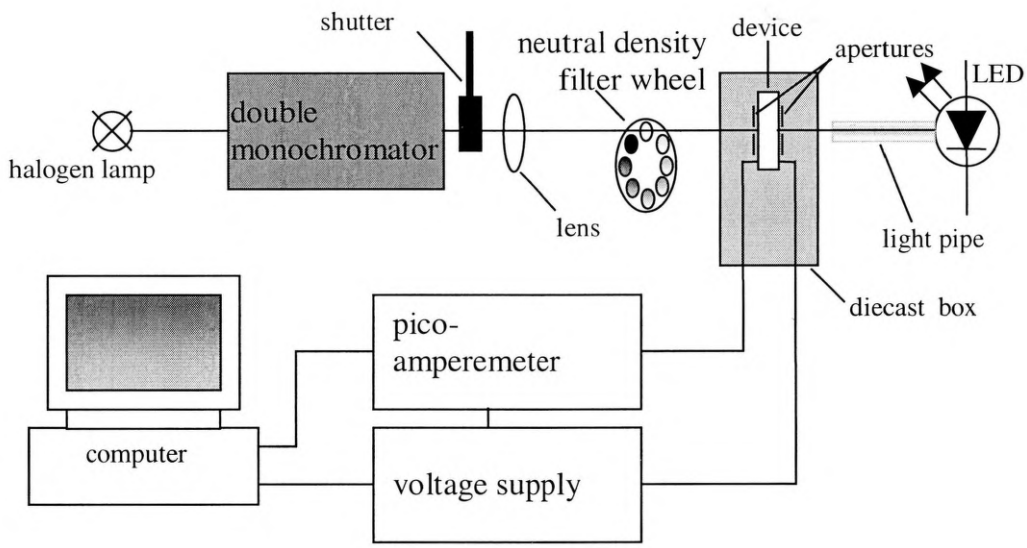

Figure 3.3: Experimental set-up for steady state measurements.

always settled photocurrent values were reached, whereas all other groups used lock-in techniques. Unless very low chopping frequencies are used for the lock-in-technique in connection with photogating experiments 'pseudo-settled' values or even values which have not properly settled can be measured (see chapter 6 section 6.5 *Transient response of the photogating effect*).

Because of slow response times in the dual beam experiment a shutter and an Electrometer (Keithley 617) were substituted for the usual chopper wheel and the lock-in technique. The measurement procedure was a dual steady state measurement, where one measurement was with bias *and* probe beam, and one with bias beam *only*. The voltage steps were controlled by the personal computer (see next section 3.2.1) and applied by the Electrometer.

In chapter 6 it will be shown that these values show the highest gains for the photogating experiment and should give the most reliable results for different samples.

The experimental set-up itself for steady-state, dual beam, gated collection efficiency measurements is shown in Figure 3.3. The probe beam was generated by a halogen bulb, was made parallel by a condenser lens in the lamp housing, and was directed onto the slit (1.5 mm) of a double monochromator (full width at half maximum (FWHM) $\leq$ 20 nm at a slit width of 1.5 mm for the used wavelength range). The intensity of the monochromatic light beam was varied with neutral density filters.

The monochromatic bias light was generated with light emitting diodes (LEDs) and incident on the sample through a light pipe, which is made of perspex. Make, type, peak wavelengths and FWHM values of the LEDs[5] used can be found in the appendix A.1.

[5] There was no difference between calibration curves taken before and after all measurements.

The sample was positioned in a diecast box, so that external electrical fields did not influence the measurements. Furthermore the inside of the diecast box was painted black so that scattered light was avoided. The deposited metal electrical contacts were connected with silver paint. Apertures were used to define the illuminated area.

3.2.1. Computer controlled measurement program

Because of long settling times and very small currents computer controlled measurements were used. A procedure based on a *Pascal* *i-v*-measurement program (Rösch, 1996) was developed to acquire two photocurrent measurements giving sufficient time for settling, i.e. for the measurement with bias beam illumination *only* and with probe *and* bias illumination.

The whole experiment was controlled by a personal computer apart from the probe beam wavelength and the probe beam photon flux: the computer program first switched the bias LED on and waited for a certain time to let the LED reach a steady light output. While the shutter for the probe light was closed, a voltage was applied and a set of n measurements of the current was taken. The average of the n measurements was compared with a second set of n measurements taken after a time interval t. If the two average values differed too much, (this can be set in the program) a third set of n measurements was taken after a time delay of $2t$, and compared with the second set until two average values did not differ more than a chosen value. The normal value for n (the number of measurements) was $n = 20$, for the interval time $t = 1$ s, and for the maximum deviation of two measurements series 0.1 %. After this first set of measurements was taken the position of the shutter changed so that for the same voltage the same procedure was carried out for the measurement with additional incident probe beam.

As described above the whole program is based on an *i-v* measurement in which the next voltage is applied only after the position of the shutter blocks the probe light. The measurements were mainly made using voltages of V = 1.0 V (forward) to V = – 20.0 V (reverse).[6]

The following parameters were recorded:

- the *i-v* measurement values with and without probe illumination with their individual total acquisition times
- the calculated collection efficiencies values
- the used parameters like n, t, the allowed percentage variation and the direction of the measurement (forward bias to reverse bias or *vice versa*).

There was a second output file written with the measured values only for data conversion to graphs.

3.3. Transient dual beam measurement

Figure 3.4 shows the experimental set-up for all transient measurements. In contrast to the steady state measurements, the probe beam here is provided by an LED driven by a pulse generator. The measured signal is amplified using an operational amplifier (OPAMP 613) and recorded with a storage oscilloscope. Data were transferred to a PC for detailed analysis.

The beam specifications were the same as described in section 3.2, where the steady state gating experimental parameters are explained. An exception was the probe beam wavelength set to the specification of the LED used, at λ_p = 610 nm and not λ_p = 620 nm as for steady state experiments.

[6] Although a forward voltage bias value (+1 V) was taken for control purpose these values were not included in most figure which focus on reverse applied voltages (primary photocurrents).

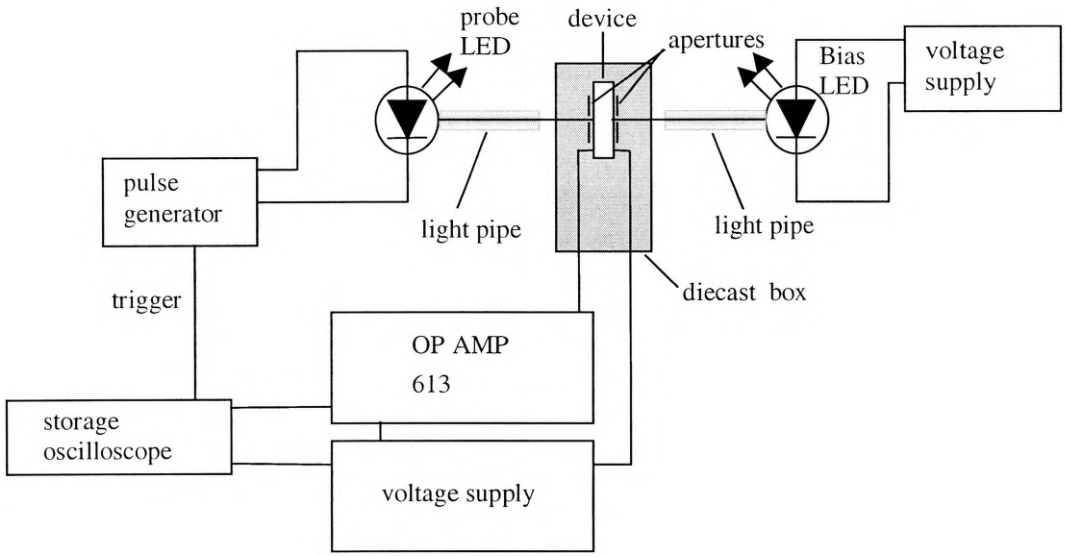

Figure 3.4: Experimental set-up for transient measurements.

The set-up was designed to measure two features of the response of a gated photocurrent:

- The first study was to measure the response with respect to chopper frequency variation. Long settling response times observed initially motivated a study using a 'simulated chopper'. The simulation of a chopper wheel was done by switching the LED on and off at different frequencies.

- A second study looked at the response times of the gating effect. For this experiment low frequencies were chosen (5mHz - 50mHz) to monitor the switch on (and switch off) response of the effect. Here a study of probe beam photon fluxes and a study of degradation on the gated response time was aim of research.

4. Simulation Program

The simulation program used is based on code developed by Wei Gao (Gao, 1995). The program 'SPIN' simulates steady state situations with electronic processes for amorphous semiconductor materials and devices under different optical excitation and applied voltage conditions. The name of the program *SPIN* stands for steady state p-i-n.

Table 4.1: Input parameters for a 0.5 μm thick a-Si:H p-i-n steady state photodiode simulation.

Device thickness	d	0.5 μm
Fermi level in doped layers	E_F-E_V *(p)*	0.35 eV
	E_C-E_F *(n)*	0.25 eV
Characteristic energies for band-tails	E_{CT}	0.025 eV
	E_{VT}	0.045 eV
Doped layer thicknesses	t_n, t_p	20 nm
Optical gap	E_g	1.8 eV
Band edge density of states	$g(E_C)$, $g(E_V)$	2×10^{21} cm^{-3} eV^{-1}
$D^{+/0}$ energy	$E^{+/0}$-E_V	0.8 eV
Defect correlation energy	U	0.35 eV
Free electron and hole mobilities	μ_n	10 cm^2 (Vs)$^{-1}$
	μ_p	1 cm^2 (Vs)$^{-1}$
Capture coefficients:		
Band - tails (CT, VT)	σ_n, σ_p	10^{-9} cm^3 s^{-1}
Neutral defects D^o	σ_n^0, σ_p^0	10^{-8} cm^3 s^{-1}
Charged defects D^+, D^-	σ_n^+, σ_p^-	10^{-7} cm^3 s^{-1}

By solving the Poisson's equation and the carrier continuity equations with a modified Gummel's approach (Gummel, 1964) a number of internal parameters can be calculated (see subsection of this chapter). While the original program was developed for solar cell simulation, it is suitable with modification for dual beam simulations.

The program subdivides the device (thickness) into thin layers[7] and solves Poisson's and the continuity equations after an initial guess of parameters, which result from the boundary conditions. These are set by the assumption of thermal equilibrium at the two outermost boundaries, hence ohmic contacts.

The following sections will give some examples and show the potential of the simulation program for a single p-side illuminated (λ = 450 nm) sample (d = 0.5 μm) with no applied bias voltage. The photon flux is chosen to $\Phi = 2\times10^{15}$ cm^{-2}s^{-1}. Further input parameters are stated in Table 4.1. All figures in this chapter are based on these conditions.

4.1. Generation and recombination

Generation in a-Si:H due to strongly absorbed light can be very high close to the illuminated contact. This example is presented, since it corresponds to the situation of the strongly absorbed 'bias' beam in the dual beam experiment. The generation profile shown in Figure 4.1 of a p-side incident beam of λ = 450 nm decreases steeply after entering the sample. The corresponding absorption coefficient $\alpha = 3.3\times10^{5}$ cm^{-1} results in an absorption depth of $1/\alpha$ = 30 nm.[8] I.e. in the case discussed here generation is

[7] These sub-layers can be equidistant or non-uniform distributed, where a non-uniform discretisation of the device show more detail in some rapidly changing or more interesting regions such as the p-i and i-n interfaces.

[8] For an incident wavelength of λ = 660 nm with an absorption coefficient of $\alpha = 1\times10^{4}$ cm^{-1} the absorption depth $1/\alpha$ = 1 μm. For this situation the generation profile can be termed homogenous.

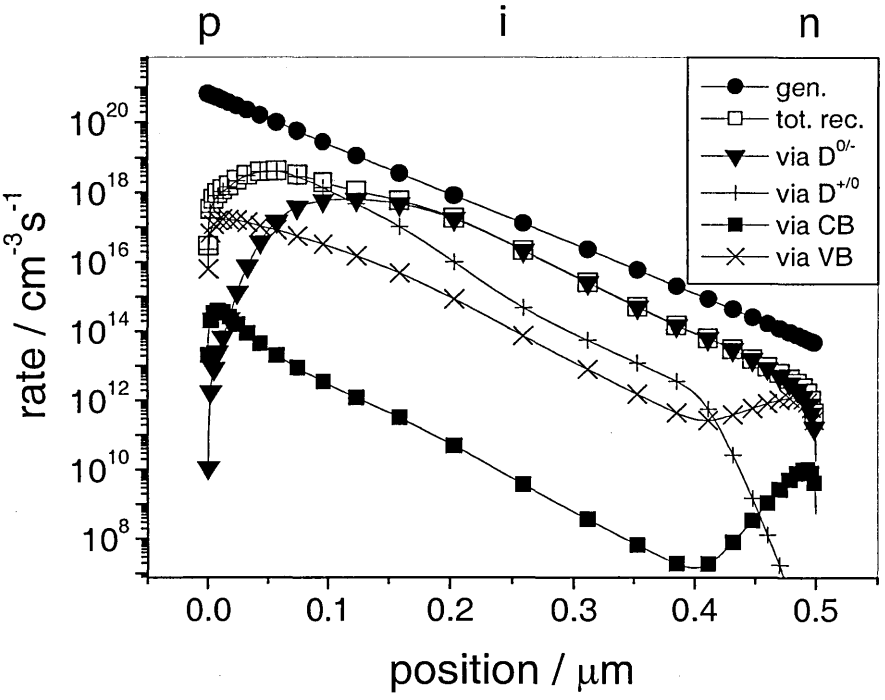

Figure 4.1: Generation and recombination profiles

observed only close to the p-i interface. Generation at the boundary is 6.6×10^{20} $cm^{-3}s^{-1}$, whereas $1/\alpha$ deep in the sample generation is 1/e less, i.e. 2.4×10^{20} $cm^{-3}s^{-1}$.

Figure 4.1 also shows the recombination rates. Recombination *via* the conduction band tail and the valence band tail are far lower than the possible recombination paths *via* the dangling bonds, although recombination *via* the valence band tail is, in most areas, more than three orders of magnitude higher than that due to the conduction band tail. This is because the valence band tail reaches deeper into the band gap. The deeper the state the higher the thermal re-emission time and hence the higher the recombination probability. Nevertheless the dominating recombination paths are found in dangling bonds. In the front of the sample via $D^{+/0}$ and in the back of the sample via $D^{0/-}$, with a cross-over approximately 0.12 μm deep in the sample. Since the dangling bond states

are deep in the band gap, the domination by these paths is not unexpected. At the front of the sample, the recombination path via $D^{+/0}$ dominates because the high number of holes in this area "fill" a high number of the dangling bonds to the D^{+} state, which then are the recombination centres for electrons. At the back of the sample, from a depth of 0.12 µm the dominating recombination path is found via $D^{0/-}$. Here the electrons are captured in D^{0} to produce D^{-}, which are recombination centres for holes in this area. The total recombination rate is mainly controlled by recombination via $D^{+/0}$ and $D^{0/-}$.

4.2. Occupation

Information about occupation states are given for free electrons and holes (Figure 4.2) and for trapped charge in the tails states and the dangling bond states (Figure 4.3 and Figure 4.4). Free charge carriers are "free" for transport duties while the more dense

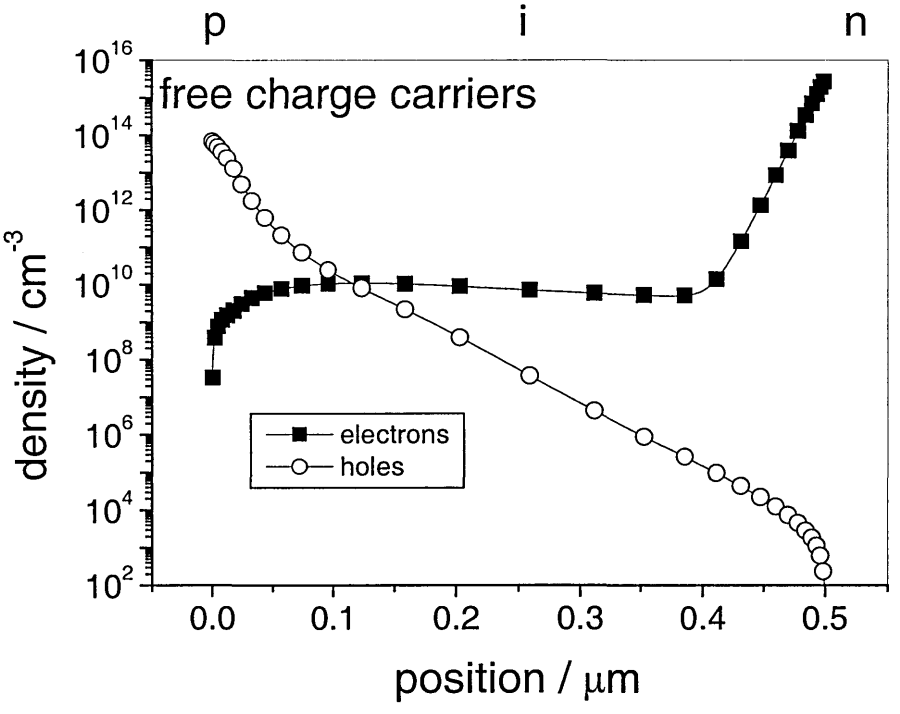

Figure 4.2: Occupation densities of free charge carriers.

trapped charge contributes to the potential, and hence electric field. Except at the front, close to the p-i interface where free holes dominate, from a depth of 0.1 μm to the back of the sample, the electrons are the dominant free charge carriers.

In Figure 4.3 and Figure 4.4 the total charge is shown as well as the single occupation densities in the different states. Figure 4.3 shows that the dominant trapped charge carriers in the front of the device, that also determine the local charge, are found in trapped valence band (VB) tail states. Figure 4.4 shows that from 0.12 μm the D^- states are taking over as the dominant charge states, which forces the sign reversal, showing as a cusp on a logarithmic scale.

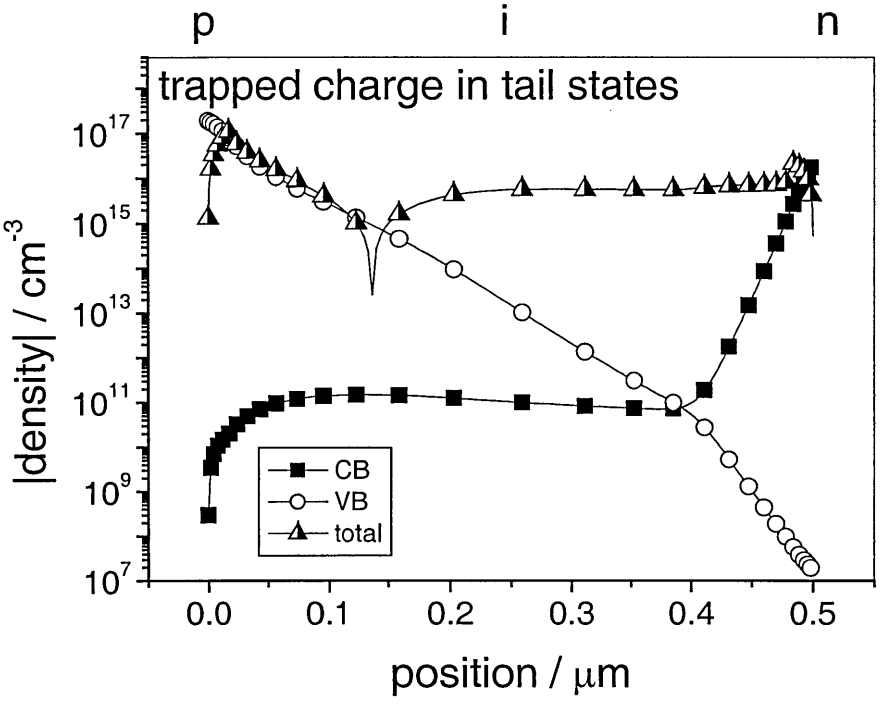

Figure 4.3: Occupation densities of trapped charge in band tail states and total charge distribution.

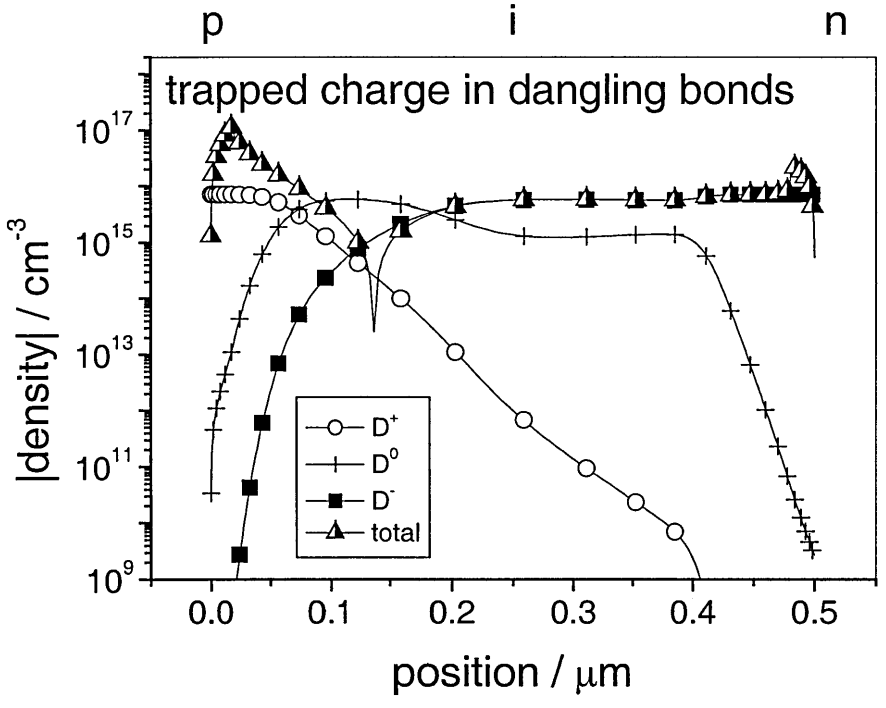

Figure 4.4: Occupation densities of trapped charge in dangling bonds and total charge distribution.

4.3. Band diagram

Figure 4.5 shows the calculated band diagram and quasi-Fermi-levels of a p-i-n diode under illumination. The Fermi-level that is observed for a diode in darkness splits, under illumination, into two quasi-Fermi-levels – one for electrons and one for holes. Although the Fermi-level or quasi-Fermi-levels never reach the conduction or valence

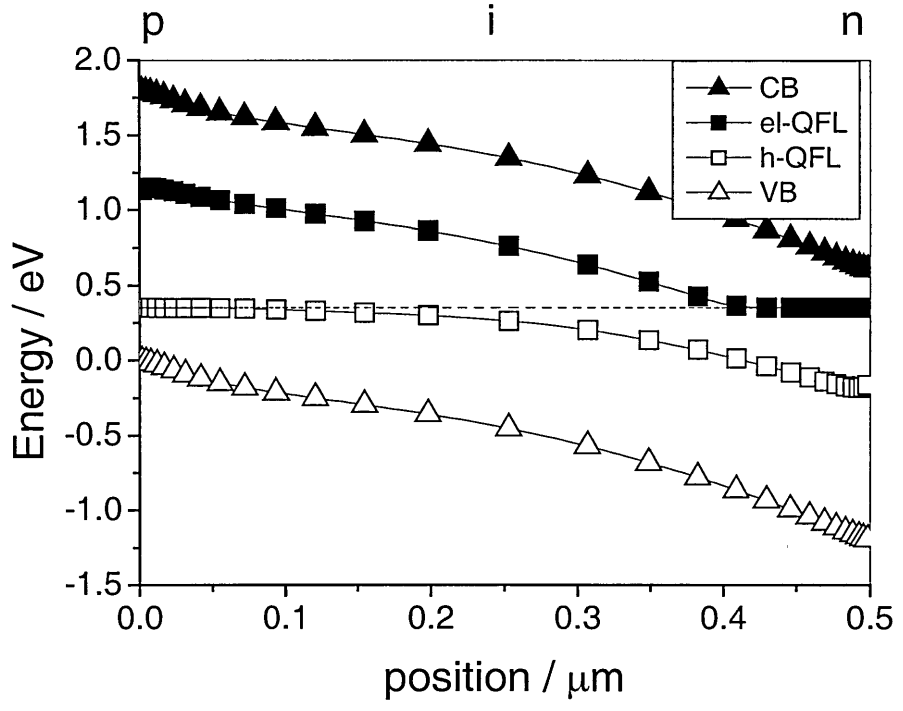

Figure 4.5: Simulated band structure of a p-i-n device with quasi-fermi-levels (the dashed line gives the dark Fermi-level for the sample without illumination).

bands the distance to the band in the doped areas gives information about the doping. The gap between valence band and Fermi-level is approximately 0.35 eV and is higher than the gap from the conduction band to the Fermi-level with an approximate value of 0.25 eV, due to the steeper tail and more efficient n-doping in a-Si:H.

4.4. Current and transport

In this section the different partial current densities for electrons (Figure 4.6) and holes (Figure 4.7) are examined. Comparison of the electron current in Figure 4.6 and hole current in Figure 4.7 with the total current shows that the current is carried mainly by electrons. Only at the very front of the sample (close to the p-i-interface) does the hole current constitute the total current. Here, as at the back (close to the n-i-interface), the majority carrier currents compete in drift and diffusion. At the front of the sample, the dominating partial currents are hole-drift and hole-diffusion currents. These currents nearly compensate for each other, but the drift current exceeds the diffusion current so that the total amount here is given by their difference.

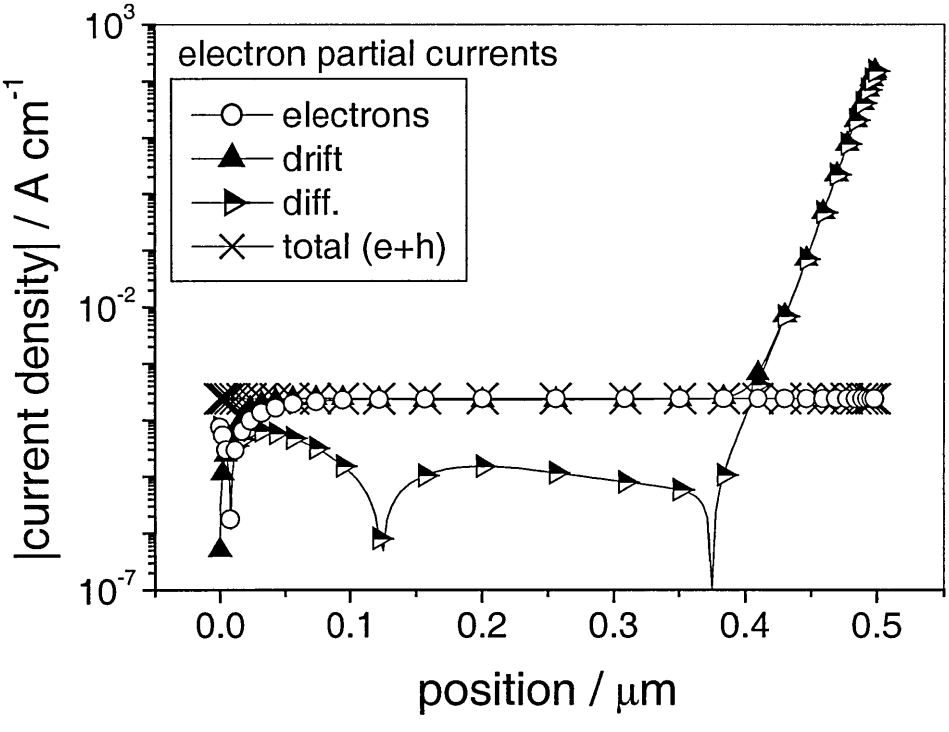

Figure 4.6: Electron partial current densities and total current density.

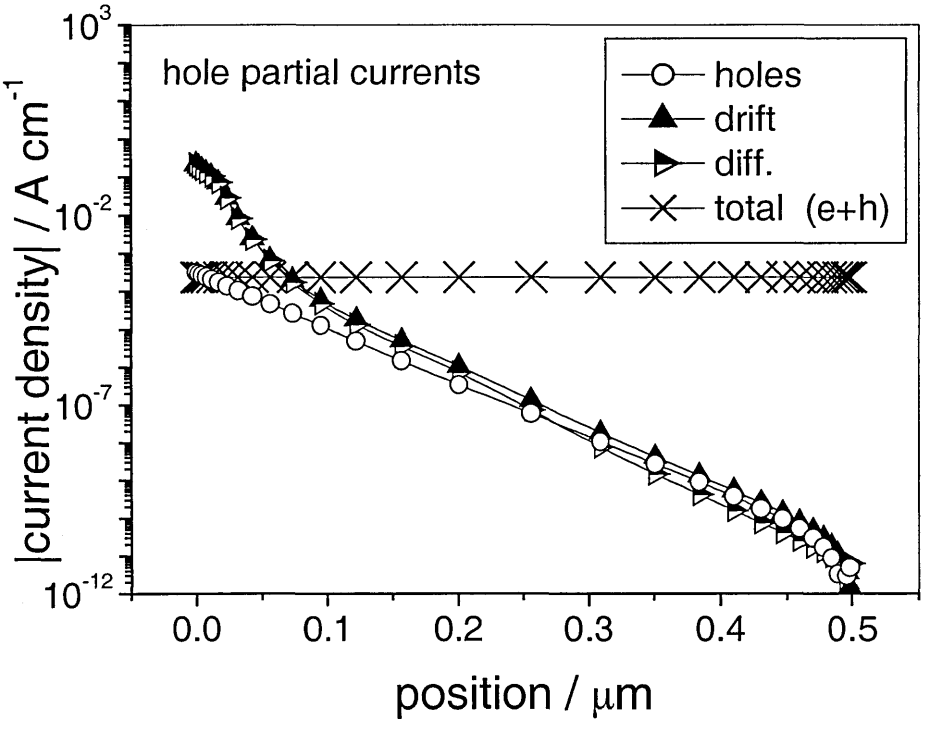

Figure 4.7: Hole partial current densities and total current density.

Elsewhere the electron-drift-current dominates all partial currents (of holes and electrons) over a wide spatial range (0.02 μm – 0.4 μm). Similarly, competing drift- and diffusion-currents for electrons are observed at the back of the device. The resulting total current is found from the difference of diffusion and drift current and is dominated by the drift current. The influence of the electron-diffusion current is small, (two orders of magnitude smaller than the total current) except in this region, hence the dominating partial current is the electron-drift-current.

4.5. Other data available from simulation

The simulation also provides data for the DOS, i.e. band tails, the dangling bond distribution and also drift and diffusion lengths and electron and hole life times. Since these data are of no interest in the situation considered here, these data are not presented

for this example. Out of these data only the dangling bond distribution is considered in later sections of this work.

Adaptation and variation of the dangling bond distribution was an important modification described in chapter 6 section 6.4.1. *Gating and inhomogeneous defect distributions*. Here the source code of the program had to be modified to achieve suitable defect distributions to fit measured results.

5. Basic device features and results

In this chapter the different sample sets are classified by giving the deposition parameters and by use of some standard measurement methods.

Deposition parameters of all the sample sets studied are shown in section 5.1. In the following sections standard characterisation methods are used to describe the samples and to estimate some device parameters: section 5.2 will show results of dark current-voltage characteristics while in section 5.3 the illuminated sample is the subject of investigation on photocurrent-voltage characterisation. Section 5.4 will show results of an ordinary single beam collection efficiency measurement. These results are discussed in the context of *'normal'* collection efficiency results but will be referred to in later investigation - of the dual beam photogated collection efficiency discussion in section 6.1 and section 6.2.

5.1. p-i-n sets and specifications

The first set of samples was deposited at the Dundee University with i-layer thicknesses of $d = 0.5\ \mu m$, $1.5\ \mu m$ and $3.5\ \mu m$. These samples (internal label of Dundee University 1326 – 1330) were all made with *plasma enhanced chemical vapour deposition* (PECVD) in an one chamber deposition unit. In all cases the doping in the n+ layer was 3000 vppm PH_3 in SiH_4 and 10000 vppm B_2H_6 in SiH_4 for the p+ layers. For all samples both doped layers are approx. 25 nm thick.

The flow rate for all process gases was 8 sccm and the working pressure in the chamber was always 220 mtorr. The radio frequency power was 3 W at 13.56 MHz and the substrate temperature was approximately 230°C. The electrodes of 0.2 mm diameter

front contact and a flat back contact were made of semitransparent Chromium with a transparency of $t \approx 0.1$.

table 5.1: Sample specifications and deposition parameters.

Sample set		Dundee Univ.	Dundee University set			IPE Stuttgart set		
	sample	970	1326 / 1327	1328	1329 / 1330	TA	TB	TC
Sample specifications								
	i-layer thickness d / µm	3.5	0.5	3.4	1.5	1	2	3.5
	doped layer thicknesses / nm	20	25			30		
Contact specifications								
	diameter / mm	2	2			2.8		
	material	Cr	Cr			TCO		
	transparency	~0.1	~0.1			~0.9		
Deposition parameters								
	PECVD no. of chambers	1	1			3		
	n^+ doping / vppm	3000	3000			-[9]		
	p^+ doping / vppm	10^4	10^4			-[9]		
	Gas flow rates / sccm	8	8			-[9]		
	Working preasure / mT	250	220			-[9]		
	Radio frequency power (13.56 MHz) / W	3	3			-[9]		
	Substrate temperature / °C	275	230			-[9]		

[9] No information given but can be assumed as standard values.

Samples with similar deposition parameters of an earlier prepared set of a thickness of d = 3.5 μm p-i-n's were also used (Dundee University identification 970).[10]

The third set of samples was deposited at the IPE (Institut für physikalische Elektronik) in Stuttgart (Germany). The i-layer thicknesses were d = 1 μm (label TA), d = 2 μm (label TB) and d = 3.5 μm (label TC) with p- and n-layer thicknesses of 30 nm. TCO electrodes for front and back contacts were used, where the front circular electrode, or 'spot' was 2.8 mm in diameter while the back contact was completely covering the glass substrate. Optical transmission for both contacts was given as $t \approx 0.9$. Information about the deposition parameters as flow rates and chamber pressure are not given, but are assumed as standard values as above. Here a three chamber system was used for the PECVD deposition.

5.2. Dark current-voltage characteristics

The dark current-voltage (*i-v*) characteristic (or dark current-density-voltage (*j-v*)) gives direct information about the diode behaviour of the device and is also an important indicator of the quality of solar cells and detectors.

Since the samples used here are detectors with poor solar cell qualities, dark *i-v* characteristics do not have quite so much practical importance as for solar cells, but contain useful information on the nature of the devices used.

[10] Actually was this set (970) the set of first measurements with QE > 1, and the set described above (1326-1328) was a second run with similar specification to have a set of new samples to investigate further in quantum efficiency values greater than unity by gating.

It is noted that the applied voltage range in comparison to usual solar-cell type a-Si:H samples with thicknesses of approximately d = 0.5 μm of V = -20 V (or later even -40 V) used in this work seems to be very high. However, taking into account the thickness of d = 3.5 μm this gives an applied electric field of approximately E = 6×10^4 Vcm^{-1}. This would be equivalent to an approximate applied voltage of V = -3 V for a d = 0.5 μm thick sample. Such a reverse applied voltage value is not even high for a "normal" sample of a thickness of d = 0.5 μm. Crandall et al. (Crandall and Sadlon, 1989) applied even higher effective electric field values (E = 100000 Vcm^{-1}, i.e. V = 100V at a d = 10 μm thick a-Si:H p-i-n sample).

In Figure 5.1 the dark current densities-voltage (j-v) characteristics are shown for typical samples from the three sets used. Since the thinner samples do have lower applied reverse voltages, the three different thicknesses of the 'IPE' set are shown in

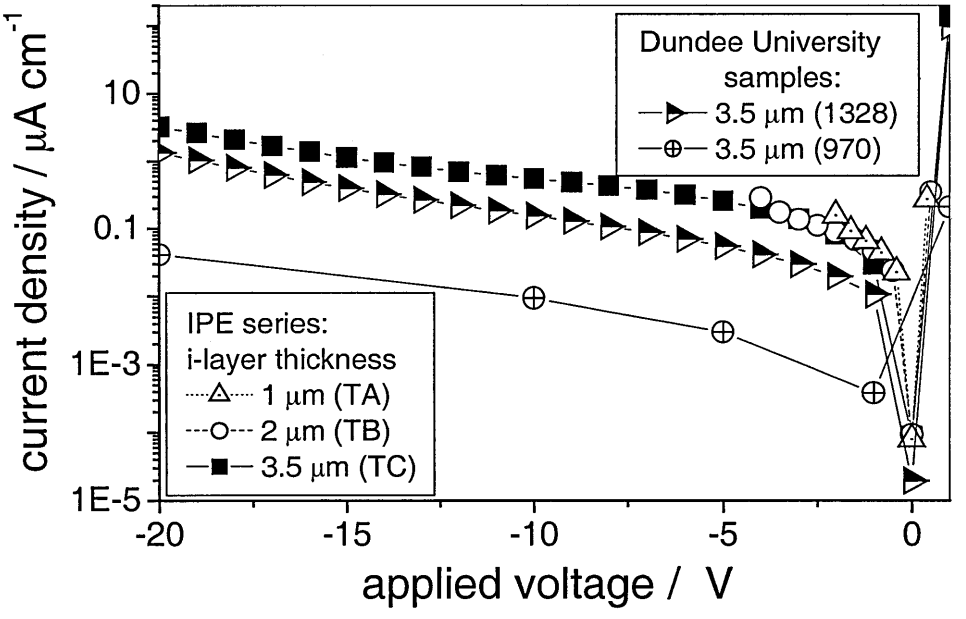

Figure 5.1: Dark j-v characteristics of typical samples.

Figure 5.2 with a different abscissa - the average internal electric field, which allows a more direct comparison of the sample behaviour over a range of thicknesses. The samples were not degraded for any of these measurements.

As described earlier (section 3.1.1 equation 3.3) the leakage dark current can contain information about the defect density, related by using

$$N_D = j_d/(\nu \exp(-\Delta E/kT)qV) \tag{5.1}$$

to defect densities shown in table 5.2. For all samples of the IPE series and for the sample no. 1328 of the Dundee University the results give reasonable defect densities with values of $N_D \leq 10^{15}$ cm^{-3} for the thinner samples (sample TA and TB) and $N_D \approx 10^{16}$ cm^{-3} for the d = 3.5 μm samples from different sources (TC and 1328). But for the sample no. 970 the defect density seems to be very low for a thickness of d = 3.5 μm.

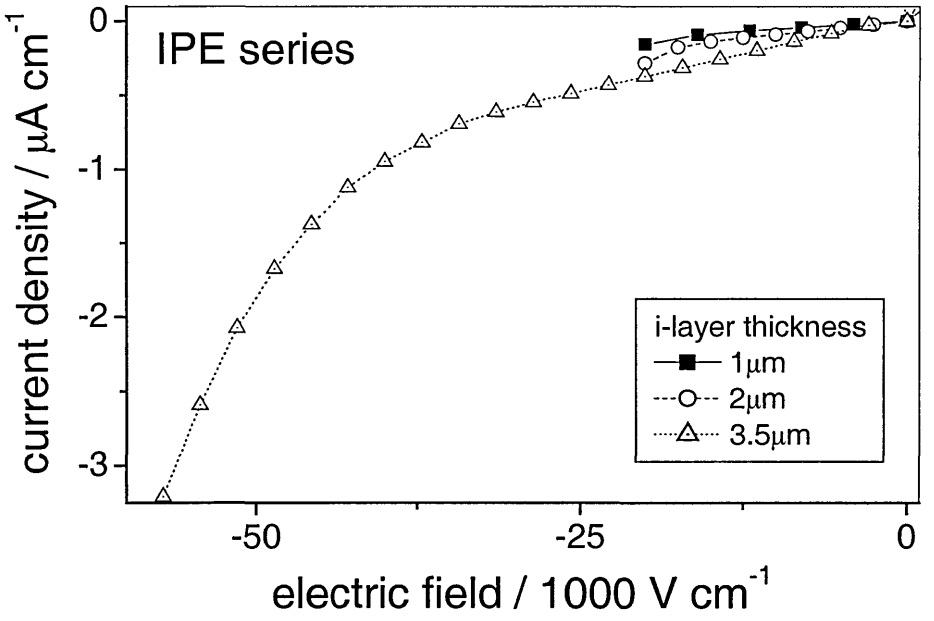

Figure 5.2: Current density - electrical field characteristics for different sample thicknesses.

table 5.2: Calculated defect densities from saturated leakage current densities.

Sample	Saturation current density j / A cm^{-3}	Defect density N_D / cm^{-3}
TA (1.0 μm)	9.4×10^{-8}	7×10^{14}
TB (2.0 μm)	1.8×10^{-7}	1×10^{15}
TC (3.5 μm)	2.9×10^{-6}	2×10^{16}
1328 (3.5 μm)	1.3×10^{-6}	1×10^{16}
970 (3.5 μm)	4×10^{-8}	6×10^{14}

Here the technique using equation 5.1 fails. A closer look at the forward response of this sample shows that the forward characteristics is very poor. The low current values for V = +1 V and V = +1.5 V could originate from a high series resistance that must have an effect on the dark-saturation-current-density to shift it to seemingly lower values.[11]

5.3. Photocurrent–voltage characteristics

(Abel et al., 1991, Zollondz, 1995, Brüggemann et al., 1997) interpreted the appearance of an S-shape *i-v* characteristic as a measure of the degradation of a sample. In Figure 5.3 *i-v* characteristics measured in this work for different states of degradation are shown. The defect dependency is obvious. The shape of the *i-v* curve changes with an increasing number of defects in the sample. The degradation steps are the same as shown later for the photogating experiment.

[11] This argument is confirmed by result of photogating measurements, which show that especially this sample no. 970 was initially degraded.

Since the degradation series is discussed in detail in section 6.1.2 and a new *i-v* analysis is introduced in section 6.4.1 to compare results of degradation in the context of photogating the reader should refer to later chapters where the *first derivative* of these S-shaped *i-v* curves is compared with photogating results.

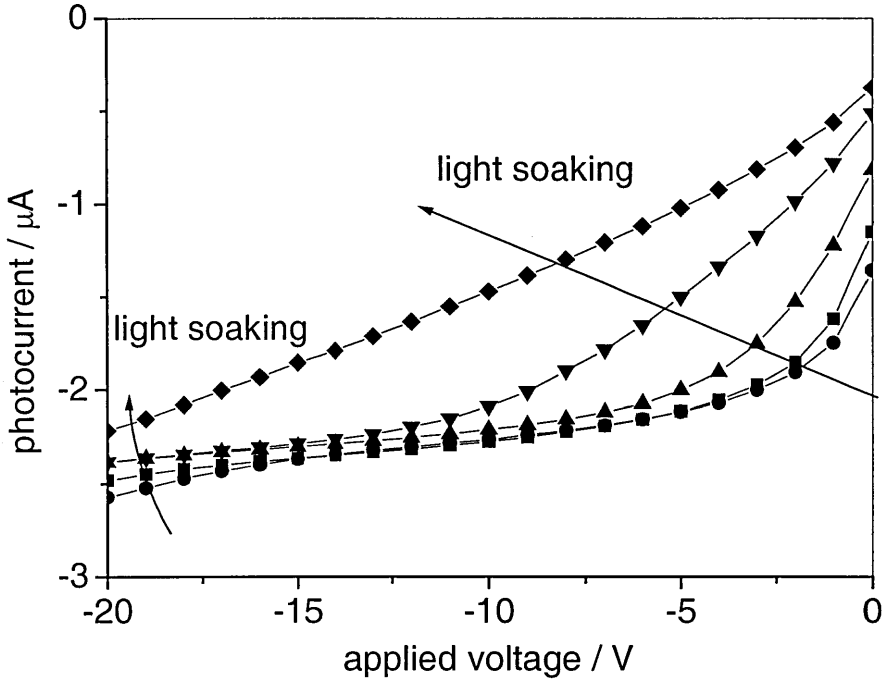

Figure 5.3: *i-v* characteristics of a sample in different states of degradation (the measurements correspond to electron gating experiments shown in Figure 6.12 (section 6.1.2 *Influence of light soaking (defect densities)*).

5.4. Collection efficiency measurements

The collection efficiency measurements presented in this section are ordinary single beam collection efficiency measurements. The experimental set-up is shown and explained in section 3.1.2. All measurements were undertaken on this set-up except for

the light soaking series, where the data were converted from *i-v* measurements (see section 3.1.2). The single beam was incident through either the p- or through the n-side.

Figure 5.4 shows the collection efficiency results from measurements on the d = 3.5 µm thick sample (IPE) illuminated on the p-side. Without an applied bias voltage the spectral collection shows a distinct maximum at a wavelength of λ = 620 nm and a broad shoulder at $\lambda \approx 520$ nm. For the higher applied voltage the collection efficiency on this shoulder approaches the peak value and a broad maximum is observed between λ = 520 nm and λ = 620 nm. Higher losses in the doped layer for lower wavelengths are found for wavelengths $\lambda \leq 520$ nm.

For n-side illumination (Figure 5.5) the two different applied voltages do not show this feature to the same extent. The maximum of collection for both applied voltages is found at $\lambda \approx 680$ nm. Nevertheless a shoulder is visible at $\lambda \approx 520$ nm and higher applied voltages should enhance this collection.

As described above the poorer collection at short wavelengths is caused by absorption in the doped layers. Since the doped layers are of the same thickness for n- and p-side, the poorer collection of n-side illumination of these wavelengths must be caused by another effect. Poorer collection, especially the very poor collection for wavelengths $\lambda \leq 600$ nm for n-side illumination is caused by the generation of charge carriers close to the illuminated n-side. Since the *holes* drift to the p-contact and electrons to the n-contact the holes have a longer path length to their contact. The situation is reversed for p-side short wavelength illumination: electrons have the longer path length to their contact. Because of the higher mobility of electrons in comparison to holes the collection is higher for p-side illumination. In principle this applies for all wavelengths since the absorption profile always declines from the incident side of illumination.

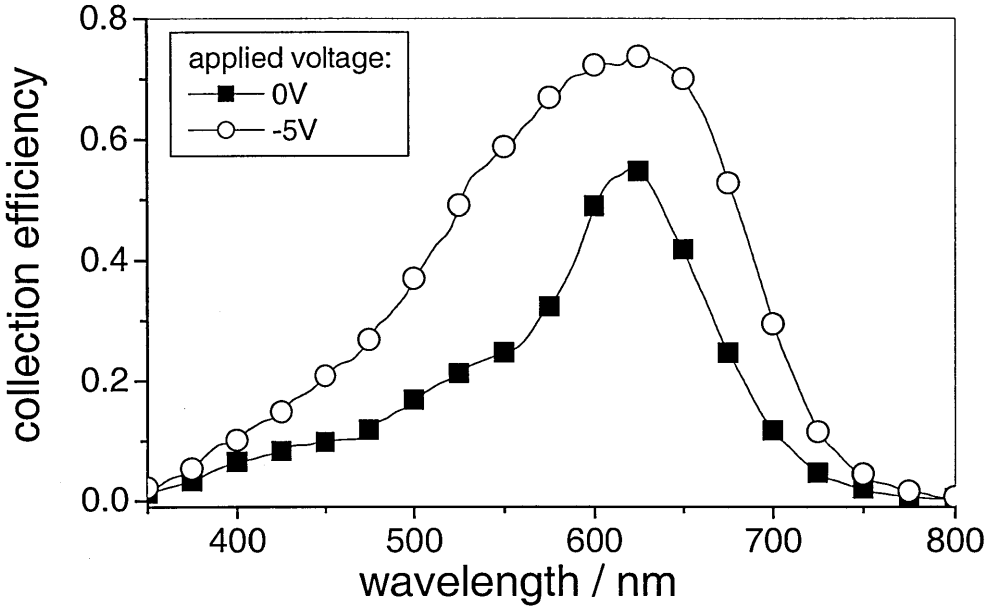

Figure 5.4: Single beam collection efficiency results with p-side illumination.

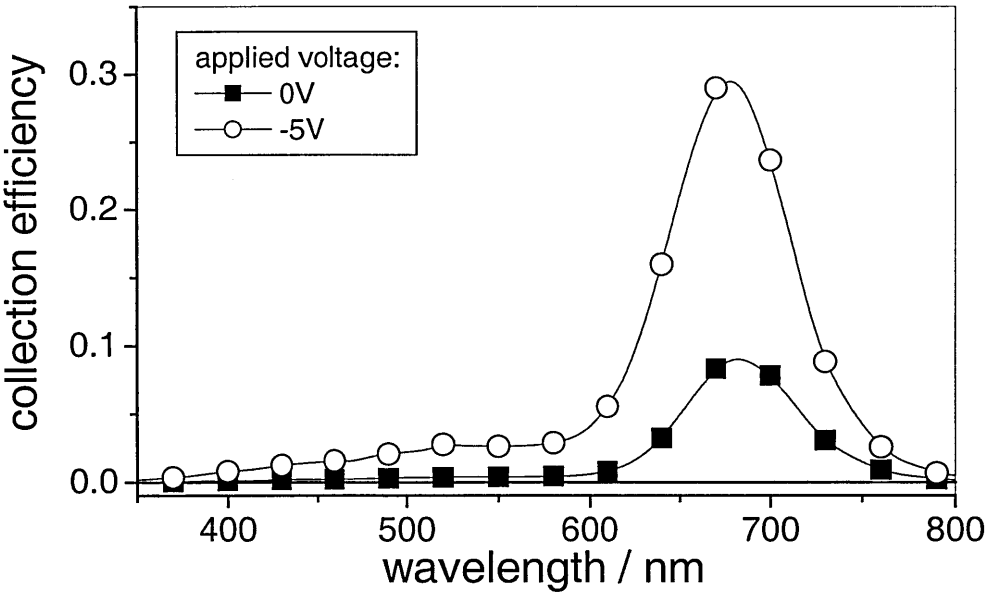

Figure 5.5: Single beam collection efficiency results with n-side illumination.

Figure 5.6 shows results from the two methods of measuring collection efficiency introduced in section 3.1.2. Although the method to calculate collection efficiency data from *i-v* measurements has to take into account the transparency of the electrical contacts, and gives an internal collection efficiency, the data fit very well to those taken from a relative measurement (external collection efficiency). This is due to the high transmission of the contact ($t = 0.9$) so that a relative error of 10 % is expected.

A second result from Figure 5.6 is that light soaking lowers the collection efficiency over the whole spectral range. The solid symbols in Figure 5.6 show ever lower collection efficiency values for all wavelengths for increased light soaking times.

Finally a study on collection efficiency measurements on different i-layer thicknesses was undertaken (Figure 5.7). For these measurements the voltage was

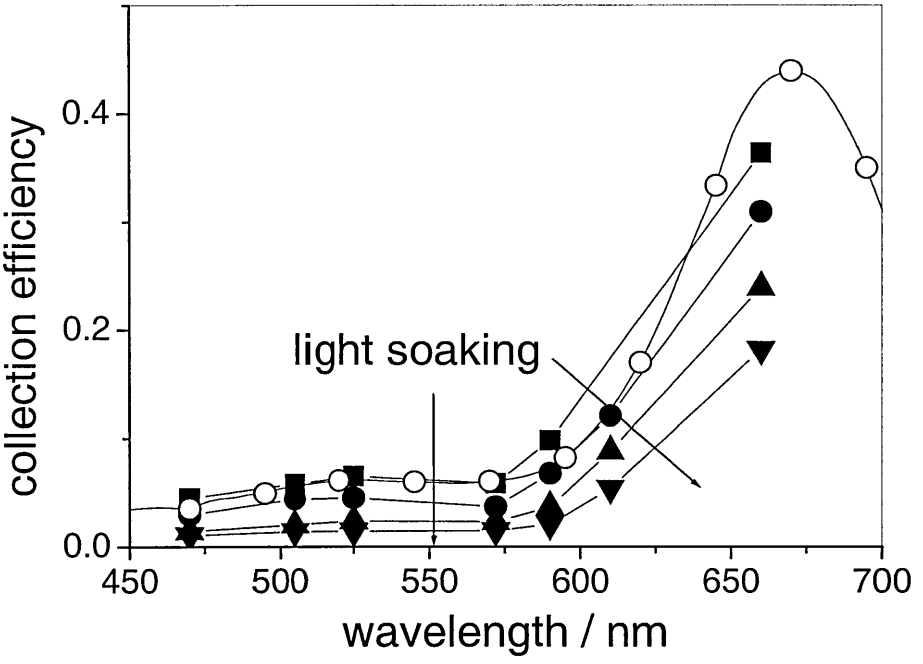

Figure 5.6: Comparison of data measured with an ordinary collection efficiency set-up (open symbols) with results from *i-v* data (full symbols), which show collection efficiency measurements for different states of degradation all taken at a bias voltage of $V = -5$ V and under n-side illumination.

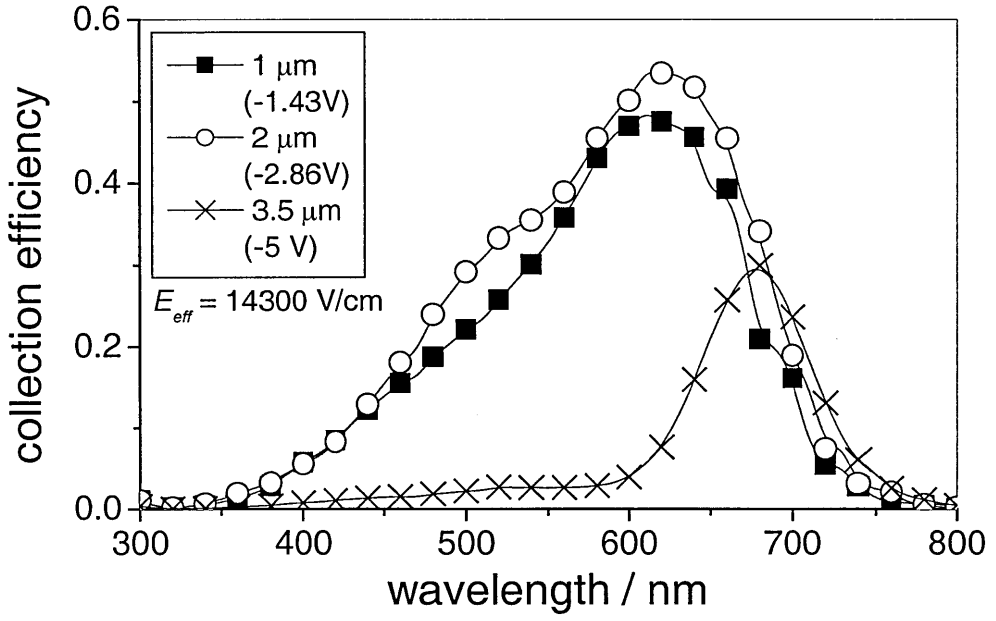

Figure 5.7: Single beam (n-side) collection efficiencies for different sample thicknesses under an applied electrical field of E_{eff} = 14300 nm.

chosen for each sample so that the average electrical field was kept constant. By adapting the voltage to the given sample thickness, i.e. applying V = –1.43 V at a sample thickness of d = 1 µm is equivalent to an electrical field of $E_{eff} \approx$ 14300 V, as is V = –2.86V applied at a d = 2 µm thick sample and V = –5 V at a d = 3.5 µm thick sample, resulting in similar conditions for collection under reverse bias. In Figure 5.7 a shift of the maximum with increasing sample thickness to longer wavelengths, i.e. lower energies, is observed. The collection is enhanced for thicker samples for the case of a nearly homogenous generation profile.

At the other end of the spectrum, i.e. for short wavelengths, the response is expected to be similar for all sample thicknesses. Having the same applied electrical field in all three cases should result in similar collection, especially since the doped layers have the same thicknesses. The results for the two thinner samples (d = 1 µm and

d = 2 μm) obey this assumption. The thickest sample (d = 3.5 μm) shows very poor collection especially for the short wavelengths. Unfortunately this sample was degraded in contrast to the other two so that the results are not directly comparable. The higher defect density results in more trapped charge and that screens the external field, so that collection is lower than expected.[12]

5.5. Summary

Deposition parameters and basic measurements were presented to introduce the sets of samples and to give the reader an understanding of the samples used in this thesis. Especially for thick samples features were discussed and explained with high applied reverse voltages and collection efficiency responses.

The section 5.3 of photocurrent-voltage characteristics should only be seen as an introduction to a later chapter (chapter 6 section 6.4 *Comparison of photogating results with i-v characteristics*) where gating collection efficiency results are compared with an *i-v* analysis.

[12] A second effect should be taken into account: due to a thicker i-layer the carriers will spend longer time drifting and thus have a higher probability of recombination.

6. Results and Discussions

The dual beam set-up was described in section 3.2 and consists in principle of the measurement of the collection efficiency for electrons (or holes), in an a-Si:H pin device when illuminated by a low intensity *probe* beam, when the device is already illuminated by a high intensity strongly absorbed *bias* beam.

Section 6.1 provides an initial *example of experimental evidence* of very high effective electron collection efficiencies, (for electrons) in a thick a-Si:H pin device, its origin in a dual *i-v* curve-measurement, and its variation with applied reverse voltage bias. It is seen in the example that as the reverse voltage is increased, the collection efficiency builds to a peak well above unity and then reduces.

The following section 6.1.1 also introduces *computer simulation*, from the outset, to reveal the internal physical processes underlying this unusual effect of photogating: first qualitatively and then, more decisively, quantitatively for *electron gating*. This allows the effect to be explained as arising from internal field modulation effects, and allows the later sections of the chapter to be followed more clearly.

In section 6.1.2, the effect of *light-soaking* (and hence defect production) on the behaviour of the collection efficiency is investigated both experimentally and by simulation.

Section 6.1.3 examines the effect of varying the probe beam flux and wavelength, showing that the gating effect reduces as the probe flux approaches the magnitude of the bias beam flux while the probe wavelength variation reveals an optimum wavelength for maximum gated collection efficiencies for the samples investigated.

In the final section of electron gating experiments, 6.1.4, the effect of varying the bias beam flux and wavelength, showing that the gating effect increases as the bias flux

is increased is reported. The requirement for strong absorption of the bias beam for observation of photogating is examined by using variation of the wavelength of the bias beam.

The analogous effects of hole photogating, in which the bias beam illuminates the 'n' side of the device are examined in section 6.2 and respective sub-sections.

A study of the effect of different i-layer thicknesses for electron and hole gating on the probe collection is the subject of section 6.3. A detailed explanation is presented with the help of simulations here of different extended electric field distributions.

Section 6.4 investigates the information obtainable from the rather more experimentally accessible basic *i-v* characteristics, in comparison with gated collection efficiencies by simulation and measurement. It is shown that the dual beam photogating experiment in conjunction with simulation can give significantly more information, including the spatial distribution of defects.

The last aspect of the photgating experiments is a study of the time response to a chopped probe beam, in section 6.5. Long settling times for the gated signal are observed and analysed in terms of charge transport and trapping kinetics.

Although several sets of samples were used (see section 5.1) one set of samples was used predominantly (probe-, bias- beam variations, hole gating and the study of the *i-v* analysis). This set was the set of the IPE Stuttgart. Furthermore most experiments were undertaken using the d = 3.5 μm. thick sample of that set (TC). Exceptions are section 6.1.2, where degradation is examined on various sets of samples (but all with a thickness of d = 3.5 μm) and in sections 6.3, where the thickness is aim of the examination (of the IPE Stuttgart set). Except where otherwise stated the d =3.5 μm IPE Stuttgart sample (TC) was used throughout the chapter.

6.1. The dual beam experiment: Collection efficiencies > 1 and electron photogating

The experimental configuration used here was described in section 3.2 and consists of the measurement of the differential collection efficiency for electrons, in an a-Si:H pin device when illuminated by a low intensity *probe* beam, through the n-side contact, when the device is already illuminated by a high intensity strongly absorbed *bias* beam through the p-side contact.

As explained in section 3.2, the collection efficiency values for the additional current which flows on application of the probe beam, are calculated using equation 3.8

$$QE(V) = (j_{bp} - j_b)/(q\Phi_p). \tag{6.1}$$

In Figure 6.1 the two necessary measured *j-v* curves with and without additional probe beam illumination are shown, for sample Stuttgart TC (details see section 5.1)

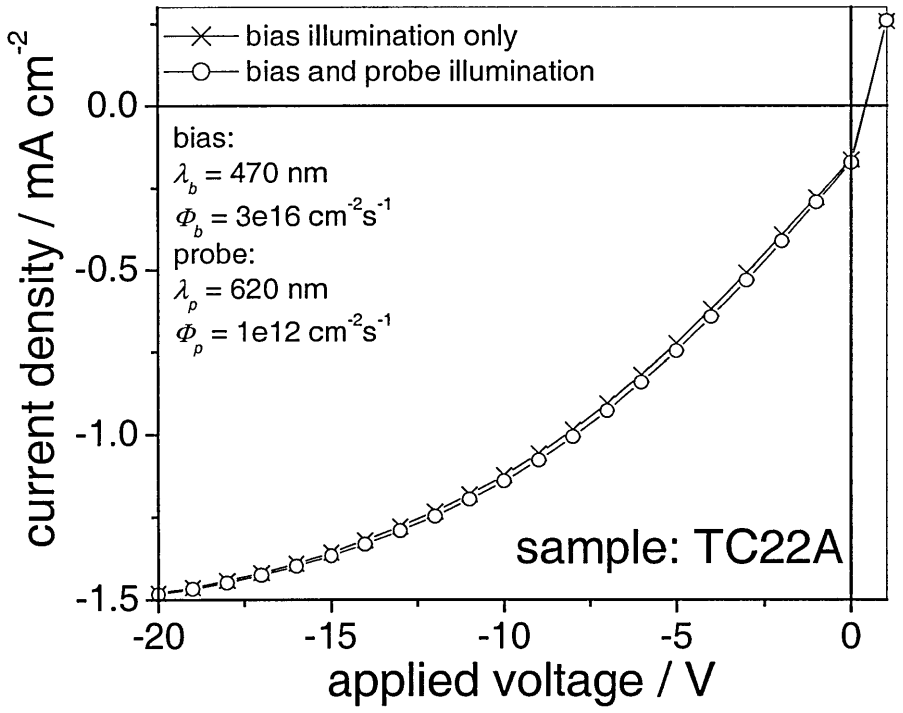

Figure 6.1: *i-v*-characteristics with bias *and* probe illumination and bias illumination only. The difference of the two curves divided by the incident photon flux of the probe beam gives the collection efficiency of the probe beam (Figure 6.2).

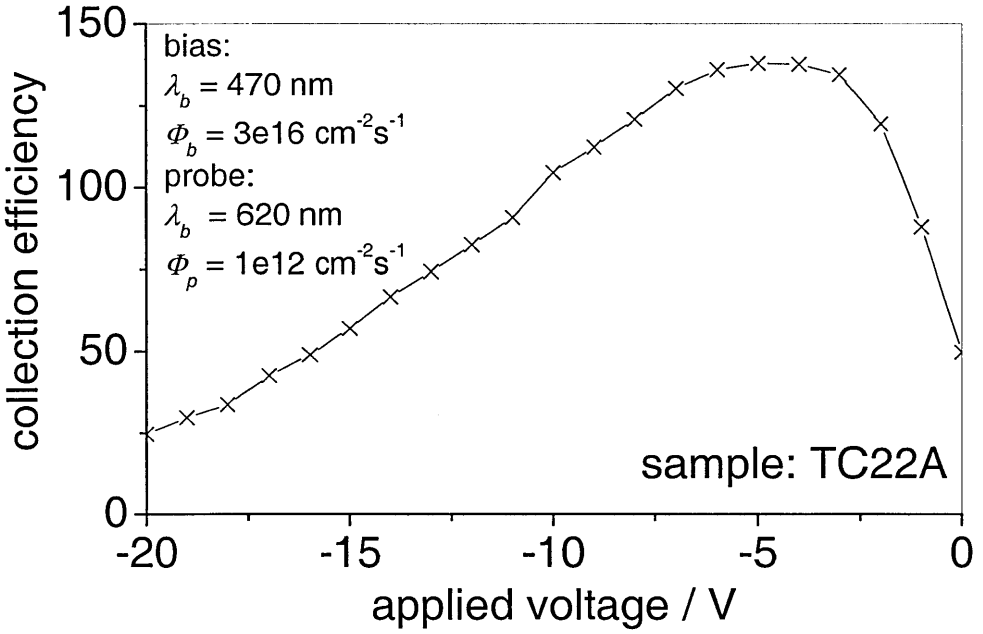

Figure 6.2: High collection efficiencies (compare *i-v* curves Figure 6.1) for a medium degraded sample.

while Figure 6.2 shows the resulting collection efficiency values, which are calculated for each voltage from the difference between the two *j-v* curves in relation to the incident probe beam photon flux. Because of the high ratio of Φ_b /Φ_p of up to 3.2e16/1e12 = 32000:1 the visible change in the current density in Figure 6.1 is relatively small. However, the collection efficiency values in Figure 6.2 which illustrates the dependence of collection efficiency on reverse bias voltage, indicate that the relative change in the *j-v* characteristics must be much greater than the ratio of photon fluxes. This follows from the very high collection efficiency; the peak value of 140 as shown, is absolute, not a percentage!

In this configuration, carriers created by the bias beam excitation near the p-i interface constitute the major part of the differential collected current. As the electrons created in this region must drift over almost the whole thickness of the device to be collected, while the holes are created very close to the p-side contact, the above

phenomenon is termed *electron gating* while the reversed beam set-up (n-side bias, p-side probe illumination) resulting in a longer way for holes to drift is called *hole gating*. (Zollondz et al., 1998, Zollondz et al., 1999)

Problems caused by degradation effects of the bias beam (section 6.1.4 and 6.2.4) resulted in a choice of a lower bias beam photon flux for much of the work. A default set of parameters (table 6.1) can be defined for this situation. This set of

table 6.1: default settings for electron gating experiments.

	Directed to	**Wavelength**	**Photon flux**
Bias-beam (front)	p-side	$\lambda_b = 470$ nm	$\Phi_b = 1\times10^{15}$ cm^{-2}s^{-1}
Probe-beam (back)	n-side	$\lambda_p = 620$ nm	$\Phi_b = 1\times10^{12}$ cm^{-2}s^{-1}

parameters is always used unless it is stated differently: the probe beam was kept at a photon flux of $\Phi_p = 1\times10^{12}$ cm^{-2}s^{-1} while the probe wavelength was $\lambda_p = 620$ nm. For the bias beam moderate values of $\Phi_b = 1\times10^{15}$ cm^{-2}s^{-1} and $\lambda_b = 470$ nm were used as default values.

Since initial observations showed that a-Si:H p-i-n structures with thick i-layers exhibited a greater photogating effect, all of the measurements were carried out on the $d = 3.5$ μm thick samples from different sources, while a study on thickness dependence is included in section 6.3.

6.1.1. Simulation of electron gating

Here it will be demonstrated how with a simple model, using parameters similar to the default parameters of table 6.1, such unexpected experimental behaviour can be simulated with reasonable quantitative agreement. It is therefore more useful to describe the salient simulation results at the outset, rather than in a later section, to allow the later measurements to be viewed in this context. While the peak gain of 140 in Figure 6.2 is greater than any previous published value, to the author's knowledge, for much of the work, a more moderate excitation was used, with a rather lower and more typical *experimental* collection efficiency as shown in Figure 6.3. The main difference is a lower bias photon flux to minimise degradation, and use of samples from a different source (Dundee University (sample 970)[13]) although other changes were λ_b = 450 nm,

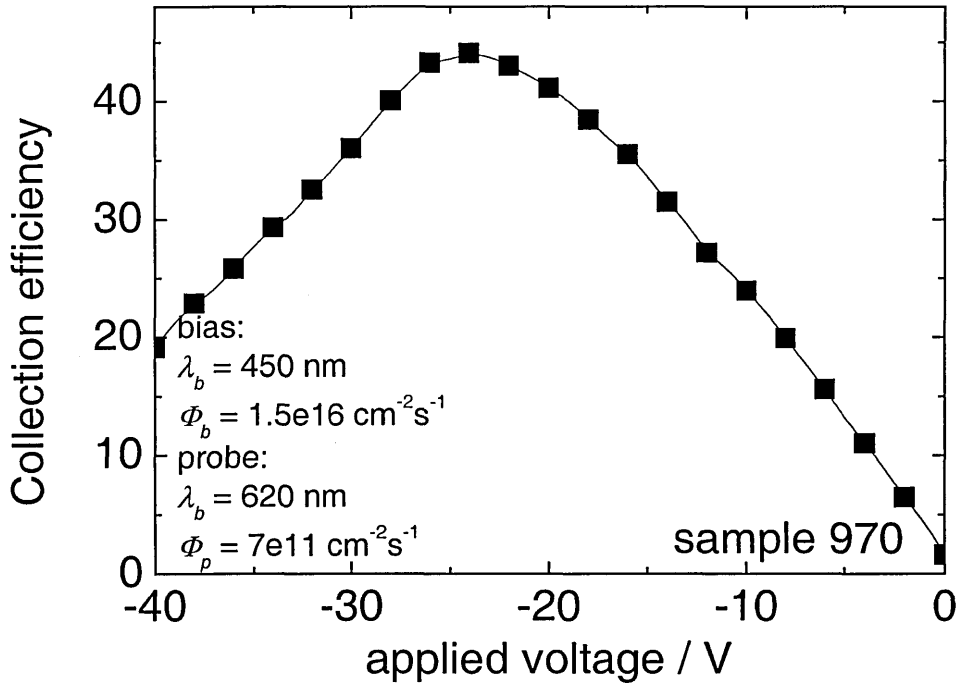

Figure 6.3: Measured gated collection efficiencies for a fairly degraded sample.

[13] For sample specifications please refer to section 5.1.

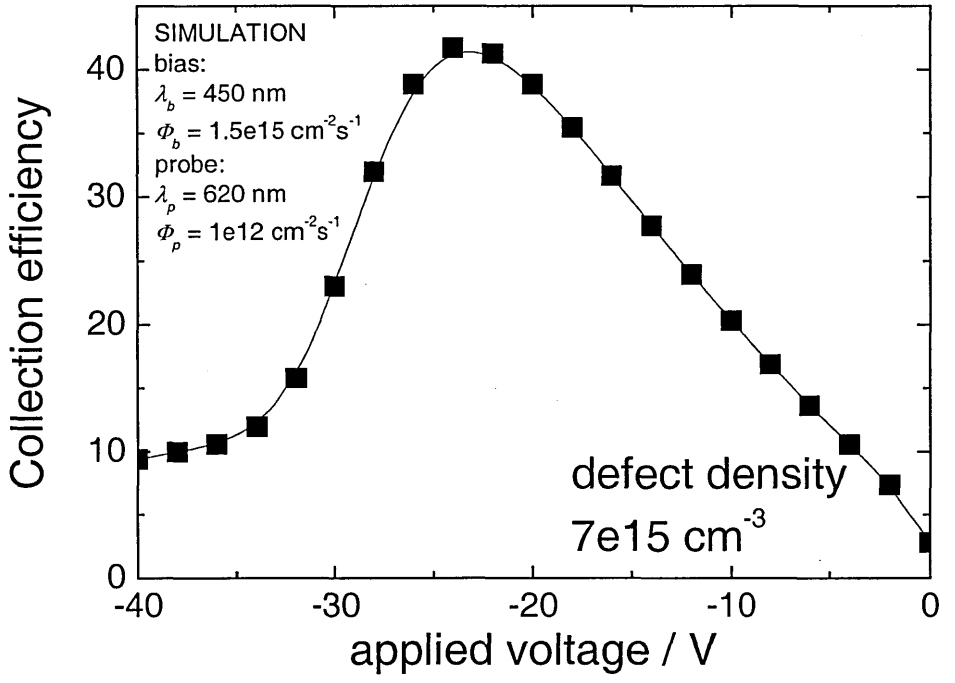

Figure 6.4: Simulated gated collection efficiencies for a fairly degraded sample (defect density: 7×10^{15} cm^{-3}; compare table 5.2).

$\Phi_b = 1.5\times10^{15}$ cm^{-2}s^{-1}, $\lambda_p = 620$ nm, $\Phi_p = 7\times10^{11}$ cm^{-2}s^{-1}.

To analyse the phenomenon, the simulation program SPIN (see chapter 4) was used. To fit the measured result in Figure 6.3, the parameters shown in table 6.2 were used. First results of the simulation program are shown in Figure 6.4. All following simulations in this section are calculated on the basis of these fitted internal parameters and a defect density of 7×10^{15} cm^{-3}.

To understand how the effect can be caused, first the internal electric field should be observed: Figure 6.5 shows the computed internal electric field distributions under bias illumination, for different applied reverse voltages. It can be seen that the internal electric field reaches very small magnitudes in the region near to the side where

the bias light is incident and strongly absorbed (p-side): in a region within 1 μm of the p-i interface.(Zollondz, 1995, Binnewies, 1997)

Figure 6.6 shows the same simulated data as Figure 6.5 but here with a logarithmic ordinate. It can be seen that the electric fields not only fall to very small values but also reverse for low magnitudes of applied reverse voltage (0 V – -24 V).

table 6.2: Input parameters for the a-Si:H p-i-n steady state photodiode simulation.

Device thickness	d	3.4 μm
Fermi level in doped layers	E_F-E_V *(p)*	0.36 eV
	E_C-E_F *(n)*	0.25 eV
Characteristic energies for band-tails	E_{CT}	0.025 eV
	E_{VT}	0.045 eV
Doped layer thicknesses	t_n, t_p	20 nm
Optical gap	E_g	1.8 eV
Band edge density of states	$g(E_C)$, $g(E_V)$	2×10^{21} cm^{-3} eV^{-1}
$D^{+/0}$ energy	$E^{+/0}$-E_V	0.8 eV
Defect correlation energy	U	0.2 eV
Free electron and hole mobilities	μ_n	10 cm^2 (Vs)$^{-1}$
	μ_p	1 cm^2 (Vs)$^{-1}$
Capture coefficients:		
Band - tails (CT, VT)	σ_n, σ_p	10^{-9} cm^3 s^{-1}
Neutral defects D^o	σ_n^0, σ_p^0	10^{-8} cm^3 s^{-1}
Charged defects D^+, D^-	σ_n^+, σ_p^-	10^{-7} cm^3 s^{-1}

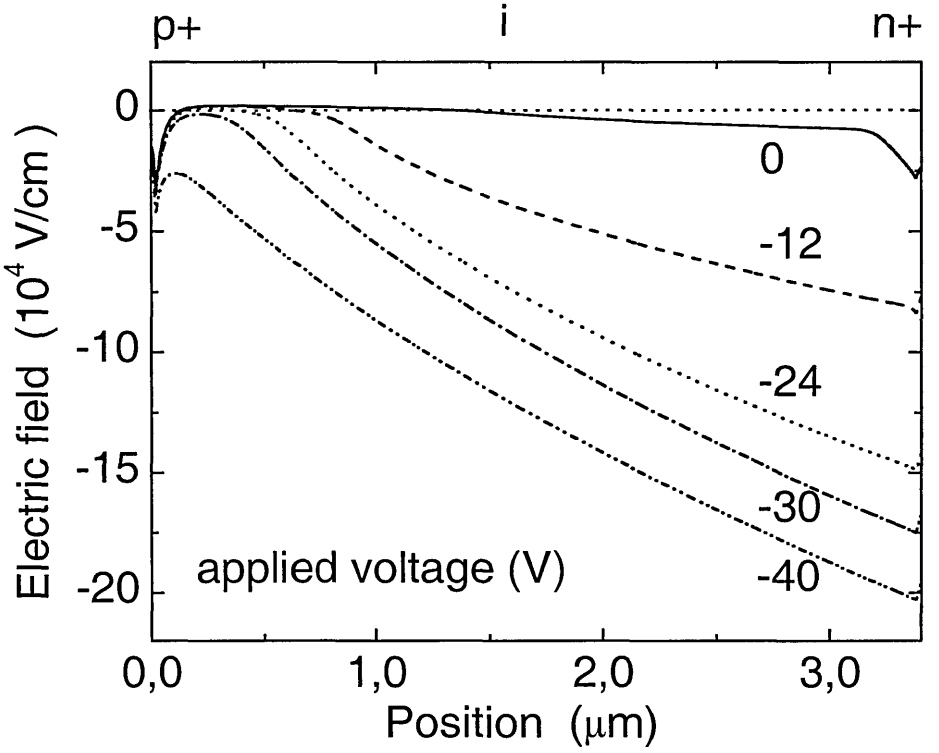

Figure 6.5: Simulated electric field distributions for applied reverse voltages with (bias) illumination only (defect density value of 1×10^{15} cm^{-3}).

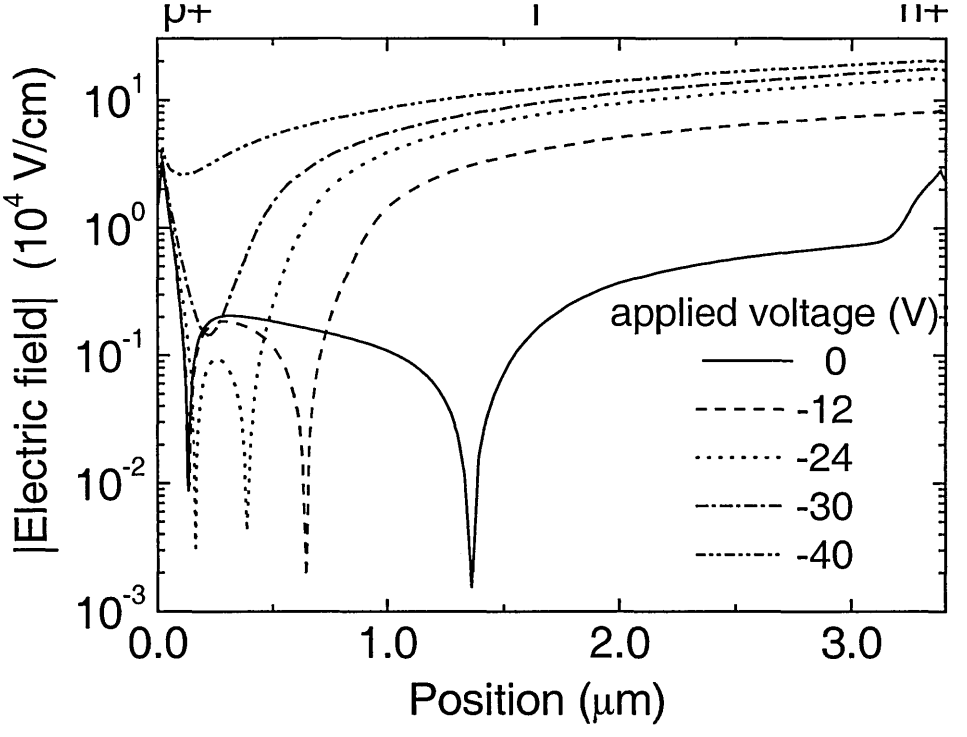

Figure 6.6: Absolute values of the internal electric field distributions as in Figure 6.5, but plotted with a log ordinate.

What looks like a broad minimum in Figure 6.5 shows for these low voltages a *cross over* to positive field values. However, for high applied reverse voltages the field does not exhibit such a reversal and the low field region is narrower for higher applied voltages. Comparison with Figure 6.3 shows that this field reversal is not necessary for high collection efficiency. High values occur even when the voltage magnitude is above –24 V, (which gives the highest collection). High collection efficiencies still exist at voltages of –30 V and –40 V. Therefore – and for clarity – the phenomenon of photogating will be explained at a non-reversing field minimum. But it should be emphasised here that, in principle, the reversal makes no difference in the explanation of the phenomenon, because a field enhancement, i.e. a higher negative field by the additional probe beam illumination is the reason for collections greater than one.

In Figure 6.7 the (non reversing) field minimum at –28 V is shown with bias illumination *only*, (as in Figure 6.5 and Figure 6.6), and also the internal electric field distribution with bias *plus* additional probe illumination. The curves are almost

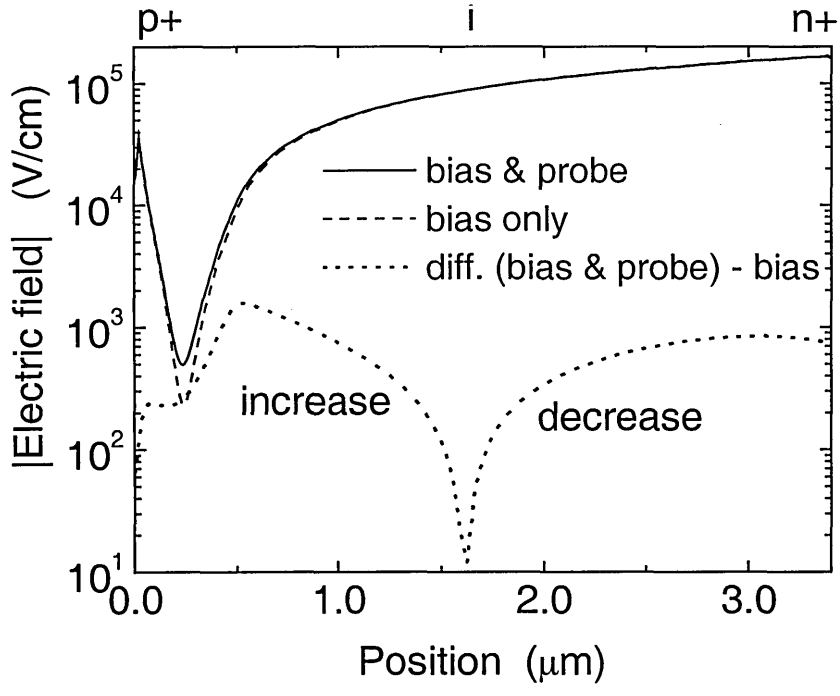

Figure 6.7: Internal electric field distributions without and under additional probe illumination.

coincident, showing that the field change is very small. The third curve therefore shows the *change* of the electric field itself. Even if the change in electric field terms is very low, a *decrease* in the magnitude of the electric field at the back of the device, and an *increase* in the region of the field minimum can be seen.

The decrease of the internal electric field in the back of the sample (in relation to the bias beam illumination side) is caused by trapping of the probe-beam-generated holes when these are drifting to the front (p^+) contact, under reverse applied voltage. It is difficult to show this trapping progress because the number of photo carriers generated by the probe beam is far lower than the bias beam generated photo carrier density. In order to understand the process, the space charge situation will be looked into. Figure 6.8 shows the space charge distribution in the bias only illuminated p-i-n sample. In the region near the p^+ interface the total space charge is dominated by holes

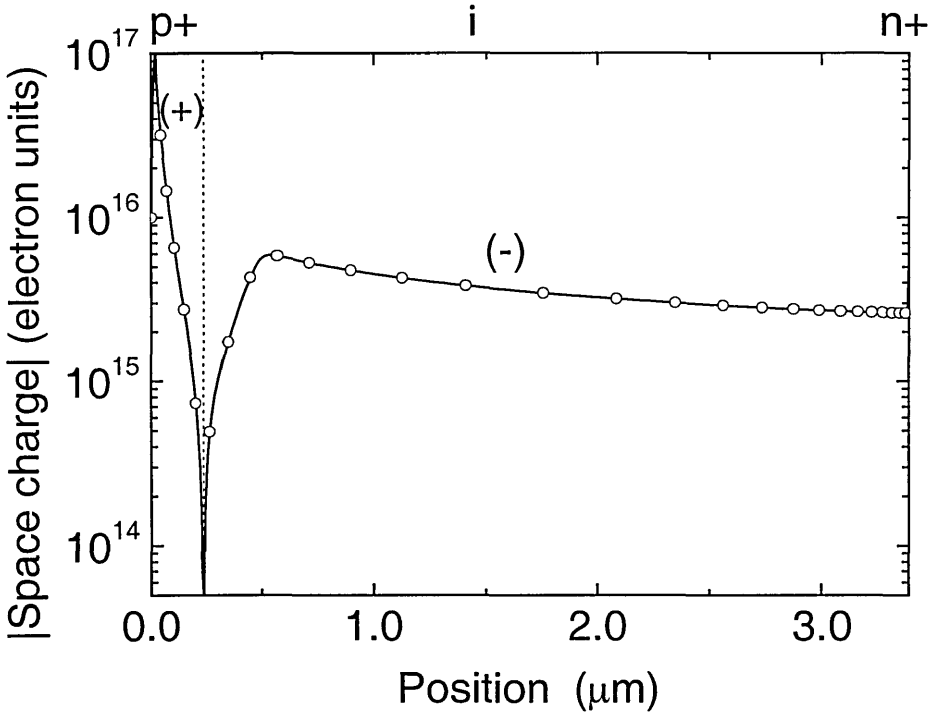

Figure 6.8: Total space charge distribution.

trapped in the valence band. In the rest of the sample, the negative space charge of doubly occupied D^- states dominate space charge. Adding the probe beam with weakly absorbed photons (λ_p = 620 nm, α = 2.2×10^{-4} cm^{-1}) feed these D^- states with holes, which are drifting to the p$^+$ contact, changing the D^- state to a D^0 or even to a D^+ state. In either case, this change in charge screening raises the magnitude of the internal electric field in the *low field region* (i.e. near the front of the device) resulting in increased electron drift – of electrons *created by the bias beam* (hence: generation profile of the bias beam in Figure 6.9), out of this region.

A useful alternative view is to consider the *recombination* of the excess carriers. For clarity and in consideration of the small changes Figure 6.9 shows only the *nett* recombination and generation rates from the bias beam only and the bias and probe illumination. Partial recombination paths were calculated and summed up for this Figure. To the right of the sample the main recombination path is

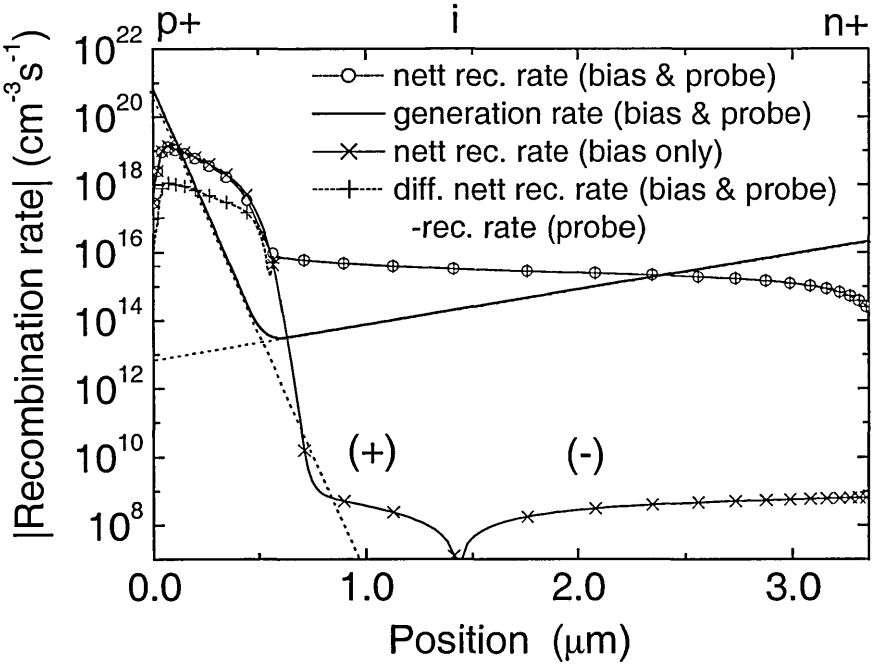

Figure 6.9: Generation and recombination rates

$e^- + D^0 \Rightarrow D^-$; $h^+ + D^- \Rightarrow D^0$. With bias illumination only recombination in this region is very low - in fact it is *reversed,* i.e. thermal *release* from defects, which can be observed, with very low generation rates (10^8 to 10^9 $cm^{-3}s^{-1}$). Addition of the probe beam generated photo carriers results in hole (drifting to the p^+ contact) trapping in this area and a net positive recombination rate, via the $D^{-/0}$ path, in the back of the device.

Close to the p-i interface the dominating recombination path also proceeds via the defects: $h^+ + D^0 \Rightarrow D^+$; $e^- + D^+ \Rightarrow D^0$. But here, within 0.5 μm of the p contact a significant *decrease* of recombination is found with additional probe illumination. The magnitude of the local *reduction* in recombination 1.1×10^{18} $cm^{-3}s^{-1}$ in comparison to 2.5×10^{16} $cm^{-3}s^{-1}$ probe beam generation rate at the n side of the device, far exceeds the increased generation by the probe beam, accounting for collection efficiencies of greater than unity.

6.1.2. Influence of light soaking (defect densities)

Since the photogating effect is based on a process that is controlled by trapping and release of charge carriers in localised states, *viz.*, dangling bonds (see previous section), degradation should influence the collection efficiency measurements (see section 2.5).

The following set of measurements Figure 6.10 are the first measured data of the effect of degradation on high collection efficiencies, to the author's knowledge and were published in (Zollondz et al., 1996, Main et al., 1999). The sample was a 3.5 μm thick a-Si:H sample of a Dundee University set (no. 970).

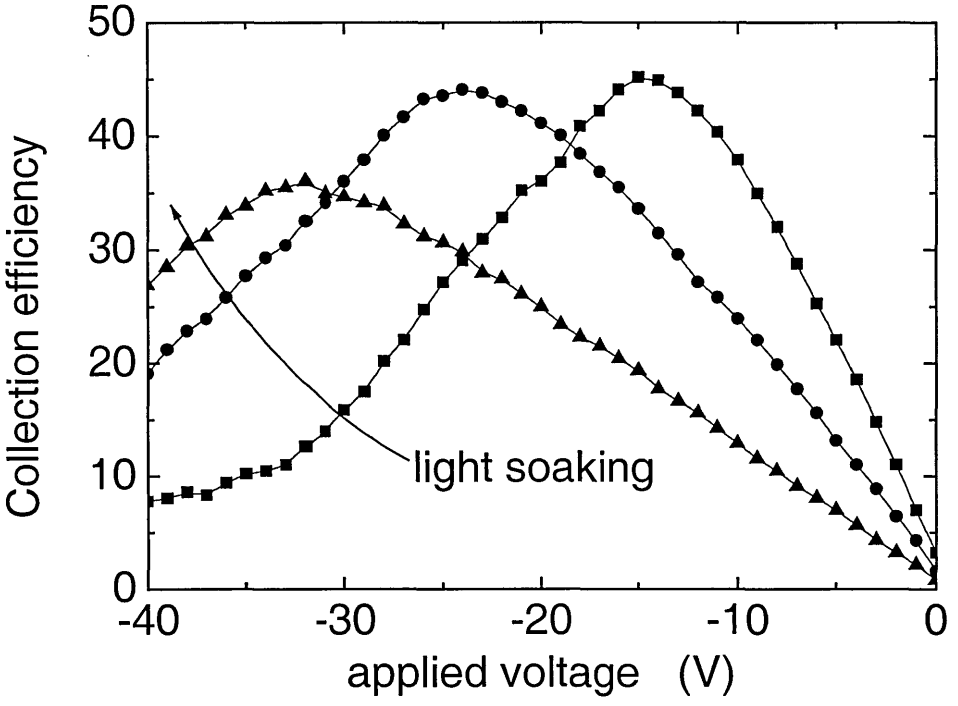

Figure 6.10: Experimental determined collection efficiencies *vs.* applied voltage for different degradation states (University of Dundee sample no. 970, $d = 3.5\mu m$).

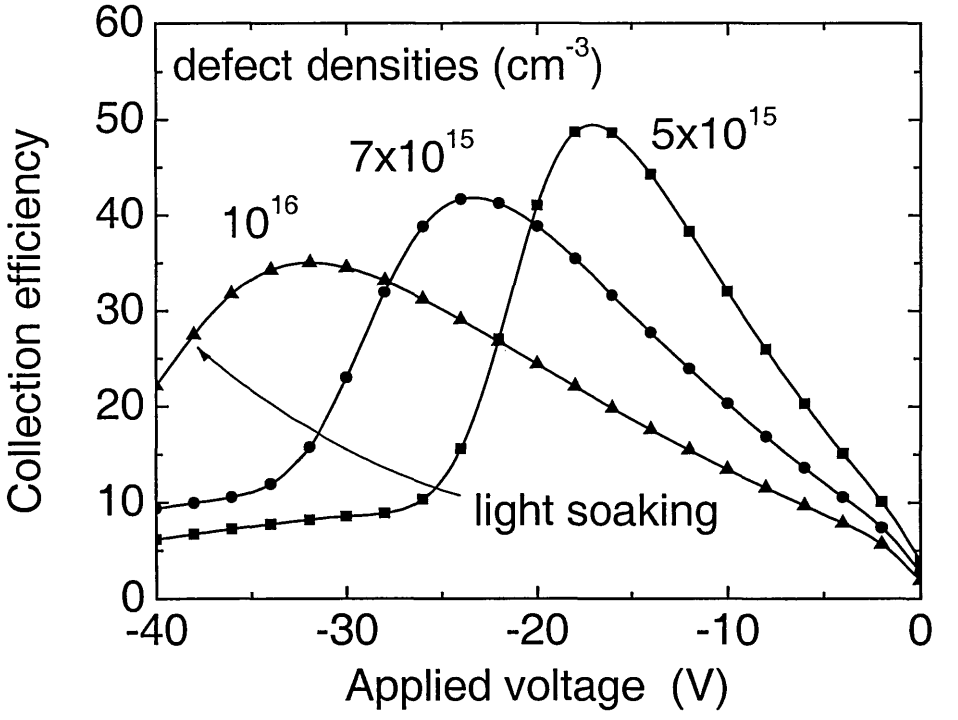

Figure 6.11: Calculated collection efficiencies *vs.* applied voltage for different defect densities.

The diode was light soaked with water filtered light from a halogen lamp that had a sun like spectrum at AM 1 (93.5 mW/cm^2) through the n-side. Illumination times of t = 0, 380, and 980 min were used. Following this, for the experiment, bias illumination was from the p-side with λ_b = 450 nm under a photon flux of $\Phi_b = 1\times10^{15}$ cm^{-2}s^{-1}. Additional probe beam illumination was through the n-side with $\lambda_p = 620$ nm and a photon flux of $\Phi_p = 7\times10^{11}$ cm^{-2}s^{-1}. Figure 6.10 shows the result of n-sided light soaking with AM 1 exposures.

Light soaking shifts the maximum noticeably to higher reverse voltage values. In comparison Figure 6.11 shows the calculated collection efficiency for the same experimental parameters (Figure 6.10) for a range of defect densities. The similarity of the measured and simulated data is evident. The simulation results given in section 6.1.1 are based on these curves and fit well not only in magnitude but also in variation of the defect densities. This additional corroborative evidence underlines that the simulated data do reflect the nature of the physical phenomenon.

Small variations of the defect densities echo the shifting maximum in the measurement of different light soaking times. It should be stressed that a factor of 2, i.e. 5×10^{15} cm^{-3} to 1×10^{16} cm^{-3} shifts the maximum significantly (approx. 15V), so the experiment is very sensitive to defect density variation.

A second set of 3.5 μm thick samples made at the IPE (Stuttgart) was examined under similar conditions: the incident photon fluxes were the default values. The wavelength of the bias beam was changed to λ_b = 470 nm because the spectrum of the 450 nm LED showed an unexpected broad shoulder for lower energy values than the nominal 450 nm (Appendix A.1).

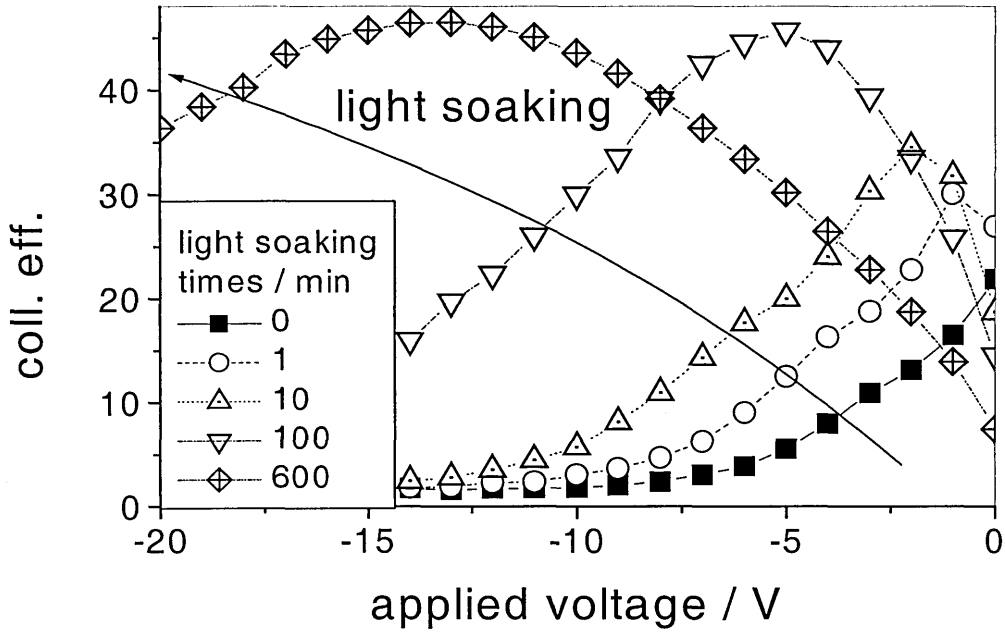

Figure 6.12: Experimental determined collection efficiencies *vs.* applied voltage for different degradation states (IPE sample TC, 3.5 μm).

Light soaking results showing high collection efficiencies after AM 1 treatment of t = 0, 1, 10, 100, 600 minutes (of a typical p-i-n sample of this set) are illustrated in Figure 6.12. Again the soaking illumination was filtered with water and the treatment was directed to the n-side of the open circuit p-i-n sample.

Comparison of the two sets of samples from different laboratories shows similar responses in the photogating experiment, including the effects of light soaking. Although, in retrospect, the Dundee sample seemed to be fairly degraded from the initial state, and hence exhibited a peak at rather higher voltages, comparable results in all other aspects were obtained, in terms of magnitude of collection, or the shifting maximum for more degraded samples.

Investigations were undertaken on a third set of samples (Dundee 1328) again from the Dundee University using the default illumination parameters. Figure 6.13 shows the results found with a typical sample from this set of p-i-n diodes. It should be pointed out that the voltage range is far lower than for the samples observed before but the sample thickness is also 3.5 μm. The defect density seems to be very low, in that the photogating maximum is found at a very low reverse voltage. A second difference to the two other sets of samples is that the peak is very narrow (hence the abscissa minimum $V = -1$ V).

For this sample, illumination, and degradation for only one minute with AM 1.5 and the conditions described above, results in a shift in the maximum (increase of the value at 0 V because the maximum is initially in the 1st quadrant) and therefore widens the shape of the maximum.

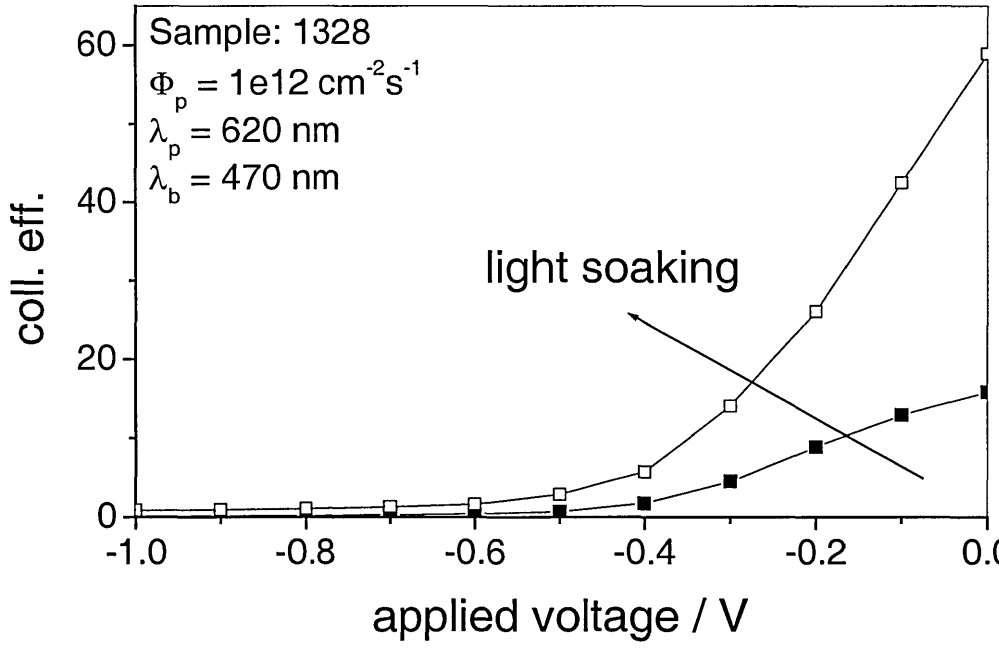

Figure 6.13: Experimental determined collection efficiencies *vs.* applied voltage for different degradation states (Dundee University sample 1328, $d = 3.5$ μm).

6.1.3. Probe beam variations

As the probe beam is the beam that is detected and taken into account for the collection efficiency, variations of the probe beam photon flux and wavelength are objects of investigation in this section. Variation in the probe beam photon flux results in a quantitative change in the photogating effect. In the next section (6.1.4) where bias beam photon fluxes are varied we will see that the *ratio* between the bias and the probe beam is an important factor in defining the magnitude of the photo gating effect. In both of these sections the experiments are undertaken on the IPE Stuttgart samples TC ($d = 3.5$ μm).

Figure 6.14 shows calculated collection efficiencies with the same parameters as for the simulations in section 6.1.1. as a function of the applied voltage. The bias beam

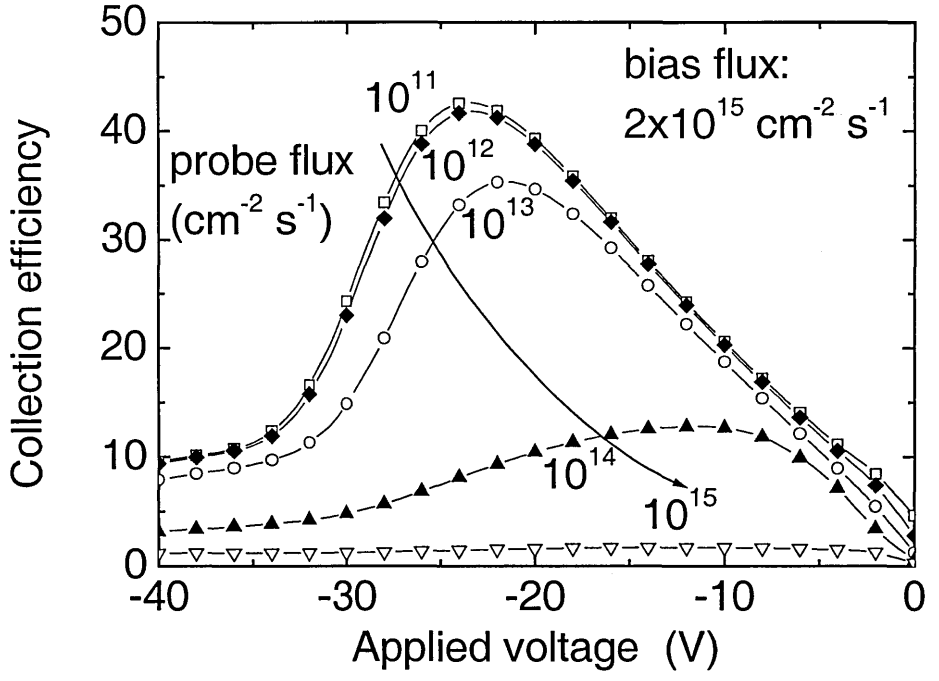

Figure 6.14: Calculated variation of the collection efficiencies with applied voltages for varied probe photon fluxes.

specifications are kept at the "default" values as the probe wavelength while the probe photon flux was varied between $\Phi_p = 1\times10^{11}$ $cm^{-2}s^{-1}$ and $\Phi_p = 1\times10^{15}$ $cm^{-2}s^{-1}$.

For photon flux values for bias and probe beam of the same magnitude, no photogating effect can be found: that is for a probe photon flux value of $\Phi_p = 1\times10^{15}$ $cm^{-2}s^{-1}$ (and bias photon flux $\Phi_b = 2\times10^{15}$ $cm^{-2}s^{-1}$). Here collection is measured at around unity. Although the internal electric field distribution does not appear to be changed much, any photogating cannot now result in a large relative collection, since the bias beam cannot now provide a gated current much greater than the probe beam-produced current. The collection of the probe beam should be at most unity plus a small gated part. This results in a value of approximately one for sufficient applied reverse voltages.

Keeping the bias photon flux constant and decreasing the probe photon flux results in a smaller probe signal but also in a non-linear increase of the photocurrent response that gives rise to the collection efficiencies greater unity. Further reduction in the probe beam, to a ratio of about 1/1000 of the bias beam intensity, leads to a saturation of the gating effect. Lowering the photon flux of the probe beam further resulting in a ratio of 1/10000 that does not enhance the gain significantly.

Figure 6.15 shows measured photogating collection efficiencies of the IPE sample (d = 3.5 μm) as the probe photon flux is varied. This can be a difficult measurement to perform. The measurement of a very small collection signal on top of a bias signal without lock-in techniques is only possible because such high gains are obtained. However, for very low probe photon flux values (in comparison to the incident bias photon flux) the probe signal is too small even if there is a high gain. Values of bias photon flux and probe photon fluxes are therefore for this one measurement different from those of simulated data in Figure 6.14 and the results are

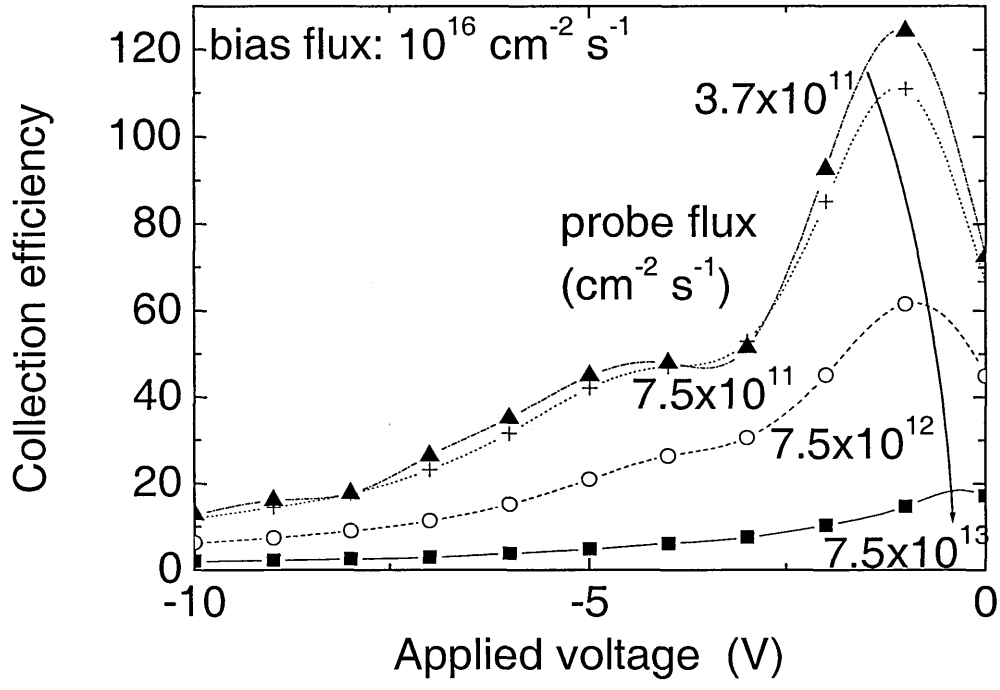

Figure 6.15: Measured variation of the collection efficiencies with applied voltages for varied probe photon fluxes.

not directly comparable to those of the simulation. The tendency described above for calculated data is, however, confirmed.

The second investigation involving probe beam dependence was the variation of the beam wavelength λ_p. In Figure 6.16 and Figure 6.17 the influence of the variation of the probe beam wavelength on the photogating effect are shown. The probe beam photon flux was at the default Φ_p = 1×10^{12} $cm^{-2}s^{-1}$ and the bias beam at Φ_b = 1×10^{15} $cm^{-2}s^{-1}$ for data of Figure 6.16 and Φ_b = 3×10^{16} $cm^{-2}s^{-1}$ for Figure 6.17 while the bias beam wavelength was kept at λ_b = 470 nm. It can be seen that the maximum for the photogating effect was found for this sample at λ_p = 620 nm, and also the maximum is very broad. Measurements of effects of variation of the probe beam

wavelength were also difficult because the experimental set-up was not designed for this kind of variation. Variation in the wavelength was done with the monochromator and the photon flux had to be adjusted with the neutral density filters and for fine 'tuning' with slight adjustments of the lens (see set-up in Figure 3.3).[14] The signal of a photodiode (BPX 65) placed in the beam was used to ensure that constant photon fluxes were achieved for the different incident wavelengths.

With a probe beam wavelength as short as λ_p = 400 nm, collection values are still far higher than unity (QE = 10 in Figure 6.16 and QE = 30 in Figure 6.17) but far lower than for the adapted probe wavelength (of 600 nm $\leq \lambda_b \leq$ 650 nm) where gains of

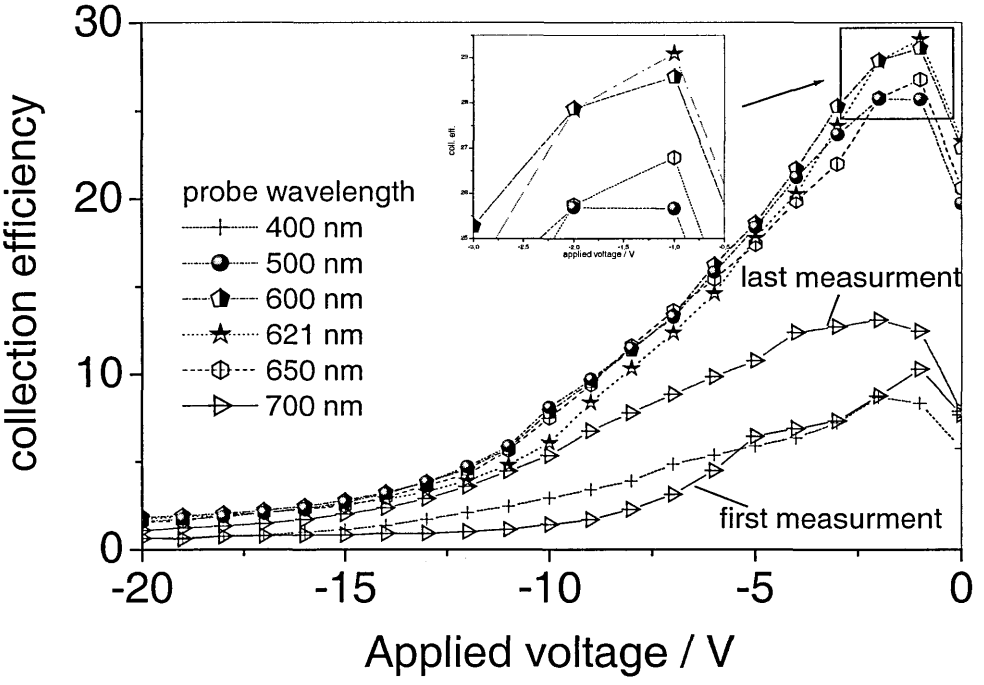

Figure 6.16: Measured variation of the collection efficiency with applied voltage for varied probe beam wavelengths, $\Phi_b = 1\times10^{15}$ cm^{-2}s^{-1}, $\lambda_b = 470$ nm.

[14] Slight movements for the adjustment of the probe beam flux should be no problem, because the beam spot was bigger than the active area on the sample and variations were made only in the middle of an homogeneous area of the spot.

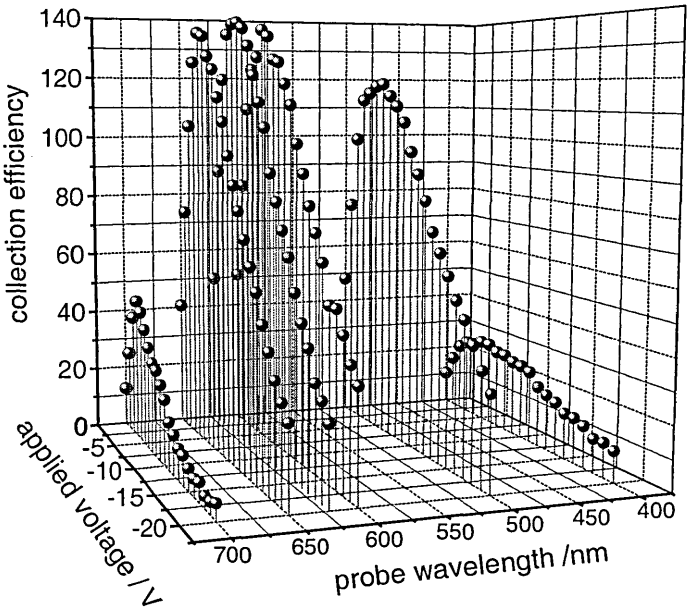

Figure 6.17: Measured variation of the collection efficiency with applied voltage for varied probe beam wavelengths, $\Phi_b = 3\times10^{16}$ cm^{-2}s^{-1}, $\lambda_b = 470$ nm.

30 respectively 140 were found. Having a high energy *probe* beam wavelength (λ_p = 400 nm, i.e. E = 3.1 eV) results in absorption close to the incident side (n-side) resulting in losses near the n-interface with similar results to the effects of the bias beam. The loss of these photocarriers by recombination lowers the number available for screening in the i-layer, and hence a diminished gating effect. On the other hand, at longer wavelengths where absorption is weak, the lower gain for λ_p = 700 nm is of the same magnitude as for λ_p = 400 nm. This is caused by a homogeneous collection of the weakly absorbed beam. The low absorption coefficient ($\alpha \approx 2.5\times10^3$ cm^{-1}) results in an absorption depth of $1/\alpha \approx 4$ μm which is greater than the sample thickness of d = 3.5 μm with, inevitably a reduction in collection efficiency.

A second interesting effect was found by taking a control measurement of the same set of parameters as was used for the first measurement, i.e. λ_p = 700 nm shows a change in the collection efficiency (see above). Degradation of the p-side incident bias light (λ_b = 470 nm and photon fluxes up to $\Phi_b = 3\times10^{16}$ cm^{-2}s^{-1}) must be assumed.[15] But wavelength dependent degradation will not be a subject of this thesis but should be an area of interest for further investigations, since the degradation effect seems to be very sensitive in the outer most areas of the device. Different absorption profiles could be used to degrade the sample in these areas variable.

[15] A whole series of these measurements was taken between the first and last measurement, so that for one probe wavelength (λ_p = 700 nm) and one bias wavelength (λ_b = 470 nm) the bias photon flux was varied from $\Phi_b = 1\times10^{12}$ cm^{-2}s^{-1} to $\Phi_b = 3.6\times10^{16}$ cm^{-2}s^{-1}. Then the procedure was to advance to the next bias wavelength (470 nm $\leq \lambda_b \leq$ 660 nm) and the variation of the photon fluxes was repeated. After all bias wavelengths, were measured (for all photon fluxes) the probe wavelength was adjusted to the next value (400 nm $\leq \lambda_p \leq$ 700 nm), starting with 700 nm(!), and the whole procedure of adjusting photon fluxes and bias wavelengths was repeated. The series with the probe wavelength of λ_p = 700 nm was the first set of measurements but was repeated to check on any degradation effects after the whole series. It was found that some results are influenced by this effect. The measurements were taken as the second series of measurements after the degradation series. It was not expected that photon fluxes of $\Phi_b = 3.6\times10^{16}$ cm^{-2}s^{-1} would influence the measurement. Further measurements of the degradation series were than taken only up to bias photon fluxes of $\Phi_b = 1\times10^{15}$ cm^{-2}s^{-1} to avoid this effect.

6.1.4. Bias beam variations

The last section 6.1.3 investigated the effects of variations in the probe beam. Now the two kinds of variation are investigated for the bias beam.

- Variation in the photon flux
- Variation in the wavelength

Figure 6.18 shows the experimental results of the variation of the bias beam photon flux for the IPE sample (d = 3.5 μm). Probe photon flux and probe wavelength were held at values of Φ_p = 1×12 $cm^{-2}s^{-1}$ and λ_p = 620 nm (maximum of photogating effect see section 6.1.3) as well as the bias wavelength of λ_b = 470 nm. The main features of the curves obtained are, that the maxima increase in their peak values and

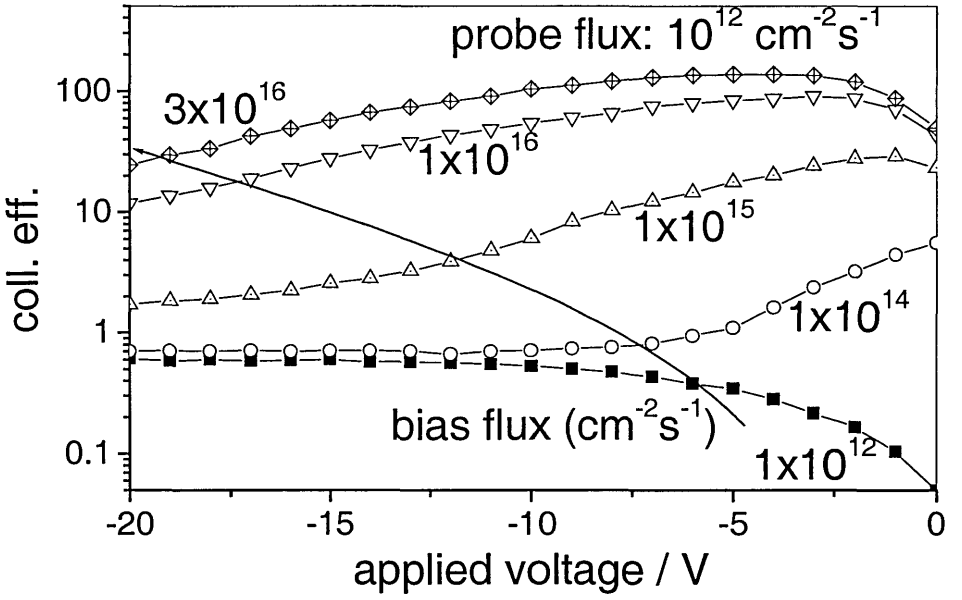

Figure 6.18: Measured variation of the collection efficiencies with applied voltages as the bias beam photon flux is varied while the probe beam is kept constant.

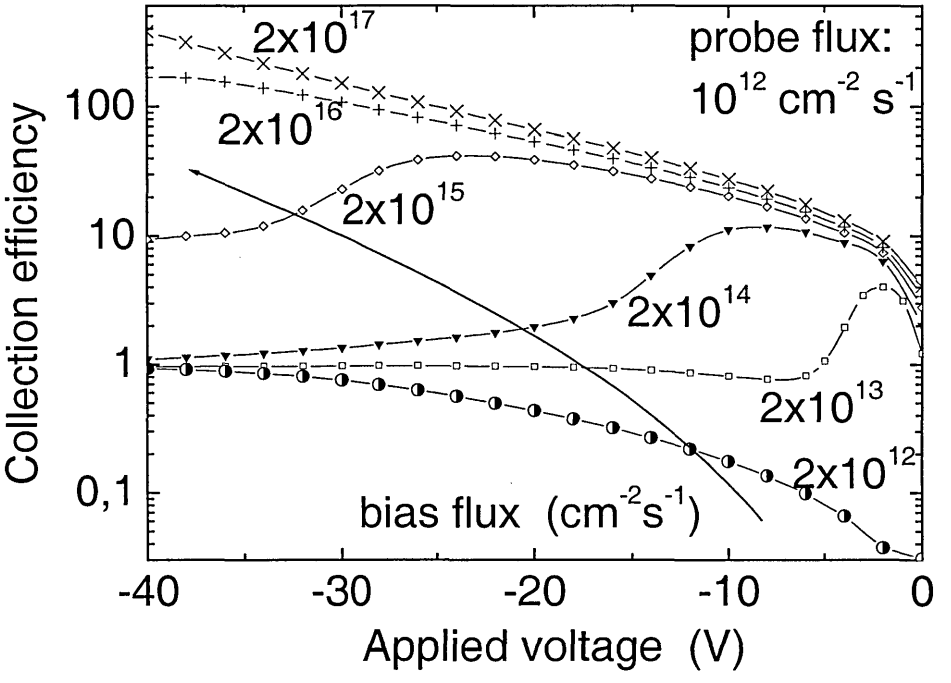

Figure 6.19: Calculated collection efficiencies for different bias beam photon fluxes.

widen as the bias flux is increased. Simulated data show the same tendency (Figure 6.19).

Although simulated data were not fitted quantitatively to the measured data, the widening and the increase of the maximum are clearly visible. Simulations of the collection efficiencies with photon flux values up to $\Phi_b = 2\times10^{17}$ $cm^{-2}s^{-1}$ seem to reach no limit even for these high values (QE = 300). It should be recognised, however, that measurement of such high values would be impossible with an undegraded sample because the bias illumination would quickly degrade the device (see section 6.1.3 where photon fluxes lower than $\Phi_b = 3.6\times16$ $cm^{-2}s^{-1}$ showed degradation effects).

A conventional view of the influence of bias beam wavelength on the collection efficiency *vs.* voltage characteristic is shown in Figure 6.20 while Figure 6.21 shows 3D plots and contour plots of experimental data illustrating the effect of degradation over the whole spectrum of bias wavelengths. The bias photon flux was kept here at $\Phi_b = 1\times10^{15}$ cm^{-2}s^{-1} ($\Phi_b = 3\times10^{16}$ cm^{-2}s^{-1} for Figure 6.20) and the probe specifications were kept for the photon flux at $\Phi_p = 1\times10^{12}$ cm^{-2}s^{-1} and for the probe wavelength at $\lambda_p = 620$ nm. The variation in a) – e) was the state of degradation of the sample as described in section 6.1.2, i.e. 0 min, 1min, 10 mins, 100 mins and 600 mins. It can be seen that for higher degradation rates the maximum not only increases as shown in Figure 6.10 to Figure 6.13 but also widens. The effect can be found for bias

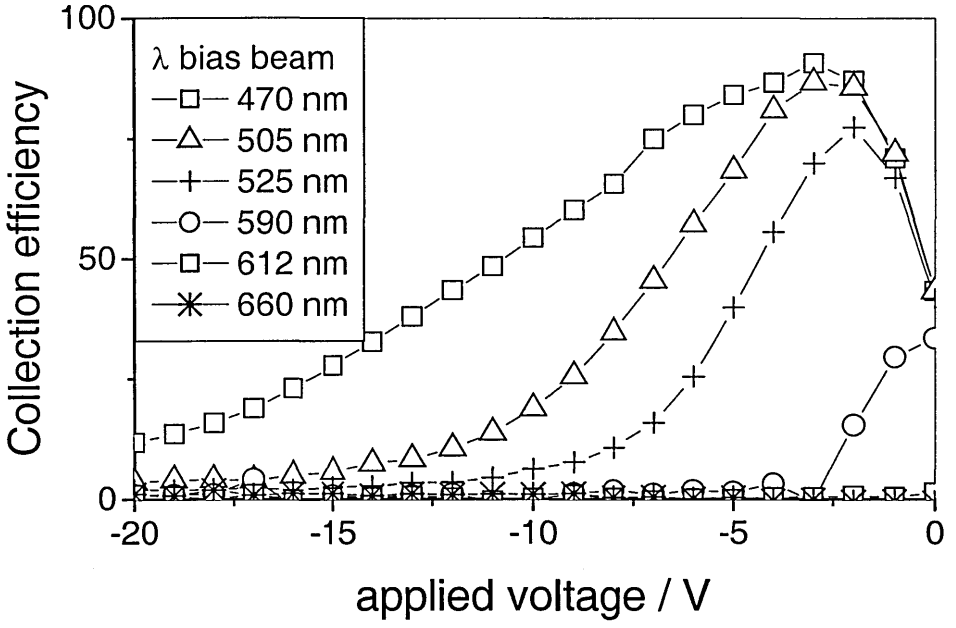

Figure 6.20: Measured collection efficiencies with applied voltages as the bias beam wavelength is varied; probe wavelength and photon flux as bias photon flux are kept at the usual values.

a)

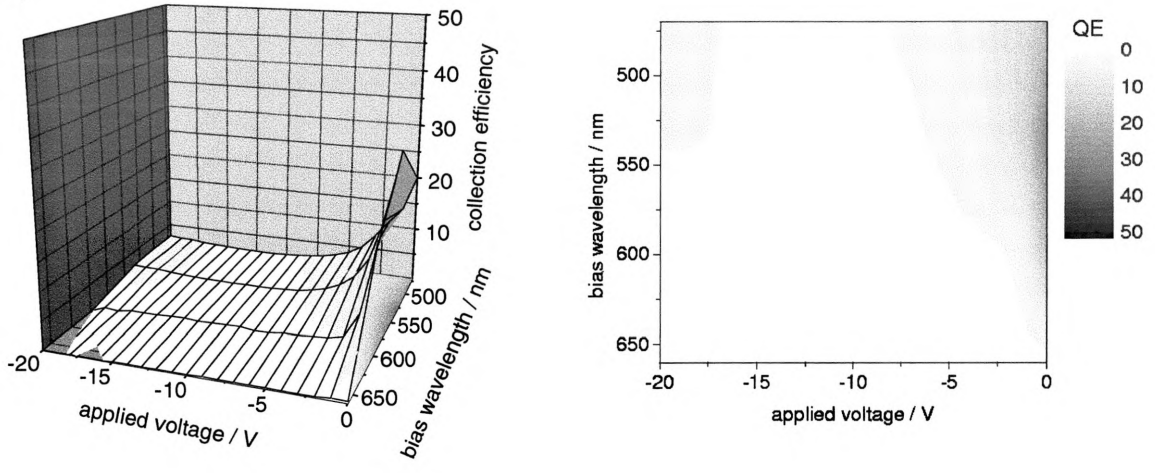

b)

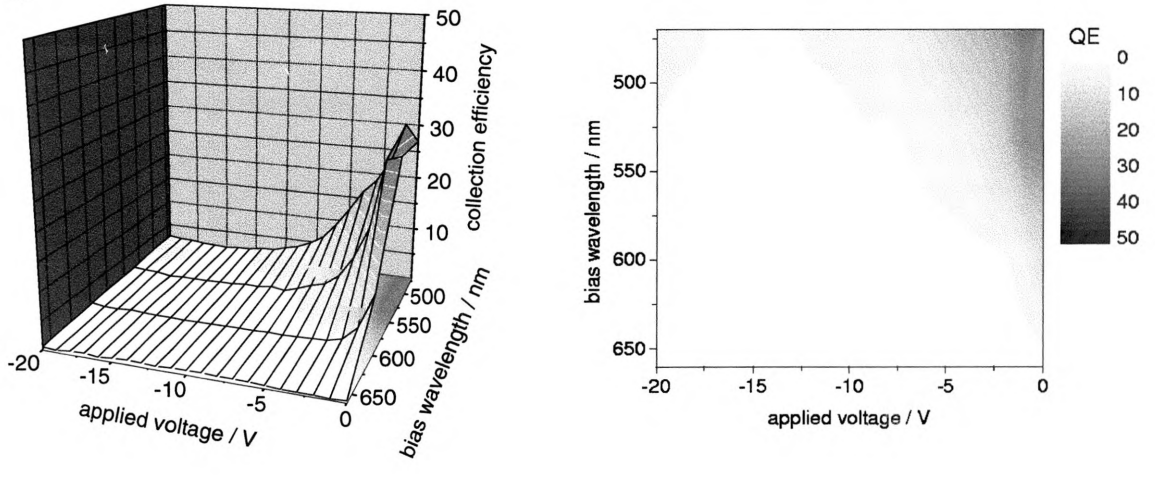

c)

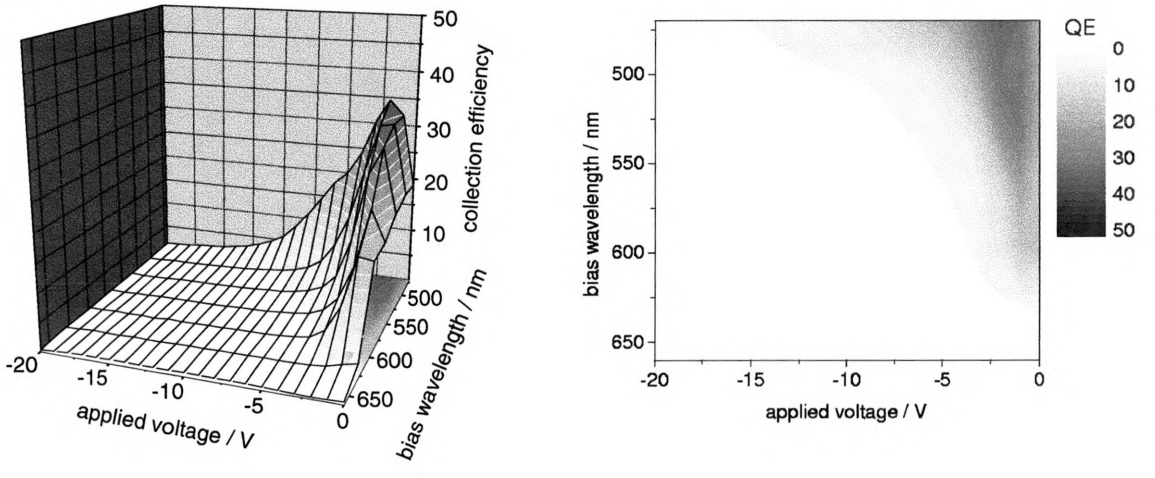

caption: see next page

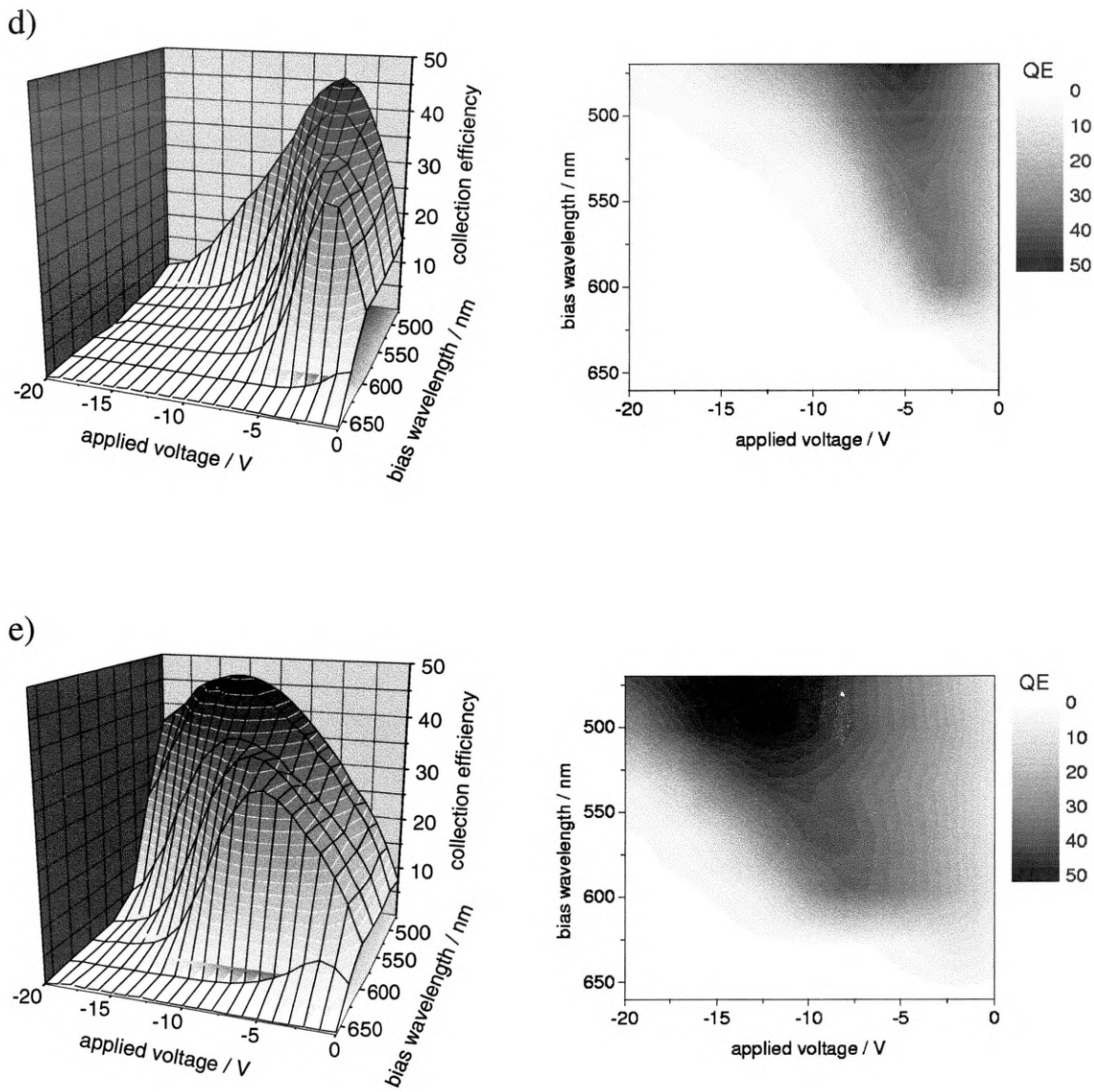

Figure 6.21: Measured collection efficiencies for varied applied voltages and for different bias wavelengths. a) – e) are for different degradation states (s.a.). Each left Figure shows a three dimensional surface plot while the right Figure is the according contour plot.

wavelengths between 470 nm ≤ λ_b ≤ 590 nm (Figure 6.21e)). Further is the maximum collection shifting: it is found for an "ideal" bias wavelength of λ_b = 470 nm at –13 V and for the bias wavelength of λ_b = 590 nm at –7 V. The reason for this steady shift (see Figure 6.21a) and e)) is found in a wider and shallower field minimum with increasing

wavelength. If the enhancement of the electric field is causing the gating one should keep in mind that there is still a local minimum in the electric field and the changes in the electric field distribution are very small. But the deepness of this minimum is crucial for how easy the release of photocarriers is.

Applying an external voltage results in higher collection of these released photocarriers. Since the bias-beam-induced field minimum is deeper for shorter wavelengths the applied voltage to produce peak collection is accordingly higher. The reason for the higher magnitude of the photogating effect for shorter wavelengths has to be seen in the steeper absorption profile for those wavelengths, i.e. the number of the electrons available for gating is far higher since the minimum is closer to the illuminated side since the photon flux is kept constant for all bias wavelengths.

6.1.5. Summary

The investigation of the response to wavelength variation of the probe beam was used to choose a suitable 'default' probe wavelength for the examined samples. Furthermore the probe beam and bias beam photon flux variations underlined the requirement that the ratio between probe and bias beam should be at least $\leq 1/10$ for gated results ≥ 1.

The degradation series in combination with the bias beam wavelength variation resulted in a number of conclusions:

- wavelength variation in the bias beam was a very sensitive determinant of high gated photo collection
- degradation shifted the observed collection peak to higher reverse voltages
- successive degradation resulted in a broadening of this maximum

- the 3D plot revealed that the maxima for higher wavelength are found at lower reverse voltages.

Supplementary investigations suggested are further work on the unwanted degradation by the illumination of the bias radiation for electron gating but especially for hole gating since this experiment reacted more sensitively to this effect (see section 6.2.4).

6.2. The dual beam experiment: Collection efficiencies > 1 and hole photogating

By reversing the electron gating experiment as described in section 6.1 in which the photogenerated electrons have the longer path to reach the contact, now ensures that the holes have to travel further than the electrons. For that reason this effect may be termed *hole gating*. (Zollondz et al., 1998, Zollondz et al., 1999) In principle the situation of hole gating is similar to that of the electron gating effect. Therefore for hole gating the same experimental set-up is used, i.e. the set-up described in section 3.2 for steady state measurements shown in Figure 3.3. Except for the sample orientation, which is reversed so that the bias beam is incident onto the n-side and the probe beam onto the p-side.

6.2.1. Hole Gating

While the electric field profile shows similar features to that in electron gating, clear differences are caused by the differing mobilities of electrons and holes. Figure 6.22 shows the internal field distribution under bias illumination *only* and under bias *and* probe illumination (compare Figure 6.7 for electron gating). Additional information and for clarity a third graph is plotted with the differences of the two curves. The field minimum caused by the n-side bias beam illumination is wider and reaches deeper into the i-layer (from the incident bias beam) in comparison to electron gating with the same parameters. Similarly, the changes of the internal electric field induced by applying the probe beam happen deeper in the i-layer. While for electron gating the position of maximum enhancement of the internal electric field was at 0.5 μm from the incident bias beam side (p-side) now the maximum of the increased field is approximately 1.2 μm deep in the i-layer for the same (reversed) beam specifications.

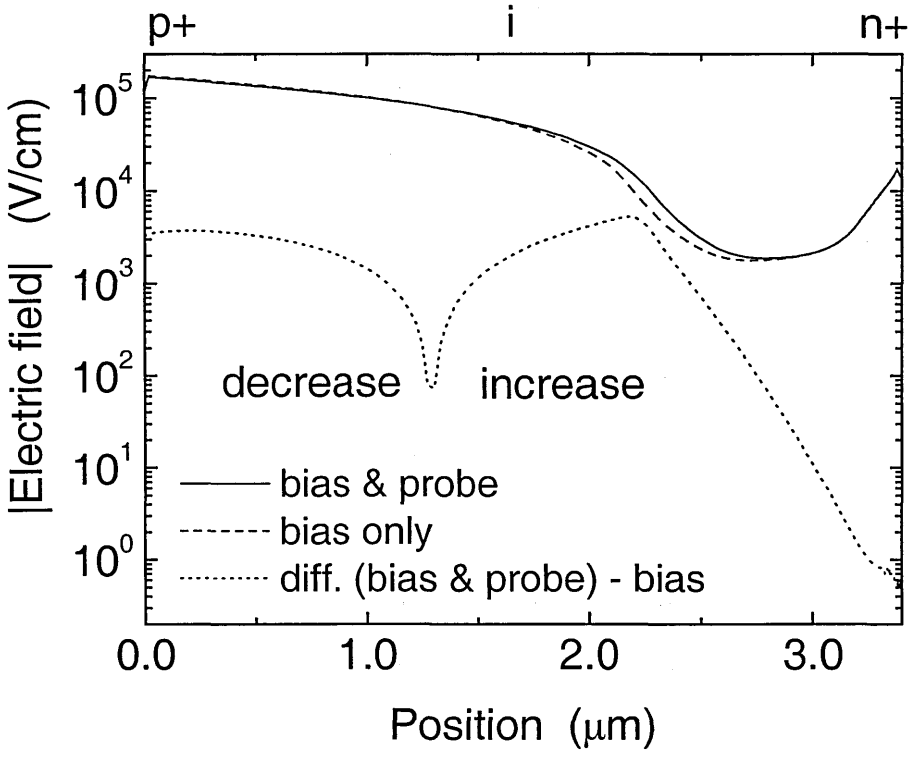

Figure 6.22: Internal electric field distributions with and without additional probe illumination for hole gating (n-side bias, p-side probe illumination).

Simulation shows that for higher defect densities the minimum of the electric field widens - i.e. a fairly degraded sample would show similar electron photogating results as an undegraded hole gating one, but only for the shape and the position of the maximum of the collection efficiency curves. The absolute values will differ because of the lower mobility of holes in a-Si:H.

table 6.3: default settings for hole gating experiments.

	directed to	**wavelength**	**Photon flux**
bias-beam (front)	n-side	$\lambda_b = 470$ nm	$\Phi_b = 1\times10^{15}$ cm^{-2}s^{-1}
probe-beam (back)	p-side	$\lambda_p = 620$ nm	$\Phi_b = 1\times10^{12}$ cm^{-2}s^{-1}

Again a preferred set of parameters is used in most experiments that may be described here as the default values for the hole gating experiments (table 6.3). This set of parameters is always used unless it is stated differently: the probe beam (p-side) was kept at a photon flux of $\Phi_p = 1\times10^{12}$ $cm^{-2}s^{-1}$ while the probe wavelength was $\lambda_p = 620$ nm. For the bias beam (n-side) values of $\Phi_b = 1\times10^{15}$ $cm^{-2}s^{-1}$ and $\lambda_b = 470$ nm were used as default values.

6.2.2. Influence of light soaking (defect densities)

As in the section for electron gating (section 6.1.2) the influence of defects is examined first, but now for the hole gating process. All these experiments are done on the same set of sample as for electron gating, i. e. the IPE Stuttgart sample ($d = 3.5$ µm). Figure 6.23 shows measured hole gating for the default illumination situation for *hole gating* as described in table 6.3 (bias wavelength of $\lambda_b = 470$ nm (n-side) for the bias beam and $\lambda_p = 620$ nm (p-side) for the probe beam with photon flux of $\Phi_b = 1\times10^{15}$ $cm^{-2}s^{-1}$ and $\Phi_p = 1\times10^{12}$ $cm^{-2}s^{-1}$, respectively). The absolute values are lower than for electron gating as expected. Still the values exceed 1 and the gating effect is obvious with gains of up to 13. A maximum can even be observed for the 1 minute degraded sample.[16] Light soaking times with AM 1 were as for the electron gating experiment

$t = 1, 10, 100, 600$ minutes, as the sample was the same one as for electron gating.

As in the electron gating results, the maximum is shifting to higher reverse voltage values with successive illumination. Degradation of only 10 minutes with AM 1

[16] This is remarkable because of bias beam degradation on the n-side the experiment was difficult to make. The system reacted very sensitively to high photon fluxes of strongly absorbed photons, especially on the n-side.

results in a shift in the maximum beyond the V = –20 V area as displayed in Figure 6.23.

For long degradation times the collection will not exceed one unless the applied voltage is high enough to force the holes to the p- contact. In comparison to the electron gating this is more difficult for hole gating because of the lower hole mobility and their lower lifetime.

Although the simulated data in Figure 6.24 show qualitatively the same features as the measured hole gating results, e.g. the maximum at high reverse voltages, the simulations do not fit well to the measured results: the only maximum that is found is too low as the whole curves are rather lower than the experimental data. Measurements show a maximum of 12 in the collection efficiency at V = –15 V while simulations show a maximum of 2.5 in the collection efficiency at V = –10 V for a defect density of 2×10^{15} cm^{-3}. The results were obtained using the same parameters which gave very good agreement between simulation and measurement of electron gating and Figure

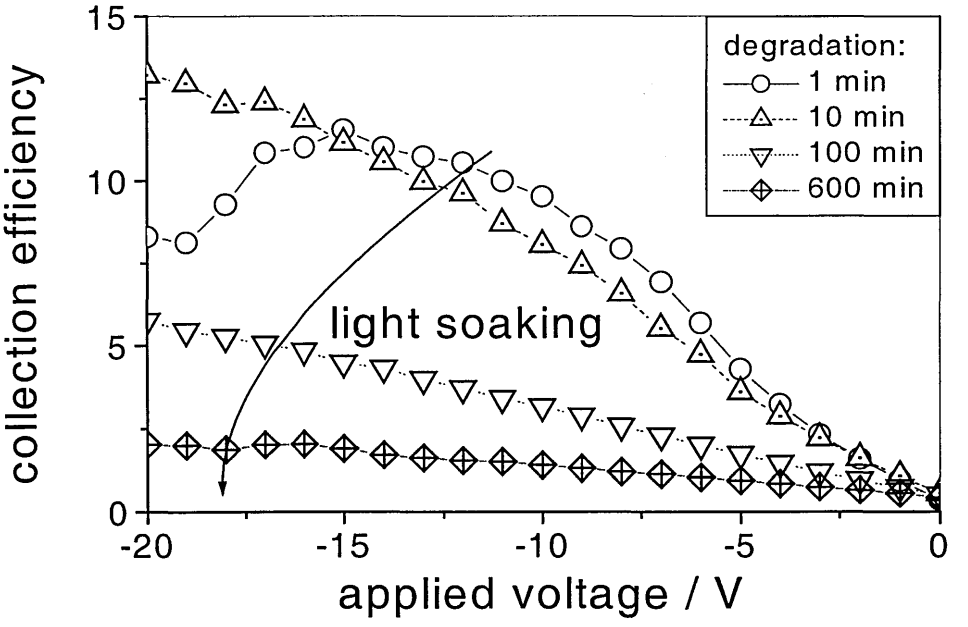

Figure 6.23: Experimentally determined hole gated collection efficiencies *vs.* applied voltage for different degradation states (IPE sample TC (3.5 µm)). Compare Figure 6.12 which shows results for the same sample and experimental adjustments but for electron gating (reversed experiment).

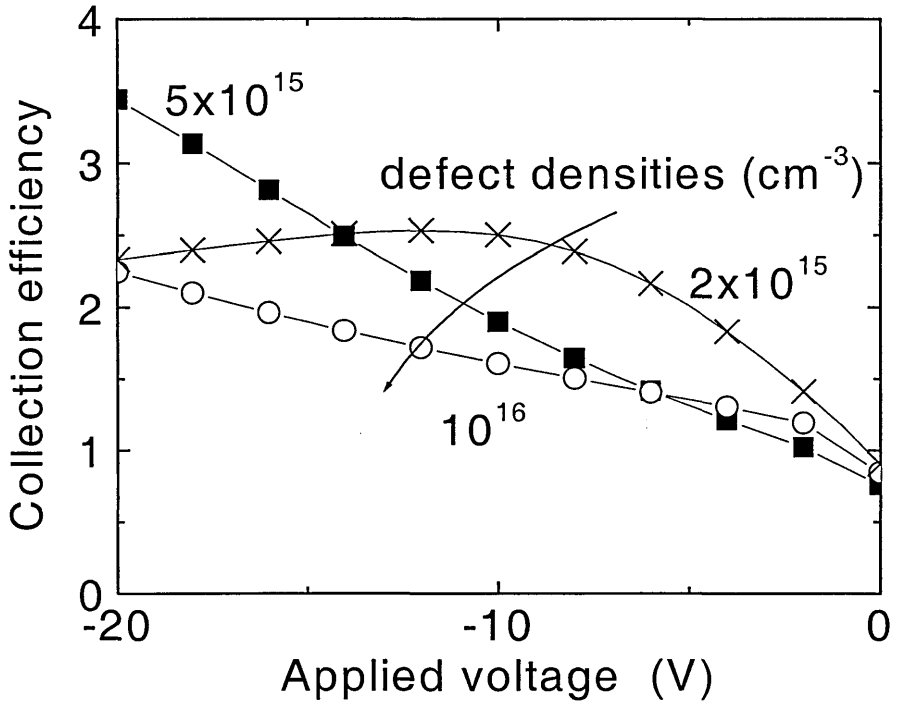

Figure 6.24: Simulated hole gating for different defect densities.

6.24 uses defect values that resulted from the electron gating experiment. Since a simple single energy function was chosen for the defects, the discrepancy may originate from this simplification in the simulation parameters. In section 6.4 an extended defect density distribution will be discussed but here the first discrepancy is found for simple single energy defect distribution.

6.2.3. Hole gating – Probe beam variations

Because of the lower gating effect for holes and due to experimental restrictions, variations of the probe photon flux were not executed. Photon flux variations for hole gating experiments should result in curves similar to those discussed in section 6.1.3 where electron gating experiments for this kind of variations are shown (Figure 6.14).

The probe beam variations discussed here are restricted to wavelength variations. In Figure 6.25 and Figure 6.26 the results of variation of the probe beam wavelength are shown for hole gating collection efficiency. The 3D plot was chosen to display the maximum response in more detail. It should be stressed here that in contrast to the corresponding graphs of electron gating, Figure 6.16 and Figure 6.17 in section 6.1.3, the bias beam photon flux is the same for both graphs ($\Phi_b = 1\times10^{16}$ cm^{-2}s^{-1}). The bias wavelength was kept at the usual value of λ_b = 470 nm and the default probe photon flux was used ($\Phi_p = 1\times10^{12}$ cm^{-2}s^{-1}). In comparison to results of electron gating, the colour response is similar: the maximum in collection efficiencies is found at the same wavelength as for electron gating, i.e. $\lambda_p \approx 621$ nm. Although the bias photon flux is a factor of 10 higher than for electron gated results in Figure 6.16 the absolute gating values are lower (compare section 6.2.2).

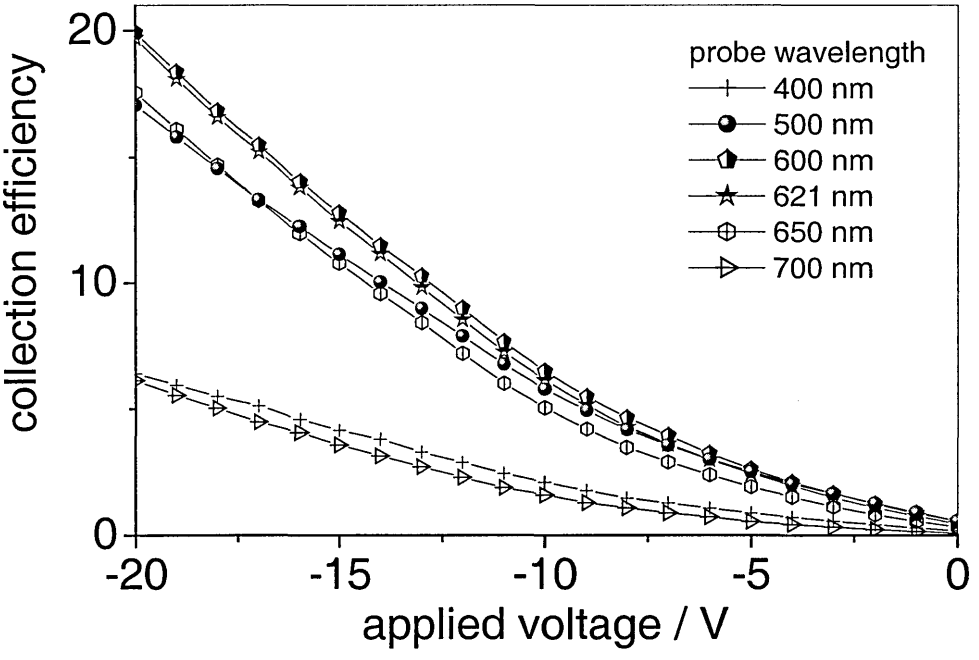

Figure 6.25: Measured variation of the collection efficiency with applied voltage for hole gating for varied probe beam wavelengths, $\Phi_b = 1\times10^{16}$ cm^{-2}s^{-1}, $\lambda_b = 470$ nm.

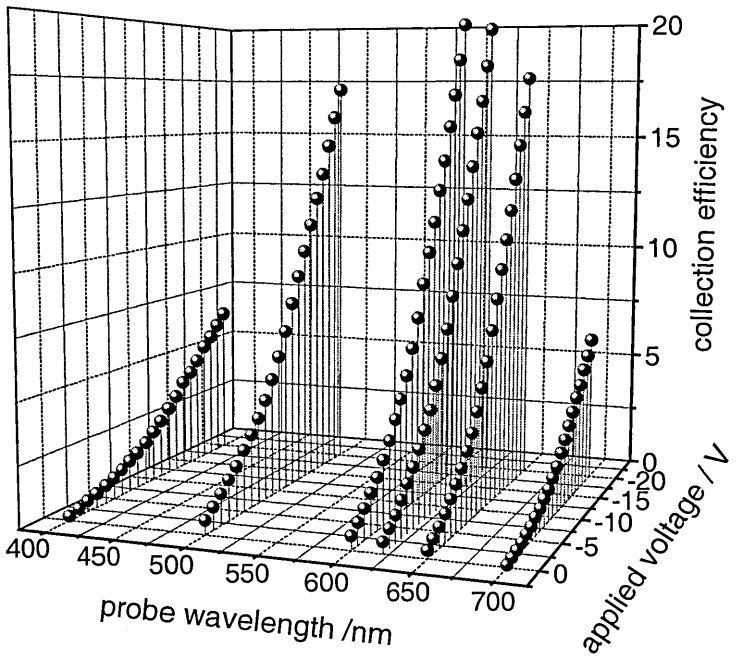

Figure 6.26: 3D-plot of measured variation of the collection efficiency with applied voltage for hole gating for varied probe beam wavelengths, $\Phi_b = 1\times10^{16}$ $cm^{-2}s^{-1}$, $\lambda_b = 470$ nm.

Again a degradation effect was found that was caused by the experiment itself. Figure 6.27 shows measurements of hole gating collection efficiency *vs.* applied reverse voltage, for same illumination parameters. These were default values with $\lambda_b = 470$ nm and $\Phi_b = 1\times10^{16}$ $cm^{-2}s^{-1}$ for the bias beam and $\lambda_p = 620$ nm of $\Phi_p = 1\times10^{12}$ $cm^{-2}s^{-1}$ for the probe beam. The first two measurements were taken successively. Almost no changes are observed. The next measurement was taken after a series of different probe wavelength variations, i.e. the sample was illuminated three times from the p-side with $\lambda_p = 400$ nm, $\lambda_p = 500$ nm and $\lambda_p = 600$ nm with a photon flux of $\Phi_p = 1\times10^{12}$ $cm^{-2}s^{-1}$ and additionally with $\lambda_b = 470$ nm of $\Phi_b = 1\times10^{16}$ $cm^{-2}s^{-1}$ from the n-side. Since the bias

illumination with its high photon flux was applied for each measurement, i.e. three times, the degradation effect is higher in relation to the observed effect before.

The fourth measurement was taken after a series of bias beam variations (on the n-side): λ_b = 470 nm, λ_b = 505 nm, λ_b = 525 nm, λ_b = 590 nm, λ_b = 612 nm and λ_b = 660 nm with $\Phi_b = 1\times10^{16}$ cm^{-2}s^{-1} and additional p-side probe illumination of λ_p = 620 nm and $\Phi_p = 1\times10^{12}$ cm^{-2}s^{-1}. Again an effect of degradation is observed.

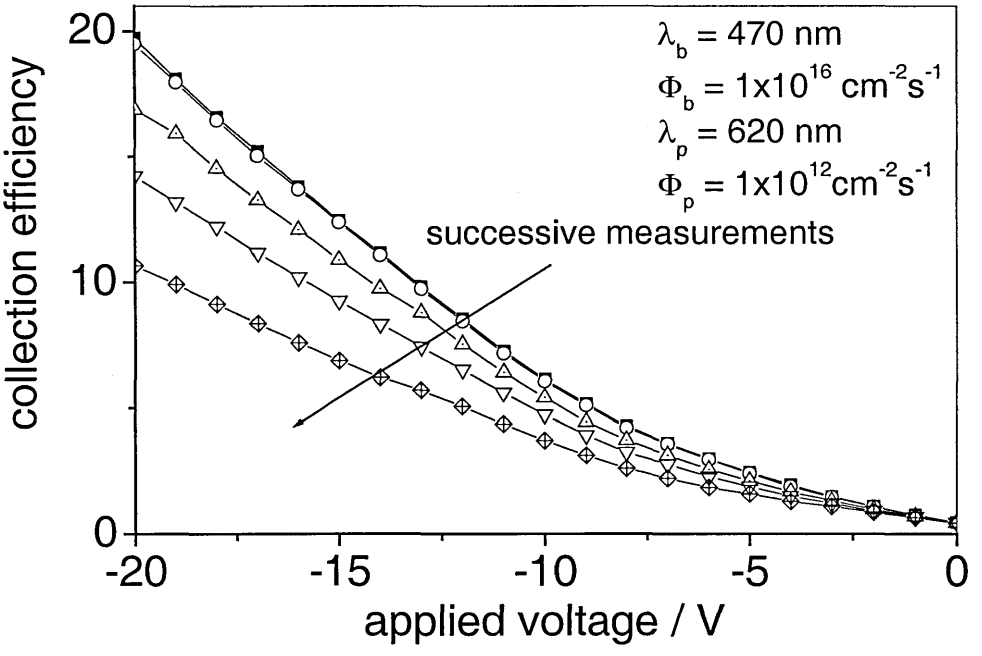

Figure 6.27: Series of measurements with the same illumination parameters during measurement procedure.

Note that for the p-side probe influence the photon flux was $\Phi_p = 1\times10^{12}$ cm^{-2}s^{-1} while for the n-side, the photon flux was four orders of magnitude higher ($\Phi_b = 1\times10^{16}$ cm^{-2}s^{-1}).

The last measurement was done after a series of variations of bias light photon fluxes. Here the illumination was varied on the n-side at a wavelength of λ_b = 470 nm to an extreme value of $\Phi_b = 3\times10^{16}$ cm^{-2}s^{-1}. The probe beam (p-side) was kept at

λ_p = 620 nm and $\Phi_p = 1\times10^{12}$ cm^{-2}s^{-1}. Again the influence of the continued illumination in lowering the gating signal is evident.

A possible degradation effect is found to be more pronounced for n-side illumination, what is caused by the asymmetrical distribution of acceptorlike and donorlike localised states. (Solomon, 1997, Shur, 1990)

For the following measurements values of $\Phi_b = 3\times10^{16}$ cm^{-2}s^{-1} were avoided for the bias beam.

6.2.4. Hole gating – Bias beam variations

For the first bias beam, variation the probe beam was kept at the usual values of λ_p = 620 nm and $\Phi_p = 1\times10^{12}$ cm^{-2}s^{-1} (n-side) and the bias beam wavelength was kept at λ_b = 470 nm while the bias beam photon flux was varied between values of $\Phi_b = 1\times10^{12}$ cm^{-2}s^{-1} and $\Phi_b = 1\times10^{16}$ cm^{-2}s^{-1}. Figure 6.28 shows the measured collection

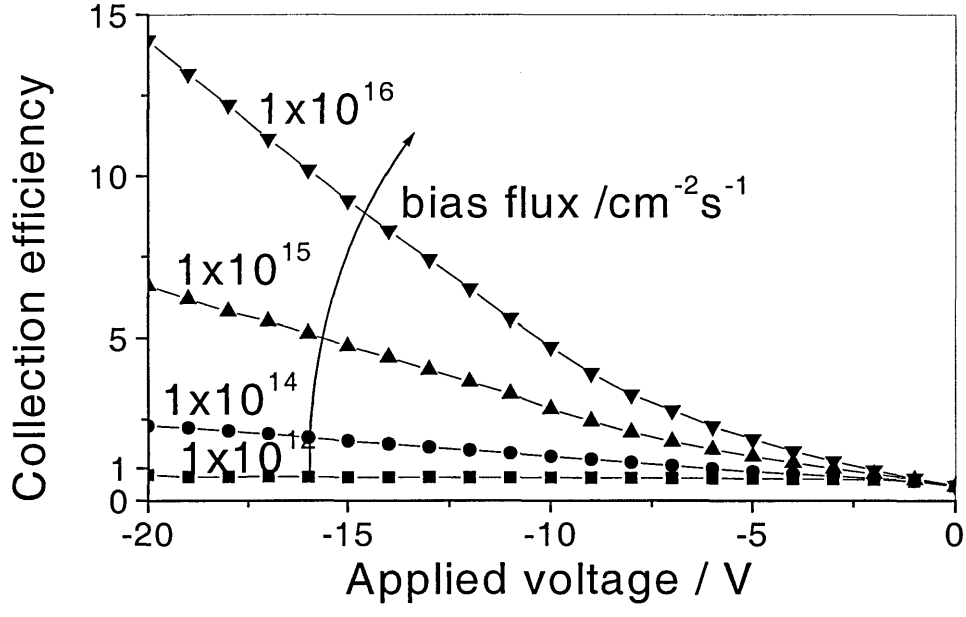

Figure 6.28: Measured variation of the collection efficiencies with applied voltages for hole gating as the bias beam photon flux is varied while the bias beam wavelength and the probe beam is kept constant (λ_b = 470 nm, λ_p = 620 nm, $\Phi_p = 1\times10^{12}$ cm^{-2}s^{-1}).

efficiencies *vs.* the applied voltage with variation of the incident bias photon flux. The maxima of collection are beyond an applied voltage of V = –20 V. For a low ratio between bias and probe photon flux a minor gating effect is observed. For a bias flux equal to the probe photon flux the collection efficiency values never exceeds 1, i.e. no gating is observed. The higher the ratio between probe and bias beam photon flux the higher the gating effect.

The effect of varying the bias wavelength is shown in Figure 6.29, where the probe specifications were kept constant and additionally the bias photon flux was held at a value of Φ_b = 1×10^{15} $cm^{-2}s^{-1}$ while the bias beam wavelength was varied. As expected, the maximum of collection is again found for a bias wavelength of λ_b = 470 nm with decreasing collection efficiency values for longer wavelengths. For λ_b = 660 nm where no field minimum can be expected the collection never exceeds unity.

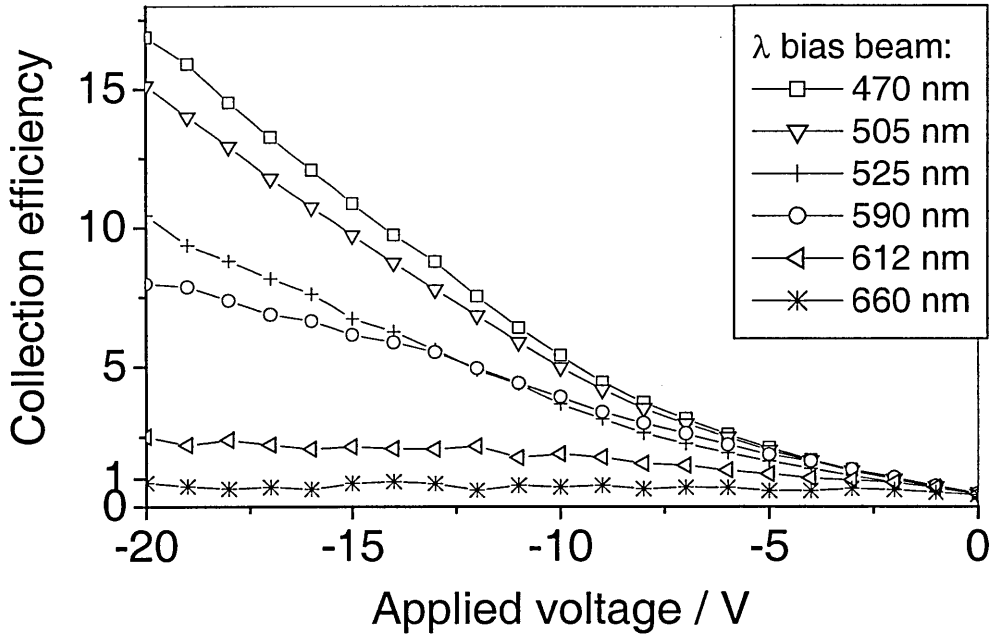

Figure 6.29: Measured hole gating collection efficiencies for varied applied voltages and for different bias wavelengths.

Figure 6.30 shows 3D plots and the corresponding contour plots (with increasing light soaking times from Figure 6.30 a) to d), (degradation time as for electron gating: t = 1, 10, 100, 600 minutes)[17]. Here the degradation effect can be observed over the whole spectrum of wavelength and over the measured interval of applied voltages. Even if the plots indicate that the degradation resulted in lower collection the situation can be also described by a maximum that shifts to higher reverse voltages. This point of view also fits the picture of electron gating and the here shown results.

While a shift in the position of the maximum for every degradation state was found for electron gating, i.e. shorter incident bias wavelengths effected maximum collection at higher reverse voltages, is not found for hole gating - or not very pronounced. A very close look at Figure 6.30 a) shows such a shift from –15 V at λ_b = 470nm to –12V at λ_b = 570 nm. The fact that this effect is not as distinct as for electron gating supports the idea that this is a deeper field minimum for lower wavelengths and therefore a need for higher applied voltage to collect the released photocarriers: as described earlier in this chapter, the field minimum for hole gating is not as deep and distinct as for electron gating (Figure 6.22) so that variation of the bias wavelength will not have such a strong effect as for electron gating.

A new feature (visible in Figure 6.30) is a local minimum in the spectrum at λ_b = 570 nm. Checks confirmed that the wavelength of the LED had not changed.[18] The reason for the 'side', or double, maxima can be found in the spectrum of single beam collection efficiency (spectral response) for n-side illumination (Figure 5.5 section 5.4). As the bias beam wavelength is varied the poor collection, except for the sharp

[17] The degradation times here were the same as for the electron gating measurements but the measurements of the undegraded sample were not made, i.e. that Figure 6.30 a) corresponds to Figure 6.21 b) (1 min of degradation), Figure 6.30 b) corresponds to Figure 6.21c) (10 mins of degradation) and so on.

[18] The calibration data were taken before all measurements and showed no difference to those taken after finishing all experiments.

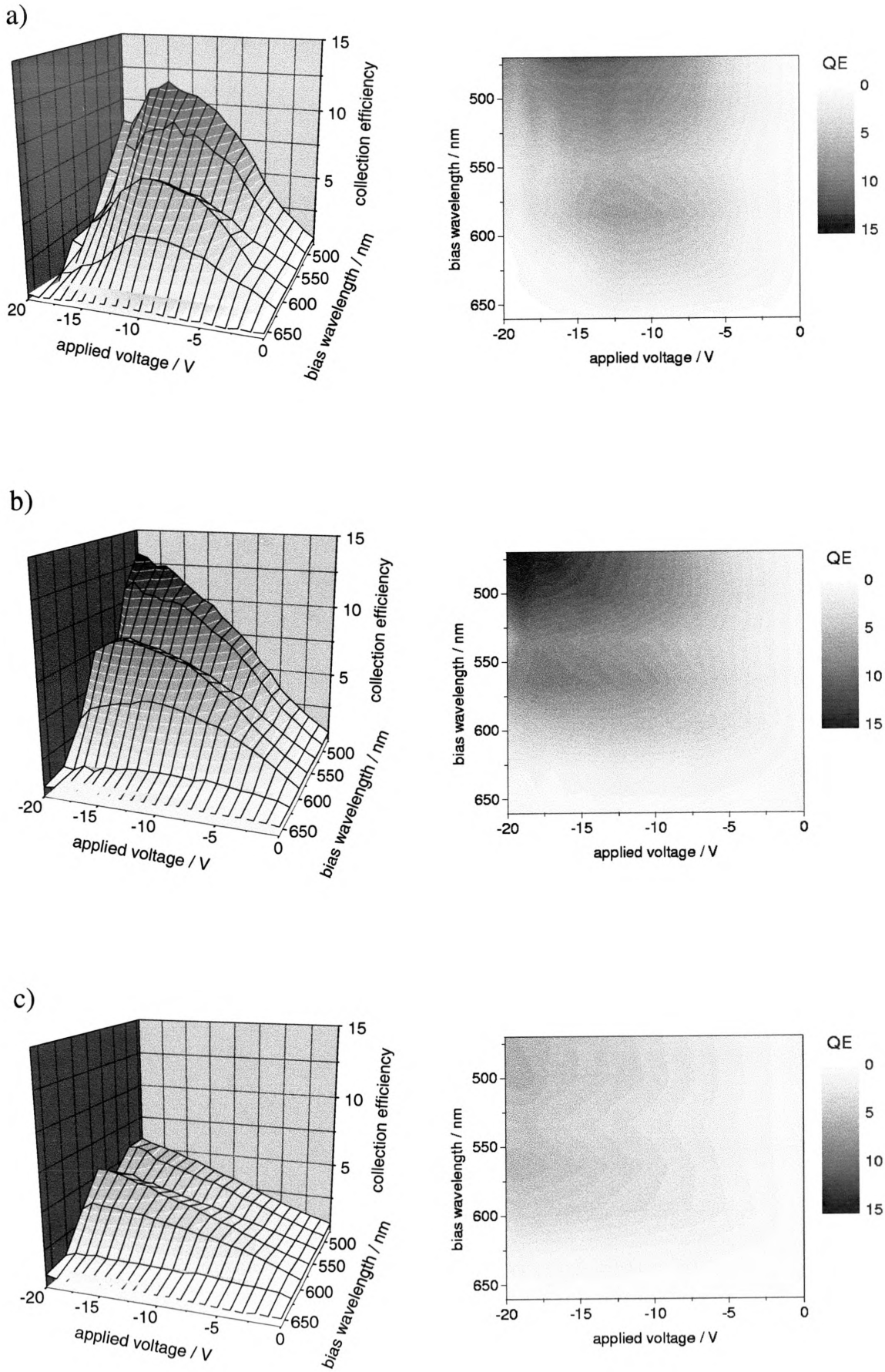

caption: see next page

d)

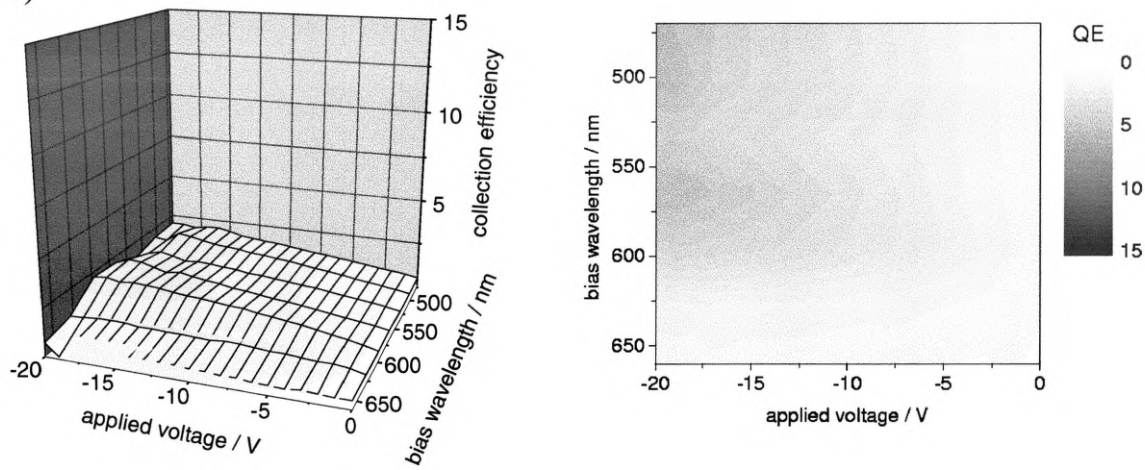

Figure 6.30: Measured hole gating collection efficiencies for varied applied voltages and for different bias wavelengths. a) - d) increasing degradation. Each left Figure shows a three dimensional surface plot while the right Figure is the according contour plot.

maximum at λ = 650 nm and a shoulder around λ = 570 nm, competes with the gated collection efficiency. Since the gated collection is very poor at the main maximum of single beam n-sided collection efficiency at λ = 650 nm the illumination at this wavelength forms no side maximum.

In contrast to that the difference in the single beam collection efficiency between λ = 470 nm and λ = 570 nm does make a difference for the gated collection efficiency - especially for low gains.

In principle this should be found for electron gating, too, but the much higher photogating gains in this case dominate the photogating result, so that the single beam collection efficiency does not effect these results noticeably, especially since the p-side single beam collection efficiency spectrum is more even.

6.2.5. Summary

With the electron gating experimental arrangement reversed, hole gated collection efficiencies were measured and explained, for the first time to the authors knowledge. In comparison to electron gating, field distributions with similar features were presented and differences were recognised. These differences gave an explanation for lower hole gating collection efficiency results in relation to electron gating collection efficiency results.

The influence of light soaking was discussed and for hole gating a far more pronounced bias beam originated degradation effect was found, that is due to the high photon flux of the bias beam directed onto the n-side that is less stable under illumination.

This fact, and the less satisfactory agreement for hole gating with similar parameters provided motivation for a study of an asymmetric defect distribution in the i-layer as a possible reason (section 6.4.1).

6.3. Photogating on different i-layer thicknesses

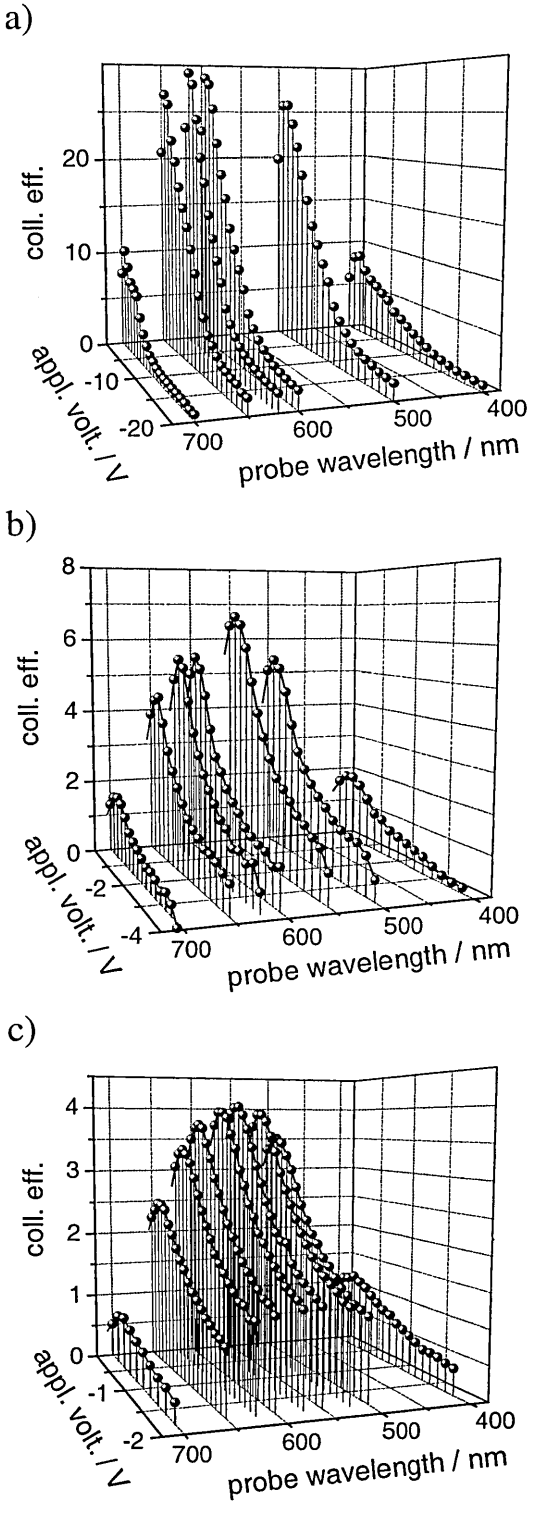

Figure 6.31: variation of the probe wavelength for electron gating for different sample thicknesses: a) d = 3.5 μm, b) d = 2 μm, c) d = 1 μm.

Since there was a series of three IPE samples from Stuttgart with different i-layer thicknesses (d = 1 μm, 2 μm, 3.5 μm) an investigation of the collection efficiencies for these was undertaken.

The probe beam wavelength was varied since differences were expected under these conditions. Bias beam variation should result, in principle, to similar results for all thicknesses. Since bias beam wavelength variations result in field minima close to the incident side that reach deeper into the i-layer the longer the wavelength, the actual differences for different sample thicknesses are expected to be relative, only. In contrast to that, the probe beam wavelength for gated collection is expected to be dependent on the i-layer thickness because the i-layer thickness should influence the effect of gating, enhancement of the internal electric field.

Figure 6.31 shows the results of collection efficiency measurements with variation of the probe beam wavelengths for different sample thicknesses, for *electron* gating. Figure 6.31a) is for the sample from the previous sections with an i-layer thickness of $d = 3.5$ μm, where result shown, in Figure 6.31b) relate to a sample with an i-layer thickness of $d = 2.0$ μm and in Figure 6.31c) to one of $d = 1.0$ μm. Bias beam parameters were kept at the usual values ($\Phi_b = 1\times10^{15}$ cm^{-2}s^{-1} and $\lambda_b = 470$ nm) as was the probe photon flux with $\Phi_p = 1\times10^{12}$ cm^{-2}s^{-1}. The variation was made in the probe wavelengths to investigate maximum gating effect for probe beam wavelength variations.

As expected the gating effect is higher the larger the i-layer thickness: a thicker i-layer results in a more easily manipulated internal electric field, because the required low field region normally takes up a wide range of the i-layer. In Figure 6.32 simulated internal electric field distributions are shown for the three sample thicknesses at zero applied voltage. The simulations are performed with a single beam set-up and thus show the situation prior to modification of the internal electric field by the probe beam. The field reversal is clearly visible for the thicker samples ($d = 3.5$ μm, 2.0 μm) while the thinnest sample does not show this effect. It should be pointed out that the differences between the $d = 3.5$ μm and the $d = 2.0$ μm thick sample are not as pronounced as with the $d = 1.0$ μm thick sample but the differences of the gated collection efficiencies of Figure 6.31 indicate a big difference. While the gating values for the $d = 3.5$ μm sample nearly reach 30 the $d = 2.0$ μm thick sample only has a maximum of 7 and the $d = 1.0$ μm has its highest values at only 4. But that these values still exceed unity shows that a field variation is possible even for the thinnest i-layer value examined.

A second observation is that the maxima of collection are found at different values for the three samples. While the maximum of gating of the $d = 3.5$ μm is found at

a probe beam wavelength of λ_p = 620 nm, for the d = 2.0 μm sample it is shifted to λ_p = 550 nm as for the d = 1.0μm.

The gating effect is controlled by the combined influence of the dual beams and the high gain normally outweighs the possible influence of the single probe beam collection (as described in section 6.2.4). When gating is as high as 30 for a 3.5 μm thick sample, the influence of the single beam collection efficiency must be seen as negligible, because only a small fraction has its origin directly from the probe beam (30/1). But for a gating factor of 7 for the d = 2.0 μm thick sample or even 4 of the d = 1.0 μm thick sample must show a higher influence of the *single* probe beam collection itself but still should be seen as small in comparison to the gated signal.

The reason for a shift in the maxima for different i-layer thicknesses must lie in the dual beam experiment itself. Highest gains are obtained for probe illumination which is absorbed in the area of the higher field (plateau between 2.0 μm

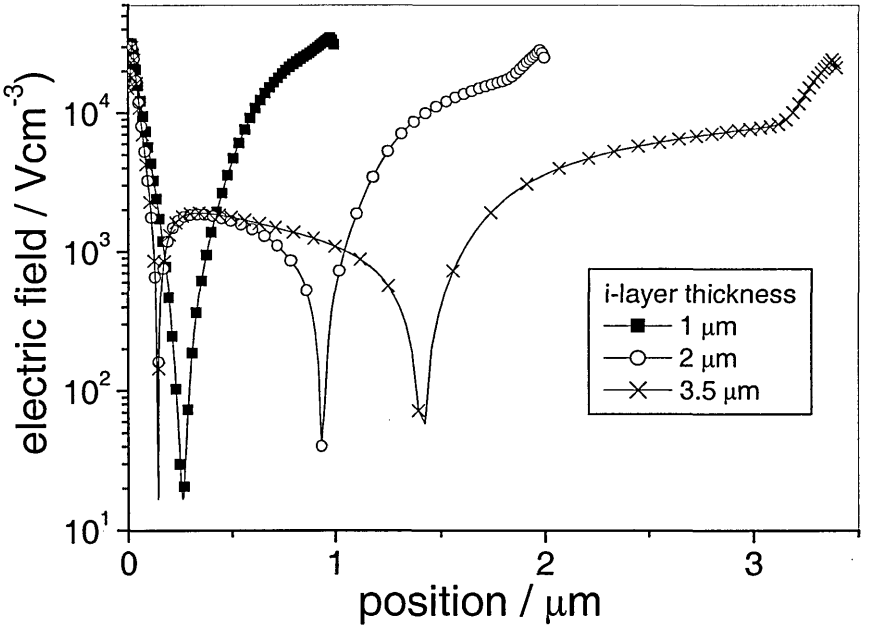

Figure 6.32: Internal electric field distributions for different i-layer thicknesses (d = 3.5 μm, 2.0 μm, 1.0 μm) at V = 0V.

and 3.0 µm) in the i-layer (compare the simulated field distribution of the $d = 3.5$ µm thick sample in Figure 6.32). Here the electric field is lowered by screening with photogenerated holes that are trapped while drifting to the p-contact. For thinner samples the area of the field plateau is narrower and therefor the maximum gain must result from a beam that is absorbed in this narrower area, requiring a higher absorption coefficient. Surface losses are a competing process and the higher field results in lower trapping ratios for thinner samples.

The expected tendency is more obvious for the hole gated results since the collection efficiency values here are even lower. Figure 6.33a) – c) shows the results for different i-layer thicknesses of hole gated results. In comparison to the electron gating results (Figure 6.31) the axis that shows the applied voltage and the axis that shows the probe wavelength are

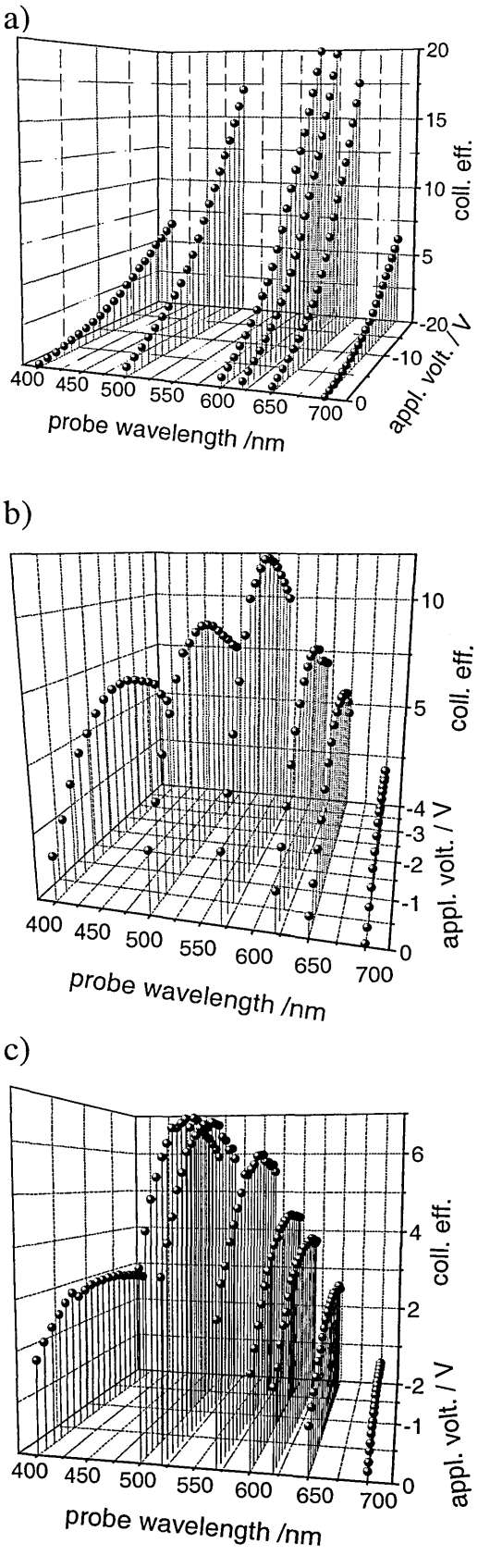

Figure 6.33: Variation of the probe wavelength for hole gating for different sample thicknesses: a) $d = 3.5$ µm, b) $d = 2$ µm, c) $d = 1$ µm.

reversed for a better view. The absolute values seem to be higher than for electron gating, but note that a higher bias beam photon flux was chosen for this series of measurements to $\Phi_b = 1\times10^{16}$ $cm^{-2}s^{-1}$ (*cf.* $\Phi_b = 1\times10^{15}$ $cm^{-2}s^{-1}$ for electron gating in Figure 6.31) because of lower hole gating values. The other parameters are the same. The shift of the maximum is observed here through all thicknesses: while the maximum of gating is found for the $d = 3.5$ μm thick sample at $\lambda_p = 620$ nm the maximum of the $d = 2.0$ μm thick sample is found at $\lambda_p = 570$ nm and for the $d = 1.0$ μm $\lambda_p = 500$ nm. These results underline the conclusions discussed for the electron gating results, *viz.* a narrower field minimum for thinner samples.

6.3.1. Summary

Investigations of photogating by electron and hole collection were examined for a series of three i-layer thicknesses. As expected the gated collection efficiency is smaller the thinner the i-layer. This is caused by a higher field distribution for thinner samples that is not as easy manipulated as for thicker samples.

Probe beam wavelength variations resulted in a maximum observed collection efficiency for shorter wavelengths, for thinner samples. The explanation with a narrower high field screening "plateau" was given resulting in steeper required absorption profiles for maximum collection.

6.4. Comparison of photogating results with *i-v* characteristics

In principle, similar information to the photogating results of degradation is already contained in the 'S-shape' of the *i-v* characteristics (Abel et al., 1991, Zollondz, 1995, Carius, 1997, Brüggemann et al., 1997) as shown in Figure 6.34. In this section it will be shown that in the photogating experiment *more* information can be revealed than from the analysis of the S-shaped *i-v* curves.

The S-shape *i-v* characteristic appears to be associated with the situation in which charge is generated near one contact of the device, producing a local field minimum. The generated charge recombines preferentially in this region, and is only fully collected when the applied field is sufficiently high to significantly modify this existing field profile. This is exactly the condition set up by the short-wavelength bias illumination in the present work. In the middle of the 'S' the slope of the characteristic goes through a maximum. A qualitative relation between the slope *dI/dV* and the photogating effect may be explained as follows. In the case of the photogating effect, charge introduced by the probe beam and trapped in the i-layer, provides screening, and thus slightly modifies the field in the 'front' of the device. In the simple *i-v* measurement, a small change in the applied field will similarly affect the internal field distribution in the device, including a small change in the low-field 'recombination' region. Thus the two effects have similar origins, but are of course not identical in detail.

Figure 6.34 shows *i-v* characteristics as they were calculated for bias beam only illumination (compare Figure 5.3 section 5.3). A study of degradation as in section 6.1.2 is difficult because any change of the form of the *i-v* curve seems not to have as many clear features to analyse as the shift in the collection maximum or the form of the maximum observed in electron gating results. It seems therefore, that a proper study may not be possible. Since the form of the *i-v* curve changes in a specific way and the *slope* of the curve plays an important part as described above, analysis was performed of the first derivative of the *i-v* curves of Figure 6.34a. The result is shown in Figure

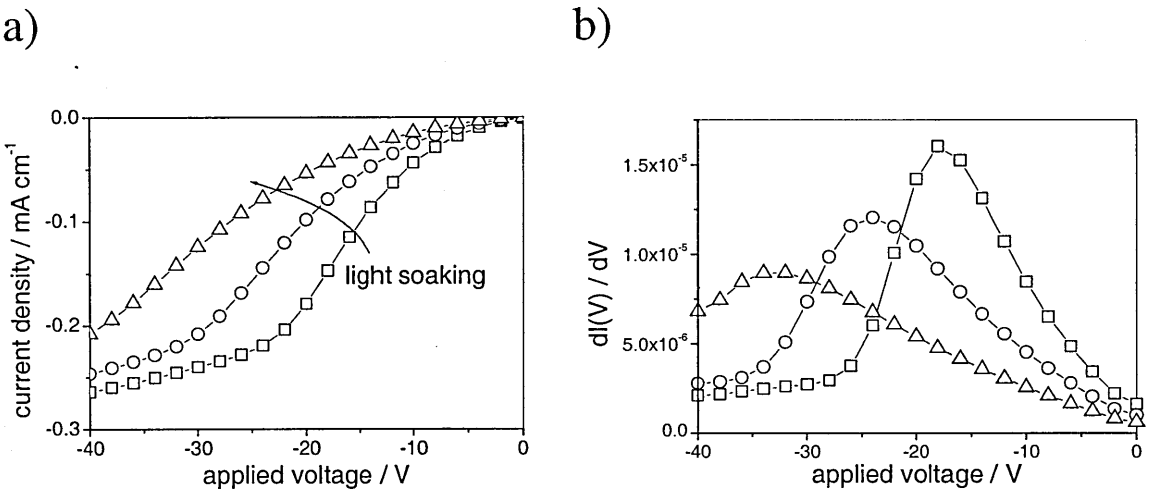

Figure 6.34: Simulated *i-v* characteristics (bias beam only) (a) as they are calculated for Figure 6.11 section 6.1.2 and their first derivatives (b).

6.34b. Without the involvement of a probe beam the information obtained from the high collection efficiency results for this simulation is already evident in a simple *i-v* analysis. To compare these results, in Figure 6.35 the simulations of high collection efficiency as presented in section 6.1.2 and the results of the *i-v* derivative analysis are shown in one graph. The maxima are found at the same reverse voltages and the shape

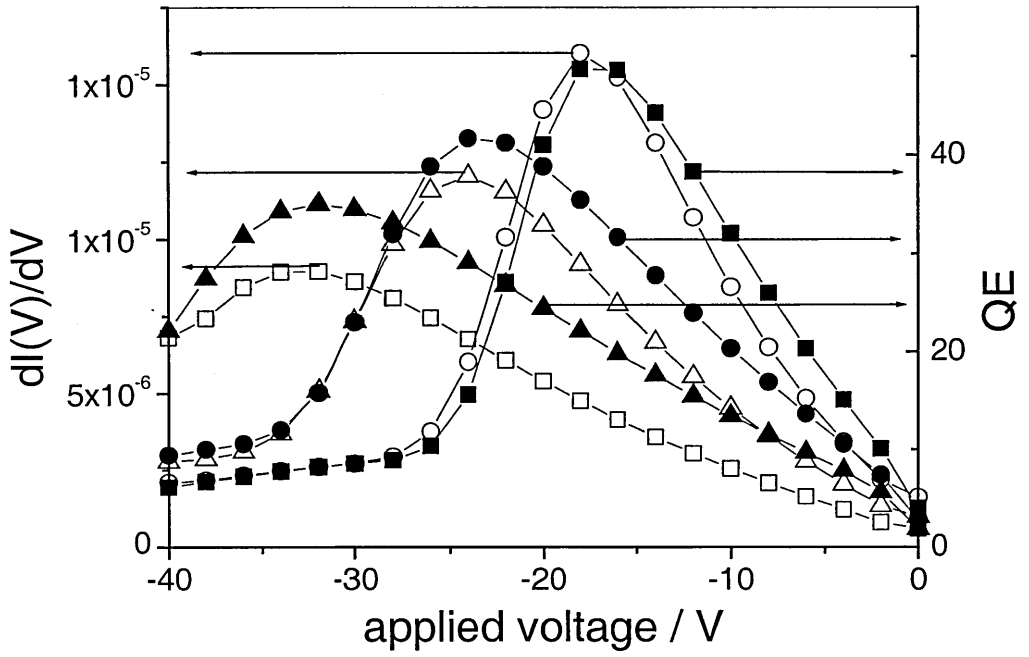

Figure 6.35: Comparison of different defect densities for simulated collection efficiency results (full symbols) and for the first derivative of simulated *i-v* characteristics (bias beam illumination only!) (open symbols).

of each maximum matches. The only difference is found in the relative values of the maxima.

So far all figures discussed in this section are simulated but would fit measured results very well since the simulations were done to fit measured results (compare Figure 6.10 and Figure 6.11 in section 6.1.2). Figure 6.36a shows *i-v* curves, of the *measured* degradation series discussed in section 6.1.2 and their first derivatives (Figure 6.36b), but here in contrast to Figure 6.10 with two additional lower degradation states.[19] The two additional degradation times with AM 1 were t = 0 min and t = 10 min while the earlier stated values shift to t = 110 min, t = 490 min and t = 1090 min. All simulation never showed lower maximal values in collection efficiency for lower

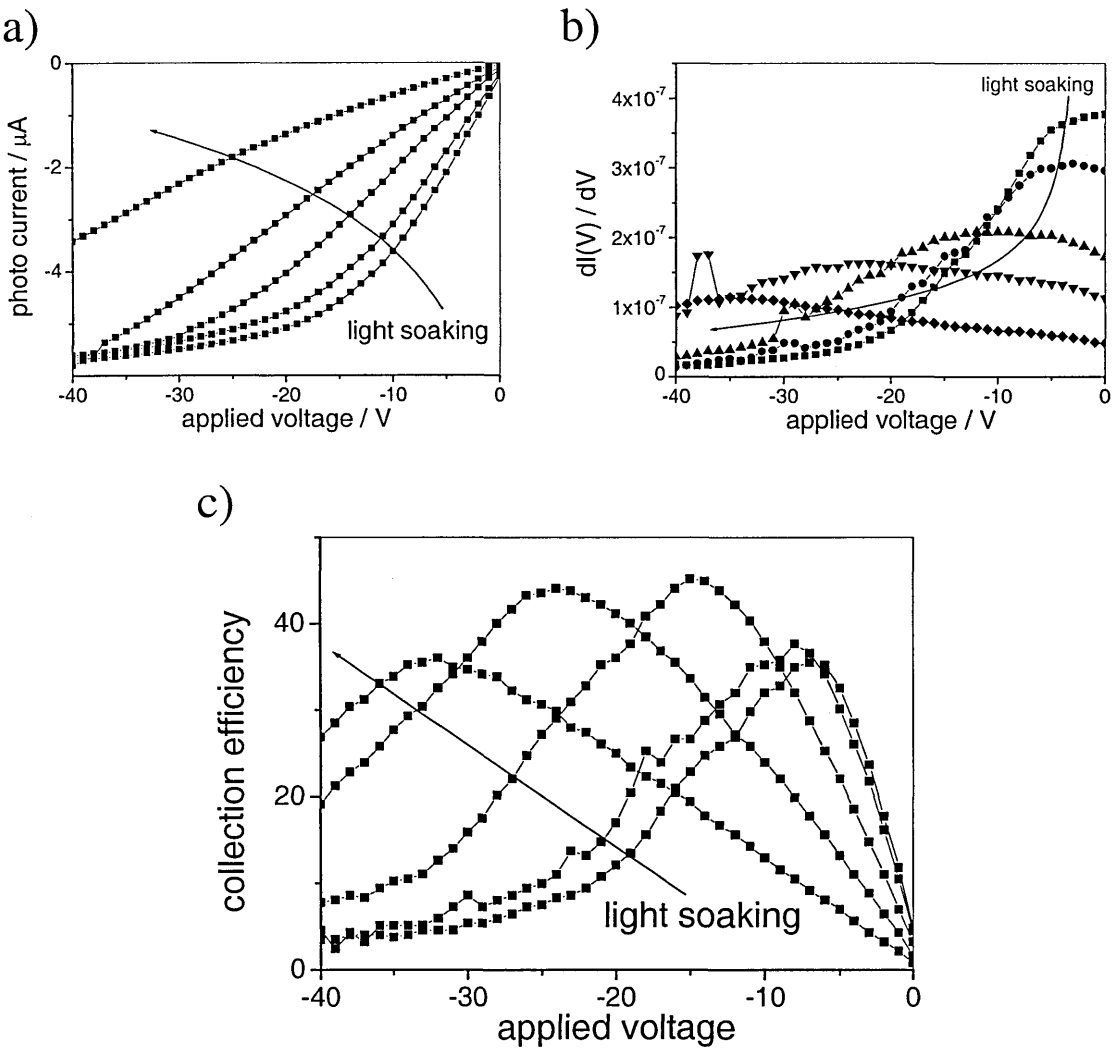

Figure 6.36. Measured *i-v* characteristics (bias beam only) (a) and the their first derivatives (b). and appropriate gated collection efficiency (c).

applied voltages for less degraded samples. Initially, an error in the first degradation series ever measured was assumed. But later measurements (as in Figure 6.12 and Figure 6.13) confirmed the tendency of a lower gating effect for less degraded samples. It was found that the simplification in the simulation parameters, i.e. ascribing a spatially homogeneous single level (with correlation) to the defect distribution a while giving reasonable agreement for degraded samples, was responsible for the failure of simulation to describe decreasing maxima for lower degradation states.

[19] Since simulation of these two curves failed the measurements were first rated as incorrect. Later further measurements confirmed the results that additional investigation was done.

6.4.1. Gating and inhomogeneous defect distributions

In this section a study of inhomogeneous defect distributions are undertaken and their effect on electron gating results. Electron gating means here again that the bias

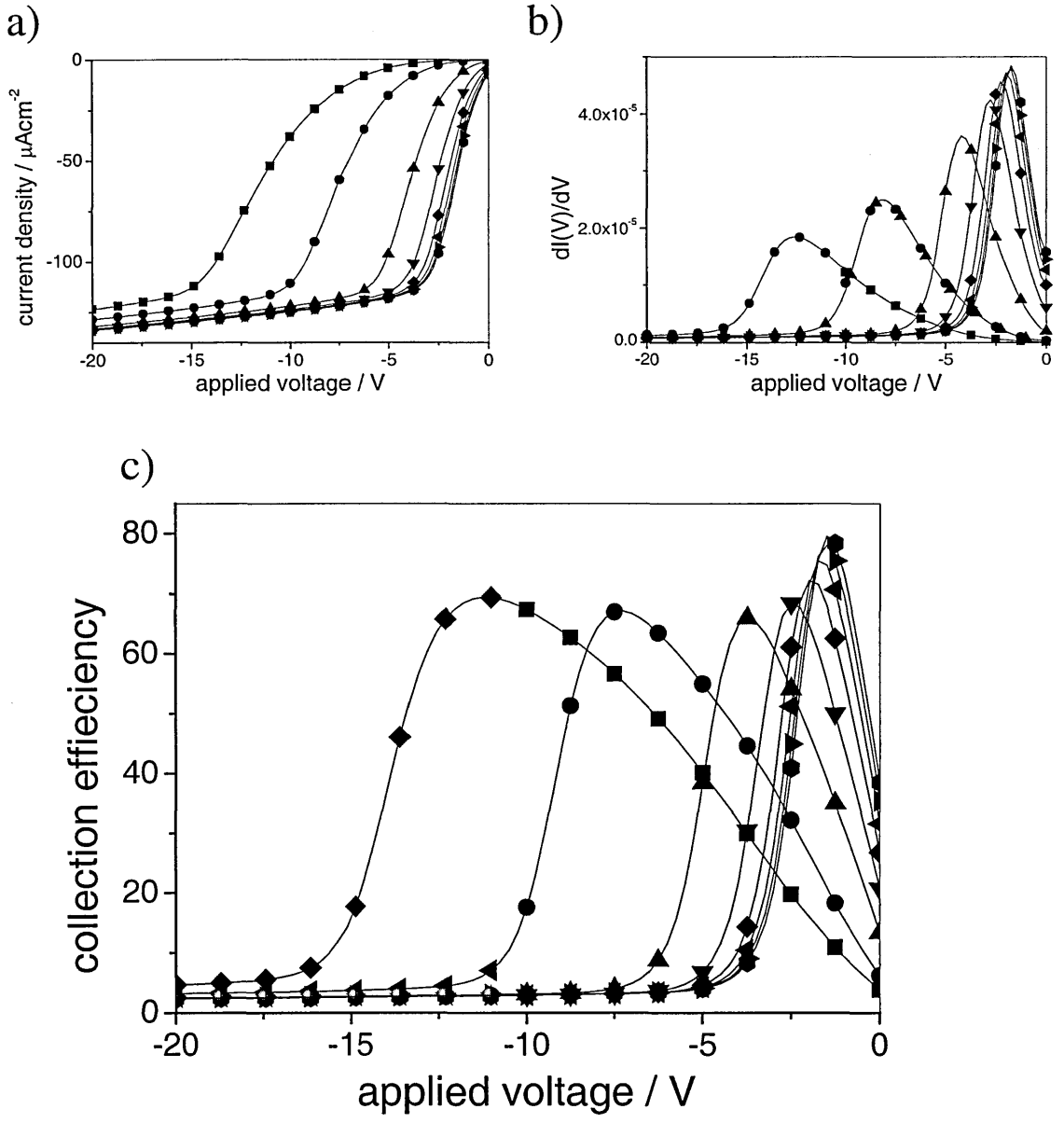

Figure 6.37: Simulated *i-v* characteristics (bias beam only) (a) and the their first derivatives (b). and appropriate gated collection efficiency (c) for a defect distribution as stated in Figure 6.38 and gaussian energy defect distribution (width 0.16 eV).

beam is incident to the p-side and the probe beam onto the n-side.

Here, where the first real difference is found between gated collection efficiency with *decreasing* maximum values Figure 6.36c) for lower degraded samples and *i-v* analysis with its ever *increasing* maximum values Figure 6.36b) for the less degraded

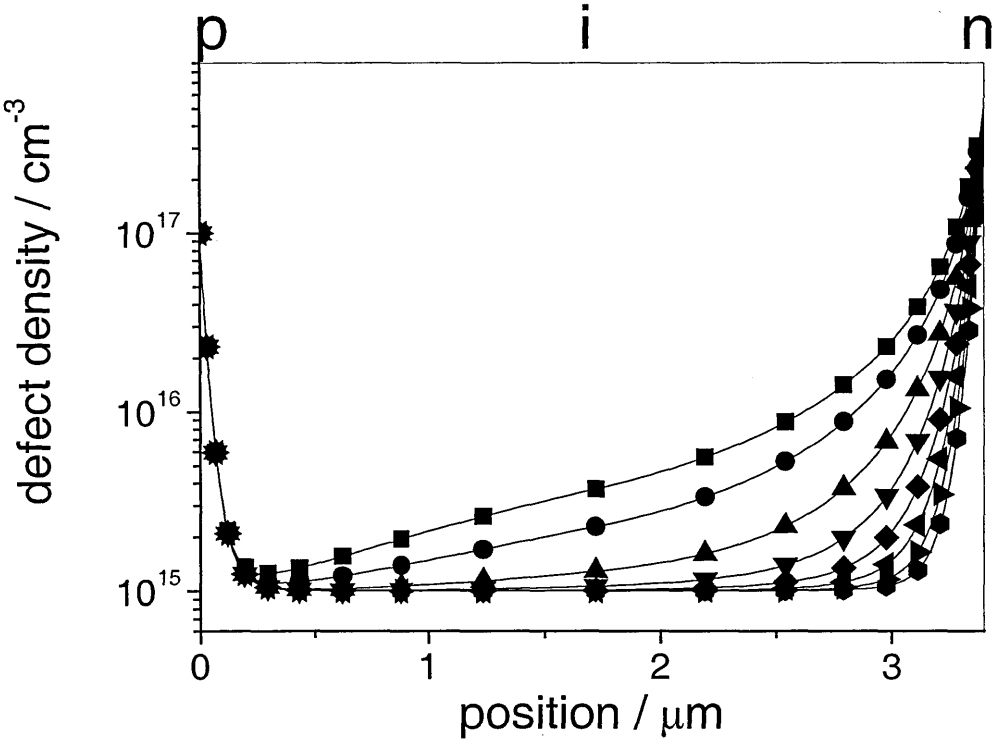

Figure 6.38: Defect distribution in the i-layer for simulations in Figure 6.37.

state, it is asserted that the collection efficiency results contain further information which the *i-v* analysis does not reveal.

Simulation with a defect distribution as shown in Figure 6.38 results in *i-v* curves (a), their derivatives (b) and collection efficiency distributions (c) shown in Figure 6.37. This distribution was chosen because the n-side is more sensitive to degradation by illumination (Shur, 1990, Block, 1993, Solomon, 1997). Furthermore the sloping inhomogeneous defect distribution from n- to p-layer was chosen here because the

sample was degraded through the n-contact (AM 1). Now the simulation shows the same tendency of decreasing maximal values for lower degraded samples, i.e. deeper penetration results in higher collection efficiency values.

Light soaking with AM 1 seems to penetrate and affect first a region close to the surface of the illuminated side, and after longer soaking times when, the penetration seems to have effected the whole i-layer, results in a roughly constant defect distribution.

But there could be a second plausible reason for the decreasing maximal values for less degraded samples. Figure 6.39 shows a defect distribution that could develop for the undegraded sample by monochromatic, intense bias illumination that is strongly absorbed at the p-side as was used for the electron gating experiments. It is conceivable that the radiation of λ_b = 470 nm at photon fluxes of up to $\Phi_b = 3.6\times10^{16}$ cm^{-2} s^{-1} could

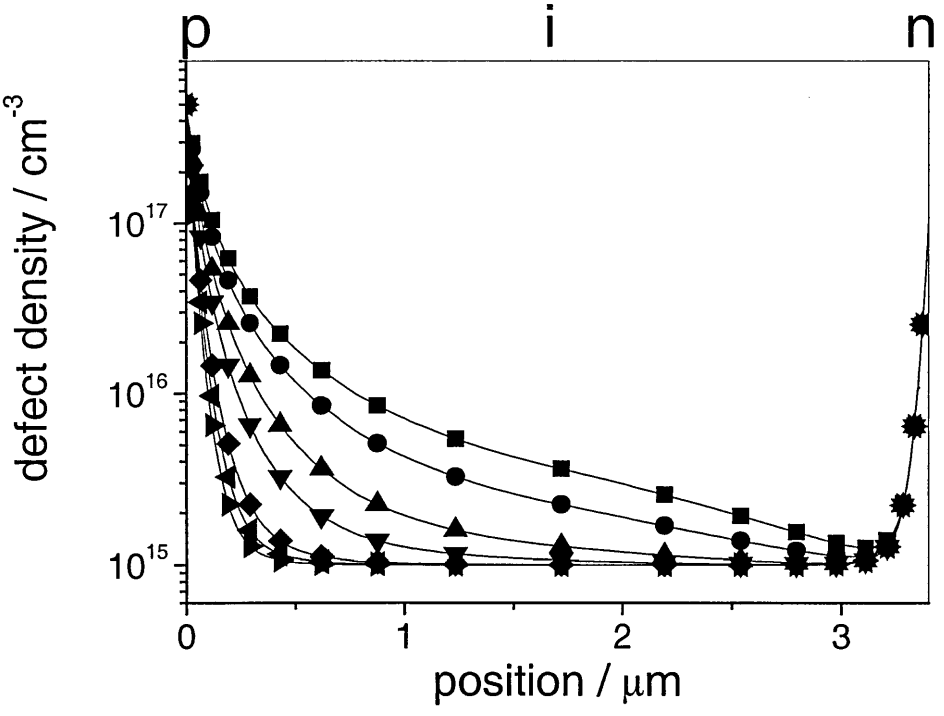

Figure 6.39: Defect distribution in the i-layer for simulations in Figure 6.40.

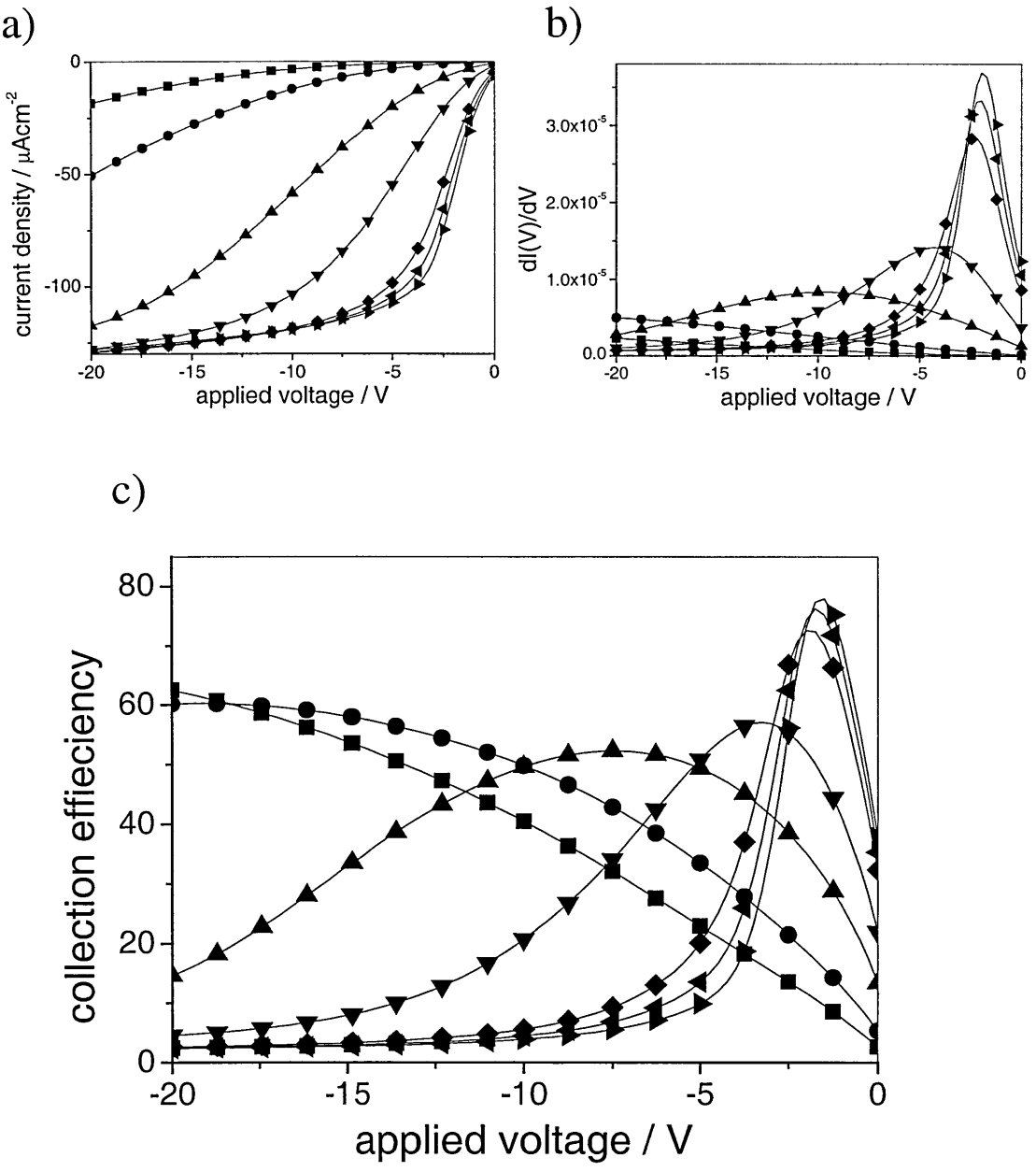

Figure 6.40: Simulated *i-v* characteristics (bias beam only) (a) and the their first derivatives (b) and appropriate gated collection efficiency (c) for a defect distribution as stated in Figure 6.39 and gaussian energy defect distribution (width 0.16 eV).

affect a sample that has a low defect density. In Figure 6.40 the resulting *i-v* curves (a), their first derivatives (b) and the gated collection efficiencies (c) show similar features as the asymmetric mirror imaged defect density distribution of Figure 6.38.

It can be assumed that the real effect is a mixture of these two presented rationales: degradation will be effected by the light soaking and by the unwanted bias illumination degradation because the result of the photogated collection efficiency seems to respond to the two totally different defect distributions in a similar way.

It should be stressed that an analysis of the first derivative of the *i-v* curve does not resolve a gradient (as the gating results) in the defect distribution, since the results of a constant level defect distribution and a sloped one result in always increasing maxima. Differences are impossible to recognise and therefore may not be susceptible to analysis.

6.4.2. Summary

The study of a new technique to look at the *first derivative* of the *single beam i-v* characteristics showed parallels to the *dual beam* photogated collection efficiency results. Light soaking can be observed and examined with this technique to a certain extent, producing a non distinguishable result for asymmetric or an inhomogeneous defect distributions for the single beam analysis. These distributions are however detectable with the dual beam photogating experiment.

Even for a gradient in the defect distribution for either the p- or n- side the photogating measurement gives a clearly distinct result.

A closer study on the degradation effect on *dI/dV*, avoiding bias beam degradation, but with directed high energy degradation could be subject of further work to examine this effect, avoiding bias-light produced degradation.

Furthermore would be a study with deliberate degradation of monochromatic high photonflux illumination on the gated collection efficiencies a method of investigating on the effect of *inhomogeneous* degradation.

6.5. Transient response of the photogating effect

The time-development of the gating effect in response to the probe beam is now investigated, for two reasons:

- The first reason was that a number of publications showed very different values of gating (Maruska et al., 1984, Hou and Fonash, 1992, Rubinelli, 1994, Chatterjee, 1994, Bae and Fonash, 1996, Binnewies, 1997). Although different sample structures and materials were examined in these papers the variation between the results of the different works was in the present author's view too high. One possible cause could have lain in variation of the chopping frequencies used to measure the photogating effect. If the response time of the effect were slow, then such differences could have a significant effect on the measured photogated current. For this reason, a series of different chopper frequencies was used to investigate the time dependency of resulting gated current. Since the probe beam was the beam that is chopped in the usual gating experiment, investigation of the probe beam was undertaken.
- The second reason was that a number of published works report on single beam 'switch on' or 'switch off' experiments. (Stannowski, 1997, Cordes, 1997) Investigation on the probe beam response showed that for high fluxes, of the order of magnitude of the bias beam, where no gating is observed, behaviour similar to a single beam response is seen but for lower probe beam photon fluxes a slower response time was observed and this slower response will be examined closer.

For the transient measurements the set up shown in Figure 3.4 section 3.3 was used. In Figure 6.41 the collection efficiency results of different simulated chopper frequencies are shown for the three examined sample thicknesses. For these measurements a flashing LED was used to simulate the different chopper frequencies in a range of 5 mHz up to 10 kHz. Photon flux and wavelength of bias and probe beam

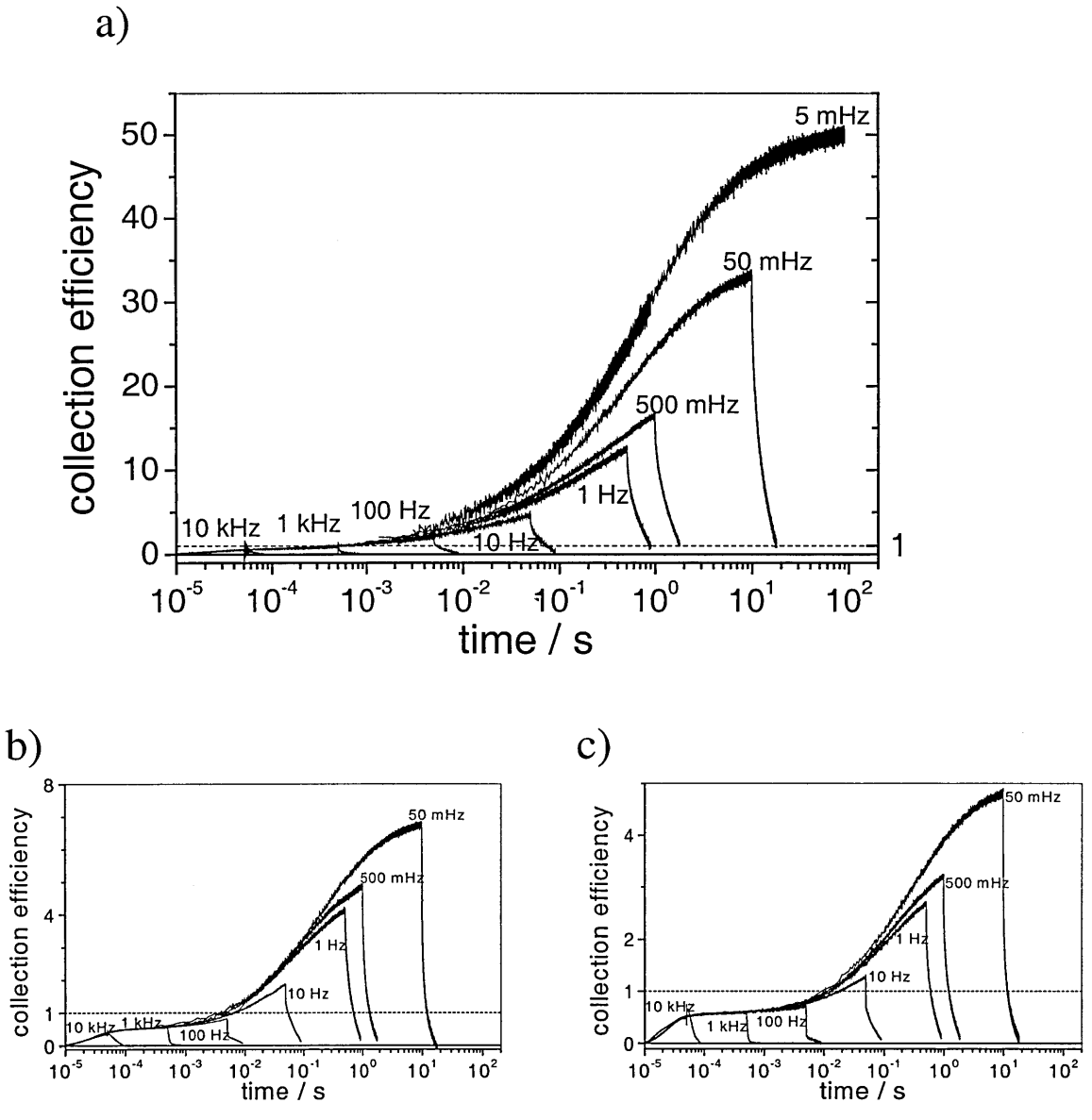

Figure 6.41: Collection efficiencies in dependency of the (chopper) frequency of the probe beam for three sample thicknesses: d = 3.5μm (a), 2.0 μm (b), 1.0 μm (c).

were chosen optimally, i.e. Φ_b = 1e15 $cm^{-2}s^{-1}$, λ_b = 470 nm and Φ_p = 1e12 $cm^{-2}s^{-1}$, λ_p = 610 nm.[20] Very high collection efficiencies of 40 or more for the thickest sample, as presented in this work, can only be seen at very low chopping frequencies (mHz) or steady state measurements. Noting that collection efficiencies were reported of less than 2 in all early publications (Maruska et al., 1984, Hou and Fonash, 1992, Rubinelli, 1994, Chatterjee, 1994, Bae and Fonash, 1996, Binnewies, 1997) and assuming that samples were chosen with high gains, leads one to suggest that all these groups were working in an area of 10 – 100 Hz - which are usual chopper frequencies. Unfortunately none of the cited authors stated the frequency he was using but all stated that they were using lock-in technique with a chopped probe beam.

Comparison of results presented at the 1999 MRS meeting (Unold et al., 1999) as a poster and of a diploma thesis (Binnewies, 1997) confirm the results presented here. Unold et al. presented maximum gating factors[21] of 10 at a chopper frequency of 10 Hz for a d = 1.8 μm thick p-i-n a-Si:H sample. Assuming a similar (n-side) single beam collection as presented in Figure 5.7 for the d = 2.0 μm thick sample and taking into account that high gating was observed around V = 0 V results in an assumed collection efficiency of ≈ 2. That fit very well with the result in Figure 6.41b). At a frequency of 10 Hz and for a sample thickness of $d \approx$ 0.5 μm Unold et al. found gating factors of 1. That implies that collection efficiency values never exceed 1 unless gating is observed. Since the gating factor of the $d \approx$ 0.5 μm thick sample never exceeded unity in their work the collection efficiency must have never exceeded 1, too. But with the very low results of collection efficiency values for a sample thickness of $d \approx$ 1.0 μm at a chopper

[20] By using a LED for the probe beam instead of the monochromator and Ha-lamp for steady state measurements a small shift from maximal collection values at λ_p = 620 to λ_p = 610 nm had to be accepted.

[21] The gating factor is defined as the quotient of gated (external) collection efficiency (under bias illumination) and single probe beam (external) collection efficiency.

frequency of 10 Hz presented in Figure 6.41c) confirms these findings, since a lower thickness results in even lower gated collection efficiency values.

The second author (Binnewies, 1997) used frequencies of 8 – 30 Hz and checked that the rising edges were less than 5 % of the whole signal duration. This possible misleading observation may arise from the apparent plateau in time response shown in Figure 6.41b) and c) at times $< 10^{-2}$ s.

A second result from Figure 6.41 is that for all examined thicknesses the time dependency seems to be similar. It was expected that thinner i-layer values would result in a faster response. But a comparison of the results is difficult: different degradation states resulted in very different maxima of collection efficiency (section 6.1.2). While the two thinner samples were undegraded the 3.5 μm sample was highly degraded (section 5.2). Additional differences in the i-layer thicknesses required voltages applied at the maximum of collection in all three cases, i.e. V = - 0.2 V for the 1.0 μm thick sample, V = - 0.25 V for the 2.0 μm thick sample, and V = - 15 V for the 3.5 μm thick sample.

To have a closer look at the photogating time response in Figure 6.42, the time response of an electron gated current on the left (a) and a hole gated experiment on the right hand side (b) are shown for the thickest sample (d = 3.5 μm). The frequency was chosen as 50 mHz and the applied voltage as V = -15 V. Here the time dependency of the 'switch on' experiment is shown for a probe beam photon flux of $\Phi_p = 2\times10^{12}$ cm^{-2}s^{-1}. The measurements show that an initial fast increase of the signal to a collection efficiency value < 1 for electron and hole gating.[22] The value is lower than full collection (especially for hole gating), but taking into account the spectral response

[22] Because of a lower gating maximum value the hole gating results are better to describe and therefore discussed further, although the electron gating experiment shows similar time dependent features.

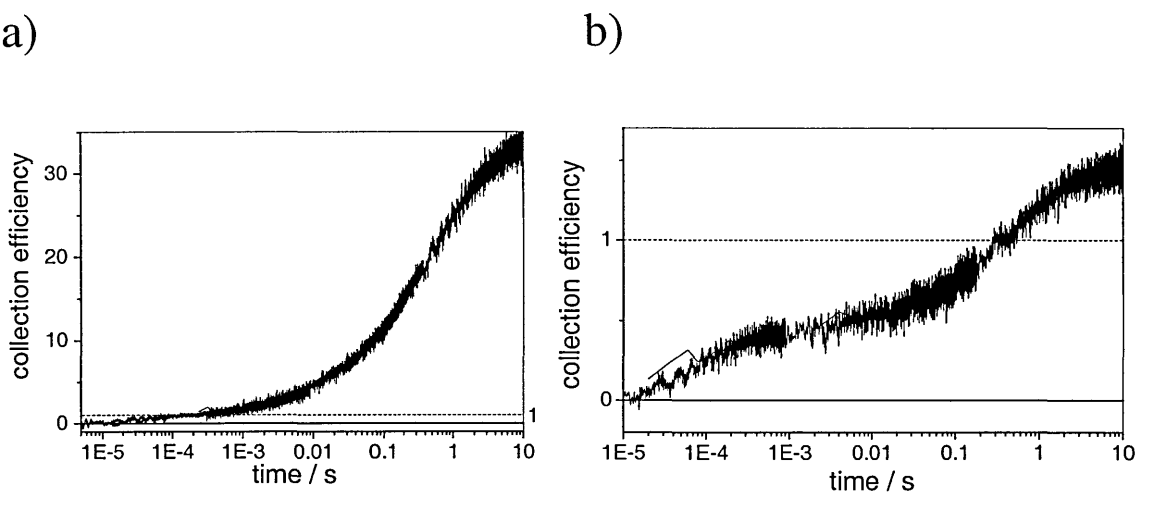

Figure 6.42: Transient collection efficiency for a hole gating experiment.

results, it is of the order expected for single beam collection, i.e. approximately 0.5 for a beam of a wavelength of $\lambda = 610$ nm incident from the p-side (compare section 3.1.2). That means that an initial response is found at $t_{trans} \leq 10^{-5}$ s to reach an intermediate value after $t_{trans} = 1\times10^{-3}$ s to the maximum usual collection.[23] This intermediate value even exhibits a plateau as observed from $t_{trans} \approx 3\times10^{-4}$ s to $t_{trans} \approx 3\times10^{-3}$ s until the gating effect builds up. In principle this is observed for all gating experiments.

Figure 6.43 shows the time dependency of collection efficiencies for different probe beam photon fluxes with beam specifications as for Figure 6.42b) (hole gating). Increasing the photon flux *does not* result in a faster initial response. The visible shift is due to restrictions of the amplifier.[24] But a lower intermediate ungated value for higher photon fluxes is expected to reach the respective gated value.

[23] The initial response can be resolved only up to 1×10^{-5} which was restricted by a preamplifier that was used to resolve the low currents.

[24] A minimum response time of $t = 1\times10^{-5}$ s relates to the curves with a photon flux of $\Phi_p = 1\times10^{13}$ cm^{-2} s^{-1} and $\Phi_p = 1\times10^{14}$ cm^{-2} s^{-1} while a response time of $t = 7\times10^{-5}$ s had to be accepted for a photon flux of $\Phi_p = 1\times10^{12}$ cm^{-2}.

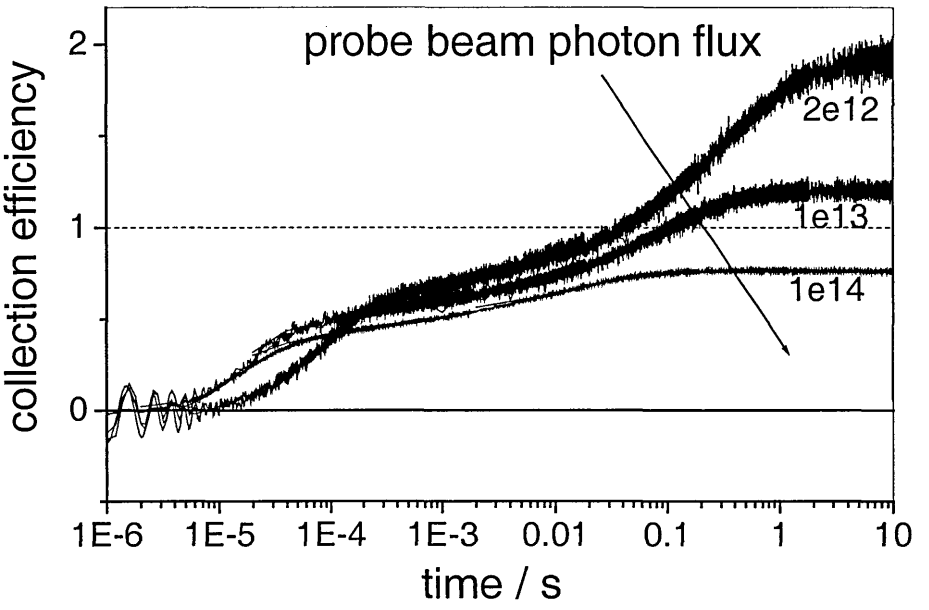

Figure 6.43: Transient collection efficiencies for different probe beam photon fluxes (hole gating).

The information from time domain measurement of the initial response and for the slower gated collection efficiency response could be used to provide information on the possible gap states involved. Although drift currents and diffusion currents can be involved, especially for the mechanism of gated collection efficiency measurements, the long response time must originate from trapping and emission effects which will be the response dominating process.

It is suggested that the observed features of the electron photogating response depend on a number of factors. At very short times, probe-photogenerated charge of both signs will be trapped into the respective tail states in the i-layer. This process cannot be observed in this experiment. At longer times electrons will drift to the n-i interface to be collected, while many of the holes will begin to be captured into the doubly occupied D^- defect states in the bulk of the device. This process should result in a turnover in the 'primary' current through the device – i.e. the ungated current

produced by the probe beam itself, and may indeed be the short-time feature visible on the Figures, although instrumental response times could interfere with this observation. It is suggested that the 'plateau' which follows the short-time turnover, is an indication of transport of the primary photocurrent, limited by multi-trapping into the defects. So this region is not a plateau, but is a continuation of the step response rise of the primary photocurrent, with a lower slope, corresponding to a greater fraction of the charge being trapped – i.e. with a lower drift mobility. It is then suggested that the upturn at longer times indicates the eventual filling (or part-filling) of defects in the i-layer by drifting holes. Such a process may be rate limited simply by the supply of photogenerated holes by the weak probe beam excitation. Correlated with this filling process is the screening effect which it produces, which in turn controls the photogating. Thus, as the defects become filled, this second component of the current, associated with release of electrons from the low field region, rises.

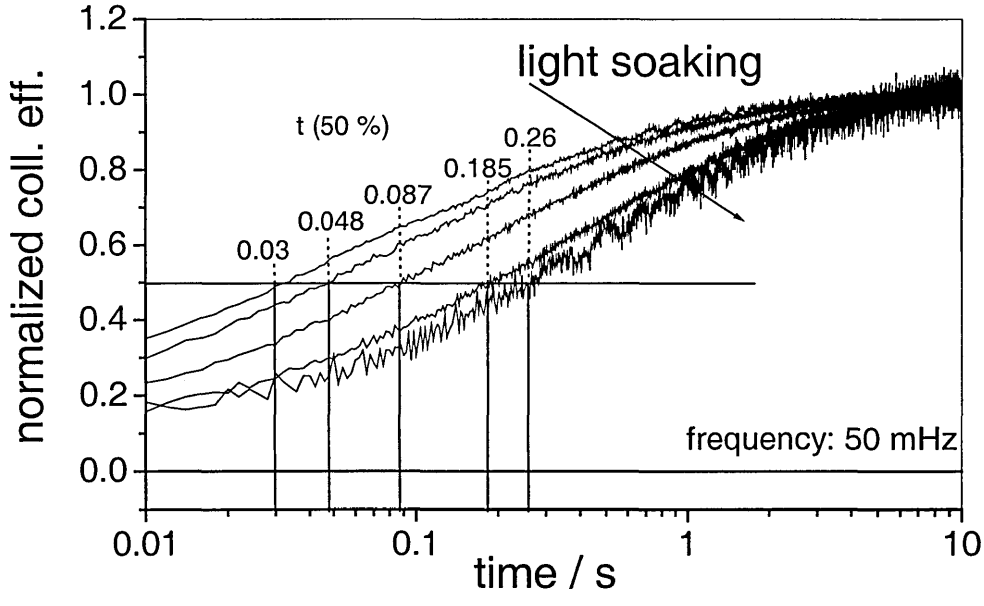

Figure 6.44: Transient response of the photogated part for different states of degradation.

If long response times relate to deep gap states, a degradation series should show longer response times for higher degraded samples because effective field changes will only be observed after the dominating defect state are reloaded. If the number of defects is higher it will take longer for this process. Figure 6.44 shows the response times and the 50 % rise-times τ_{on}. For higher degradation times the 50 % rise-time τ_{on} is shifting to longer times because of the increased number of defects that are involved. The shift of τ_{on} between the undegraded and highest degraded sample is with one order of magnitude high, especially since τ_{on} changes from τ_{on} = 0.03 s to τ_{on} = 0.26 s. For an application this difference in time response would make a big difference.

6.5.1. Summary

The measurement series with a flashing LED revealed that photogating results needed long settling times. Although it could not be investigated which chopper frequencies were used for photogating experiments in literature a rough estimation could be made. Either very low chopper frequencies (mHz) should be used or steady state measurements should be made to have comparable settled results.

Furthermore were the long settling times (transient measurements) related to deep gape state trapping, which are important for the enhancement in the field minimum that is found from steady state measurements and simulations and which dominate the time response of the gated collection efficiency measurements.

Finally was shown that the long term time response is sensitive to the defect density, i.e. long light soaking times increased the gated 50 % rise-time by one order of magnitude and underlined the involvement of deep level gap states.

7. Colour detection with the photogating effect

The results of spectral collection for electron gating of the bias beam in section 6.1.4 *Bias beam variations* in reasonable time intervals section 6.5 *Transient response of the photogating effect* intends the idea to use the gating effect in an application as colour detector. In contrast to existing colour detectors where the technology of multilayer cells (Stiebig et al., 1996, Caputo et al., 1996, Topic et al., 1998, Neidlinger et al., 1997, Knipp et al., 1998, Stiebig et al., 1998, Stannowski et al., 1999, Zimmer et al., 1999) or simple three solar cells lateral positioned with different optical filters or bandgaps are used here in principle the detector is based on a simple p-i-n structure to detect the whole visible spectrum.

The structure of a possible colour detector is given in Figure 7.1. The set-up is chosen as an electron gating experiment because higher gain values propose this, although a hole gated detector is possible, too. The set-up can be seen as a ready-made detector or as a single unit of an array. The back (probe) illumination of the LED should

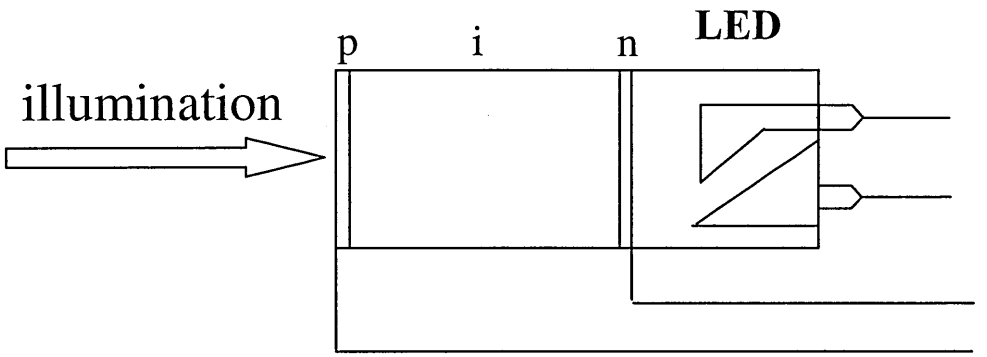

Figure 7.1: Schematic set-up of a colour detector unit for an electron gating layout.

be at the wavelength with a maximum gating effect (hence dependent on the thickness), from the n-side, either can be directed onto the whole area of an array, as far as the illumination is homogeneous over the whole detector back side, or for each single unit. The wavelength for the back illumination in this example was chosen to λ_p = 620 nm for the d = 3.5 μm thick sample (compare section 6.3 *Photogating on different i-layer thicknesses*) and the photon flux to $\Phi_p = 1\times10^{12}$ cm^{-2} s^{-1} as in previous sections.[25] The wiring is in comparison to other colour detector systems restricted to two wires for each unit (apart from the LEDs but which can be connected in series separately in the back of the array). Since the gating measurement is a two step measurement both information, *colour* and *photon flux* can be resolved from these two measurements.

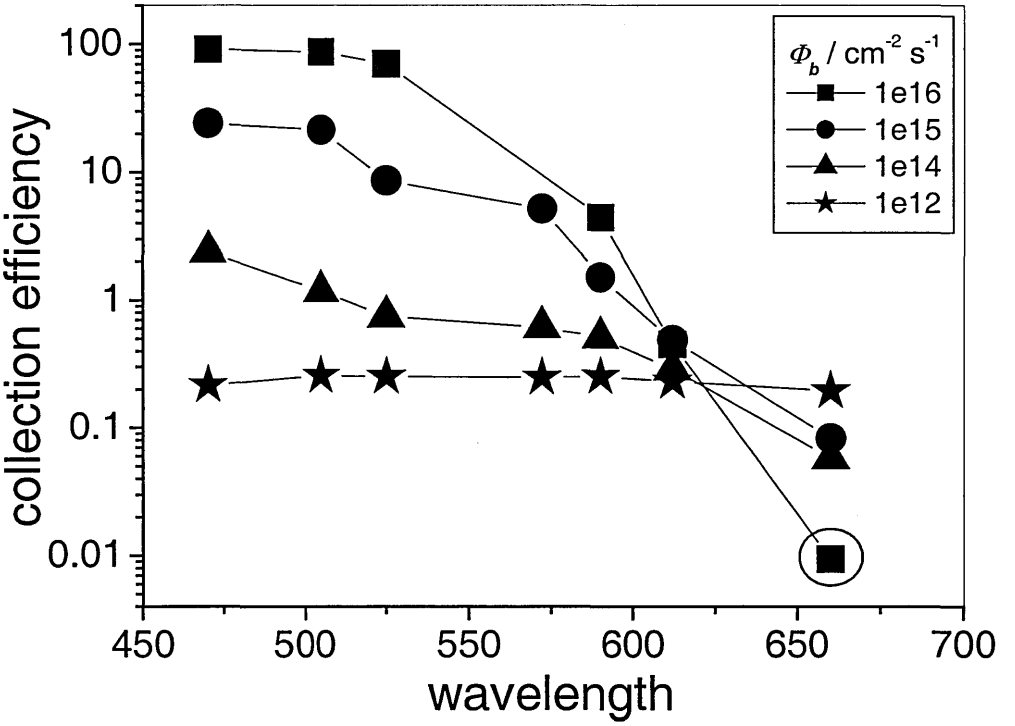

Figure 7.2: Colour resolution of the "to be detected" (bias) beam for different incident photon fluxes (of that beam).

[25] For lower back (probe) illumination photon fluxes a wider range of photon fluxes of the "to be detected" (bias) beam could be achieved.

Figure 7.2 gives the spectral response of the "to be detected" (bias) beam for different incident photon fluxes of that beam. The data points result from a cut at V = -3 V of Figure 6.18 in section 6.1.4 with all applied wavelength (like in figure Figure 6.20). Here, in Figure 7.2, the spectral dependency in a range of λ_b = 470 nm to λ_b = 660 nm is obvious for photon fluxes $\Phi_b \geq 1\times10^{13}$ cm^{-2} s^{-1}. For a photon flux of $\Phi_b \geq 1\times10^{12}$ cm^{-2} s^{-1} no gating is observed that no colour dependency is observed. For a lower probe beam photon flux the range of the "to be detected" (bias) beam could be extended to lower photon fluxes. The back (probe) photon flux should always be lower by a factor of 10 in relation to the "to be detected" (bias) beam (compare section 6.1 *The dual beam experiment: Collection efficiencies > 1 and electron photogating*).

With increasing photon flux the colour dependency increases, i.e. the gating effect rises to very high values for short wavelengths while it *decreases* for long wavelengths.

This effect of inverse gating was not further investigated but must result form the crossing over of the internal electric field for low reverse voltages, where collection can be under certain circumstances lower because the reversed field is lowered by the incident probe illumination, i.e. separation of photocarriers is lower. This effect has to be seen again in relation to the incident photon fluxes of the bias beam and is thus very small, but high enough to influence the result of the collection of the probe beam. The circled around symbol in Figure 7.2 is in fact negative but was set to a small positive value to show the tendency in the logarithmic scale.

Having now the *colour* dependency of the gated signal does not include the information about the photon flux – or to be more precise has some information about the photon flux that could be used to double check later results but not the result that gives us an definite value of the incident photon flux of the "to be detected" (bias) beam. The measurement of collection efficiency results from an originally *i-v-*

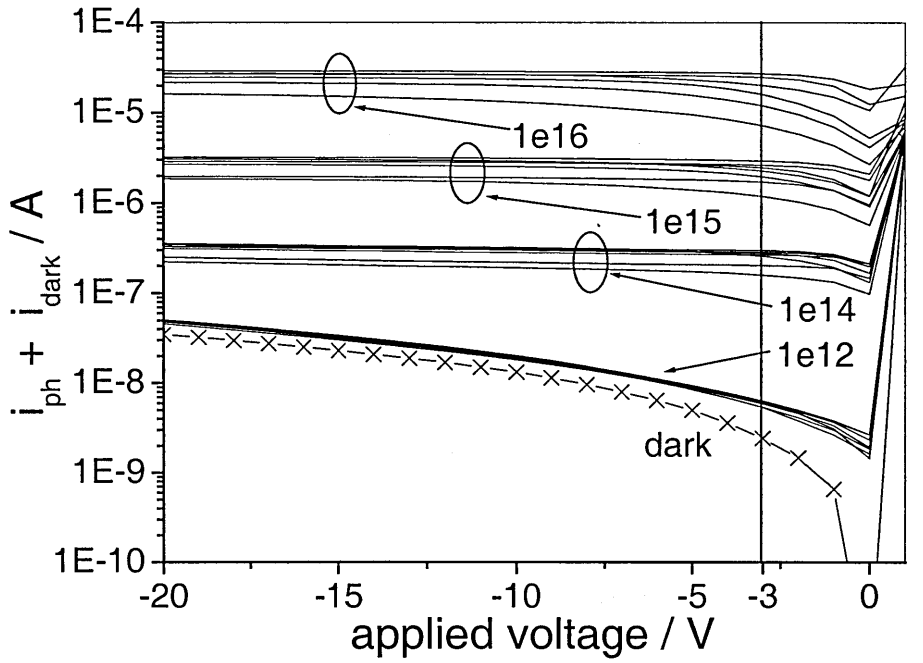

Figure 7.3: *i-v* characteristics (photo current and dark current) for the "to be detected" (bias) illumination of different photon fluxes.

measurement like in Figure 7.3, which shows the single beam results from the "to be detected" (bias) beam. The saturated current values at V = –20 V would give best results to make an estimation of the bias beam photon flux. But even at V = –3 V an estimation could be made.[26] The curves in Figure 7.3 that cross through the ellipsoids are of one photon flux. As described in section 5.4 the collection efficiency of the blue bias beam is poorer because of losses in the doped layer where entering the device resulting that not all curves saturate at the same values. This is a problem of the estimation of the photon flux but will here be accepted.[27] Figure 7.4 shows the results of a cross cut at V = –3 V of Figure 7.3 and underlines this problem.

[26] The value of V = –3 V had to be taken since the sample was undegraded and is needed for the colour resolution.

[27] A solution to this problem could be incorporation of carbon in the (p-)doped layer (where the "to be detected" (bias) beam is entering the device in the electron gating set-up). Addition of carbon in the doped layers extends the band gap in the doped layer and thus lowers collection in the defect rich doped area. (Street, 1991).

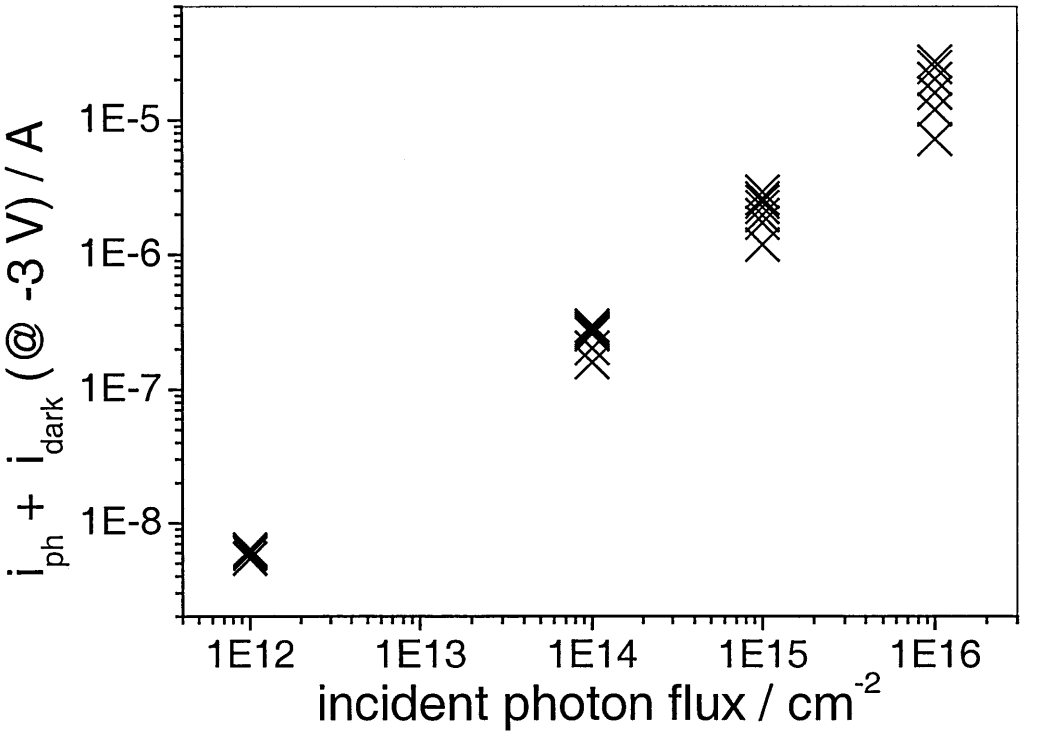

Figure 7.4: Current values resulting from the cut at –3 V in Figure 7.3.

But even with this problem would an exact determination of photon flux and colour be possible by cross checking. Having in mind that the colour detection shows clear differences in the result for critical points: e.g. the lowest point of the highest photon flux $\Phi_b = 1\times10^{16}$ cm^{-2} s^{-1} originates from the wavelength of $\lambda_b = 470$ nm while the highest value of the photon flux of $\Phi_b = 1\times10^{15}$ cm^{-2} s^{-1} is the result of $\lambda_b = 660$ nm. Comparing these two pairs of values in the spectral dependency of Figure 7.2 results in very good resolved values of:

- QE = 100 for $\lambda_b = 470$ nm and $\Phi_b = 1\times10^{16}$ cm^{-2}
- QE = 0.1 for $\lambda_b = 660$ nm and $\Phi_b = 1\times10^{15}$ cm^{-2}

That now, having these results, the first estimation of the photon flux can be rechecked. With powerful computers of today these calculations should be possible in very short time intervals even for big arrays.

Conclusions

Photogating measurements with collection efficiencies exceeding unity show a variety of new aspects of a-Si:H p-i-n devices. The "principle" of the dual beam experiment of photogating with collection efficiencies exceeding unity could be explained and described as a field enhancement by a probe beam that gates photocharge carriers generated by a bias beam. Because of the ratio of more than 1:10 of the probe beam photon flux to the bias beam photon flux these additional photocarriers contribute and produce collection efficiencies greater than one. This argument is supported by measurement and simulation, where a close fit of simulated data to measured results was be presented and thus simulation allowed an insight into internal parameters of the device, e.g. the internal electric field that is normally hidden from the experimenter.

The effect of a shifting collection efficiency maximum with increasing light soaking times, i.e. defect degradation, was found and explained. In this case the defects involved dominate the internal electric field with their localised charge and the effect depends on their number. The higher the number of defects the higher the local screening of the external field and deeper the local field minimum, resulting in a shift to higher applied voltages in order to release the maximum of additional photogenerated charge carriers.

A second view on defect analysis was found by comparing the photogating results with results from an *i-v* analysis. For the purpose of comparing the *i-v* results with the photogating experiments a new approach with the first derivative of the *i-v* data was introduced. A study of both techniques, mainly on simulated data, revealed that the *spatial distribution* of defects, decreasing from the doped areas through the middle of the sample could be resolved in the photogating results but not in the *i-v* analysis.

Further work on this subject on light soaking experimnents with monochromatic illumination is indicated. This kind of carefully directed light soaking, dependent on the absorption length of the incident radiation, should be combined with simulated results to improve the knowledge of degradation by light soaking of a-Si:H devices. It would then be possible to apply this information to proceed to AM 1.5 light soaking to extend the understanding of the processes of the degradation in a-Si:H solar cells.

The effect of variation of the illumination conditions on photogating, including wavelength and photon flux of both beams was studied, as well as a study on the effect of light soaking on the colour response associated with the bias beam. A further aspect on wavelength variations was the study of probe beam variation within the scope of different i-layer thicknesses with following results:

The study of the photon flux variation on bias and probe beam resulted in a minimum ratio of probe beam photon flux to bias beam photon flux of 1:10 to have resulting gating values greater than one. Variation of the probe beam wavelength for different thicknesses of the i-layer resulted in a shift to lower wavelengths for thinner samples. The reason for this shift was given by the electric field *plateau* that forms by the bias beam on the side opposite to the illumination, hence to the side of the sample where the probe beam is directed to. Since this *plateau* is found to be shorter the thinner the i-layer, higher absorption is needed to find maximum gating values.

Variations of the bias beam wavelength and of the state of degradation resulted in shifting maxima with degradation to higher reverse voltages but the effect is found to be more pronounced for short wavelengths. The explanation is that with the increasing number of defects the field minimum is more pronounced, so that, to release charge carriers from this region, a higher reverse voltage is needed to support the gating effect. The difference between the strong effect for short wavelengths and the weaker effect for

longer wavelength lies in the more pronounced field minimum for short wavelengths, so that the effect is found to be less distinct for a broader minimum, i.e. longer wavelengths.

Most of the results could be confirmed in a new experiment termed by the author *hole gating*. For hole gating in contrast to the conventional gating (that should be termed in this new context *electron gating*) the position of the field minimum is such that the released charge carriers with the longest path are holes – whereas for electron gating the electrons have the longest path. The effect of hole gating was found to be lower due to a different electric field distribution than that of electron gating but mainly because of the lower mobility of holes in comparison to electrons. Unsatisfying results for hole gating simulations in contrast to well fitted electron gating simulations with same simulation parameters resulted in a study of asymmetric defect distributions. Although fits for both measured gating experiments, i.e. electron- and hole-gating, results could not be presented but it is suggested that the solutions should be found in an asymmetric defect distribution over the i-layer.

The studies on the transient photocurrent experiment are the first such measurements done on the photogating experiment to the authors knowledge. Most important here must be seen the finding of long settling times so that results from previous experiments with lock-in-technique must be seen critically.

An explanation of the progress of gating was given where was argued that long settling times were related to deep gap state trapping, which are important for the enhancement in the field minimum that is found from steady state measurements and simulations and which dominate the time response of the gated collection efficiency measurements. A study of the time response of the gating experiment on degradation

showed increasing 50% rise-times for higher degraded samples, which supports the argument of deep gap states involved.

Two possible applications can be seen as the results form this work: first a possible defect analysis in ready made p-i-n samples and second an application as a colour detector. It should be possible to relate the shifting maximum to the number of defects. But also with further work focusing on the defect distribution, it should also be possible to analyse the device after production for quality engineering or for understanding of light soaking progress in the working state of the device. The colour detector has a problem in the time response but it could be shown that, in principle, a wavelength analysis of the incident bias beam could be read out in the photocurrent response of the bias beam and the gated photocurrent of the probe beam. Two possible solutions should be investigated: first the principle could be used with another defect engineered material, where the deep defects are "designed" in number and position in the band gap so that the time response could be enhanced; a second point concerns the time domain found for hydrogenated amorphous silicon. Is it sufficient and if not how could the response speed be enhanced? This leaves at least two possible ways of further work in enhancing the colour detection by the photogating phenomenon.

References

Abel, C. D. (1993), thesis, Institut für physikalische Elektronik Universität Stuttgart, Stuttgart.

Abel, C. D., Paes, H. and Bauer, G. H. (1991), In Amorphous Silicon Technology - 1991, Ed. Thomson, M. J., MRS Spring Meeting (MRS Pittburgh, 1991), Vol. 219, pp. 851.

Anderson, D. A. and Spear, W. E. (1977) *Phil. Mag. B,* **35,** 1.

Anderson, P. W. (1958) *Phys. Rev.,* **109,** 1492.

Bae, S. and Fonash, S. J. (1996) *J. Appl. Phys.,* **79,** 2213.

Baranovskii, S. D., Thomas, P. and Adriaenssens, G. J. (1995) *J. Non-Cryst. Solids,* **190,** 283.

Binnewies, T. (1997), thesis, Carl von Ossietzky, Oldenburg.

Block, M. (1993) *J. Non-Cryst. Solids,* **164-166,** 701.

Bonc, V. L. and Kalasnikov, S. G. (1982), DVW, pp. 210.

Boyce, J. B. and Ready, S. E. (1988) In *Amorphous Silicon and Related Materials*, Vol. A, (Ed, Fritzsche, H.) World Scientific, Chicago, pp. 29-62.

Brüggemann, R., Zollondz, J.-H., Main, C. and Gao, W. (1997), In Amorphous and Microcrystalline Silicon Technology - 1997, Eds. Hack, M., Schiff, E. A., Wagner, S., Matsuda, A. and Schropp, R., MRS Spring Meeting (MRS Pittsburgh, 1997), Vol. 467, Ch. 143, pp. 759.

Caputo, D., Irrera F., Palma, F., Rachele, S. R. and Tucci, M. (1996) *J. Non-Cryst. Solids,* **198-200,** 1172.

Carius, R. (1997), personal communication.

Carlson, D. E. and Wronski, C. R. (1976) *Appl. Phys. Lett.,* **28,** 671.

Chatterjee, P. (1994) *J. Appl. Phys.*, **75,** 1093.

Chevallier, J., Wieder, H., Onton, A. and Guarnieri, C. R. (1977) *Solid State Commun.*, **24,** 867.

Chittick, R. C., Alexander, J. H. and Sterling, H. F. (1969) *J. Electrochemical Soc.*, **116,** 77.

Chittick, R. C. and Sterling, H. F. (1985),, (Eds, Adler, D. and Schwartz, B. B.) Plenum, New York, pp. 1.

Cody, G. D., Abeles, B., Wronski, C., Stephens, C. R. and Brooks, B. (1980) *Solar Cells,* **2,** 227.

Cordes, H. (1997), thesis, Carl von Ossietzky Universität, Oldenburg.

Crandall, R. S. (1983) *J. Appl. Phys.*, **54,** 7176.

Crandall, R. S. and Sadlon, K. (1989) *Mat. Res. Soc. Symp. Proc.*, **149,** 423.

Dersch, H., Stuke, J. and Beichler, J. (1981) *Appl. Phys. Lett.*, **38,** 456.

Elliot, S. R. (1983) *Physics of amorphous materials,* Longman, pp. 250.

Fiorini, P. and Mittiga, A. (1992) In *Amorphous & Microcrystalline Semiconductor Devices*, Vol. 2, (Ed, Kanicki, J.), Boston, pp. 283-334.

Fuhs, W. (1999), In *Themen 2000 Sonne - Die Energie des 21. Jahrhunderts Strategien zur Kostensenkung von Solarzellen*, ForschungsVerbund Sonnenenergie (FVS), pp 14-20.

Gao, W. (1995), thesis, University of Abertay Dundee.

Goetzberger, A., Voß, B. and Knobloch, J. (1994) *Sonnenenergie: Photovoltaik,* Teubner.

Gummel, H. K. (1964) *IEEE Trans. Electron Devices,* **11,** 455.

Hall, R. N. (1951) *Phys. Rev.*, **38,** 228.

Hall, R. N. (1952) *Phys. Rev.*, **87,** 387.

Hamakawa, Y. (1980) *Proc. Of the 14th IEEE-PVC,*, 1074.

Hauschildt, D., Fischer, R. and Fuhs, W. (1980) *Phys. Stat. Sol.,* **(b)105,** 563.

Hirabayashi, I., Morigaki, K. and Nitta, S. (1980) *Jap. J. Appl. Phys.,* **19,** 357.

Hou, J. Y. and Fonash, S. J. (1992) *Appl. Phys. Lett.,* **61,** 186.

Jackson, W. B. and Amer, N. M. (1982) *Phys. Rev. B,* **25,** 5559.

Johnson, N. M., Herring, C. and Chadi, D. J. (1986) *Phys. Rev. Lett.,* **56,** 769.

Knipp, D., Stiebig, H., Fölsch, J., Finger, F. and Wagner, H. (1998) *J. Appl. Phys.,* **83 (3),** 1463.

Kreutzmann, A. (2000), In *Photon*, 2/2000, pp. 54.

Krühler, W., Pfleiderer, H., Plättner, R. D. and Stetter, W. (1984) *AIP Conf. Poc.,* **120,** 311.

LeComber, P. G. and Spear, W. E. (1970) *Phys. Rev. Lett.,* **25,** 509.

Maeda, K. and Umezu, I. (1991) *J. Appl. Phys.,* **70,** 2745.

Main, C., Zollondz, J.-H., Reynolds, S., Gao, W. and Rose, M. J. (1999) *J. Appl. Phys.,* **85,** 296.

Maruska, H. P., Hicks, M. C., Moustakas, T. D. and Friedman, R. (1984) *IEEE Trans. Electron Devices,* **ED-31,** 1343.

McMahon, T. J., Yacobi, B. G., Sadlon, K., Dick, J. and Madan, A. (1984) *Journal of Non-Crystalline Solids,* **66,** 335.

Mott, N. F. (1969) *Philos. Mag.,* **19,** 835.

Mui, K., Basa, D. K. and Smith, F. W. (1987) *Phys. Rev. B,* **35,** 8089.

Munekata, H., Shiozaki, A. and Kukimoto, H. (1981) *J. Lum.,* **24, 25,** 43.

Neidlinger, T., R., B., Brummack, H. and Schubert, M. B. (1997) *ESSDERC Stuttgart.*

Orenstein, J. and Kastner, M. A. (1981) *Solid State Commun.,* **40,** 85.

Overhof, H. and Thomas, P. (1989), Springer, pp. 13.

Pankove, J. I., Carlson, D. E., Berkeyheiser, J. E. and Wance, R. O. (1983) *Phys. Rev. Lett.*, **51,** 2224.

Perez Mendez, V., Cho, G., Fujieda, I., Kaplan, S. N., Qureshi, S. and Street, R. A. (1989) *MRS Symp. Proc.*, **149,** 621.

Pierz, K., Hilgenberg, B., Mell, H. and Weiser, G. (1987) *Journal of Non-Crystalline Solids,* **97/98,** 63.

Robertson, J. (1991) *Phil. Mag. B,* **63,** 47.

Rösch, M. (1996), personal communication.

Rose, A. (1963) *Concepts in Photoconductivity and Allied Problems,* Interscience, New York, pp. 5.

Rubinelli, F. A. (1994) *J. Appl. Phys.*, **75,** 998.

Rubinelli, F. A., Hou, J. Y. and Fonash, S. J. (1993) *J. Appl. Phys.*, **73,** 2548.

Schade, H. and Pankove, J. I. (1981) *Journ. de Phys.*, **42,** 327.

Schmela, M. and Kreutzmann, A. (2001), In *Photon*, 2 /2001, pp. 12.

Searle, T. M., Jackson, W. A. and Austin, I. G. (1987) *Journal of Non-Crystalline Solids,* **97,98,** 991.

Shockley, W. and Read jr., W. T. (1952) *Phys. Rev.*, **87,** 835.

Shur, M. (1990) *Physics of semiconductor devices,* Prentice-Hall, pp. 495.

Snell, A. J., Mackenzie, K. D., Spear, W. E., LeComber, P. G. and Hughes, A. J. (1981) *Appl. Phys.*, **24,** 357.

Solomon (1997), personal communication.

Spear, W. E. (1974) In *Proc. Int. Conf. on Amorphous and Liquid Semiconductors*, (Eds, Stuke, J. and Brenig, W.) Taylor and Francis, London, pp. 1.

Spear, W. E. and LeComber, P. G. (1975) *Solid State Commun.*, **17,** 1193.

Spear, W. E., Loveland, R. J. and Al-Sharbaty, A. (1974) *J. Non-Cryst. Solids,* **15,** 410.

Staebler, D. L. and Wronski, C. R. (1977) *Appl. Phys. Lett.,* **31,** 292.

Stannowski, B. (1997), thesis, Rheinisch-Westfälischen Technischen Hochschule, Aachen.

Stannowski, B., Stiebig, H., Knipp, D. and Wagner, H. (1999) *J. Appl. Phys.,* **85 (7),** 3904.

Stiebig, H., Knipp, D., Zimmer, J. and Wagner, H. (1998) *IEEE Transaction on electron devices,* **45,** 1438.

Stiebig, H., Ulrichs, C., Kulessa, T., Fölsch, J., Finger, F. and Wagner, H. (1996) *Journal of Non-Crystalline Solids,* **198-200,** 1185.

Street, R. A. (1991) *Hydrogen(er)ated amorphous silicon,* Cambridge University Press, Cambridge.

Stutzmann, M., Jackson, W. B. and Tsai, C. C. (1985) *Phys. Rev. B,* **32,** 23.

Tauc, J. (1974) *Amorphous and Liquid Semiconductors,* Plenum Press, New York.

Tauc, J., Grigorovici, R. and Vancu, A. (1966) *Phys. stat. sol.,* **15,** 627.

Tiedje, T. and Rose, A. (1980) *Solid State Commun.,* **37,** 49.

Topic, M., Smole, F., Furlan, J. and Kusian, W. (1998) *J. Non-Cryst. Solids,* **227-230,** 1326.

Unold, T., Binnewies, T., Brüggemann, R. and Bauer, G. H. (1999), In Amorphous and Heterogeneous Silicon Thin Films: Fundamentals to Devices - 1999, Eds. Branz, H. M., Collins, R. W., Okamoto, H., Guha, S. and Schropp, R., MRS Spring Meeting (MRS Warrendale Pa. USA, 1999), Vol. 557, pp. 875.

Urbach, F. (1953) *Phys. Rev.,* **92,** 1324.

Vanecek, M., Abraham, A., Stoika, O., Stuchlik, J. and Kocka, J. (1984) *Phys. Stat. Sol.,* **(a) 83,** 617.

Wolf, H. F. (1969) *Silicon Semiconductor Data,* Verlag Pergamon Press.

Zimmer, J., Knipp, D., Stiebig, H. and Wagner, H. (1999) *presented at the ICAMS 18, Snowbird Utah.*

Zollondz, J.-H. (1995), thesis, Carl von Ossietzky Universität, Oldenburg.

Zollondz, J.-H., Brüggemann, R., Reynolds, S., Main, C. and Gao, W. (1996), In Amorphous Silicon Technology - 1996, Eds. Hack, M., Schiff, E. A., Wagner, S., Matsuda, A. and Schropp, R., MRS Spring Meeting (MRS Pittsburgh, 1997), Vol. 420, Ch. 141, pp. 251-256.

Zollondz, J.-H., Main, C., Gao, W., Reynolds, S., Brüggemann, R. and Rose, M. J. (1998), In Thin film materials and devices - developments in Science and Technology - 1998, Eds. Marshall, J. M., Kirov, N., Vavrek, A. and Maud, J. M., (World Scientific, 1999), pp. 333-336.

Zollondz, J.-H., Main, C. and Reynolds, S. (1999), In Amorphous and Heterogeneous Silicon Thin Films: Fundamentals to Devices - 1999, Eds. Branz, H. W., Collins, R. W., Okamoto, H., Guha, S. and Schropp, R., MRS Spring Meeting (MRS Warrendale Pa. USA, 1999), Vol. 557, pp. 475-480.

A. Appendix

A.1. LED specifications

Wavelength / nm prod. decl./measured	FWHM / nm prod. decl./measured	Lum. intensity / mcd @ 20 mA	Made
430 / 427	80 / 70[1]	510	Ledtronics
470 / 477	20 / 25	1500[3]	Marl / Ledtronics
505 / 505	50 / 40	2000	Ledtronics
525 / 524	--[2] / 32	2200	Ledtronics
572 / 575	10 / 13	1200	Ledtronics
590 / 597	--[2] / 17	2500	Ledtronics
612 / 620	20 / 13	8500	Ledtronics
612 / 620	20 / 13	6500	Ledtronics
660 / 662	--[2] / 23	4100	Ledtronics

[1] With a brought shoulder to longer wavelengths (as stated from the producer). Measurements even showed a side maximum at $\lambda = 454$ nm with 89% of the maximum peak height at $\lambda = 427$ nm.
[2] No producer's declaration.
[3] @ 30 mA

A.2. Publications and conference presentations arising from this work

Paper presented at the MRS spring meeting, San Francisco, 1996:

J.-H. Zollondz, R. Brüggemann, S.Reynolds, C. Main, W. Gao,
The study of space charge effects by spectral response, steady state charge collection and transient photocurrents in thick a-Si:H pin-diodes, published in Amorphous Silicon Technology - 1996, eds. M. Hack, E.A. Schiff, S. Wagner, A. Matsuda and R. Schropp, MRS Symposium Proceedings (MRS Pittsburgh, 1997), Vol. 420, Ch.141, pp.251-256, 1997.

THE STUDY OF SPACE CHARGE EFFECTS BY SPECTRAL RESPONSE, STEADY STATE CHARGE COLLECTION AND TRANSIENT PHOTOCURRENTS IN THICK a-Si:H pin-DIODES

J.-H. ZOLLONDZ[1], R. BRÜGGEMANN, S. REYNOLDS*, C. MAIN*, W. GAO* and G.H. BAUER
FB Physik, Carl von Ossietzky Universität Oldenburg, 26111 Oldenburg, F.R. Germany
* Dept. of Electrical Engineering, University of Abertay Dundee, Bell St, Dundee, Scotland

ABSTRACT

Charge collection, transient photocurrents and collection efficiency under additional bias illumination were used to characterize 3-4 micron thick a-Si:H pin-diodes. The wavelength dependent decrease or increase in the spectral response, depending on the bias flux and absorption depth, is related to the distribution of the electric field, recombination and majority carrier diffusion. At higher photon flux an overshoot in the transient photocurrent after switch-on of steady illumination indicates the time scale for the changes in internal variables. Collection efficiencies under large bias monochromatic photon flux well in excess of the maximum value of 100 % for probe beam generated carriers are observed with a large amplification ratio. These efficiencies sensitively depend both on the applied voltage and the defect density. Numerical modelling reveals the influence of internal variables on the transient and steady state photocurrents under the different illumination conditions.

INTRODUCTION

The understanding of the photocurrent response and the knowledge about the related distributions of internal variables are important for the understanding of the physics of amorphous silicon (a-Si:H) pin diodes. The influence of space charge leads to an additional complication in the picture of describing the properties of the diode as simple analytical descriptions which assume a spatially constant electric field $\mathcal{E}$ [1] and therefore fail under these conditions. Space charge induced variations for the S-shaped current-voltage characteristics (e. g. [2]) need to be taken into account.

Here we report on a variety of techniques (steady state charge collection, spectral response or collection efficiency under additional bias illumination for a wide range of photon fluxes and transient photocurrent after switch-on of steady state illumination) to study the influence of space charge effects in thicker pin-diodes. The related features for thick diodes are much more pronounced than for thin solar cells. Notably, the overshoot transient photocurrent is found to be much larger in our thick diode as compared to related experiments with solar cells [3], where a larger effect is only found for illumination through the n-side [4,5]. Spectral response under the presence of an additional bias beam was shown to lead to collection efficiencies larger than one in a-Si:H diodes structures, early in [6] and later in [7–11]. The effect is very small so that results of it were also presented without commenting [12]. The simulation of the dynamic internal collection efficiency (DICE) showed that DICE-values larger than one are possible [13, 14], again indicating a larger effect for the thicker device. Our conclusions from the study of the thicker device with more apparent effects can be applied to thinner diodes with appropriate modifications.

EXPERIMENTAL PROCEDURES AND MODELLING

Experimental Details

Figure 1 sketches the two beam experimental setup for collection efficiency measurements, where bias and probe beam can optionally be guided through the p- or n-side. The bias beam is provided either by a halogen lamp with a bandpass filter or by an LED, both with FWHM

[1]e-mail: zollondz@cip.physik.uni-oldenburg.de

of 50 nm. For charge collection studies bias light photon fluxes of $10^{13} - 10^{15}\,\mathrm{cm^{-2}s^{-1}}$ and for the probe light of 10^{11} and $10^{12}\,\mathrm{cm^{-2}s^{-1}}$ were used. Probe beam induced photocurrents were monitored by a lock-in (19 Hz). Due to extreme relaxation times of the photocurrent of tens of seconds for high flux bias illumination ($10^{15}\,\mathrm{cm^{-2}s^{-1}}$), the traditional lock-in-technique was not applicable in this case. The photocurrents with and without a probe beam were measured under these conditions in the steady state and substracted.

Transient photocurrent were measured by switching an LED of $\lambda = 450\,\mathrm{nm}$ to steady state illumination and simultaneously triggering a digital signal amplifier. The current is pre-amplified by a specially designed fast current pre-amplifier (risetimes $< 70\,\mathrm{ns}$) in order to measure the current over more than 6 orders of magnitude in time. The overall response time of the measurement system was less than 1 μs.

The measurements were made at room temperature with a number of 3.5 μm thick pin-diodes with 200 Å a-Si:H p- and n-layers. The optical transmission at $400\,\mathrm{nm} < \lambda < 700\,\mathrm{nm}$ of the semitransparent Cr-contacts on the amorphous silicon is $\approx 30\,\%$.

Definitions and strategy

Two definitions for the determination of the collection efficiency from the photocurrent j_{ph} were applied for the results below. The internal collection efficiency η_{int} under bias illumination at a given reverse bias voltage U_r was calculated as

$$\eta_{int} = \frac{j_{ph}(\lambda_p, U_r)}{j_{ph}(\lambda_p, U_r = 25\mathrm{V})}. \tag{1}$$

The external collection efficiency under bias illumination with flux Φ_b is determined as

$$\eta_{ext} = \frac{j_{ph}(\Phi_p + \Phi_b) - j_{ph}(\Phi_b)}{e\Phi_p}, \tag{2}$$

where contact transmission is taken into account for Φ_p. Note that the maximum value for η_{ext} is 1 if all and only probe light generated carriers are collected.

Apart from the experimental determination of collection efficiency and transient photocurrent, numerical modelling of steady state [14,15] and transient properties [5,16] gave additional insight.

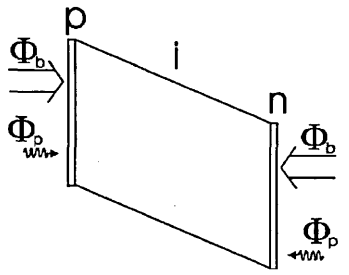

Figure 1: Illumination situation (bias-beam: index b, probe-beam: index p).

RESULTS AND DISCUSSION

Space charge influence on charge collection

For both bias and probe beam from the p-side, the wavelength dependent η_{int} (Fig. 2 a)) shows a distinct dependence on Φ_b and bias wavelength λ_b. For $\lambda_b = 400\,\mathrm{nm}$ an increased flux Φ_b leads to an increase/decrease in η_{int} in the red/blue with low η_{int} up to λ_p of about 550 nm. For $\lambda_b = 700\,\mathrm{nm}$ a reverse behaviour with larger/smaller η_{int} in the small/large λ_p-region is found. The simulated $\mathcal{E}$-distribution for the illumination with bias beam is given in Fig. 2 b). The absolute values of the field drop to very low values in the whole bulk of the i-layer ($\lambda_b = 700\,\mathrm{nm}$) while in the p/i-interface region up to about 0.5 μm an increase in the field is calculated, which results from increased positive dangling bond (DB) charge, screening the bulk of the i-layer. For increasing blue p-side bias illumination the different behaviour of η_{int} is reflected in the different $\mathcal{E}$-distribution, which shows a sharp decrease/increase in the left/right part of the i-layer in Fig. 2 b). The simulation results compare nicely with the experimental observation. E. g. with increasing bias flux the decrease (increase) in $\mathcal{E}$ in the generation (bulk) region is reflected by the decrease (increase) in collection efficiency for small

(large) wavelengths. At larger α the width of the low field region is larger than the absorption depth $1/\alpha$ which we also deduce from the experimental Fig. 2 a). The absorption depth for $\lambda_p = 550\,\text{nm}$ is about $0.1\,\mu\text{m}$, giving a ratio of low field region to bias absorption depth of about 8. Additional results show that this ratio drops for smaller bias α which gives a first hint to diffusion of majority carriers into the i-layer which widens the recombination region.

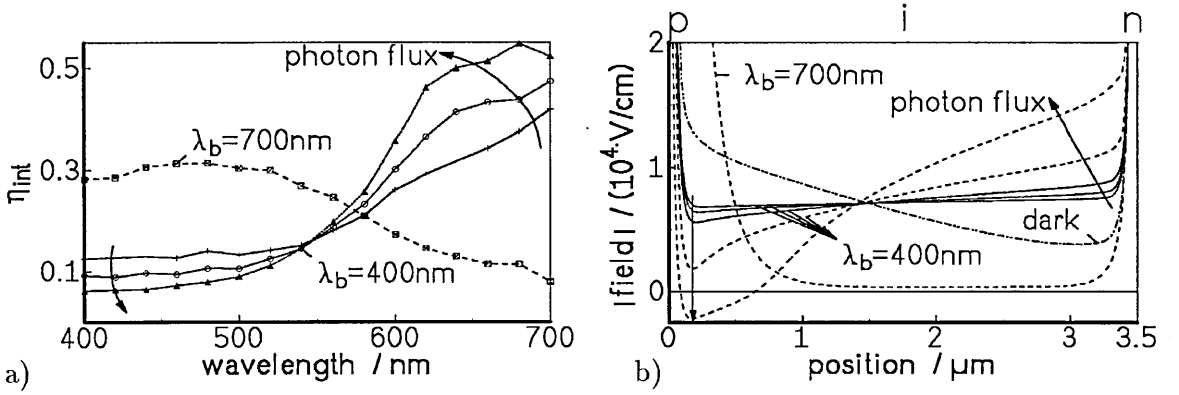

Figure 2: Experimental η_{int} for both p-side probe and bias illumination ($\lambda_b = 400, 700\,\text{nm}$) at -2 V (a). Simulated $\mathcal{E}$ for the experimental situation (absolute magnitude) (b).

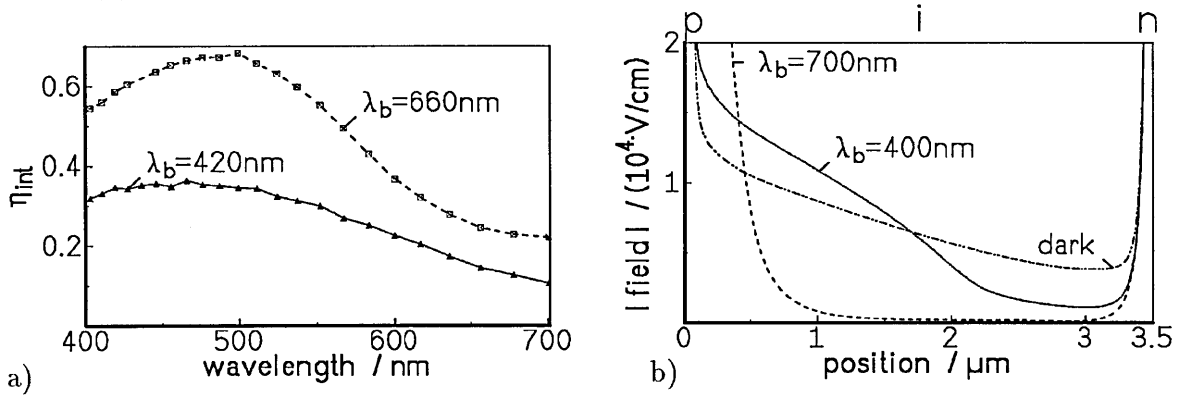

Figure 3: Experimental η_{int} for p-side probe and n-side bias illumination ($\lambda_b = 420, 660\,\text{nm}$) (a). Simulated $\mathcal{E}$ (b). Note the wider low field region for 400 nm as compared to Fig. 2 b).

Figure 3 a) shows experimental η_{int} with p-side probe but n-side bias illumination. Similarly, the simulated $\mathcal{E}$ for n-side bias is given in Fig. 3 b) for the dark as well as for red and blue bias illumination. For low absorption coefficients ($\lambda_b = 660$ or 700 nm) there is a nearly homogeneous absorption profile so that photoinduced field changes have to be the same, independent on the "illumination side". This is illustrated in the same shape of η_{int} in Figs. 2 a) and 3 a) and in the field of Figs. 2 b) and 3 b) for red bias.

$\mathcal{E}$ for blue n-side bias (Fig. 3 b)) shows a wide minimum, extending to more than $1\,\mu\text{m}$ into the i-region, while the field increases over the left part of the i-layer. The p-side probe illumination can discriminate between the two situations of p- or n-side bias, which can be seen in the increase in η_{int} at shorter wavelengths for $\lambda_b = 420\,\text{nm}$ in Fig. 3 a).

In order to discuss the illumination situation in more detail Figs. 4 and 5 show some internal variables under n-side bias illumination for $U_r = 2\,\text{V}$. Similar results hold for p-side bias illumination, under which electrons drift accross the diode. The partial currents for electrons are presented in Fig. 4 where the horizontal line represents the (negative) total electron current density. The dominance of the (positive) electron diffusion current, which is directed into the i-layer against $\mathcal{E}$, over the (negative) electron drift current results in a partial current of positive polarity deep in the i-layer next to the n-layer. The diffusion component can dominate because $\mathcal{E}$ is so low as seen in Fig. 3 b).

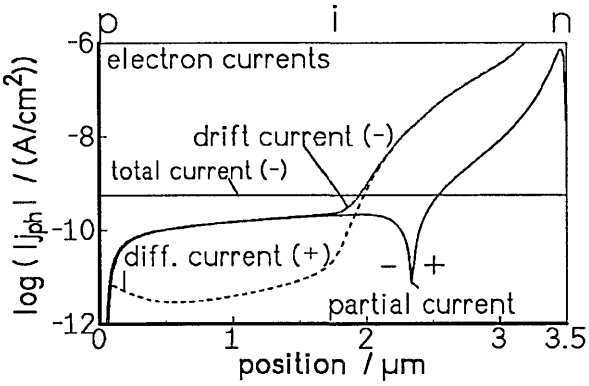

Figure 4: Simulated electron currents under n-side bias illumination (λ_b=400 nm). Note the large diffusion component with opposite sign for the majority carrier on the right.

The simulation shows that majority carrier diffusion from the generation region into the i-layer determines the width of the low field region. Locally the recombination rate R exceeds the generation rate (Fig. 5 a)). Minority carrier diffusion has only a minor effect. The strength of the low field is determined by the dominance of charged DB under illumination in most of the i-layer which are converted by the traversing hole carriers and by which the field is screened in the generation region (Fig. 5b)).

The behaviour of majority and minority carriers at either side of the pin-diode (e.g. majority holes in the p/i-interface region) corresponds to each other if the illumination direction is changed to the p-side. Minorities, which traverse the diode to be collected at the opposite contact, exhibit some contact back diffusion loss in both illumination situations (e.g. see [1] for steady state and [17] for transient properties of this effect).

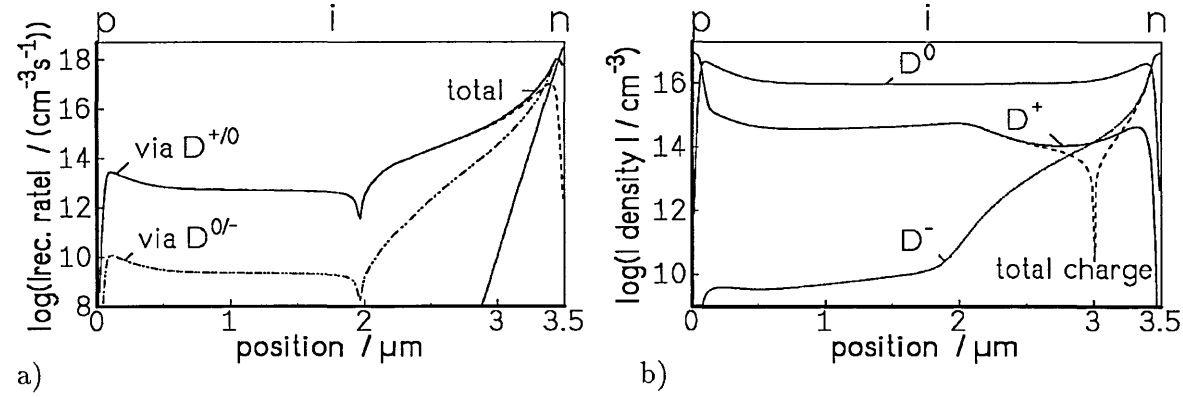

Figure 5: Simulated R and exponential generation rate on the right, $\lambda = 400$ nm (a). Regions with R larger than the generation rate exist. R is negative left to the dip at 2 μm because of net emission from DB. Charged dangling bond densities (b).

Overshoot phenomena in transient photocurrents

The above effects of strong local changes in the distribution of charge in DB and $\mathcal{E}$ under high Φ are reflected in measurements of transient j_{ph} after switch-on of p-side steady state illumination ($\Phi = 6 \times 10^{15}\,\mathrm{cm^{-2}s^{-1}}$, $\lambda = 450$ nm). Fig. 6 a) shows transients for different U_r. A change in slope is observed after the response time of the system at about 0.3 μs. All curves exhibit an overshoot before they reach steady state values. A shift in the position and shape of the maximum at larger voltages can be distinguished from the plateau, which is found until about 10^{-4} s at low U_r. Even at the largest U_r of 40 V steady state collection is smaller than in the ms-time range where at the maximum j_{ph} is close to the eΦ-value for maximum collection.

Figure 6 b) shows a number of simulated current transients for $\alpha = 2 \times 10^5\,\mathrm{cm^{-1}}$, $\Phi = 5 \times 10^{14}\,\mathrm{cm^{-2}s^{-1}}$ of a 3.5 μm diode. All curves exhibit a similar behaviour and drop from a plateau, coming close to maximum collection of $e\Phi = 8 \times 10^{-5}\,\mathrm{Acm^{-2}}$, to the final value. Although the agreement with the experimental curves is not satisfactory, the simulation can reveal that these overshoot phenomena start to set in, if hole diffusion, that is majority carrier diffusion, from the generation region into the i-layer becomes significant. Then the spatial distribution of the recombination rate shows a widening of the recombination region to values exceeding the absorption depth. The low field region with large recombination

loss is established after many ms, well in excess of the free carrier capture time, because photogenerated free carriers need to be captured to a significant amount by dangling bonds in order to lead to recharging of these centres.

The development of the sharper maximum with increasing U_r has not yet been reproduced by the modelling. This feature appears at U_r at which significant collection is obtained and where the S-shaped current-voltage characteristics (cf. e.g. [2]) departs from the low current values. As argued above, the majority carrier hole diffusion plays an important role, and partial suppression of this effect may lead to the appearance of the sharper maximum, but more clarification is certainly needed.

In a comparable experiment majority carrier diffusion, as discussed here, has been identified by numerical modelling as playing a decisive part in the undershoot phenomenom of photocurrent decays after termination of steady illumination [5, 16]. As mentioned in the introduction, the overshoot effect for illumination through the p-side for solar cell type diodes [3–5] was much smaller as compared to the case with the thicker diodes here. The comparison indicates that the larger relative field strength in thin pin-diodes suppresses the dominance of the diffusion current.

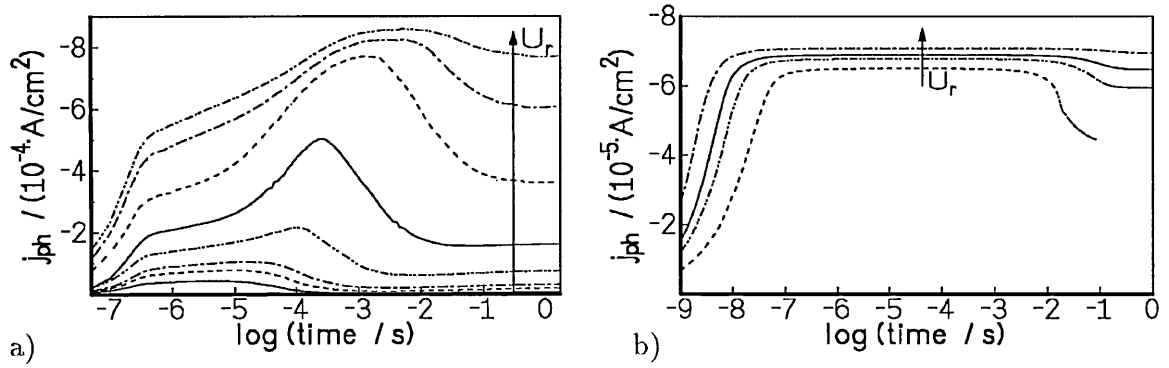

Figure 6: Large overshoots in the transient j_{ph} after switch-on of p-side illumination (λ = 450 nm) (U_r = 0, 1, 2, 5, 10, 20, 30, 40 V) (a). Simulated j_{ph} (U_r = 2, 6, 10, 20 V) (b).

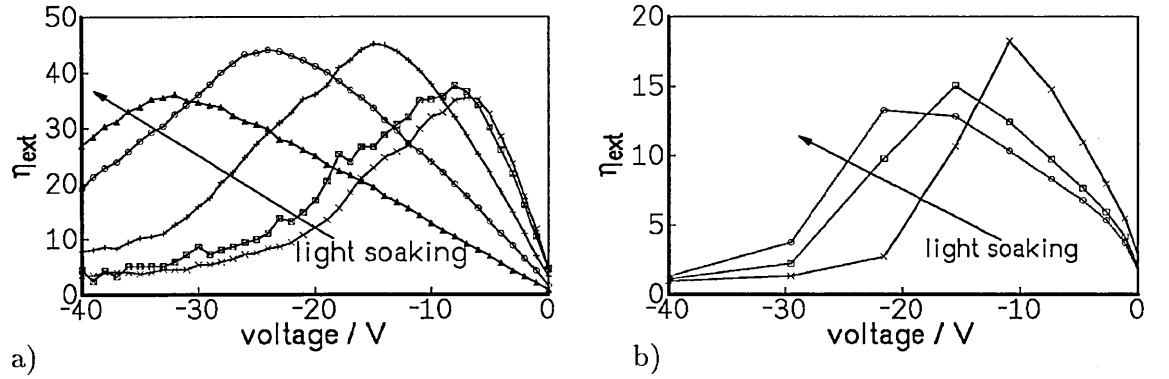

Figure 7: Experimental η_{ext} greater than one after increasing stages of light soaking. n-side probe (λ_p = 620 nm) and p-side bias illumination (λ_b = 450 nm) with a large ratio Φ_b/Φ_p (a). Simulated η_{ext} with small changes in defect density ($5, 8, 10 \times 10^{15}$ cm^{-3}) (b). Note that $\eta_{ext} = 1$ means full collection of probe light generated carriers.

Collection efficiency greater than one

The photoinduced field and free carrier density changes result in extremely large collection efficiencies under special conditions [14]. Fig. 7 a) shows a set of experimental η_{ext} for different U_r after light soaking the diode through the n-side with water-filtered light from a halogen lamp (AM 1.5 with 0, 10, 110, 490 and 1090 min). Bias illumination in Fig. 7 a) was from the p-side with λ_b = 450 nm under a high flux of 2×10^{15} cm^{-2}s^{-1}. Additional probe beam illumination was through the n-side with λ_p = 620 nm and 10^{12} photons cm^{-2}s^{-1}. Each η_{ext}

curve decreases towards low and high voltage and shows a maximum well in excess of the maximum value of 1 for total collection of probe light generated carriers. The values are also much larger than results reported for solar cells (e.g. [6, 10]). η_{ext} is very sensitive to the density of defects in the device, too. Light soaking shifts the maximum notably to higher U_r. Figure 7 b) illustrates that the simulation, for which no fitting attempt has been made here, reproduces the qualitative experimental findings with η_{ext} exhibiting a maximum as a function of U_r. The small increase in defect density by a factor of 2 shifts the maximum in η_{ext} to larger U_r.

As described by Gao et al. [14] a reservoir of free carriers builds up in the low $\mathcal{E}$-region under large bias flux, e.g. of electrons in the p/i-interface region in Fig. 2 b). The tiny changes in $\mathcal{E}$, induced by the additional red bias light, are large enough to have an additional number of these reservoir (bias generated) electrons extracted, which are then added to the probe beam extracted carriers, increasing η_{ext} well above unity.

The maximum in η_{ext} with respect to voltage can be understood intuitively from the following two arguemnts. If U_r is too low, recombination losses are too large, even for the bias generated electrons. At large U_r the largest fraction of bias generated electrons gets collected and no low field region is formed (as the simulation also confirms). η_{ext} thus drops towards unity at high U_r as no reservoir is built up from which additional electrons can be collected. These intuitive arguments also explain why η_{ext} remains low around 1 in thin pin-diodes as the built-in potential results in larger $\mathcal{E}$ throughout the device, reducing the built-up of an electron reservoir. For degraded solar cells η_{ext} is more likely to increase under the probe/bias-conditions discussed here because of stronger band bending and low $\mathcal{E}$ in the i-layer.

CONCLUSIONS

Thick a-Si:H pin-diodes are more sensitive to space charge influences than thin solar cell type diodes, where only the degraded solar cell may be similar in behaviour. Three phenomena are presented, which result from large changes of the internal variables under specific illumination conditions: increase/decrease of red/blue response in the steady state, large overshoot in the transient photocurrent, where for both of which the role of diffusion in the low field region is emphasized, and apparent collection efficiencies much greater than unity (amplification ratio up to 50). The field changes depend strongly on the defect density so that the phenomena presented here can be further exploited for degradation studies and device characterization.

ACKNOWLEDGEMENTS

The authors acknowledge the partial support by the DAAD and the British Council via ARC-collaboration and by the Stifterverband für die deutsche Wissenschaft.

REFERENCES

1. R.S. Crandall, J. Appl. Phys. **54**, 7176 (1983); **55**, 4418 (1984).
2. C.-D. Abel, H. R. Paes, G.H.Bauer, in *Amorphous Silicon Technology-1991*, ed. M.J. Thompson et al. (Mat. Res. Soc. Proc. **219**, Pittsburgh, 1991) p. 851.
3. C. Ulrichs, T. Eickhoff, H. Wagner, J. Non-Cryst. Sol. **164-166**, 705 (1993).
4. H. Wieczorek, W. Fuhs, phys. stat. sol. (a) **114**, 413 (1989).
5. R. Brüggemann, C. Main, G.H. Bauer, J. Non-Cryst. Sol. **164-166**, 663 (1993).
6. H. P. Maruska, M. C. Hicks, T. D. Moustakas, R. Friedman, IEEE Trans. El. Dev. **ED 31**, 1343 (1984).
7. J. Y. Hou, S. J. Fonash, Appl. Phys. Lett. **61**, 186 (1992).
8. F. A. Rubinelli, J. Y. Hou, S. J. Fonash, J. Appl. Phys. **73**, 2548 (1993).
9. F. A. Rubinelli, J. Appl. Phys. **73**, 2548 (1993).
10. S. J. Fonash et al., Optical Engineering **33**, 2065 (1994).
11. P. Chatterjee, J. Appl. Phys. **75**, 1093 (1994).
12. C. M. Fortmann, D. Fischer, in *Conf. Record 23rd IEEE PVSC* (IEEE, New York, 1993), p. 971.
13. W. Gao, R. Brüggemann, unpublished (1994).
14. W. Gao, C. Main, R. Brüggemann, J.-H. Zollondz, R.A.G. Gibson, J. Non-Cryst. Sol., (1996) in print.
15. W. Gao, PhD thesis, University of Abertay Dundee (1995).
16. R. Brüggemann, C. Main, G.H. Bauer, in *Amorphous Silicon Technology-1992*, ed. by M.J. Thompson et al. (Mat. Res. Soc. Proc. **258**, Pittsburgh, 1992) p. 729.
17. C. Main, J. Berkin, R. Brüggemann, J.M. Marshall, J. Non-Cryst. Sol. **137&138**, 439 (1991).

Co-author of a paper presented at the MRS spring meeting, San Francisco, 1997:

R. Brüggemann, J.-H. Zollondz, C. Main, W. Gao,
Conditions for collection efficiencies greater than one hundred percent, published in Amorphous and Microcrystalline Silicon Technology - 1997, eds. M. Hack, E.A. Schiff, S. Wagner, A. Matsuda and R. Schropp, MRS Symposium Proceedings (MRS, Pittsburgh 1997), Vol 467, Ch 143, pp. 759-764, 1997.

CONDITIONS FOR COLLECTION EFFICIENCIES GREATER THAN ONE HUNDRED PERCENT

R. BRÜGGEMANN[‡,*], J. H. ZOLLONDZ[♯,‡], C. MAIN[♯], W. GAO[♯]
‡ FB Physik, Carl von Ossietzky Universität Oldenburg, 26111 Oldenburg, F.R. Germany
* Institut für Physikalische Elektronik, Universität Stuttgart, Pfaffenwaldring 47, 70569 Stuttgart, F. R. Germany
♯ School of Engineering, University of Abertay Dundee, Bell St, Dundee DD1 1HG, Scotland

ABSTRACT

An account is given for the conditions under which the collection efficiency in hydrogenated amorphous silicon pin-diodes increases to values larger than 100 %. By specific bias illumination through the p-side bias generated photocarriers are collected under certain probe beam conditions of the collection efficiency measurement, leading to apparent large collection efficiencies. By numerical modelling we investigated the influence of the diode thickness, bias photon flux and probe absorption coefficient as well as applied voltage for possible sensor applications which may utilise this optical amplifying principle. The alternative with bias light through the n-side and probe light through the p-side is also explored. Collection efficiency values determined by the photogating of bias generated holes become only slightly larger than 100 % in contrast to the electron case where values in excess of 3000 % are presented.

INTRODUCTION

We reported the observation of very large collection efficiencies well in excess of 100 % for thicker hydrogenated amorphous silicon (a-Si:H) pin-diodes [1, 2]. In the experimental situation of illuminating with a short wavelength bias beam the 'photogating effect' is utilised by which bias beam generated photocarriers are collected in the probe beam collection measurement, leading to the extremely high apparent collection efficiencies. The effect is much larger in our thick diodes than has been reported for thin solar cell type diodes where, if at all, collection efficiencies were found to be only slightly larger than 1 [3–5]. In this paper we explored situations by experiment and numerical modelling, which lead to high collection efficiencies. We investigate the dependence of the effect on the diode thickness, bias beam intensity, the applied reverse bias voltage and the selection of probe beam wavelength. The alternative of illuminating either through the p- or n-side of the diode is also studied.

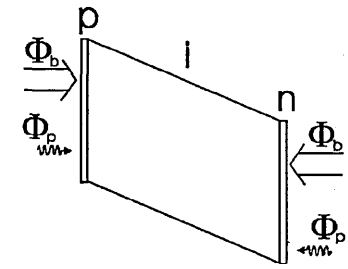

Figure 1: Illumination situation (bias-beam: index b, probe-beam: index p).

EXPERIMENTAL PROCEDURES AND MODELLING

In our experiments and modelling the collection efficiency is defined as an external efficiency. Under bias illumination with flux Φ_b the efficiency is determined from the photocurrent density j_{ph} and the probe beam flux density Φ_p by

$$\eta_{ext} = \frac{j_{ph}(\Phi_p + \Phi_b) - j_{ph}(\Phi_b)}{e\Phi_p}, \qquad (1)$$

where contact transmission is taken into account for Φ_p. Note that, depending on the thickness and the absorption coefficient of the sample, not all of the probe beam photons may be absorbed. The photon flux is measured with a standard photodiode at the position of the sample and alternatively as a cross-check from the saturation photocurrent of the sample at large reverse bias, thus using the sample as a calibration. The maximum value for η_{ext} is 1 if all photons of Φ_p are absorbed and only probe light generated carriers are fully collected.

Figure 1 sketches the two beam experimental setup for collection efficiency measurements, where bias and probe beam can optionally be guided through the p- or n-side. The bias beam is provided either by a halogen lamp with a bandpass filter or by an LED, both with FWHM of 50 nm. The photocurrents with and without a probe beam were measured in the steady state and subtracted. The measurements were made at room temperature with a number of 3.5 μm thick pin-diodes with 200 Å a-Si:H p- and n-layers. The optical transmission between 400 and 700 nm of the semitransparent Cr-contacts on the amorphous silicon is $\approx 30\,\%$.

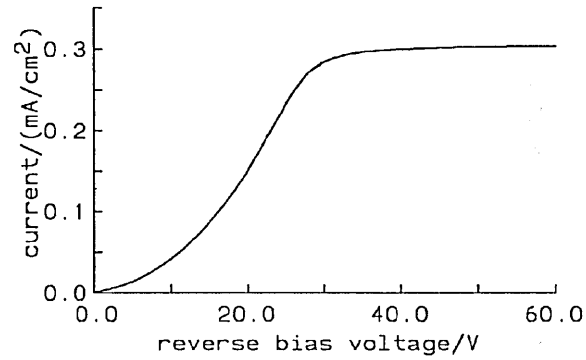

Figure 2: Simulated current-voltage characteristic for a 3.5 μm thick pin-diode up to very high reverse bias under illumination through the p-side with a flux of $2 \times 10^{15}\,\mathrm{cm^{-2}s^{-1}}$.

Modelling of the steady state response of the pin-diodes was performed by numerically solving Poisson's equation and the full set of continuity and rate equations with a procedure already applied in Refs. [2,6].

RESULTS AND DISCUSSION

Figure 2 shows a typical simulated current-voltage characteristic for a 3.5 μm thick pin-diode up to very high reverse bias under illumination through the p-side with a flux of $2 \times 10^{15}\,\mathrm{cm^{-2}s^{-1}}$. The absorption coefficient $\alpha = 10^5\,\mathrm{cm^{-1}}$ results in a sharply decreasing generation rate within the diode. The S-shape is also found experimentally [7,8] and is a signature for strong space charge effects at low reverse bias. The electric field is screened by a large amount of photogenerated electrons and holes which lead to a redistribution of the dangling bond (DB) charge. The DB become more negative in most of the i-layer by capture of traversing electrons resulting in a low field region near the p/i-interface [1,2].

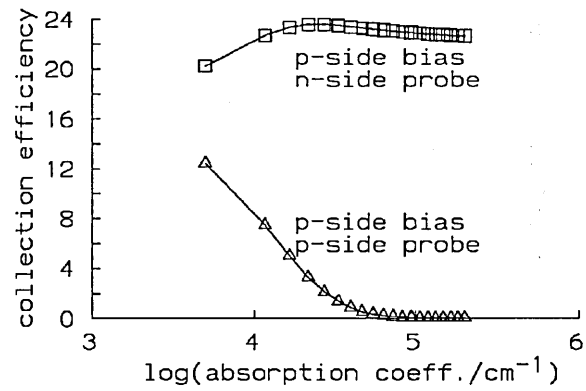

Figure 3: Simulated η_{ext} for the blue bias illumination conditions of Fig. 2. The probe beam illumination is through the p- or n-side with varying absorption coefficient.

An S-shape I/V-characteristic is often related for observing η_{ext}-values which become larger than one as illustrated in Fig. 3 where the collection efficiencies for the bias illumination

conditions of Fig. 2 are shown, calculated at a reverse bias voltage V_r of 20 V. The probe beam illumination with varying absorption coefficient which is represented on the abscissa is either directed through the p- or n-side.

For both bias and probe illumination through the p-side (△-curve in Fig. 3), η_{ext} is significantly lower. If at larger α the absorption depth of the probe beam is within the low field region in the vicinity of the p/i-interface, η_{ext} drops to zero. At low α both curves converge to a common η_{ext}-value as the probe generation rate becomes homogeneous. The figure also contains some technological relevance. If the n-side contact is not transparent the combination of p-side bias and p-side probe illumination also leads to η_{ext} larger than 1 if the probe beam absorption coefficient is small. Note that the maximum η_{ext} equals 1 if only probe beam generated carriers are collected.

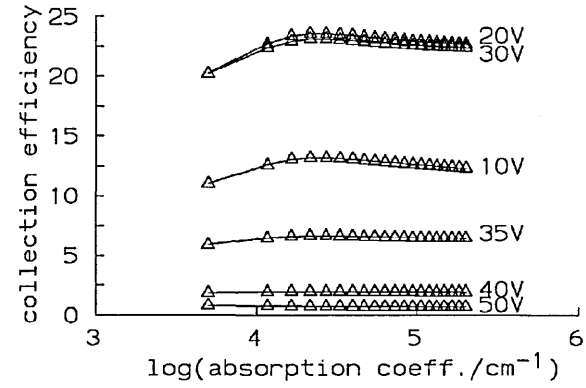

Figure 4: Simulated V_r-dependence of η_{ext} for the conditions of Fig. 2 for n-side probe illumination. α of the probe beam was varied with keeping Φ_p constant at 10^{11} cm^{-2}s^{-1}.

Concentrating on p-side bias, n-side probe illumination, the simulated V_r dependence of η_{ext} is depicted in Fig. 4 for the bias illumination conditions of Fig. 2. The absorption coefficient of the probe beam was varied with keeping Φ_p constant at 10^{11} cm^{-2}s^{-1}. A strong voltage dependence is observed with the largest values in the voltage region before saturation of the bias photocurrent (see Fig. 2), where the bias photocurrent is relatively large. At high reverse bias the photogating effect is absent and η_{ext} drops below one. η_{ext} depends on the number of absorbed photons and depending on the α it is possible that photons are reflected at the back contact and leave the diode without being absorbed so that η_{ext} does not necessarily equal unity at high V_r.

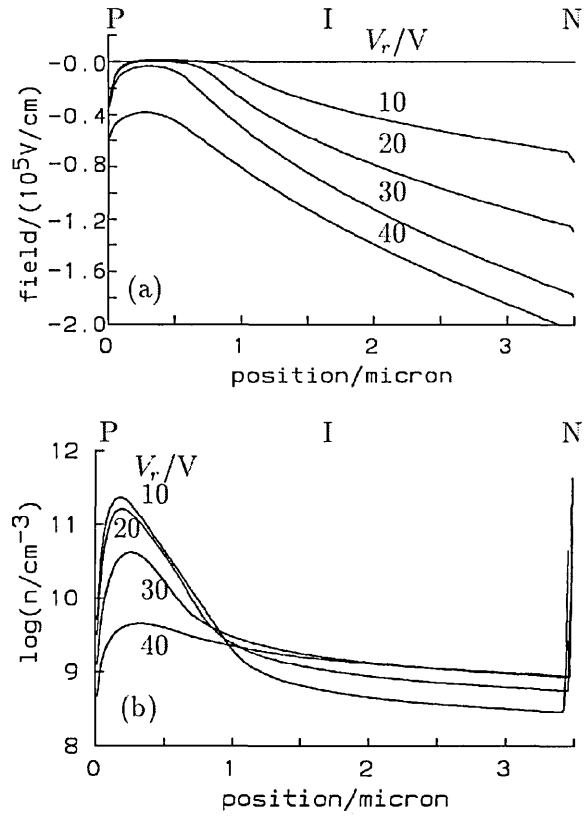

Figure 5: Simulated electric field distribution (a) and free electron density (b) for different V_r under the blue bias illumination conditions of Fig. 2.

The simulation allows a view into the diode by displaying the calculated electric field distribution (Fig. 5(a)) and free electron density (Fig. 5(b)) for the blue bias illumination conditions of Fig. 2. A low field region and also a reservoir with a large density of bias photogenerated electrons can be identified which builds up at medium reverse bias in the left part of the i-layer. The electric field may even change its sign but this effect is not

necessary for high η_{ext}. Carriers are collected from the reservoir under the probe illumination which can be identified by our calculation of the differences of the variables for probe+bias and probe illumination. These differences also show that the electric field is enhanced in the low field region by the probe beam induced charge. For red probe beam illumination with a homogeneous generation of electrons and holes the density of negatively charged DB is reduced in the bulk of the i-layer by the availability of holes from the probe illumination. On the other hand, the density of positively charged DB also decreases in i-layer region close to the p-layer. The larger field and the resulting reduced recombination rate then lead in the collection of additional bias generated carriers. Perhaps surprisingly, even at high V_r a region with a lower field is maintained so that a constant field approximation is not applicable for these illumination conditions with $\alpha = 2 \times 10^5$ cm^{-1}. The simulation shows that the width of the low field region is determined by the movement of holes from the generation region into the i-layer. More details of simulation results can be found in [2].

We note that the choice for a large α corresponding to the absorption of the bias beam is necessary for the effect of apparent $\eta_{ext} > 1$. If α decreases and the photogeneration rate becomes more homogeneous, the features depicted in Fig. 5 disappear and the field is not screened by the negative DB in the i-layer.

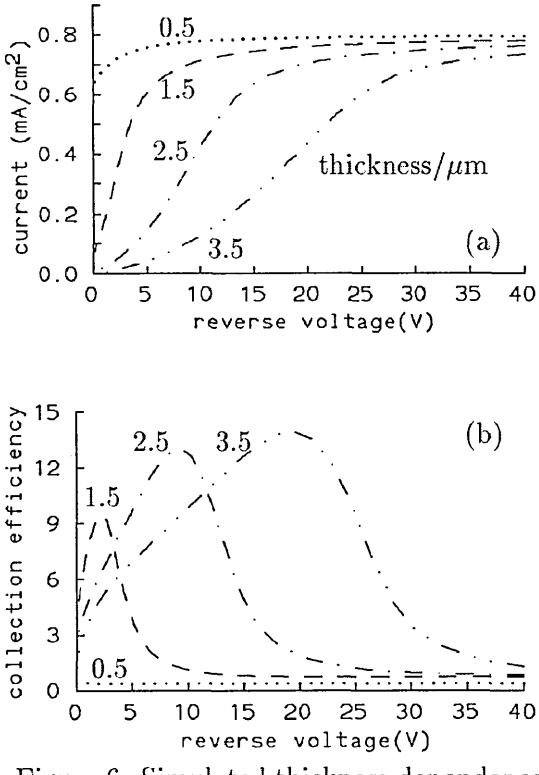

Figure 6: Simulated thickness dependence of the bias beam I/V-characteristic (a) and η_{ext} (b) for $\Phi_b = 5 \times 10^{15}$ cm^{-2}s^{-1} and $\Phi_p = 10^{13}$ cm^{-2}s^{-1}.

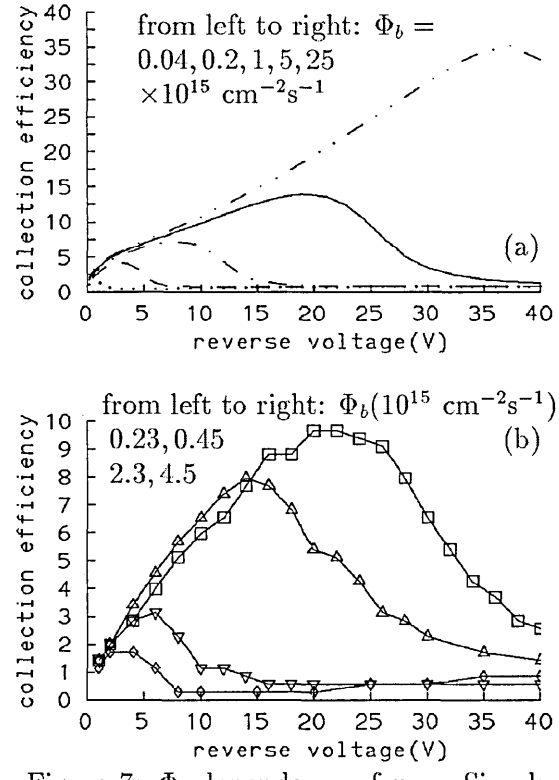

Figure 7: Φ_b-dependence of η_{ext}. Simulation results (a) and experimental results with 3.5 μm thick diode (b). p-side bias, n-side probe.

Some pronounced effects are found when varying the thickness of the diode. Fig. 6 shows both the stationary bias I/V-characteristic (a) for blue bias illumination and the collection efficiency under additional red probe beam illumination (b). Fig. 6(a) illustrates that the collection of bias beam generated photocarriers is drastically reduced in the thicker diodes. In the thinnest diode with its larger intrinsic field, the effect of space charge is reduced. The

steady state I/V-curve shows nearly full collection at all reverse voltages. The reduction in bias collection and the lower photocurrent for the thicker diodes is correlated with an increased accumulation of DB-charge. For the thicker diodes the charge reservoir and the low field region similar to Fig. 5 build up. Note, that for this blue bias very large voltages are needed for full collection.

The collection efficiency (Fig. 6(b)) is thus also influenced by the thickness. For the thinnest diode η_{ext} is just below 1 in the whole voltage range. Full collection of the probe beam generated carriers is achieved and no additional bias beam generated carriers are available. With the thicker diodes η_{ext} increases drastically to maximum values of 1400 %. It takes a larger V_r to reach the maximum in η_{ext} for the thicker diodes because additional voltage is needed to extract the carriers from the reservoir. The maximum value becomes larger for the thicker diodes as the density in the reservoir becomes larger. At largest V_r, where the bias beam generated carriers are collected without the assistance of the probe beam, η_{ext} drops to 1. Here, in contrast to the thinnest diode, all impinging photons are absorbed.

Figure 7 details how η_{ext} varies with the intensity of the bias beam for p-side bias/n-side probe illumination. Fig. 7(a) shows simulated results for Φ_b between 4×10^{13} and 2.5×10^{16} cm^{-2}s^{-1} with $\alpha = 2 \times 10^5$ cm^{-1}. The probe beam flux Φ_p with $\alpha = 5 \times 10^3$ cm^{-1} was kept constant at 10^{13} cm^{-2}s^{-1}. Corresponding experimental results are shown in Fig. 7(b). Wavelengths in the blue and red spectral range of 420 (621) nm were chosen for the experimental bias (probe) beam illumination. Here, Φ_b was changed between 2.3×10^{14} and 4.5×10^{15} cm^{-2}s^{-1}. Φ_p was kept constant at 7.2×10^{12} cm^{-2}s^{-1}.

The experimental results are in good qualitative agreement with the simulations results apart from the largest simulated Φ_b which could not be made available with the experimental set-up used. Note the different scale of the ordinates in Figs. 7(a) and 7(b). The higher the bias flux the larger the space charge effect and thus the influence of the low field region and the reservoir. For the more pronounced lower field region at higher Φ_b a larger voltage is needed for extraction from the reservoir which on the other hand becomes a larger source and leads to higher values for η_{ext}.

Figure 8 illustrates a comparison with the alternative for directing the blue bias illumination through the n-side for mainly collecting holes, which is much less efficient than electron collection. η_{ext} for p-side bias, n-side probe in comparison to n-side bias, p-side probe illumination are displayed for varying the absorption coefficient of the probe beam for the same photon fluxes and at $V_r = 10$ V. The largest values in η_{ext} arise from the combinations of p-side bias, n-side probe for photogating of electrons. The behaviour is the same as in Fig. 3. For n-side bias, p-side probe η_{ext} remains low due to the overall low efficiency of hole collection.

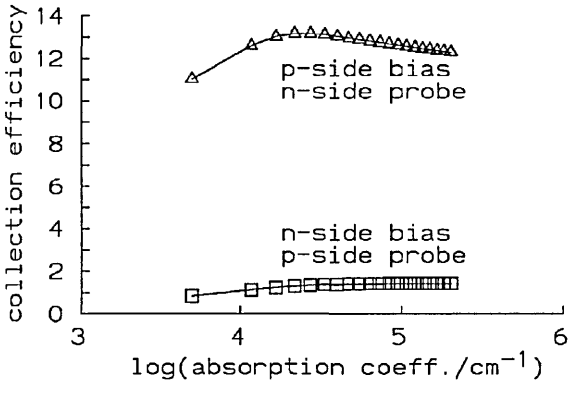

Figure 8: Simulated η_{ext} for p-side bias, n-side probe and n-side bias, p-side probe for the same photon fluxes and at $V_r = 10$ V.

CONCLUSIONS

We have identified conditions at which the collection efficiency in a dual beam experiment exceeds 100 %. Favourable conditions for the effect are thicker pin-diodes in order to utilise space charge effects whereas the effect is very small at thinner solar cell type diodes. The applied voltage must be large enough to assist collection. Most of the bias beam generated carriers are collected anyway without probe beam assistance at high reverse voltage and thus cannot be utilised for the $\eta_{ext} > 1$-effect. Unless homogeneous probe beam generation can be adjusted p-side and n-side probe beam illumination conditions lead to greatly different values for η_{ext} under p-side bias illumination. The effect is largest for p-side bias and n-side probe illumination which requires transparency of both contacts. If only one transparent contact is available p-side bias and p-side probe illumination also lead to η_{ext} larger than one if the absorption coefficient of the probe beam is small. A basic condition resulting in very large η_{ext} is a high intensity p-side bias beam with a small absorption depth whereas a homogeneously distributed bias photogeneration profile results in $\eta_{ext} \leq 1$. Our simulation results are in good qualitative agreement with our experimental findings of which we presented the bias beam intensity dependence.

ACKNOWLEDGEMENTS

The authors acknowledge partial support by the DAAD and the British Council via ARC-collaboration.

REFERENCES

1. J.-H. Zollondz, R. Brüggemann, W. Gao, S. Reynolds, C. Main, G. H. Bauer, in *Amorphous Silicon Technology - 1996*, ed. E. A. Schiff, M. Hack, A. Madan, M. Powell, and A. Matsuda, (Mat. Res. Soc. Proc. **420**, Pittsburgh, 1996), pp. 697-702.
2. W. Gao, C. Main, R. Brüggemann, J.-H. Zollondz, R.A.G. Gibson, J. Non-Cryst. Sol. **198 - 200**, 1221 (1996).
3. S. J. Fonash, J. Hou, F. A. Rubinelli, M. Bennett, S. Wiedeman, L. Yang, J. Newton, Optical Engineering **33**, 2065 (1994).
4. P. Chatterjee, J. Appl. Phys. **75**, 1093 (1994).
5. A. Mittiga, in *Amorphous Silicon Technology - 1995*, ed. M. Hack, E. A. Schiff, A. Madan, M. Powell, and A. Matsuda, (Mat. Res. Soc. Proc. **337**, Pittsburgh, 1995), pp. 657-662.
6. W. Gao, Thesis, University of Abertay Dundee (1995).
7. C.-D. Abel, H. R. Paes, G. H. Bauer, in *Amorphous Silicon Technology-1991*, ed. M.J. Thompson et al. (Mat. Res. Soc. Proc. **219**, Pittsburgh, 1991), pp. 851-857.
8. J.-H. Zollondz, Thesis, Carl von Ossietzky Universität Oldenburg (1995).

Abstract of a talk held at the Chelsea Meeting on Amorphous and Organic Semiconductors, London, 1997:

J.-H. Zollondz, C. Main, R. Brüggemann, S. Reynolds, W. Gao, G. H. Bauer,
The relation between photoinduced space charge and collection efficiencies greater than one in thick a-Si:H p-i-n diodes.

The relation between photoinduced space charge and collection efficiencies greater than one in thick a-Si:H pin-diodes

J.-H. Zollondz[1], C. Main[1], R. Brüggemann[2], S. Reynolds[1], W. Gao[1*], G. H. Bauer[2]
[1] School of Engineering, University of Abertay Dundee, Scotland
[2] Fachbereich Physik, Carl von Ossietzky Universität Oldenburg, Germany

An extensive experimental characterisation of collection efficiencies has been carried out for thick a-Si:H pin diodes (3-4μm) in reverse bias, using a dual-beam (bias - probe) technique. The method involves measurement of the collection efficiency for a low intensity probe excitation applied simultaneously with high intensity bias excitation. The wavelength of each beam was varied over the range 400nm - 700nm, hence varying the absorption depth, and the direction of illumination was changed - i.e. on the p- or n- side, for each beam. In this way the study investigated situations in which the spatial profiles of internal variables such as electric field and space charge were subject to substantial variation. For example, in the case of strongly absorbed bias light, then variation of the probe wavelength or direction of illumination allows us to study the fate of additional probe generated carriers in the region of high bias generation rate or outside this region.

With bias and probe excitation both on the p-side, the form of the spectral response of the probe -beam collection efficiency was found to be very dependent on the bias beam wavelength. Such behaviour can be related to the internal field distribution in the device. In the study, certain conditions were found to result in very high collection efficiencies, much greater than unity, for the probe-generated carriers. The conditions required for this observation normally involved strongly absorbed bias light incident on the p- side of the device, and probe light incident on the n-side. This situation is essentially a primary photodetector with built-in gain !

We explain these effects using a detailed numerical model for amorphous semiconductor junction devices, which gives information on the spatial variation of microscopic processes, field, space charge and recombination within the pin device. In particular, the conditions for very high collection efficiency have been established. The physics behind the effect involves the 'photogating' of bias - produced carriers by the relatively weak probe beam, which modulates the internal field profile. Similarly, the influence of bias beam wavelength on the form of the probe beam collection efficiency spectrum can be explained by the presence of local field minima, which are controlled by majority carrier diffusion. We believe that this feature is also the reason for maxima of the photocurrent in transient measurements after switch on of the illumination.

---

[*] Now at NREL, Golden Co., USA

Abstract of a talk presented as co-author at the *Chelsea Meeting on Amorphous and Organic Semiconductors*, London, 1998:

C. Main, S. Reynolds, J.-H. Zollondz, R. Brüggemann,
Photoconductivity decay from the Steady State in Amorphous Semiconductors.

PHOTOCONDUCTIVITY DECAY FROM THE STEADY STATE IN AMORPHOUS SEMICONDUCTORS

C. Main, S. Reynolds, J-H Zollondz, and R. Brüggemann[#]

University of Abertay Dundee, School of Engineering, Bell Street Dundee DD1 1HG
[#] Fachbereich Physik, Carl von Ossietzky Universität, 26111 Oldenburg, Germany

Abstract

This paper presents analysis, computer modelling and experimental measurements of the photoconductive decay which occurs on cessation of illumination, in amorphous semiconductors. This situation differs in several respects from the impulse response widely used in transient photoconductivity (TPC) studies. For example, traps will initially be occupied up to a quasi - Fermi level, rather than empty, and recombination, which determines the pre-'switch-off' photocurrent will be expected to play a more significant role in the decay at short times.

Early work [1] made the assumption that the rate limiting step in the decay process was the thermal release of trapped carriers from the vicinity of the quasi Fermi level, which leads to a simple expression to obtain the carrier drift mobility, using the measured steady state photocurrent and initial decay rate. Such an analysis also gives a simple relation between the generation rate dependence of the steady photocurrent, and that of the observed decay time. Measured decay rates, however are often much faster than that predicted by the above assumption, and the generation rate dependencies do not follow the relation expected [2,3]

In this paper, we explore by analysis and computer simulation, the processes of relaxation of the excess carrier distributions, and examine the relative roles of re-trapping and recombination in exemplar cases of exponential trapping state profiles, with linear (monomolecular) and non-linear (bimolecular) recombination. A rich variety of possible decay behaviour is revealed, of which the early work is only a subset. We also present simulation of the photo-decay in a realistic model of an amorphous semiconductor such as a-Si:H and its alloys, including conduction and valence band-tail trapping, and dangling bond defects. The modelled photo-decay is very different to the TPC case, and may even be dominated by minority holes over certain time - ranges.

We present preliminary results of measurements of the decay from steady state in films of a-$Si_{1-x}C_x$:H and other materials and compare these results with the analysis and model predictions.

References

1. T.D. Moustakas and K. Weiser, Phys. Rev. B 12, 2448, 1975.
2. G.J. Adriaenssens, S.D. Baranovskii, W. Fuhs, J. Jansen and Ö.Öktu, Phys. Rev. B 51, 9661, 1995
3. R. Brüggemann, Solid State Commun. 101, 199, 1997

Paper presented at the *Paper Presentation Workshop*, University of Abertay, 1998:

J.-H. Zollondz

The relation between photoinduced space charge and collection efficiencies greater than one in thick a-Si:H pin- diodes.

THE RELATION BETWEEN PHOTONINDUCED SPACE CHARGE AND COLLECTION EFFICIENCIES GREATER THAN ONE IN THICK a-Si:H PIN-DIODES

J.-H. Zollondz

Division of Applied Physics and Materials
School of Engineering
University of Abertay Dundee

ABSTRACT
Charge collection, transient photocurrents and the external collection efficiency under additional bias illumination were used to characterise 3-4 μm thick a-Si:H pin-diodes. Different bias light illumination results in an increase or decrease of the photoresponse of a probe beam. Under large bias photon flux, in relation to the probe beam, collection efficiency values higher than 1, i.e. higher collection than 100% , can be received. These efficiencies sensitively depend both on the applied voltage and the defect density. Numerical modelling reveals the influence of internal variables, like the electric field, on the steady state photocurrents under the different illumination conditions.

1. INTRODUCTION

Applications of a-Si:H, such as solar cells or detectors, are often made in form of a p-i-n structure. However, because of the complexity of amorphous material, information about internal parameters is often obtained by measurements of thin homogenous mono layer films.
Here I report on a possiblity to get a qualitative information about one of the internal parameters, the defect density, from measurements in a p-i-n structure. Under certain conditions of a simple two beam setup collection efficiencies greater than one can be obtained, in early work by (Maruska et al., 1984) and later by (Hou et al., 1992, Rubinelli et al., 1993, Fonash et al., 1994, Chatterjee, 1994). The collection efficiency is determined by measurements of the photocurrent and by knowledge of the incident photon flux. These high collection efficiencies depend sensitively on the defect densities.

2. METHODS

2.1 Experimental Details

Figure 1 sketches the two beam experimental setup for collection efficiency measurements, where the bias beam can optionally be guided through the p- or n- side. For charge collection studies bias light photon fluxes of $10^{13} - 10^{15}\mathrm{cm}^{-2}\mathrm{s}^{-1}$ and for the probe light of 10^{11} and 10^{12} $\mathrm{cm}^{-2}\mathrm{s}^{-1}$ were used. The measurements were made with a 3.5 μm thick p-i-n diode with 200 Å a-Si:H p- and n-layers. The optical transmission at 400 - 700 nm of Cr-contacts on the amorphous silicon is ≈ 30 %.

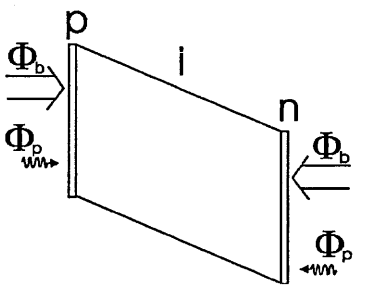

Figure 1: Illumination situation (bias–beam: b, probe–beam: p).

2.2 Definitions and Strategy

Two definitions for the determination of the collection efficiency from the photocurrent i_{ph} were applied for the results below. The internal collection efficieny η_{int} under bias illumination at a given reverse bias voltage V_r was calculated as

$$\eta_{int} = \frac{i_{ph}(\lambda, V_r)}{i_{ph}(\lambda, V_r = 25V)}. \quad (1)$$

The external collection efficiency η_{ext} under bias illumination with photon flux Φ_b is determind as

$$\eta_{ext} = \frac{i_{ph}(\Phi_p + \Phi_b) - i_{ph}(\Phi_b)}{e\Phi_p} \quad (2)$$

where reflection is taken into account for Φ_p. Note that the maximum value for η_{ext} is 1 if all and only probe light generated carriers are collected.

Apart from these results modelling (Gao, 1996, Gao, 1995) under the same conditions was used to understand the changes in the internal parameters.

3. RESULTS AND DISCUSSION

For illumination of both bias and probe beam from the p-side, the wavelength dependent η_{int} (Fig. 2a) shows a direct dependence on Φ_b and bias wavelength λ_b. For $\lambda_b = 400\,\text{nm}$ an increased flux Φ_b leads to an increase in the collection of red probe light while blue probe light collection is worse. The turning point is about 550 nm. For $\lambda_b = 700\,\text{nm}$ a reverse behaviour with large/small η_{int} in the small/large λ_b-region for the probe light is found. The simulated electric field distribution ($\mathcal{E}$) for the same parameters as the collection efficiency measurements is given in Fig. 2b). The electric field drops to very low values over most of the i-layer ($\lambda_b = 700\,\text{nm}$) while in the p/i-interface region up to about 0.5 μm an increase in the field is calculated, which results from the increased positive dangling bonds (DB) charge screening the bulk of the i-layer. For blue p-side illumination the different behaviour of η_{int} is reflected in the $\mathcal{E}$-distribution, which shows a sharp increase in the electric field in the region of the i-layer next to the illuminated side and an increase in the back of the sample (Fig. 2b)). The simulation results fit nicely with the measured collection efficiency measurements: higher collection efficiency values under red bias light for short wavelength, e.g. short absorption depths; and lower

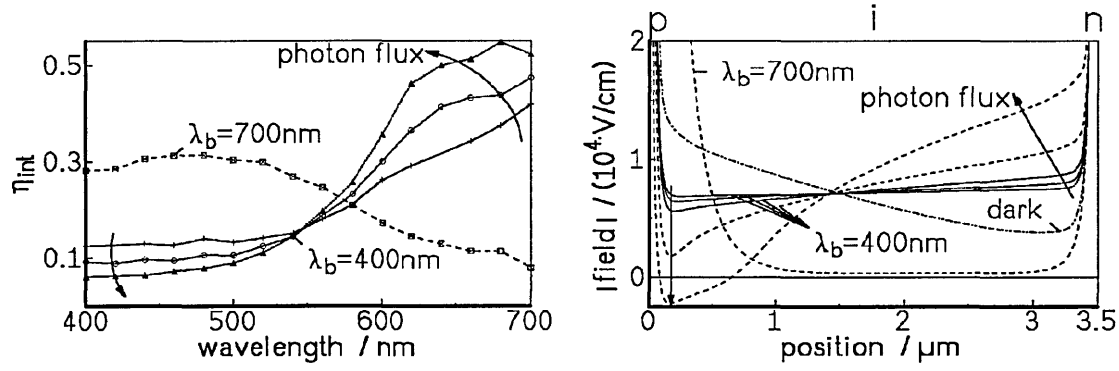

Figure 2: (a) Experimental η_{int} for both p-side probe and bias illumination (λ = 400, 700 nm). (b) Simulated $\mathcal{E}$ for the experimental situation.

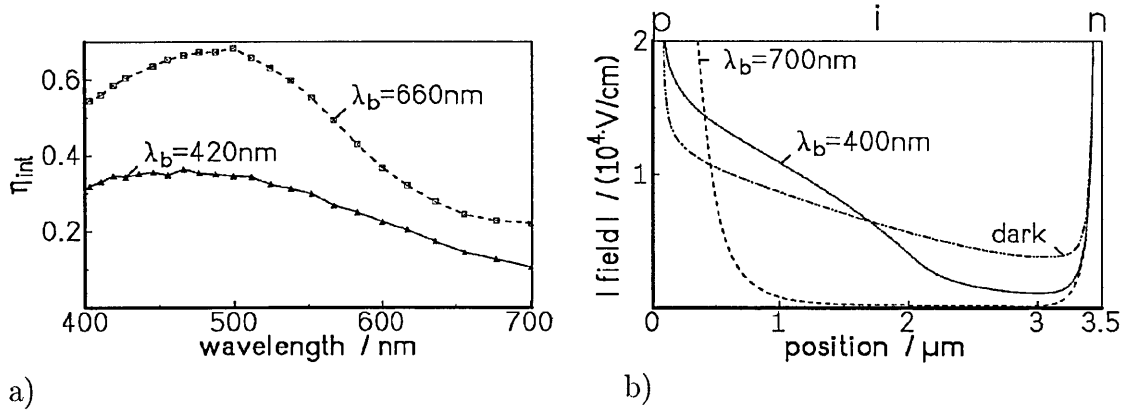

Figure 3: (a) Experimental η_{int} for p-side probe and n-side bias illumination (λ = 400, 660 nm). (b) Simulated $\mathcal{E}$. Note the wider field region for 400 nm as compared to Fig. 2b)

values for η_{int} by illumination of blue bias light, that results in a low field region at absorption depth ($1/\alpha$) of wavelengths that are worse collected ($\lambda \leq 550$ nm). At large absorption coefficient (α) the width of the low field region is larger than the absorption depth, which we also deduce from the experimental (Fig. 2a)). The absorption depth for $\lambda = 550$ nm is about 0.1μm which corresponds to the position of minimum field, giving a ratio of low field region to bias absorption depth of about 8. Additional results show that this ratio drops for smaller bias α which gives the first hint to diffusion of majority carriers into the i-layer.

Figure 3a) shows experimental η_{int} for p-side probe but n-side bias illumination. Similarly, the simulated electric field $\mathcal{E}$ for n-side bias is given in Fig. 3b) for the dark as well as for red and blue bias illumination. For low absorption coefficients (λ = 660 nm or 700 nm) the absorption depth is higher than the thickness of the sample, e.g. the absorption profile is nearly homogeneous and photoinduced field changes have to be the same independent on the "illumination side". This is illustrated for η_{int} in Fig. 2a) and Fig. 3a) and for the field in Fig. 2b) and Fig. 3b) for red bias.

The field $\mathcal{E}$ for blue n-side bias (Fig. 3a) shows a wide minimum, extending to more than 1 μm from the n-layer into the i-region, while the field increases over the left part of the i-layer. The p-side illumination can discriminate between the two situations of n-side bias, which can be seen in the increase in η_{int} at shorter wavelengths for $\lambda = 400$ nm in Fig. 3a).

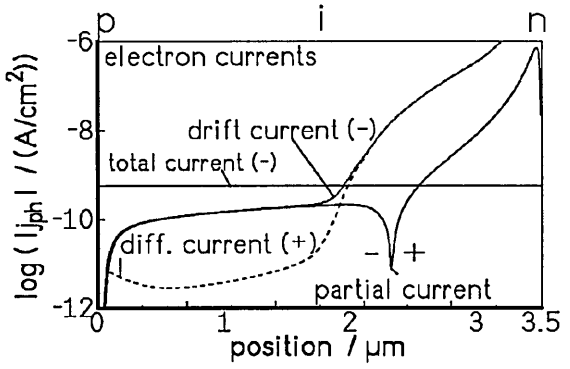

Figure 4: Simulated electron currents under n-side bias illumination ($\lambda_b = 400$ nm). Note the large diffusion component with opposite sign for the majority carrier on the right.

In order to discuss the illumination situation in more detail Fig. 4 and Fig. 5 show some internal variables under n-side bias illumination for $V_r = 2$ V. Similar results hold for p-side bias illumination, under which electrons drift across the diode (from p to n). The partial currents for electrons are presented in Fig. 4 where the horizontal line presents the (negative) total electron current density. The dominance of the (positive) electron diffusion current, which is directed into the i-layer against

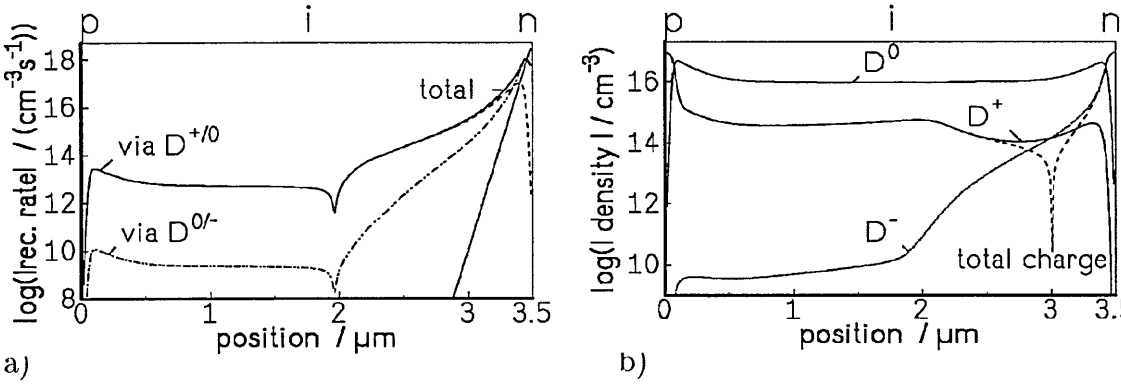

Figure 5: Modeling recombination rates (a) and occupation densities (b) for n-sided illumination of $\lambda = 400\,\mathrm{nm}$.

$\mathcal{E}$, over the (negative) drift current results in a partial current of positive polarity deep in the i-layer next to the n-layer. The diffusion component can dominate because $\mathcal{E}$ is so low as seen in Fig. 3b). The simulation shows that majority carrier diffusion from the generation region into the i-layer determines the width of the low field region. Locally the recombination rate R exceeds the generation rate (Fig. 5a)). Minority carrier diffusion has only a minor effect. The strength of the low field is determined by the dominance of charged DB under illumination in most of the i-layer which are converted by the traversing hole carriers and by which the field is screened in the generation region (Fig. 5b)). The behaviour of majority and minority carriers at either side of the pin-diode (e.g. majority holes in the p/i-interface region) corresponds to each other if the illumination direction is changed to the p-side. Minorities, which traverse the diode to be collected at the opposite contact, exhibit some contact back diffusion loss in both illumination situations (Crandall, 1983, 1984, Zollondz, 1995). The photoinduced field and free carrier density changes result in extremely large collection efficiencies under special conditions (Gao et al., 1996). Fig. 6a) shows a set of experimental η_{ext} for different V_r after light soaking the diode through the n-side with water-filtered light from a halogen lamp (AM 1.5 with 0, 10, 110, 490 and 1090 min). Bias illumination in Fig. 6a) was from the p-side with $\lambda_b = 450\,\mathrm{nm}$ under a high flux of $2 \times 10^{15}\,\mathrm{cm^{-2}s^{-1}}$. Additional probe beam illumination was through the n-side with $\lambda_p = 620\,\mathrm{nm}$ and $10^{12}\,\mathrm{photons\,cm^{-2}s^{-1}}$.

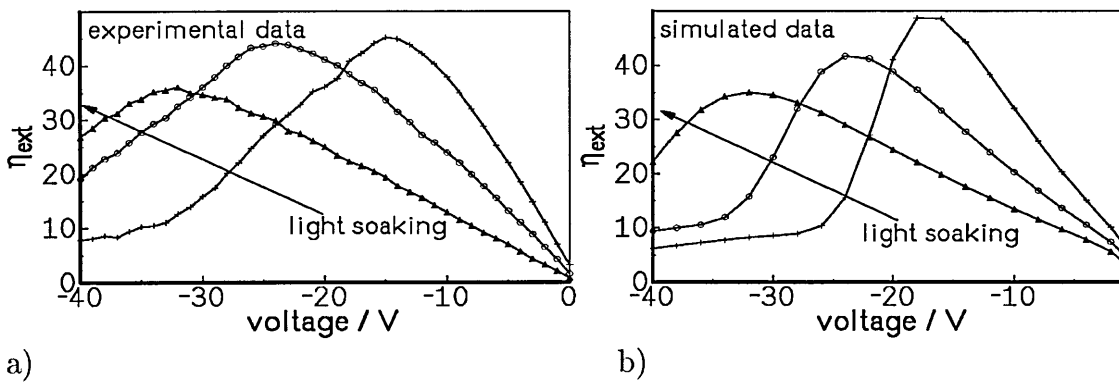

Figure 6: (a) Experimental η_{ext} greater than one after increasing stages of light soaking. n-side probe ($\lambda = 620\,\mathrm{nm}$) and p-side bias illumination ($\lambda = 450\,\mathrm{nm}$) with a ratio $\Phi_b/\Phi_p = x$. (b) Simulated η_{ext} with small changes in defect density ($5,7,10 \times 10^{15}\,\mathrm{cm^{-3}}$). Note that $\eta_{ext} = 1$ means full collection of probe light generated carriers.

Each η_{ext} curve decreases towards low and high voltage and shows a maximum well in excess of unity for total collection of probe light generated carriers. The values are also much larger than results reported for solar cells (e.g. (Maruska et al., 1984, Fonash et al., 1994)). η_{ext} is very sensitive to the density of defects in the device, too. Light soaking shifts the maximum notably to higher V_r. Figure 6b) illustrates that the simulation, reproduces the experimental findings with η_{ext} exhibiting a maximum as a function of V_r. The small increase in defect density by a factor of 2 shifts the maximum in η_{ext} to larger V_r.

As described by Gao et al. (1996) a reservoir of free carriers builds up in the low $\mathcal{E}$-region under large bias flux, e.g. of electrons in the p/i-interface region in Fig. 2b). The tiny changes in $\mathcal{E}$, induced by the additional red bias light, are large enough to have an additional number of these reservoir (bias generated) electrons extracted, which are then added to the probe beam extracted carriers, increasing η_{ext} well above unity.

For thin pin-diodes η_{ext} remains low around 1 as the built-in potential results in larger $\mathcal{E}$ throughout the device, reducing the built-up of an electron reservoir. For degraded solar cells η_{ext} is more likely to increase under the probe/bias-conditions discussed here because of stronger band bending and low $\mathcal{E}$ in the i-layer.

4. CONCLUSIONS

Thick a-Si:H pin-diodes are more sensitive to space charge influences than thin solar cell type diodes, where only the degraded solar cell may be similar in behaviour. Two phenomena are presented, which result from large changes of the internal variables under specific illumination conditions: increase/decrease of red/blue response in the steady state, where the role of diffusion in the low field region is emphasized, and apparent collection efficiencies much greater than unity (amplification ratio up to 50). The field changes depend strongly on the defect density so that the phenomena presented here can be further exploited for degradation studies and device characterization.

ACKNOWLEDMENTS

The authors acknowledge the partial support by the DAAD and the British Council via ARC-collaboration and by the Stifterverband für die deutsche Wissenschaft.

REFERENCES

Chatterjee, P., J. Appl. Phys. **75**, 1093 (1994).

Crandall, R.S., J. Appl. Phys. **54**, 7176 (1983), **55**, 4418 (1984).

Fonash S. J., et al., Optical Engineering **33**, 2065 (1994).

Gao, W., Main, C., Brüggemann, R., Zollondz, J.-H., Gibson, R.A.G., J. Non-Cryst. Sol., (1996).

Gao, W., PhD thesis, Dept. of Electrical Engineering, University of Abertay Dundee.

Hou, J. Y., Fonash, S. J., App. Phys. Lett. **61**, 186 (1992).

Maruska, H. P., Hicks, M. C., Moustakas, T. D., Friedmann, R., IEEE Trans. ED **31**, 134 (1984).

Rubinelli, F. A., Hou, J. Y., Fonash, S. J., J. Appl. Phys. **73**, 2548 (1993).

Zollondz, J.–H., Diploma thesis, Carl von Ossietsky Universität Oldenburg (1995).

Paper presented at the ISCMP on Thin Film Materials and Devices - Developments in Science and Technology Varna / Bulgaria, 1998:

J.-H. Zollondz, C. Main, W. Gao, S. Reynolds, R. Brüggemann, M.J. Rose, *Investigation of qunatum efficiencies much larger than unity in a-Si:H p-i-n structures*, published in: Thin film materials and devices - developments in Science and Technology, eds. J.M. Marshall, N Kirov, A Vavrek, J.M. Maud (World Scientific 1999) pp. 333-336, 1998.

Varna98 - INVESTIGATION OF QUANTUM EFFICIENCIES MUCH LARGER THAN UNITY IN a-Si:H p-i-n STRUCTURES
J.-H. Zollondz*, C. Main*, W.Gao#, S. Reynolds*, R.Brüggemann• and M. J. Rose°

INVESTIGATION OF QUANTUM EFFICIENCIES MUCH LARGER THAN UNITY IN a-Si:H p-i-n STRUCTURES

J.-H. Zollondz*, C. Main*, W.Gao#, S. Reynolds*, R.Brüggemann•
and M. J. Rose°

School of Engineering, University of Abertay Dundee, Dundee DD1 1HG, Scotland, United Kingdom
#National Renewable Energy Laboratories, Golden, Colorado 80401-3393
• F.B. Physik, Carl von Ossietzky Universität Oldenburg, D-26111 Oldenburg, Germany
° Department of Applied Physics and Electronic & Manufacturing Engineering, University of Dundee, Dundee DD1 4HN, Scotland, United Kingdom

ABSTRACT

A quantum efficiency much larger than unity is observed under reverse bias voltage conditions, in hydrogenated amorphous silicon p-i-n structures. High collection efficiencies are measured for low-level probe illumination of the device n-side with red light, with simultaneous bias illumination from the device p-side with strongly absorbed blue light. The photogating effect responsible varies experimentally with reverse bias voltage, and collection efficiencies for the probe excitation of up to 50 are obtained. Detailed computer simulations corroborate such high values of quantum efficiency and the underlying mechanisms for the effect are revealed. We present the influence on quantum efficiency of bias light wavelength and photon flux, probe light photon flux, applied voltage and defect density.

1. Introduction

Quantum efficiencies (QE) greater than unity in hydrogenated amorphous silicon (a-Si:H) based p-i-n structures were the subject of recent works,[1-3] not only for physical understanding but also for possible a-Si:H based detectors. The external gain, which is based on internal field changes, responds sensitively to small changes in external variation of intensity of a bias beam (or wavelength) and to internal changes, *via* degradation of the p-i-n device. The experiments reported here and in our previous work[4-6] are undertaken at *reverse* bias voltage and for a low-level probe beam and a much larger bias beam such that only primary photocurrents flow. Thus any gain must involve the modulation of the bias-created photocurrent by the probe beam.

Hou and Fonash[2] and Rubinelli[3] pointed out that strongly absorbed blue bias light can create a low-field region in the front of the i-layer, i.e. near the p-i interface, while increasing the field in the back of the i-layer. Illumination with weakly absorbed light from either side generates holes throughout the device which, if trapped in sufficient numbers toward the back of the device, result in a field increase in the front low field region. This allows the release of blue-bias-light-produced carriers previously unable to traverse the front part of the device before recombining.

Varna98 - INVESTIGATION OF QUANTUM EFFICIENCIES MUCH LARGER THAN UNITY IN a-Si:H p-i-n STRUCTURES
J.-H. Zollondz*, C. Main*, W.Gao#, S. Reynolds*, R.Brüggemann* and M. J. Rose°

2. Experimental and modelled results

In this work we measured and simulated the photocurrent response of thick a-Si:H p-i-n diodes (3.5 μm) under various degradation and illumination situations with a two beam experiment. For the bias beam we used a wavelength of 450 nm and a photon flux of $\Phi_b = 1.5 \times 10^{15}$ cm^{-2} s^{-1} from the p side and for the probe beam a wavelength of 621 nm and $\Phi_p = 7.4 \times 10^{11}$ cm^{-2} s^{-1}. Since the device exhibited a relatively slow response, a dc method was used for QE measurements. The probe QE is determined as

$$QE = (I_{BP} - I_B)/(qA\Phi_p), \quad (1)$$

where A is the device cross-section area and q is the electronic charge. The effects of light soaking were investigated by illuminating annealed devices in a series of increasing exposure times, from the p- side with light from an AM1 source, but fitted with a water filter. The devices were in open circuit condition during exposure.

Figure 1 shows the QE *vs* applied reverse bias, measured after successive AM1 light soaking exposures. In each case, the QE exhibits a peak, and this peak shifts rapidly to higher reverse voltages as the light soaking time is increased. In Figure 2 the computed QE *vs* reverse bias is shown for the same beam illuminations as in Figure 1, i.e. bias 420 nm p-side and probe 621 nm n-side. The similarity between simulation and experiment is clear, with very high values in evidence, although the magnitude of the peak in the QE shows a bigger variation with defect density in simulation.

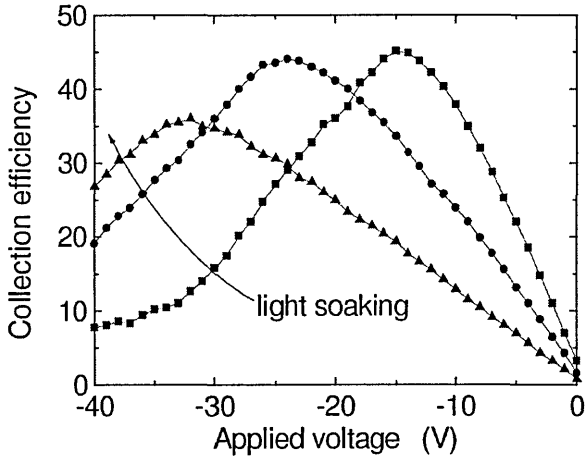

Figure 1: Experimentally determined quantum efficiencies *vs* applied reverse bias, after successive AM1 light soak exposures, using 450 nm blue bias illumination flux $\Phi_b = 1.5 \times 10^{15}$ cm^{-2} s^{-1} and red probe illumination of wavelength 620 nm, flux $\Phi_p = 7.4 \times 10^{11}$ cm^{-2} s^{-1} incident on the n-side.

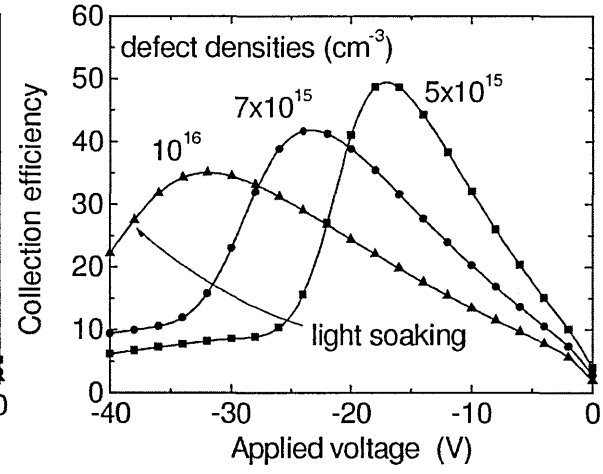

Figure 2: QE *vs* reverse bias obtained by numerical modeling for red probe and blue bias illumination conditions equivalent to those used experimentally (Fig. 1), for defect densities 5, 7 and 10×10^{15} cm^{-3} s^{-1}.

Varna98 - INVESTIGATION OF QUANTUM EFFICIENCIES MUCH LARGER THAN UNITY IN a-Si:H p-i-n STRUCTURES
J.-H. Zollondz*, C. Main*, W.Gao#, S. Reynolds*, R.Brüggemann* and M. J. Rose°

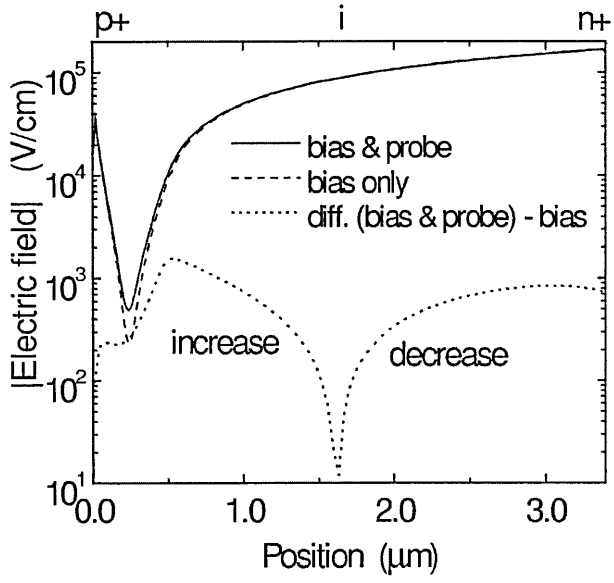

Figure 3: The effect of the addition of probe illumination on the internal field. The top two curves represent the internal field profile at -28 V reverse voltage, with bias illumination alone, and then with the addition of probe illumination. The third curve is the *change* in field on application of probe illumination.

The internal field shows a sharp minimum under bias illumination near to the p-i interface (Figure 3). Additional illumination of the probe beam changes the field only by a small amount. But it can be seen that there is a *decrease* in field over the back of the device, and an *increase* at the front, which in *relative* terms is greatest in the low field region. The phenomenon causing the modulation in the field profile is trapping of holes generated by the weakly absorbed probe beam, as they drift towards the front of the device.

Simulation of the total space charge and occupation rates show that, to the back of the device, trapped electrons in D^- states dominate the space charge, while in the front of the device close to the p-i interface, holes trapped in the valence band tail dominate the space charge. The result of the field modulation by the probe beam is that it promotes release of the electrons from the low field region.

Further simulations (Figure 4) show that at a constant photon flux of the bias beam of $\Phi_b = 1.5\times10^{15}$ cm^{-2} s^{-1} and variation of the probe beam from 1×10^{10} cm^{-2} s^{-1} to 1×10^{14} cm^{-2} s^{-1} for very low probe fluxes, the QE becomes independent of the probe flux. As the probe flux approaches the magnitude of the bias flux, the QE falls toward unity and below. Variation of the bias flux to high relative values in relation to the probe beam results in very high QE values approaching 400. Experimentally, a higher probe beam flux would be necessary to observe the phenomenon with any accuracy under these conditions.

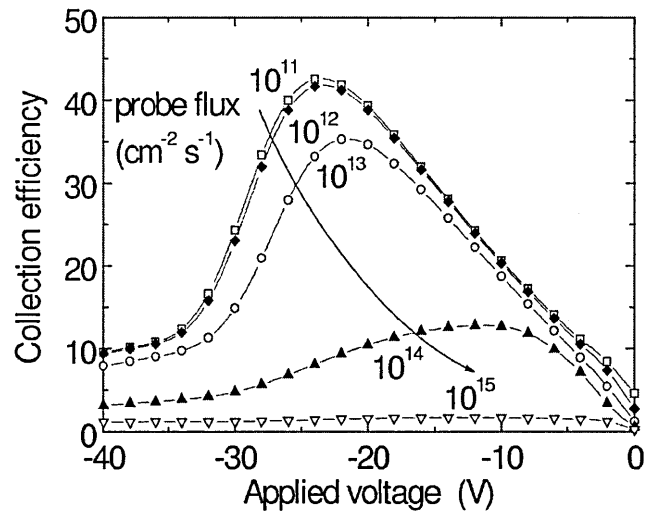

Figure 4: The variation of QE with applied voltage while the bias beam is held constant at a flux of 2×10^{15} cm^{-2} s^{-1} and the probe beam is varied. For very low probe flux, the QE becomes flux-independent.

Varna98 - INVESTIGATION OF QUANTUM EFFICIENCIES MUCH LARGER THAN UNITY IN a-Si:H p-i-n STRUCTURES
J.-H. Zollondz*, C. Main*, W.Gao#, S. Reynolds*, R.Brüggemann* and M. J. Rose°

Simulation shows that it is possible to have hole gating also (Figure 5). Under a reverse beam situation, i.e. for the bias beam wavelength 450 nm and a photon flux of $\Phi_b = 1.5 \times 10^{15}$ cm^{-2} s^{-1} from the **n** side and for the probe beam a wavelength of 621 nm and a photon flux of $\Phi_p = 7.4 \times 10^{11}$ cm^{-2} s^{-1} incident from the **p** side. Illuminating the diode with the bias beam through the n side results in a more extended field minimum, now appearing next to the n-i interface. This now reversed situation means that holes are gated and results in QE values up to 5.

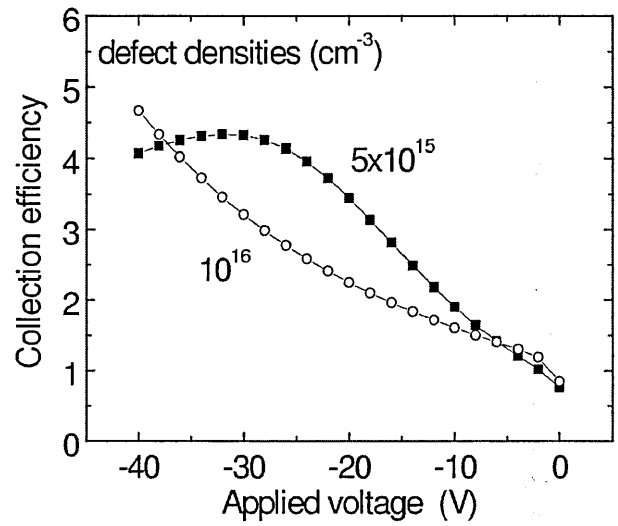

Figure 5: QE *vs* reverse bias obtained by numerical modeling for red probe and blue bias illumination conditions equivalent to those in fig.2, for defect densities 5 and 10 $\times 10^{15}$ cm^{-3}. Bias here incident from the n- and probe from the p-side.

3. Conclusions

We have demonstrated by experiment and computer modelling, that under *reverse bias* a quantum efficiency much greater than unity can be achieved by a photogating effect in thick a-Si:H p-i-n diodes. Photogating gain values of up to 50 times have been measured, and conditions for even larger gains have been predicted. Whether such characteristics have application in optical detection systems is not yet clear. In initial studies, the speed of response is quite slow, and the large bias-beam induced photocurrent must introduce additional noise into any such detector. Computer modelling indicates that the magnitude and detailed features of the effect are sensitive functions of the density and cross-section parameters used for defects, and hence such measurements can serve a useful diagnostic function. Further, we modelled photogating values up to 5 in a reverse beam situation. This indicates that holes can be gated, too.

4. Acknowledgements

The authors acknowledge funding from the British Council and DAAD via an ARC collaboration. One of the authors (J.-H. Zollondz) is grateful to the University of Abertay Dundee for the provision of a research studentship.

5. References

[1] H. Hou and S. J. Fonash, Appl. Phys. Lett. 61, 186 (1992)
[2] A. Rubinelli, J. Appl. Phys. 75, 998 (1994)
[3] P. Chatterjee, J. Appl. Phys. 75, 1093 (1994)
[4] J.-H. Zollondz, W. Gao, R. Brüggemann, C. Main, and G. H. Bauer, *MRS Symposium Proceedings vol. 420,* (MRS Pittsburgh, 1996), Ch.141, 251-256 (1996)
[5] R. Brüggemann, J.-H. Zollondz, C. Main, and W. Gao, *MRS Symposium Proceedings Vol 467,* (MRS, Pittsburgh 1997) Ch 143, 759-764 (1997)
[6] C. Main, J.-H. Zollondz, S.Reynolds, W. Gao, R. Brüggemann, and M. J. Rose, Accepted for publication in J. Appl. Phys.

Co-author of a paper presented at the ISCMP on *Thin Film Materials and Devices - Developments in Science and Technology* Varna / Bulgaria, 1998:

C. Main, S. Reynolds, J.-H. Zollondz, R. Brüggemann,
Decay from steady state photoconductivity in amorphous semiconductors, invited contribution published in: Thin film materials and devices - developments in Science and Technology, eds. J.M Marshall, N Kirov, A Vavrek, J.M Maud (World Scientific 1999) pp. 191-198, 1998.

Tenth ISCMP Decay from Steady State Photoconductivity .... C. Main et al. page 1
In "Thin film materials and devices - developments in Science and Technology" eds. JM Marshall, N Kirov, A Vavrek, JM Maud (World Scientific 1999) 191-198.

DECAY FROM STEADY STATE PHOTOCONDUCTIVITY IN AMORPHOUS SEMICONDUCTORS

C. Main, S. Reynolds, J.- H. Zollondz and R. Brüggemann*
School of Science and Engineering, University of Abertay Dundee, Dundee DD1 1HG, Scotland, United Kingdom and
**F.B. Physik, Carl von Ossietzky Universität Oldenburg, D-26111 Oldenburg, Germany*

ABSTRACT

This paper presents analysis, computer modelling and experimental measurements of the photoconductive decay which occurs on cessation of illumination, in amorphous semiconductors. We explore the processes of relaxation of the excess carrier distributions, and examine the relative rôles of re-trapping and recombination in an exemplar case of an exponential trapping state profile, with linear (monomolecular) recombination. A rich variety of possible decay behaviour is revealed. We examine critically several plausible intuitive explanations of the decay process, including (a) the assumption that the rate limiting step in the decay process is the thermal release of trapped carriers from the vicinity of the quasi - Fermi level, and (b) multiple re-trapping at the quasi - Fermi level prior to recombination. Actual decay rates, however are often much faster than that predicted by these assumptions, and the generation rate dependencies do not follow the relation expected. These explanations are shown in detail to be largely erroneous. Results of experimental measurements of the decay from steady state and TPC in films of a-$Si_{1-x}C_x$:H are presented. While these appear initially to be at variance with the predictions of the present work, we demonstrate that the observations can be reconciled fully with theory, albeit in an unexpected way.

1. Introduction

Some recent publications[1-4], have reported on the decay of photocurrent from the steady state in amorphous semiconductors, after steady illumination has been switched off. Analysis of this situation has been the subject of numerous works dating back at least to the classic work of Ryvkin[5] and Rose[6] in the 1950s and 60s. Most other studies to date on amorphous semiconductors have concentrated however on the photocurrent response to *impulse* optical excitation, i.e. the transient photocurrent experiment (TPC). In this experiment, an excess carrier density ΔN is created by a short pulse of uniformly absorbed light in a semiconductor sample fitted with coplanar ohmic contacts, and the subsequent decay of the photocurrent is monitored. Under these conditions, *and* provided recombination is not significant, then the instantaneous photocurrent is also a measure of the instantaneous effective mobility of the ensemble of ΔN excess carriers.

Tenth ISCMP Decay from Steady State Photoconductivity .... C. Main et al. page 2
In "Thin film materials and devices - developments in Science and Technology" eds. JM Marshall, N Kirov, A Vavrek, JM Maud (World Scientific 1999) 191-198.

In amorphous semiconductors, transport of free carriers may be interrupted by trapping in the distribution of localised states in the gap, so that at any moment only a small (and time-varying) fraction of the excess carriers is free. Alternatively, transport may occur by hopping between localised sites. Generally, at long times recombination losses reduce the total excess carrier density, and the photocurrent is no longer proportional to the effective instantaneous mobility of the original cohort of ΔN excess carriers. Typically, in amorphous silicon for example, at room temperature, recombination may not have a significant effect on TPC transients up to times as long as 10s.

In contrast to TPC, in the switch-off experiment, conditions just prior to cessation of illumination are dominated by *recombination - viz* the steady state excess electron density is given by $dn = G\tau_R$ where τ_R is the recombination lifetime. This lifetime may be a constant, in the case of monomolecular recombination, or may be dependent on the generation rate G. It is natural then to assume that recombination ought to play an important part in the switch-off photocurrent decay *from the outset*, in contrast to the TPC experiment. However, since high densities of traps exist in amorphous semiconductors, it is not expected that the initial decay time τ_i of photocurrent should reflect *directly* the recombination time for free electrons, since excess carriers would be expected to interact with traps, slowing down the response. All of the above implies that interpretation of switch-off decay could be much more difficult than for TPC.

The first intuitive model we present contends that the decay from steady state occurs by recombination of free electrons, but the initial decay of the whole excess group is determined by the rate at which electrons trapped in states at the quasi-Fermi energy are released thermally to the conduction band prior to recombining. The rate limiting step, and hence the observed decay time, under this assumption, is just the thermal release time τ_e of charge at the quasi Fermi energy, E_{Fn}, *viz:*

$$\tau_e = \upsilon^{-1}\exp\left(E_{Fn}/kT\right) = \tau_i . \qquad (1)$$

The second intuitive model asserts that for any free electron, multiple trapping occurs in states close to the quasi-Fermi energy prior to the electron finally recombining. In this case, the argument runs, for every free electron recombining, there will be renewal from the reservoir of trapped electrons, most of which (in the context of an exponential band-tail) are close to E_{Fn}. The observed initial decay time will then be some multiple of the free electron recombination time, as determined by the steady state ratio of trapped to free electron densities, since this ratio should reflect the relative times spent free and trapped by any given electron. In this approach,

$$\tau_m = \frac{\tau_e + \tau_t}{\tau_t} \times \tau_R \approx \frac{n_t}{n} \times \tau_R \approx \tau_i \ , \qquad (2)$$

Tenth ISCMP Decay from Steady State Photoconductivity .... C. Main et al. page 3
In "Thin film materials and devices - developments in Science and Technology"
eds. JM Marshall, N Kirov, A Vavrek, JM Maud (World Scientific 1999) 191-198.

where n and n_t are the free and trapped electron densities, and τ_t ($<< \tau_e$) is the trapping time into states close to the quasi Fermi energy.
It is evident that while the above arguments may seem plausible, they do not agree in detail. We will demonstrate the inadequacies of each approach below, by numerical modelling which also provides a framework of insight for more appropriate approximate analytical treatments, results of which are presented below.

Following the above, we then direct attention to measurements of the photocurrent decay from steady state in thin film specimens of the amorphous alloy a-$Si_{1-x}C_x$:H, in an attempt to apply the insights gained from simulation. As will be seen, the real world introduces additional features making a direct explanation in terms of the model cases appear impossible, but which yield ultimately to an 'oblique' approach.

2. Computer Modelling Results and Discussion

To visualise accurately the time-evolution of both free and trapped charge following switch-off or an impulse excitation, a numerical solution scheme has been developed by the authors[7] In this section, we present the results of a computer simulation of the decay from steady state in a deceptively simple system consisting of an exponential band tail and a fixed recombination time for free electrons. These are used to support simple analytical expressions for the decay under different conditions. The parameters employed are :

Band edge density of states	$g(E_C)$	4×10^{21} cm^{-3} eV^{-1}
Characteristic temperature for band tail	T_C	290 K
Attempt-to-escape frequency	ν	1×10^{12} s^{-1}
Free electron recombination time	τ_R	6.9×10^{-8} s
Temperature	T	200 K

These parameters thus give $\alpha = \dfrac{T}{T_c} = 0.69$

Figure 1 shows the decay curves of free electron density for prior steady volume generation rate G ranging from 10^{14} to 10^{22} cm^{-3}s^{-1}. It is immediately evident that there are several well-defined regions in which power-law decay occurs. These are classified below, and the indices are compared with the approximate analytical expressions obtained in this work. Discussion of this rich variety of decay forms will follow after further insights gained from simulations.

		index	analytical index
Low excitation	short times	- 0.7	$-\alpha$ = - 0.69
(G < 10^{16} cm^{-3}s^{-1})	long times	- 1.7	$-(1+\alpha)$ = - 1.69
High excitation	short times	- 3.0	$-1/(1-\alpha)$ = - 3.22
(G > 10^{20} cm^{-3}s^{-1})	long times	- 1.7	$-(1+\alpha)$ = - 1.69

Tenth ISCMP Decay from Steady State Photoconductivity .... C. Main et al. page 4
In "Thin film materials and devices - developments in Science and Technology" eds. JM Marshall, N Kirov, A Vavrek, JM Maud (World Scientific 1999) 191-198.

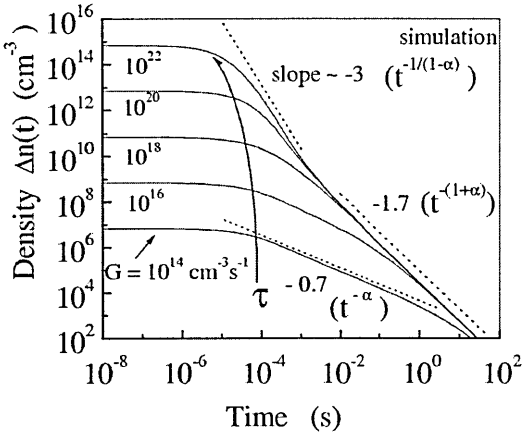

Figure 1. Computed decay of excess electron density following switch-off of steady generation. Recombination time 7×10^{-8}s.

In figure 2 we plot on a log - log scale the relation between the time to decay to 50% of the steady state density $\tau_{1/2}$, *vs* the prior steady generation rate G. We choose this definition of initial decay time for convenience. Together with the computed curve, are superimposed the curves obtained using the two intuitive models described in section 1. We also display on the right ordinate axis of the figure an energy scale corresponding to the time scale on the left, using the relation $E(t) = kT\ln(\upsilon t)$.

The results from the simulation show that at low excitation, the decay time is independent of generation rate, and that for G above about 10^{19} cm^{-3}s^{-1}, the decay time follows the relation $\tau_{1/2} \propto G^{-\beta}$, with β = 0.28. Anticipating our analytical result, in this work it was found that under the conditions prevailing the index β = 1-α, giving an analytical value of 0.31, close to that found by simulation. We note that the value predicted by the analyses in earlier work, of $\beta = \gamma = 0.59$, does not hold, although strictly speaking, this applies to the bimolecular case.

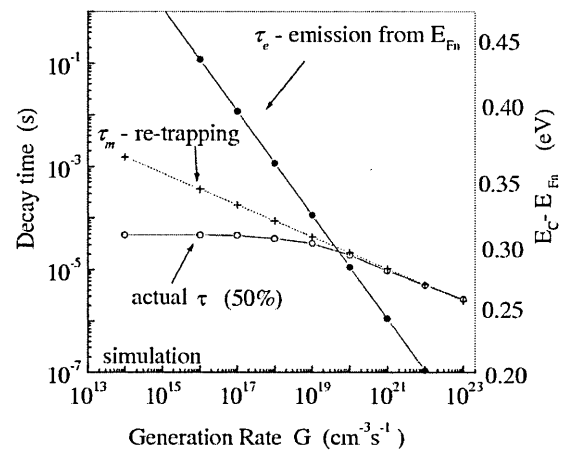

Figure 2. 50% decay time *vs* Generation rate, for computed decays and for two intuitive models.

It is also clear from fig 2 that the predictions of the 'intuitive' models for the decay are not generally in agreement with the simulation. The model which assumes that emission from states at the quasi-Fermi energy controls the decay is clearly invalid over the whole range of G, while the simple multi-trapping model is in agreement at high excitation, but incorrectly predicts a variation of decay time with G at low excitation. The main clue as to what is happening is that the three curves intersect at a single point. The right hand axis indicates an associated energy depth of about 0.3 eV. The significance of this critical energy E_{crit} in the model is that it corresponds to the level in the DOS for which the probability of free electron trapping into any deeper state is just equal to the probability of recombination, i.e

Tenth ISCMP Decay from Steady State Photoconductivity .... C. Main et al. page 5
In "Thin film materials and devices - developments in Science and Technology" eds. JM Marshall, N Kirov, A Vavrek, JM Maud (World Scientific 1999) 191-198.

$$\int_{-\infty}^{E_{crit}} C_n g(E)dE = 1/\tau_R \qquad (3)$$

where C_n is the capture coefficient of the tail states for free electrons, giving, approximately,

$$E_{crit} \approx kT_c \ln(\nu \tau_R/\alpha). \qquad (4)$$

Thus in any given decay, electrons already trapped below E_{crit} will upon release, recombine rather than be re-trapped below E_{crit}. Of course, many trapping and release events will occur for any such released electron, in shallow states prior to eventual recombination, but these transitions are not rate limiting.

Figures 3 and 4 illustrate the consequences of this observation, and help explain the various forms of the decay. Figure 3 shows the time - evolution of the trapped charge distribution during decay after a high steady generation rate $G = 10^{22}$ cm^{-3}s^{-1} which places the quasi-Fermi energy E_{Fn} (in this case equal to the trapped charge quasi-Fermi energy) *above* the critical energy E_{crit}. During the first part of the decay, while the peak of the excess distribution lies above E_{crit}, the decay thus takes place under conditions in which re-trapping is more likely than recombination. The trapped charge packet moves downward without change of form as it is uniformly depleted by recombination loss. Under these conditions, the intuitive 'multi-trapping' concept is actually valid, and the effective instantaneous decay time is determined by Eq. (2) as described in section 1 above, where the trapped charge density n_t is essentially the integrated charge close to the peak of the distribution. The steepness of the decay in this time - region, i.e. $i(t) \propto t^{-1/(1-\alpha)}$ is a consequence of the variation of the 'multiplying' factor n_t/n during the decay.

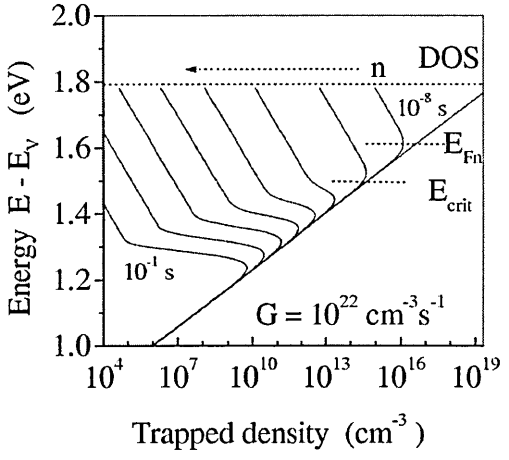

Figure 3. Trapped electron distributions at various times, from 10^{-8}s to 10^{-1}s after switch-off. Generation rate G=10^{22} cm^{-3}s^{-1}

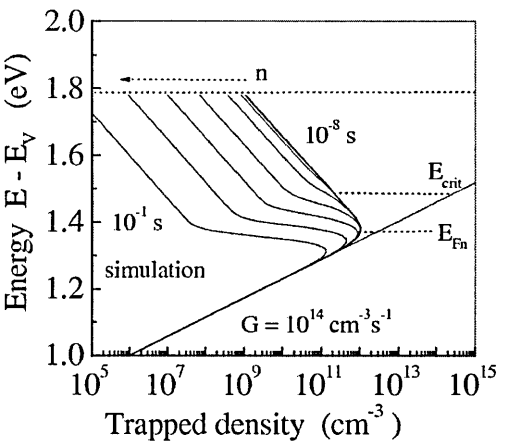

Figure 4. Trapped electron distributions at various times, from 10^{-8}s to 10^{-1}s after switch-off. Generation rate G=10^{14} cm^{-3}s^{-1}

Tenth ISCMP Decay from Steady State Photoconductivity .... C. Main et al. page 6
In "Thin film materials and devices - developments in Science and Technology" eds. JM Marshall, N Kirov, A Vavrek, JM Maud (World Scientific 1999) 191-198.

When the peak of the trapped charge distribution reaches E_{crit}, a qualitative change occurs in the progression of the decay. Now the decay is simply rate limited by emission of trapped charge from states at energy $E_d(t) = kT\ln(\upsilon t)$. This causes the evident 'kink' in the shape of the distribution, a feature which also occurs in the post-transit or post-recombination portions of TOF and TPC respectively, and results in the same power-law decay as seen in these experiments, $i(t) \propto t^{-(1+\alpha)}$.

Figure 4 shows the time-evolution of the trapped charge distribution during decay after a low steady generation rate $G = 10^{14}$ $cm^{-3}s^{-1}$ which places the quasi-Fermi energy E_{Fn} *below* the critical energy E_{crit}. During the first part of the decay, charge is lost uniformly by states down to E_{crit} but *no deeper*. The initial decay time is thus set by the emission time from E_{crit} , and *not* E_{Fn} , accounting for both the faster than expected decay (since E_{crit} lies above E_{Fn}), and the generation rate independence of the decay time in this regime. The decay assumes a shallow power law form $i(t) \propto t^{-\alpha}$ as charge is stripped out in this way in from a trapped distribution which is increasing in density with depth, until the peak of the charge distribution at E_{fn} is reached. At this point, the familiar post-recombination form is observed, and the decay reverts to the form $i(t) \propto t^{-(1+\alpha)}$.

3. Experimental Results and Discussion

In this section we report on experimental photocurrent decay measurements on a-$Si_{1-x}C_x$:H films produced by PECVD deposition at IPE Stuttgart, and fitted with coplanar electrodes. Film thickness was 1 μm, and the gap dimensions were typically 0.5 mm wide and 1 cm long. The material's optical (Tauc) gap is 1.87 eV . Uniform excitation was obtained using a high output red LED emitting at 660 nm (Stanley H3K). Constant current drive was used, employing a dc supply with suitable series resistor. Rapid 'turn-off' was ensured for a wide range of feed resistance by using an FET switch shunting the LED. In this way, the RC time constant for the LED drive current switch-off was kept low, independent of the feed resistance value.

Firstly, from the pre-switch off steady state photocurrent, the steady state power law index γ is found to be 0.9 at room temperature, indicating an approximately constant free electron lifetime, or in terms of the Rose model[6], the quasi Fermi energy is moving through a DOS which is only slowly varying. Figure 5 shows a typical decay from steady state, at 290K, for an incident photon flux of 1.4×10^{17} $cm^{-2}s^{-1}$, giving generation rate G ~ 10^{21} $cm^{-3}s^{-1}$. The decay time for this excitation is seen to be about 10^{-6} s. After a shallow decay section at short times, the long time decay for this excitation, and for a range of values down to ~ 10^{18} $cm^{-3}s^{-1}$ is of power law form, with index $\beta = -0.68$. This is remarkably shallow. In all cases studied above by simulation and analysis, the expected long-time decay in the presence of recombination should be steep - at least t^{-1} in form. We superimpose on the figure, TPC data measured on the same sample. It can be seen that the long time decay is very similar in form to that of the switch-off case. It is usually accepted that in the case of dispersive transport (as observed here) the pre-recombination section of TPC will exhibit a power law

Tenth ISCMP Decay from Steady State Photoconductivity .... C. Main et al. page 7
In "Thin film materials and devices - developments in Science and Technology"
eds. JM Marshall, N Kirov, A Vavrek, JM Maud (World Scientific 1999) 191-198.

slope of less than unity and a post-recombination slope of greater than unity. Since the decay from steady state is supposedly controlled by recombination from the outset, then the similarity between the curves is problematic.

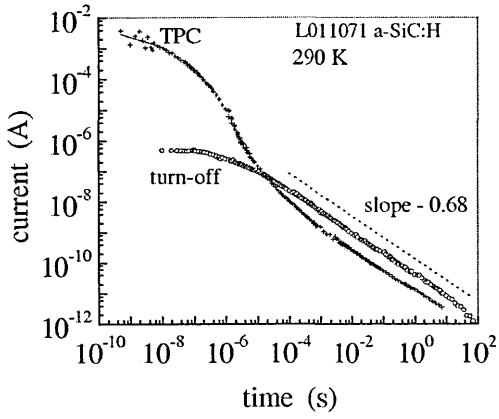

Figure 5. Experimental switch-off and TPC decays in a-$Si_{1-x}C_x$

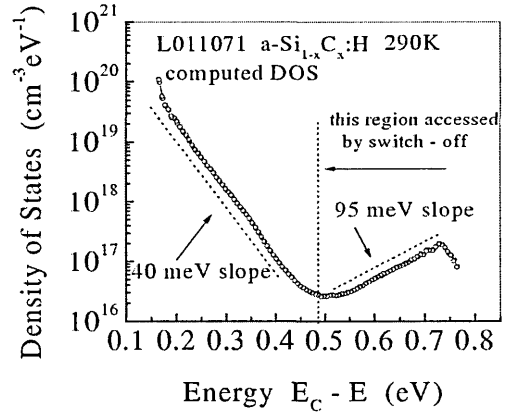

Figure 6. DOS computed for a-$Si_{1-x}C_x$ from TPC data using Fourier Transform method.

One possible explanation for this apparently inconsistent behaviour makes use of the concepts developed above, but with an unexpected 'twist'. We must invoke a *negative effective temperature* to characterise the states in which the excess electrons reside - i.e. the density of states involved must *rise* toward the middle of the gap. This is a quite reasonable assertion, as we will demonstrate. We have shown in earlier work that it is possible, using a Fourier transform technique, to deconvolute TPC data in a model-independent way, to compute the DOS profile[8]. Figure 6 shows the DOS obtained in this way for the silicon carbide film under investigation. It is evident that there is a conduction band tail, exponentially distributed, with characteristic energy 40 meV. However, at energies deeper than 0.47 eV, the DOS *rises* again in a fashion which may be described, in this case, with a single *negative* characteristic energy of about -95 meV (or a deep 'T_{CD}' = -1100K). This deeper part of the DOS is probably associated with dangling bond defects. Whether the distribution levels out, or peaks, nearer the gap centre, is not possible to discern because of the limited time-range of the TPC data.

Applying the appropriate result from the analysis of decay under monomolecular conditions, we obtain, for the long-time decay, a value of dispersion parameter $\alpha = T/T_{CD} = -0.27$, and a power law index $\beta = -(1+\alpha) = -0.73$, which is relatively close to the observed slope of -0.68.

Some justification may be necessary for the above, perhaps unexpected, interpretation. Firstly, we can estimate from the steady state photocurrent that the region of the DOS through which the quasi-Fermi level has been moved, is indeed in the deep section, below 0.47 eV. In this situation, it is likely that the electron lifetime does not vary substantially as the quasi-Fermi energy is moved upward, since it would be moving through a decreasing DOS. Thus we expect to have $\gamma \approx 1$, as observed. Next, during the 'emission-limited' part of the decay when $E_d(t)$ is progressing downward through this same section of the

DOS, as the emission rate decreases with time, the density of trapped charge at $E_d(t)$ is increasing. This accounts for the shallowness of the decay, in accordance with the negative effective dispersion factor. Lastly, we address the question of the similarity between the TPC and decay from steady state, at long times. The question to explain is that in the TPC case, we do not expect that recombination is occurring to any extent during this time range. Instead, since in the TPC case, the states are only part occupied, there is significant deep trapping into states further down than $E_d(t)$ since these are present in higher density than those at $E_d(t)$.

4. Conclusions

We have demonstrated that even in relatively simple model cases, the decay from steady state photoconductivity in amorphous semiconductors can assume a rich variety of forms which are largely determined by the relative probabilities of free carrier *capture* by traps and recombination centres. Computer modelling serves to illustrate clearly the internal processes of such photodecay. Plausible 'intuitive' models for the initial rate of decay, involving e.g. emission from or multi-trapping in states near the Quasi-Fermi energy have been shown to be erroneous or limited in application. Thus use of initial decay measurements to determine carrier mobility is not generally valid. Measurements of the switch off decay and transient photocurrents in a-$Si_{1-x}C_x$:H may be explained in terms of the above, but only by invoking a negative effective characteristic energy for the distribution of the localised states involved.

5. References

[1] G.J.Adriaenssens, S.D.Baranovskii, W.Fuhs, J.Jansen and Ö.Öktü, Phys. Rev B51, 9661, 1995
[2] R.Brüggemann, Solid State Comms. 101, 199, 1997.
[3] H.Cordes, G.H.Bauer and R.Brüggemann, *in press*
[4] P.Popovic, E.Bassanese, F.Smole, J.Furlan, S.Grebner and R.Schwarz, J.Appl. Phys. 82, 4504, 1997
[5] S.M.Ryvkin, *Photoelectric Effects in Semiconductors* (Consultants Bureau New York 1964), ch6.
[6] A.Rose, RCA Rev. 12, 362, 1951.
[7] C.Main, J.Berkin and A.Merazga, in *New Physical Problems in Electronic Materials,* ed M.Borissov,N.Kirov,J.M.Marshall, and A.Vavrek, (World Scientific Press, Singapore, 1991) pp 55-86.
[8] C.Main, in *Amorphous and Microcrystalline Silicon Technology-1997,* ed. M. Hack, E.A. Schiff, S. Wagner, A. Matsuda and R. Schropp, MRS Symp. Proc., Vol 467, (MRS, Pittsburgh 1997) Ch.143, pp.167-178

6. Acknowledgements

The authors thank H-D Mohring, IPE Stuttgart, for sample preparation, the British Council and DAAD for support under the British - German ARC scheme, and the University of Abertay Dundee for a postgraduate studentship.

Co-author of a paper presented in J. App. Phys., 1999

C. Main, J.-H. Zollondz, S. Reynolds, W. Gao, M.J. Rose,

Investigation of collection efficiencies much larger than unity in a-Si:H p-i-n structures,

J. Appl. Phys., Vol. 85, pp. 296-301, 1999.

Paper presented at the MRS spring meeting, San Francisco, 1999:

J.-H. Zollondz, C. Main, S. Reynolds,
Collection efficiencies greater than unity by electron gating or hole gating in a-Si:H p-i-n diodes, published in Amorphous and Heterogeneous Silicon Thin Films; Fundamentals to Devices - 1999, ed. H. W. Branz, R. W. Collins, H. Okamoto, S. Guha and R. Schropp, MRS Symposium Proceedings, (MRS Warrendale Pa. USA 1999), Vol 557, pp. 475-480, 1999.

COLLECTION EFFICIENCIES GREATER THAN UNITY BY ELECTRON OR HOLE GATING IN a-Si:H p-i-n DIODES

J.-H. ZOLLONDZ, C. MAIN, S. REYNOLDS
School of Science and Engineering, University of Abertay Dundee, Dundee DD1 1HG, UK,
phrhz@tay.ac.uk

ABSTRACT

We report measured electron and hole gating in thick a-Si:H (3.5 μm) p-i-n diodes under reverse bias conditions. Previous publications have shown very high collection efficiency values for electron gating (p-side bias, n-side probe) of up to 50 (i.e. 5000%) for measured and simulated data and predictions of up to 400 (i.e. 40000%) from simulations. Reversing the usual sides of illumination for (electron) gating a situation can be created where, by n-side bias and p-side probe illumination, holes can be gated to travel through the sample to be collected at the contact. Even though the holes have much lower mobility, by this process we can still obtain collection efficiencies greater than unity. This measurement is more difficult because of unwanted illumination by stray bias beam photons on the more sensitive p-side, caused by reflections within the apparatus. Simulation of this situation corroborates qualitatively the measured data. A wide ranging study of the gating phenomenon in relation to different incident wavelengths and photon fluxes for bias and probe beam is reported. We present comparisons of electron and hole gating by measurement and simulation and explain the phenomenon for both electron and hole gating in terms of field changes near to the incident bias interface.

INTRODUCTION

Collection efficiencies or quantum efficiencies (QE) greater than unity have been reported by a number of groups [1-6], including our own. Electron photogating is the explanation for such a phenomenon. An external 'gain' results from internal field changes produced when a low level probe beam is applied in the presence of a much larger bias beam (< 1:100).

Hou and Fonash [1], and Rubinelli [2], explained the electron photogating phenomenon as follows. Strongly absorbed bias light creates a low-field region in the front of the i-layer, near the p-i interface, while increasing the field in the remainder of the i-layer. Additional illumination with a weakly absorbed probe beam generates holes throughout the sample. Trapping of these holes results in a field increase in the front low field region. This increase of the internal electric field in a region of high absorption of the bias beam results in a higher collection of the photocarriers generated by the bias beam.

In contrast to much earlier work we use a combination of reverse bias and steady state measurement. We illuminate first by the bias beam only and take a steady state measurement after the current is settled. Then we add the probe beam and measure the current again after it is settled. We observed long settling times (of the order of seconds) for both measurements, especially for the high collection efficiency situations. In this case, a steady state measurement is more appropriate than using a chopped beam and lock-in technique which gives lower collection efficiency values.

EXPERIMENTAL SETUP AND DEFINITIONS

In this work we measured and simulated the photocurrent response of thick (3.5μm) a-Si:H p-i-n diodes under various illumination situations with a two beam steady state experiment. As bias beam source we used high power LEDs, which can reach photon fluxes up to 3×10^{16} cm^{-2} s^{-1} with typical FWHM of 10 – 20 nm. The probe beam was produced by a halogen lamp, *via* a double monochromator. The bias wavelength was 450 nm and the photon flux was of the order of 1×10^{16} cm^{-2} s^{-1} in the cases where it was required to be constant. For the probe beam we used a wavelength of 622 nm and a photon flux of the order of 1×10^{12} cm^{-2} s^{-1} when the probe beam was required to be constant. A steady state measurement technique was chosen, because the response time of the sample was very slow (of the order of seconds).

The probe collection efficiency is determined as

$$QE = \frac{j_{ph}(\Phi_p + \Phi_b) - j_{ph}(\Phi_b)}{e\Phi_p} \qquad (1)$$

where $j_{ph}(\Phi_p+\Phi_b)$ is the photocurrent under probe and bias illumination with the photon flux Φ_p and Φ_b respectively. Note that the maximum value for QE should not exceed 1 if all and only probe light generated carriers are collected.

EXPERIMENTAL AND SIMULATED RESULTS

The measurements on degradation effects are made on a 3.5 μm p-i-n a-Si:H sample with 200Å p- and n-layers. The optical transmission of the Cr-contacts in the visible range of the spectrum was measured as ~30%. All other measurements were undertaken on a 3.5 μm thick a-Si:H p-i-n diode with ITO contacts with typical transmissions of 90% and comparable doped layer thicknesses.

Electron gating

We use the term electron gating for the case where electrons, if released at the field

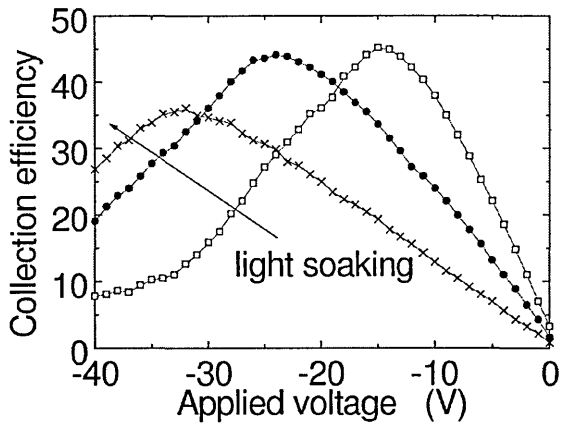

Figure 1: Experimentally determined collection efficiencies *vs* applied reverse bias, after successive AM1 light soak exposures.

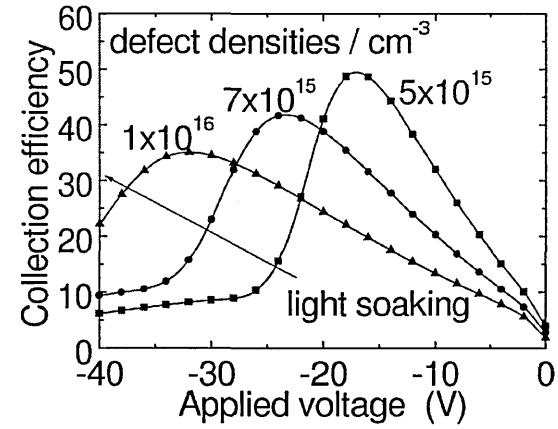

Figure 2: Numerically modelled QE *vs* reverse bias; illumination conditions equivalent to those used experimentally (Fig. 1).

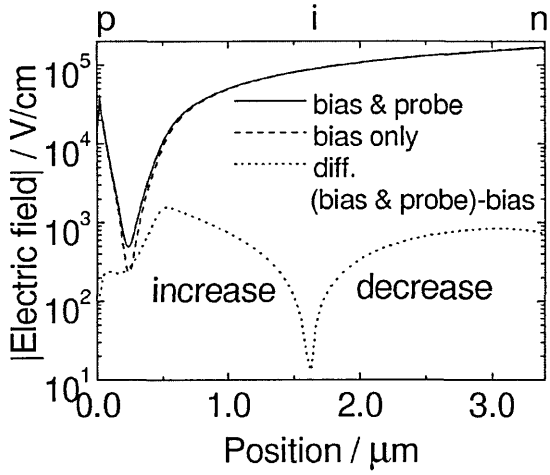

Figure 3: The effect of the addition of probe illumination on the internal electric field at -28 V reverse voltage. One of the curves is the *change* in field on application of probe illumination.

minimum near the p-i interface must travel to the n-contact to be collected (reverse bias). This is the case where the strongly absorbed bias beam is incident through the p-side contact while the probe beam is incident through the n-side.

Figures 1 and 2 show measured and simulated data of collection efficiency values *vs* applied bias voltage after different light soaking times [4] for electron gating. For this experiment and simulation the wavelength of the bias beam and probe beam were 430 nm and 622 nm respectively. The peak observed in the collection efficiency response shifts to higher voltages for longer light soaking times, and hence higher defect densities. Comparison with simulated data shows that even a small change in the defect densities $\approx 2\times10^{15}$ cm^{-3} gives a big shift in the position of the maximum (~10 V shift) and a clear decrease of the maximum (~10%). This measurement is thus a sensitive indicator of defect density variation as a p-i-n device is progressively degraded.

To explain the phenomenon, we make use of Figure 3 which shows the internal electric field distribution. The dashed line represents the electric field at –28 V, with bias illumination only. Such a field minimum occurs for illumination with a steep absorption profile. Additional n-side probe illumination (solid line) results in a field increase near the p-i interface while a decrease over the rest of the sample is found. The maximum relative field change is in the region of the field minimum. Because generation of the charge carriers by the bias beam is high in this region, more are now collected. Because the photon flux of the bias beam is higher than the probe flux by orders of magnitude, collection efficiency values of up to 140 (14000%) can be measured and explained. Collection efficiencies higher than unity can be alternatively viewed as resulting from changes in recombination rates [6].

Figure 4 shows *measured* collection efficiencies for varying photon fluxes of the bias beam. For bias beam photon flux values of 1×10^{12} $cm^{-2}s^{-1}$ the collection efficiency values never exceed 1. Even for 1×10^{14} $cm^{-2}s^{-1}$ the collection efficiency values only exceed 100% for low reverse voltages and by a small margin. Increasing the flux, i.e. increasing the difference between probe and bias beam, results in high collection efficiency values, up to 140 (14000%)

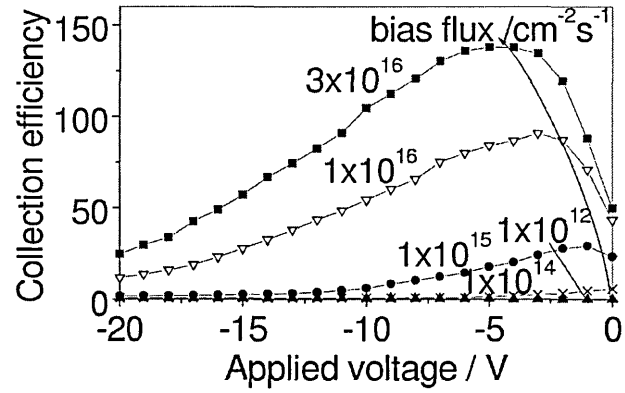

Figure 4: Experimentally determined collection efficiencies *vs* applied reverse bias. The bias beam flux is varied while the probe beam flux is held constant at 1×10^{12} cm^{-2} s^{-1}.

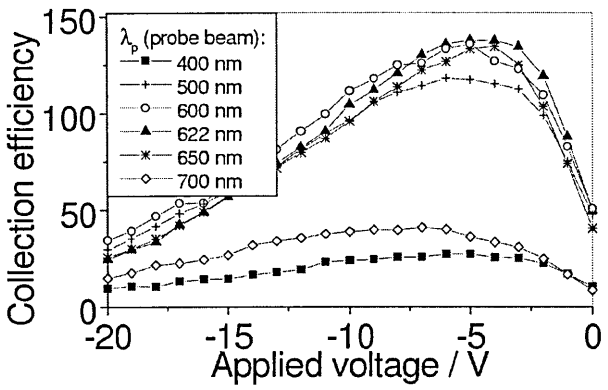

Figure 5: QE *vs* reverse bias for varied probe wavelengths ($\Phi_p = 1\times10^{12}$ cm^{-2} s^{-1}) and blue bias illumination conditions (λ_b = 470 nm, Φ_b = 3×10^{16} cm^{-2} s^{-1}).

for the maximum bias photon flux of 3×10^{16} cm^{-2}s^{-1}.

Note that these very high values were taken with a steady state measurement, in contrast to lower values obtained by ac methods by other groups.

Results of variation of the probe *wavelength* while keeping the bias wavelength constant at 450 nm and constant photon fluxes of 3×10^{16} cm^{-2}s^{-1} for bias and 1×10^{12} cm^{-2}s^{-1} for probe illumination are shown in Figure 5. Different probe wavelengths produce different changes in the field minimum formed by the bias beam. However the result of this modification of the internal electric field in the region of the field minimum seems to be quite similar for probe beam wavelengths between 500 nm and 650 nm. For 400 nm and 700 nm, collection is far lower, but still higher than unity. For a probe beam of 700 nm the collection efficiency is lower because the absorption depth $1/\alpha$ is approximately of the order of the sample thickness so that the change in the field minimum is not as big as for lower wavelengths. If the incident probe wavelength is 400 nm, which is highly absorbed, this results in losses in the n-doped layer and in a secondary field change far from the "main" field minimum. A lower collection of gated carriers results.

Variation of the bias beam wavelength results in a very different picture. In Fig. 6 the measured data are shown. Here the probe wavelength was kept at 622 nm and a photon flux of 1×10^{12} cm^{-2}s^{-1} while the bias photon flux was 1×10^{16} cm^{-2}s^{-1} for each wavelength used. As long as a significant field minimum can be expected (from 470 nm – 525 nm wavelength) a high gating value is measured. Decreasing maxima for decreasing wavelength are found because the field minimum widens and shifts deeper in the i-layer for illumination at lower wavelength as the absorption is less for these wavelengths. This results in a relatively lower release of gated photo carriers. For wavelengths of 590 nm and 612 nm the minimum widens further, until for 660 nm there is no field minimum evident. Over this range, collection of gated photo carriers decreases to zero.

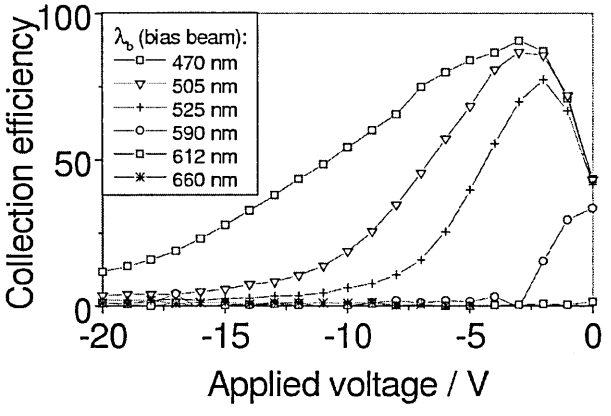

Figure 6: QE *vs* reverse bias for varied bias wavelengths ($\Phi_b = 1\times10^{16}$ cm^{-2} s^{-1}) and red probe illumination conditions (λ_p = 622 nm, $\Phi_p = 1\times10^{12}$ cm^{-2} s^{-1}).

Hole gating

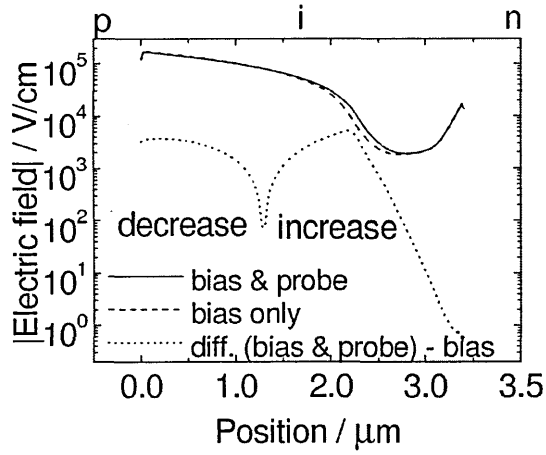

Figure 7: QE *vs* reverse bias obtained by numerical modelling for red probe and blue bias illumination conditions equivalent (reversed) to those in Fig.3.

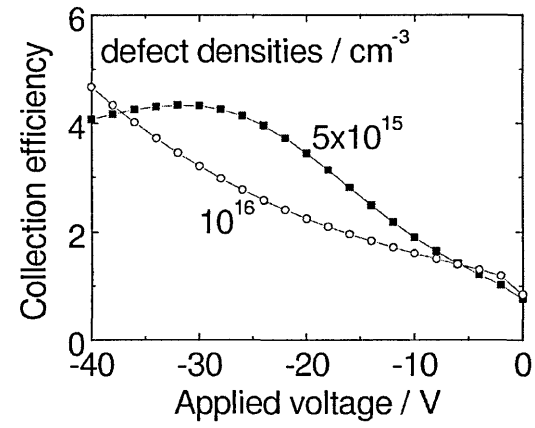

Figure 8: QE *vs* reverse bias obtained by numerical modelling for red probe and blue bias illumination conditions equivalent to those in Fig.2.

We now examine the case of inverting the experiment for electron gating (with p-sided bias and n-sided probe illumination) to n-sided bias and p-sided probe illumination, which results in a field minimum next to the n-layer. Similarly to the electron gating situation an increase in the internal electric field minimum is the reason for a gating effect. Figure 7 shows that this minimum is broader than its analogue for electron gating and deeper in the i-layer for the same simulation parameters as for Fig. 2 but with reversed illumination sides for bias and probe beams.

We call this process *hole gating* because under reverse bias voltage when photocarriers from the region of this minimum are released, holes have a longer way to be collected at the p-contact, just as electrons drift through nearly the full i-layer in electron gating.

Figure 8 shows simulated collection efficiencies for the hole gating experiment. This results in a maximum at high reverse voltages. The results look similar to those of electron gating for a fairly degraded sample but the QE values are far lower. The simulated data do match the measured data in form (see Fig. 9) for the same input parameters as for Fig. 2, but we could not fit the simulated results quantitatively to get the same peak values as measured. The reason for that could be that variation of the defect density with a uniform profile does not reflect the real defect density distribution in the sample. Degradation for a sample of 3.5 µm will happen in the layers near the doped areas.

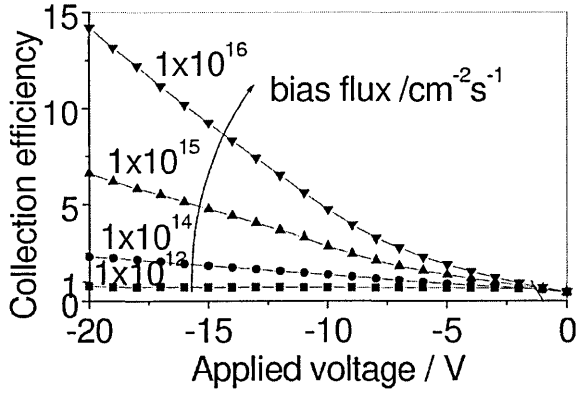

Figure 9: QE *vs* reverse bias obtained by numerical modelling for red probe and blue bias illumination conditions equivalent to those in Fig. 3.

Figure 9 shows similar results as in Fig. 4: collection is far higher for higher

bias photon fluxes while keeping the probe photon flux at 1×10^{12} $cm^{-2}s^{-1}$. For a low ratio between bias and probe photon flux a small effect is observed. For a probe flux equal to the bias photon flux the collection efficiency values never exceed 1, i.e. no gating is observed.

In Fig. 10 hole gating collection efficiency values *vs* reverse bias voltage are shown. As in Fig. 6 the probe wavelength was kept at 622 nm with a photon flux of 1×10^{12} $cm^{-2}s^{-1}$ while the bias photon flux was 1×10^{16} $cm^{-2}s^{-1}$ and the bias wavelength was varied.

This variation of the bias wavelength results in a wide spread in the response for the collection efficiency values: lowest collection efficiencies for a red bias beam up to highest values for a blue bias beam. Again the gating effect is observed for those wavelengths that form a clear field minimum. For 660 nm bias beam wavelength, where no electric field minimum can be expected, the collection efficiency never exceeds unity.

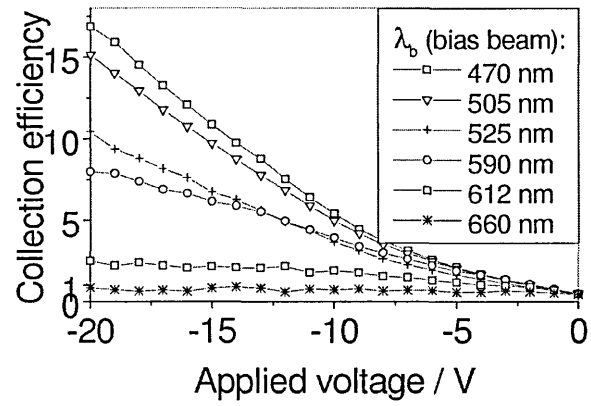

Figure 10: QE *vs* reverse bias for varied bias wavelengths (Φ_b = 1×10^{16} cm^{-2} s^{-1}) and red probe illumination conditions (λ_p = 622 nm, Φ_p = 1×10^{12} cm^{-2} s^{-1}, p-side).

CONCLUSIONS

Under a reverse bias voltage situation and bias beam illumination, probe beam collection efficiencies greater that unity for electrons or holes can be achieved. This photogating effect can reach gain values up to 140 for electron gating in thick a-Si:H p-i-n samples, which are the highest measured values so far to our knowledge. We achieved this by taking long relaxation times into account, using a steady state technique instead of the previously reported lock-in methods. The photogating effect is very sensitive to variations in defect density and provides a high resolution diagnostic tool to investigate degradation or quality of a p-i-n diode. Variation of the wavelength of the probe and bias beam give an understanding of field dependent processes involved in the gating effect.

ACKNOWLEDGMENTS

The authors acknowledge funding from the British Council and DAAD via an ARC collaboration. One of the authors (J.-H. Zollondz) is grateful to the University of Abertay Dundee for the provision of a research studentship.

REFERENCES

1. J. Hou and S. J. Fonash, Appl. Phys. Lett. **61**, 186 (1992).
2. A. Rubinelli, J. Appl. Phys. **75**, 998 (1994).
3. P. Chatterjee, J. Appl. Phys. **75**, 1093 (1994).
4. J.-H. Zollondz, W. Gao, R. Brüggemann, C. Main, and G. H. Bauer (Mater. Res. Soc. Proc. **420**, Pittsburgh, PA 1996) p. 251-256.
5. R. Brüggemann, J.-H. Zollondz, C. Main, and W. Gao (Mater. Res. Soc. Proc. **467**, Pittsburgh, PA 1997) p. 759-764.
6. C. Main, J.-H. Zollondz, S.Reynolds, W. Gao, R. Brüggemann, and M. J. Rose, J. Appl. Phys. **85**, p. 296-301 (1999).

Co-author of a paper presented at the MRS spring meeting, San Francisco, 1999:

C. Main , S. Reynolds, J.H. Zollondz, R. Brüggemann,
Photoconductivity transient response from the steady state in amorphous semiconductors, published in Amorphous and Heterogeneous Silicon Thin Films; Fundamentals to Devices - 1999, ed. H. W. Branz, R. W. Collins, H. Okamoto, S. Guha and R. Schropp, MRS Symposium Proceedings, (MRS Warrendale Pa. USA 1999), Vol 557, pp. 421-426, 1999.

MRS Symp. Proc. 557, 1999, 421 - 426

PHOTOCONDUCTIVITY TRANSIENT RESPONSE FROM THE STEADY STATE IN AMORPHOUS SEMICONDUCTORS

C. MAIN*, S. REYNOLDS*, J.- H. ZOLLONDZ* and R. BRÜGGEMANN**
*School of Science and Engineering, University of Abertay Dundee, Dundee DD1 1HG, Scotland, UK, c.main@tay.ac.uk
**F.B. Physik, Carl von Ossietzky Universität Oldenburg, D-26111 Oldenburg, Germany

ABSTRACT

We present analysis, computer modelling and experimental measurements of the photoconductive decay which occurs on cessation of illumination, in amorphous semiconductors. We explore the processes of relaxation of the excess carrier distributions, and examine the relative rôles of re-trapping and recombination in a model case of an exponential trapping state profile, with monomolecular recombination. A variety of possible decay behaviour is revealed. We examine several plausible intuitive explanations of the decay process, including (a) the assumption that the rate limiting step in the decay process is the thermal release of trapped carriers from the vicinity of the quasi - Fermi level, and (b) multiple re-trapping at the quasi - Fermi level prior to recombination. Actual decay rates, however are often much faster than that predicted by these assumptions, and the generation rate dependencies do not follow the relation expected. These explanations are shown in detail to be largely erroneous. Results of experimental measurements of the decay from steady state and TPC in films of a-$Si_{1-x}C_x$:H are presented. While these appear initially to be at variance with the predictions of the present work, we demonstrate that the observations can be reconciled fully with theory.

INTRODUCTION

Recent publications[1-4], have reported on the decay of photocurrent from the steady state in amorphous semiconductors, after steady illumination has been switched off. Analysis of this situation has been the subject of numerous works dating back at least to the classic work of Ryvkin[5] and Rose[6] in the 1950s and 60s. More commonly, studies on amorphous semiconductors have concentrated on the photocurrent response to *impulse* optical excitation, i.e. the transient photocurrent experiment (TPC). In this experiment, an excess carrier density ΔN is created by a short pulse of uniformly absorbed light in a semiconductor sample with coplanar ohmic contacts, and the subsequent decay of the photocurrent is followed. Under these conditions, with the *proviso* that recombination is not significant, the instantaneous photocurrent is also a measure of the instantaneous mobility of the *ensemble* of ΔN excess carriers.

In the switch-off experiment, in contrast to TPC, conditions just prior to cessation of illumination are dominated by *recombination* - *viz* the steady state excess electron density is given by $dn = G\tau_R$ where τ_R is the recombination lifetime. This lifetime may be a constant, in the case of monomolecular recombination, or may be dependent on the generation rate G. We might be led to assume that recombination should play an important part in the switch-off photocurrent decay *from the outset*, in contrast to the TPC experiment. However, since high densities of traps exist in amorphous semiconductors, it is not expected that the initial decay time τ_i of photocurrent should reflect *directly* the recombination time for free electrons, since excess carriers will interact with traps, slowing down the response. All of the above implies that interpretation of switch-off decay could be much more difficult than for TPC.

The first of the "intuitive" models we present asserts that the initial decay of the whole excess is determined by the rate at which electrons trapped in states at the quasi-Fermi energy are

MRS Symp. Proc. 557, 1999, 421 - 426

released thermally to the conduction band prior to recombining. The rate limiting step, and hence the observed decay time, is then just the thermal release time τ_e of electrons at the quasi Fermi energy, E_{Fn}, *viz:*

$$\tau_e = \upsilon^{-1}\exp\left(E_{Fn}/kT\right) = \tau_i . \tag{1}$$

The second "intuitive" model contends that for any free electron, *multiple trapping* occurs in states close to the quasi-Fermi energy prior to the electron finally recombining. In this case, for every free electron recombining, there will be renewal from the reservoir of trapped electrons, most of which are close to E_{Fn}. The observed initial decay time is then given by

$$\tau_m = \frac{\tau_e + \tau_t}{\tau_t} \times \tau_R \approx \frac{n_t}{n} \times \tau_R \approx \tau_i \ , \tag{2}$$

where n and n_t are the free and trapped electron densities, and τ_t ($<< \tau_e$) is the trapping time into states close to the quasi Fermi energy.

It is evident that while the above arguments may seem plausible, they do not agree in detail. We will demonstrate the inadequacies of each approach below, by numerical modelling which also provides a framework of insight for more appropriate approximate analytical treatments, results of which are presented below. Following this, we then direct attention to measurements of the photocurrent decay from steady state in thin film specimens of the amorphous alloy a-$Si_{1-x}C_x$:H, to apply the insights gained from simulation.

COMPUTER MODELLING: RESULTS AND DISCUSSION

The fate of both free and trapped charge following switch-off or an impulse excitation, may be visualised using a numerical solution scheme has been developed by the authors[7] In this section, we present the results of a computer simulation of the decay from steady state in a deceptively simple system consisting of an exponential band tail and a fixed recombination time for free electrons. These are used to support simple analytical expressions for the decay under different conditions. The parameters employed are listed below.

Band edge density of states	$g(E_C)$	4×10^{21} cm^{-3} eV^{-1}
Characteristic temp. - band tail	T_C	290 K
Attempt-to-escape frequency	ν	1×10^{12} s^{-1}
Free electron recombination time	τ_R	6.9×10^{-8} s
Temperature	T	200 K

These parameters thus give $\alpha = \frac{T}{T_c} = 0.69$.

Figure 1 shows the decay curves of free electron density after steady volume generation rate G ranging from 10^{14} to 10^{22} cm^{-3}s^{-1}. It is clear that there are several well-defined regions in which power-law decay occurs. These are classified below, and the indices are compared with the approximate analytical expressions obtained in this work.

MRS Symp. Proc. 557, 1999, 421 - 426

		index	analytical index
Low excitation ($G < 10^{16}$ cm^{-3}s^{-1})	short times	- 0.7	$-\alpha$ = - 0.69
	long times	- 1.7	$-(1+\alpha)$ = - 1.69
High excitation ($G > 10^{20}$ cm^{-3}s^{-1})	short times	- 3.0	$-1/(1-\alpha)$ = - 3.22
	long times	- 1.7	$-(1+\alpha)$ = - 1.69

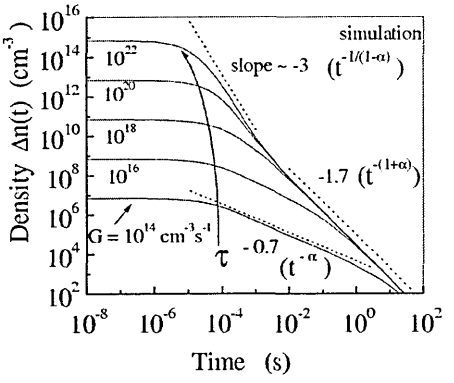

Figure 1. Simulated decay of excess electron density following switch-off of steady generation. Recombination time 7×10^{-8}s.

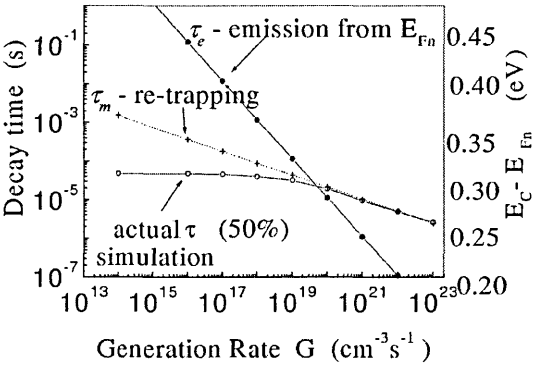

Figure 2. 50% decay time *vs* Generation rate, for computed decays and for two intuitive models.

In figure 2 we plot on a log -log scale the relation between the time to decay to 50% of the steady state density $\tau_{1/2}$, *vs* the prior steady generation rate G. With the computed curve we superimpose curves obtained using the two intuitive models described in section 1. We also display on the right ordinate axis of the figure an energy scale corresponding to the time scale on the left, using the relation $E(t) = kT\ln(\upsilon t)$. The results from the simulation show that at low excitation, the decay time is independent of generation rate, and that for G above about 10^{19} cm^{-3}s^{-1}, the decay time follows the relation $\tau_{1/2} \propto G^{-\beta}$, with $\beta = 0.28$. In this work it was found by analysis that under the conditions prevailing the index $\beta = 1-\alpha$, giving a value of 0.31, close to that found by simulation. We note that the value predicted by earlier analyses, of $\beta = \gamma = 0.59$, does not hold.

It is also clear from fig 2 that the 'intuitive' models for the decay are not in agreement with the simulation. The model which assumes that emission from states at the quasi-Fermi energy controls the decay is invalid over the whole range of G, while the simple multi-trapping model is in agreement at high excitation, but incorrectly predicts a variation of decay time with G at low excitation. It is significant that the three curves intersect at a single point, with an associated energy of about 0.3 eV. This "critical" energy E_{crit} corresponds to the level in the DOS for which the probability of free electron trapping into deeper states is equal to the probability of recombination, i.e

$$\int_{-\infty}^{E_{crit}} C_n g(E)dE = 1/\tau_R , \tag{3}$$

where C_n is the capture coefficient of the tail states for free electrons, giving, approximately,

$$E_{crit} \approx kT_c \ln(\nu\tau_R/\alpha). \tag{4}$$

MRS Symp. Proc. 557, 1999, 421 - 426

Thus in any given decay, electrons already trapped below E_{crit} will upon release, recombine rather than be re-trapped below E_{crit}. Of course, many trapping and release events will occur for any such released electron, in shallow states prior to eventual recombination, but these transitions are not rate limiting.

Figures 3 and 4 illustrate the consequences of this observation, and help explain the various forms of the decay. Figure 3 shows the time - evolution of the trapped charge distribution during decay after a high steady generation rate $G = 10^{22}$ cm^{-3}s^{-1} which places the quasi-Fermi energy E_{Fn} (in this case equal to the trapped charge quasi-Fermi energy) *above* the critical energy E_{crit}. During the first part of the decay, while the peak of the excess distribution lies above E_{crit},

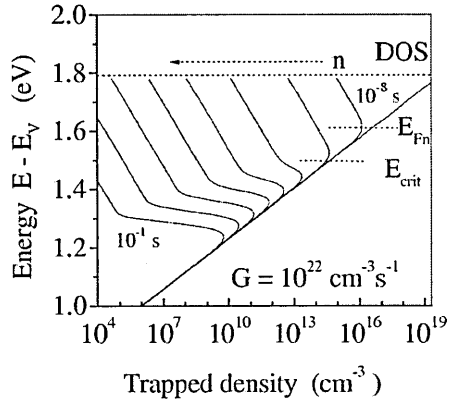

Figure 3. Trapped electron distributions at various times, from 10^{-8}s to 10^{-1}s after switch-off. Generation rate G=10^{22} cm^{-3}s^{-1}

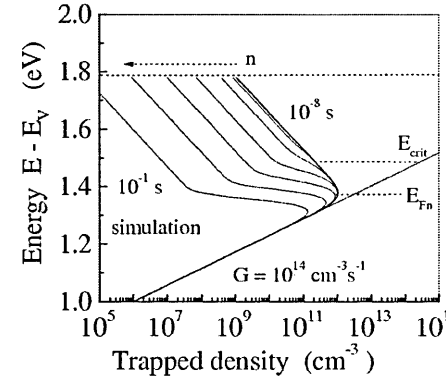

Figure 4. Trapped electron distributions at various times, from 10^{-8}s to 10^{-1}s after switch-off. Generation rate G=10^{14} cm^{-3}s^{-1}

the decay thus takes place under conditions in which re-trapping is more likely than recombination. The trapped charge packet moves downward without change of form as it is uniformly depleted by recombination loss. Under these conditions, the intuitive 'multi-trapping' concept is actually valid, and the effective instantaneous decay time is determined by Eq. (2) as described in section 1 above, where the trapped charge density n_t is essentially the integrated charge close to the peak of the distribution. The steepness of the decay in this time - region, i.e. $i(t) \propto t^{-1/(1-\alpha)}$ is a consequence of the variation of the 'multiplying' factor n_t/n during the decay.

When the peak of the trapped charge distribution reaches E_{crit}, a qualitative change occurs in the progression of the decay. Now the decay is simply rate limited by emission of trapped charge from states at energy $E_d(t) = kT\ln(\upsilon t)$. This causes the 'kink' in the shape of the distribution, a feature which also occurs in the post-transit or post- recombination portions of TOF and TPC respectively, and results in the same power-law decay as seen in these experiments, $i(t) \propto t^{-(1+\alpha)}$.

Figure 4 shows the time-evolution of the trapped charge distribution during decay after a low steady generation rate $G = 10^{14}$ cm^{-3}s^{-1} which places the quasi-Fermi energy E_{Fn} *below* the critical energy E_{crit}. During the first part of the decay, charge is lost uniformly by states down to E_{crit} but *no deeper*. The initial decay time is thus set by the emission time from E_{crit} , and *not* E_{Fn}, accounting for both the faster than expected decay (since E_{crit} lies above E_{Fn}), and the generation rate independence of the decay time in this regime. The decay assumes a shallow power law form $i(t) \propto t^{-\alpha}$ as charge is stripped out in this way from a trapped distribution which is increasing in

MRS Symp. Proc. 557, 1999, 421 - 426

density with depth, until the peak of the charge distribution at E_{Fn} is reached. At this point, the familiar post-recombination form is observed, and the decay reverts to the form $i(t) \propto t^{-(1+\alpha)}$.

EXPERIMENTAL RESULTS AND DISCUSSION

In this section we report on experimental photocurrent decay measurements on a-$Si_{1-x}C_x$:H films produced by PECVD deposition at IPE Stuttgart, and fitted with coplanar electrodes. Film thickness was 1 μm, and the gap dimensions were typically 0.5 mm wide and 1 cm long. The material's optical (Tauc) gap is 1.87 eV . Uniform excitation was obtained using a high output red LED emitting at 660 nm (Stanley H3K). Constant current drive was used, employing a dc supply with suitable series resistor. Rapid 'turn-off' was ensured for a wide range of feed resistance by using an FET switch shunting the LED. In this way, the RC time constant for the LED drive current switch-off was kept low, independent of the feed resistance value.

Firstly, from the pre switch-off steady state photocurrent, the steady state power law index $\gamma$is found to be 0.9 at room temperature, indicating an approximately constant free electron lifetime[6]. Figure 5 shows a typical decay from steady state, at 290K, for an incident photon flux of 1.4×10^{17} $cm^{-2}s^{-1}$, giving generation rate G ~ 10^{21} $cm^{-3}s^{-1}$. The decay time for this excitation is seen to be about 10^{-6} s. After a shallow decay section at short times, the long time decay for this excitation, and for a range of values down to ~ 10^{18} $cm^{-3}s^{-1}$ is of power law form, with index β = -0.68. This is remarkably shallow. In all cases studied above by simulation and analysis, the expected long-time decay in the presence of recombination should be steep - at least t^{-1} in form. We superimpose on the figure, TPC data measured on the same sample. It can be seen that the long time decay is very similar in form to that of the switch-off case. It is usually accepted that in the case of dispersive transport (as observed here) the pre-recombination section of TPC will exhibit a power law slope of less than unity and a post-recombination slope of greater than unity. Since the decay from steady state is supposedly controlled by recombination from the outset, then the similarity between the curves is problematic.

One explanation for this apparently inconsistent behaviour makes use of the concepts developed above, but with an unexpected 'twist'. We must invoke a *negative effective*

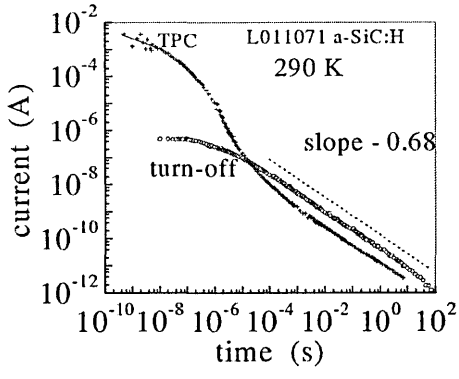

Figure 5. Experimental switch-off and TPC decays in a-$Si_{1-x}C_x$

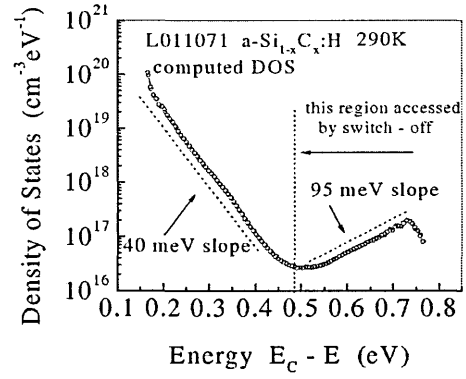

Figure 6. DOS computed for a-$Si_{1-x}C_x$ from TPC data using Fourier Transform method.

MRS Symp. Proc. 557, 1999, 421 - 426

temperature to characterise the states in which the excess electrons reside - i.e. the density of states involved must *rise* toward the middle of the gap. We have shown that a Fourier transform technique can be used to compute the DOS profile from TPC[8]. Figure 6 shows the DOS obtained in this way for the silicon carbide film. There is an exponential conduction band tail, with characteristic energy 40 meV. At energies deeper than 0.47 eV, the DOS *rises* again in a fashion which may be described, in this case, with a single *negative* characteristic energy of about -95 meV (or a deep 'T_{CD}' = -1100K). This deeper part of the DOS is probably associated with dangling bond defects. Applying the appropriate result from the analysis of decay under monomolecular conditions, we obtain, for the long-time decay, a value of dispersion parameter $\alpha = T/T_{CD} = -0.27$, with index $\beta = -(1+\alpha) = -0.73$, close to the observed slope of -0.68.

CONCLUSIONS

We have shown that even in relatively simple model cases, the decay from steady state photoconductivity in amorphous semiconductors can assume a variety of forms which are determined by the relative probabilities of free carrier *capture* by traps and recombination centres. Computer modelling illustrates clearly the internal processes of such photodecay. Plausible 'intuitive' models for the initial rate of decay have been shown to be erroneous or limited in application. Measurements of the switch off decay and transient photocurrents in a-$Si_{1-x}C_x$:H may be explained in terms of the above, by invoking a negative effective characteristic energy for the distribution of the localised states.

ACKNOWLEDGEMENTS

The authors acknowledge support from EPSRC Research Grant GR/M16696. We thank H-D Mohring, IPE Stuttgart, for sample preparation, the British Council and DAAD for support under the British - German ARC scheme, the University of Abertay Dundee for a postgraduate studentship.

REFERENCES

[1] G.J.Adriaenssens, S.D.Baranovskii, W.Fuhs, J.Jansen and Ö.Öktü, Phys. Rev B51, 9661, 1995.

[2] R.Brüggemann, Solid State Comms. 101, 199, 1997.

[3] H.Cordes, G.H.Bauer and R.Brüggemann, Phys. Rev. B58, 16160, 1998.

[4] P.Popovic, E.Bassanese, F.Smole, J.Furlan, S.Grebner and R.Schwarz, J.Appl. Phys. 82, 4504, 1997.

[5] S.M.Ryvkin, *Photoelectric Effects in Semiconductors* (Consultants Bureau New York 1964), ch6.

[6] A.Rose, RCA Rev. 12, 362, 1951.

[7] C.Main, J.Berkin and A.Merazga, in *New Physical Problems in Electronic Materials,* ed M.Borissov,N.Kirov,J.M.Marshall, and A.Vavrek, (World Scientific Press, Singapore, 1991) pp 55-86.

[8] C.Main, in *Amorphous and Microcrystalline Silicon Technology-1997,* ed. M. Hack, E.A. Schiff, S. Wagner, A. Matsuda and R. Schropp, MRS Symp. Proc., Vol 467, (MRS, Pittsburgh 1997) Ch.143, pp.167-178.

Abstract of a talk held at the Chelsea Meeting on Amorphous and Organic Semiconductors, London, 1999:

J.-H. Zollondz, C. Main, S. Reynolds,
Electron- and hole- gating: collection efficiencies greater than unity in a-Si:H p-i-n diodes

ELECTRON- AND HOLE-GATING: COLLECTION EFFICIENCIES GREATER THAN UNITY IN a-Si:H p-i-n DIODES

J.-H. ZOLLONDZ, C. MAIN, S. REYNOLDS,
School of Science and Engineering
Univ. of Abertay Dundee

We report measured 'hole gating' in thick a-Si:H (3.5 μm) p-i-n diodes under reverse bias conditions. In previous publications we have described very high collection efficiency values for *electron* gating (p-side bias, n-side probe) of up to 50 (i.e. 5000%) for measured and simulated data and predictions of up to 400 (i.e. 40000%) from simulations. Reversing the usual sides of illumination for (electron) gating a situation can be created where, by n-side bias and p-side probe illumination, holes can be gated to travel through the sample to be collected at the contact. Even though the holes have much lower mobility, in this situation we have still observed collection efficiencies greater than unity. Moreover, the measurement is made difficult because of sensitivity to unwanted illumination by stray bias beam photons on the more sensitive p-side, caused by reflections within the apparatus. Simulation of this situation again corroborates the measured data. A wide ranging study of the gating phenomenon in relation to different incident wavelengths and photon fluxes for bias and probe beam was undertaken. Different i-layer thicknesses were examined in relation to gating for these different situations. We present comparisons of electron and hole gating by measurement and simulation and explain the phenomenon in terms of field changes near to the incident bias interface irrespective of the illumination side.

Paper presented at 16th European Photovoltaic Solar Energy Conference, Glasgow, 2000:

J.-H. Zollondz, S. Reynolds, C. Main, I. Zrinscak,
Response speed of high gain two-beam photogating effects in a-Si:H pin stuctures as an indicator of defect densities, published in Sixteenth European Photovoltaic Solar Energy Conference, Volume 1, pp 667-669, London 2000

RESPONSE SPEED OF HIGH GAIN TWO-BEAM PHOTOGATING EFFECTS IN a-Si:H PIN STRUCTURES AS AN INDICATOR OF DEFECT DENSITIES

J.-H. Zollondz, S. Reynolds, C. Main and I. Zrinscak
School of Science and Engineering, University of Abertay Dundee, Dundee DD1 1HG, UK.
Tel: +44 (0)1382 308258 Fax: +44 (0)1382 308688 Email: s.reynolds@tay.ac.uk

ABSTRACT: The origin of high gain two-beam photogating in amorphous silicon pin devices is briefly discussed. Switch-on and switch-off characteristics of the photogated signal have been measured over a range of probe beam fluxes with a constant bias beam applied. The switch-on transient is dependent on probe beam flux and may be fitted by a stretched exponential function. The rise time scales roughly inversely with probe beam flux suggesting the rate-limiting step is the supply and subsequent capture of holes generated by the probe beam in the i-layer, leading to an estimated trap density of 4×10^{15} cm^{-3}. The switch-off decay is exponential in form with a time-constant of 3 s, independent of probe beam flux. This may be attributed to the emission and subsequent extraction or recombination of holes trapped in a narrow range of states some 0.7 eV deep.
Keywords: Defects – 1: Photoconductivity – 2: a-Si – 3

1. INTRODUCTION

The study of electronic defects in thin-film semiconductors is important from both a fundamental and a device viewpoint. For example, in the case of amorphous silicon (a-Si:H) solar cells, defects limit the conversion efficiency and stability of operation [1] and much research effort has been spent in understanding these effects and in improving performance. A variety of experimental techniques, such as electron spin resonance, steady-state, transient and modulated photoconductivity, and capacitance-voltage spectroscopies have been used in the study of defects, which have allowed their nature, density and energy distribution to be probed both in homogeneous films and in device structures subjected to various operational stresses.

We have recently reported [2,3] on photogating observed in two-beam experiments on thick (3.5 μm) a-Si:H pin structures under reverse voltage bias. In these experiments, a low intensity 'probe' beam is incident from one side of a pin device that is already illuminated with a higher intensity strongly absorbed 'bias' beam incident from the other side, as shown in Fig. 1.

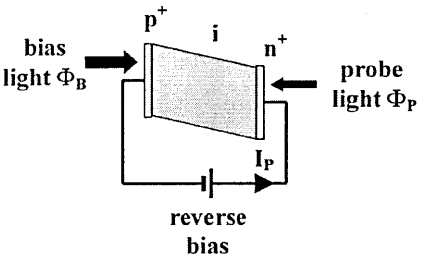

Figure 1. Two-beam photogating experimental set-up.

It is found that the current associated with the probe beam flux may considerably exceed that expected from the generation of *primary* photocurrent, yet the device is under low reverse bias and thus no additional (secondary) current is possible. Detailed computer simulations support the view that this amplification is caused by the modulation of internal fields by the space charge introduced by the probe beam, which releases charge produced by the bias beam for collection. The effect is most pronounced when the bias beam is incident from the p-side and the probe beam from the n-side ('electron gating'), in which an electron current is controlled by a hole-mediated space charge, although transposing the beams (to give 'hole gating') still results in significant amplification. This gated current is dependent on the density of traps in the i-layer that accommodate the space charge. A typical simulated internal field distribution under conditions where electron gating is predicted to occur is shown in Fig. 2. Measurement of the steady collection efficiency, backed up by computer modelling, can thus give indirect information on the density of i-layer defects, including the effect of light-induced degradation,

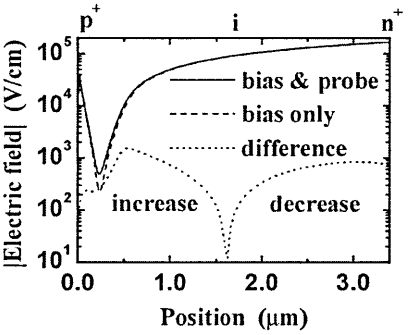

Figure 2. Internal electric field profile simulation, showing effect of probe beam.

and hence on the quality of the material in device applications.

In order to quantify these effects it is convenient to define the *collection efficiency* (CE) for this process as

$$CE = \Delta I_P / eA\Phi_P , \qquad (1)$$

where $\Delta I_P = I_P(on) - I_P(off)$ is the change in photocurrent due to the probe beam with the bias beam applied, e the electron charge, A the illumination cross-section and Φ_P the probe beam flux. Photogating is thus associated with a CE of greater than one. CE values in

excess of 50 have been measured for both electron [2] and hole [3] gating at low probe fluxes.

The work presented here concerns the time-dependence of electron gating on application, and removal, of probe illumination. Based on the predictions of steady-state computer modelling [2] we speculate that the rate-limiting step in the modulation of the internal field during switch-on is simply the supply of photogenerated holes, drifting into the i-layer from the probe beam generation region near the n-i interface, which are captured by dangling bond defects. If this hypothesis is correct, we have an independent means of determining the defect density in the i-layer of such devices. Preliminary results indicate a clear correlation between the switch-on response speed and the probe beam flux, and thus with the CE, in accordance with the above. We also report on the nature of the switch-off response and propose a mechanism involving either hole release or recombination at deep trap levels.

2. EXPERIMENTAL

The bias beam flux was produced using a blue LED (Ledtronics Inc., 470 nm peak emission wavelength) plus standard bench current supply. The probe beam flux was produced using a red LED (Ledtronics Inc., 615 nm peak emission wavelength) driven via a series resistor by a programmable function generator (Thurlby Thandar TG1304). Photocurrent transients were amplified using a current preamplifier (Burr-Brown OPA637) with variable gain, and signals were displayed and recorded using a digital storage oscilloscope (Tektronix TDS3052). Data were transferred to a PC for detailed analysis.

The a-Si:H pin sample under test was fabricated at IPE Stuttgart by PECVD, with p and n layers of 30 nm thickness and an i-layer thickness of 3.5 μm. TCO contacts of diameter 2.8 mm were used on both sides, masked to approximately 2 mm diameter by a black plastic film to avoid inadvertent illumination of the probe side of the structure by the bias beam. Prior to making the measurements presented here, the sample was degraded by exposure to AM1.5 illumination for approximately 1 min. After this treatment the CE maximum was found to occur at a reverse bias voltage of 1 V and this bias was used throughout for measurement of response speed.

3. RESULTS AND DISCUSSION

3.1 Switch-on Response

Switch-on characteristics parametric in Φ_P are shown in Fig. 3. At low flux, the rising edge of the pulse may be described empirically by:

$$\Delta I_P(t) = \Delta I_P(\infty)(1-\exp(-(t/\tau)^{\beta})) \quad (2)$$

As an example, a fit to the curve taken at $\Phi_P = 10^{13}$ cm^{-2} s^{-1} is indicated in Fig. 3, with $\tau = 7.7\times10^{-3}$ s, $\beta = 0.43$. The physical significance of this 'stretched exponential' characteristic is not yet clear. However, similar behaviour has been observed to occur in a number of physical systems, including the decay in photoconductivity in amorphous semiconductors [4], and

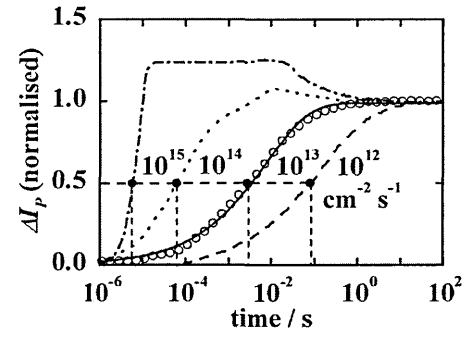

Figure 3. Photogated current switch-on *vs.* probe flux

is normally associated with a distribution of relaxation times.

A clear decrease in the 50% rise-time τ_{ON} with increasing Φ_P is observed which, from Fig. 4, can be seen to follow a power law:

$$\tau_{ON} = k\Phi_P^{-n}, \quad (3)$$

where k is a constant and n = 1.4. As reported in earlier

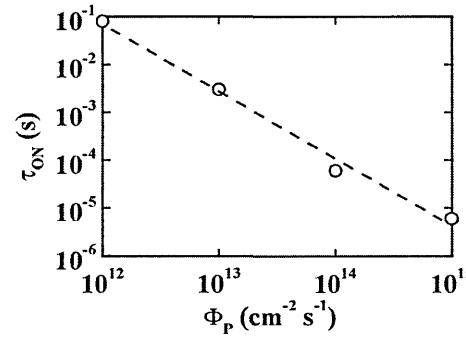

Figure 4. Switch-on response time *vs.* probe flux

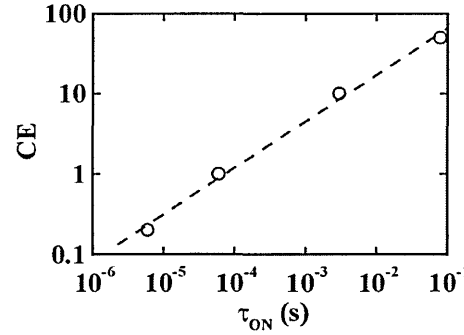

Figure 5. Collection efficiency CE *vs.* switch-on time τ_{ON}

work, the steady-state CE is also a function of Φ_P, and it is shown in Fig. 5 that τ_{ON} and CE are strongly correlated.

Previous computer simulations [2] have shown that, in the steady state, photogating results from a reduction in

the density of D^- defects by capture of holes generated by the probe beam, which converts a spatially-uniform fraction f throughout the i-layer to D^0 states. Although dependent to some extent on material parameters, in particular the relative capture rates of electrons and holes in the defects, f is predicted to be of order 0.01 in the mid-range of our measurements. We propose that the switch-on speed is limited by the rate of supply of holes to the i-layer by the probe beam. A quantitative estimate of the trap density may then be made by equating the number of probe beam photons required to turn on photogating to the number of converted traps:

$$\Phi_P A \tau_{ON} = f N_T A d \,, \qquad (4)$$

where A is the illumination cross-section and d is the i-layer width. From Fig 4, a mid-range flux of Φ_P of 3×10^{13} cm^{-2} s^{-1} corresponds to $\tau_{ON} = 5\times10^{-4}$ s, yielding $N_T = 4\times10^{15}$ cm^{-3}, in reasonable agreement with typical literature values.

From equations 3 and 4, we predict a functional dependence of the trap-conversion factor:

$$f \propto \Phi_P^{-(n-1)} . \qquad (5)$$

This relationship has not yet been investigated by simulation, but would provide a good test of the mechanism proposed here.

At probe fluxes approaching the bias flux there is evidence in Fig. 3 of an overshoot in ΔI_P at short times, prior to a low steady state CE being established. For data taken at a flux of 10^{15} cm^{-2} s^{-1} this is masked to some extent by amplifier overload. A high transient CE may be anticipated before the field at the p-i interface is perturbed by the strong probe beam, destroying the conditions needed for a high CE to be maintained.

3.2 Switch-off Response

The response to switching off the probe beam from the steady-state is shown in Fig. 6. Each curve has been

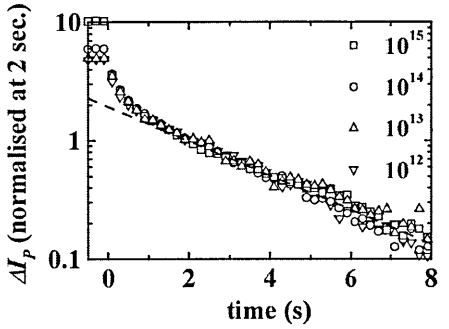

Figure 6. Switch off response *vs.* probe beam photon flux

normalised to unity on the current axis 2 s after switch-off. It can be seen that the decays follow a common curve after approximately 0.5 s, and are well-fitted in this region by a straight line on the semi-log plot, indicating an exponential decay of characteristic time τ_{OFF} = 3 s. A more rapid fall, of indeterminate functional form, occurs between 5 ms and 500 ms after switch off. Curves taken at high probe fluxes show a very rapid initial fall in current, by a factor of 2 or more, in less than 1 ms.

The similar exponential form of the switch-off decays at longer times suggests a process that is independent of probe beam intensity, and which involves a closely-spaced set of deep defect states. Possible mechanisms might include recombination via these states, or hole emission followed by extraction. The predicted emission depth $E = kT \ln(\nu\tau_{OFF})$, where ν is the attempt-to-escape frequency, is approximately 0.7 eV, assuming $\nu = 10^{12}$ s^{-1}. Although within the expected range for a-Si:H, a broader distribution of defects is more commonly associated with these materials, and thus a power-law rather than an exponential decay might be anticipated. Further experimental work and computer simulations would be required to specify this process in greater detail.

4. CONCLUSIONS

The switch-on characteristic of the probe beam in a two-beam photogating experiment is described by a stretched exponential function, implying a dynamic process that involves a distribution of relaxation times. The switch-on response time varies approximately inversely with intensity, which suggests a gating mechanism that is limited by the supply of carriers generated by the probe beam. This interpretation is consistent with earlier work based on steady-state measurements and computer simulations, which identifies the photogating effect as originating from the modulation of the bias-beam induced low field region at the p-i interface by hole capture in the i-layer. A trap density of order 4×10^{15} cm^{-3} is estimated from the data, although the exact value is dependent on material parameters. The switch-off characteristic is exponential at times > 0.5 s with a time-constant of 3 s, and is independent of probe beam intensity, suggesting that current decay is linked to hole emission from a narrow range of states some 0.7 eV below the band edge.

Work is currently in progress to simulate the dynamic response [5] of the two-beam experiment, which should give further insight the processes described here. This is necessary if measurements are to be accurately interpreted in terms of absolute trap densities, thereby offering a quantitative method for assessment of material quality and a basis for device design.

REFERENCES

[1] J. Singh, P. Stulik and R. Yang, in Thin Film Materials and Devices – Developments in Science and Technology, eds. J.M. Marshall, N. Kirov, A. Vavrek and J.M. Maud, World Scientific (1999) 29.

[2] C. Main, J.-H. Zollondz, S.Reynolds, W. Gao, R. Brüggemann and M. J. Rose, J. Appl. Phys. **85** (1999) 296.

[3] J.-H. Zollondz, C. Main and S Reynolds, MRS Symp. Proc. Ser. **557** Ch.135 (1999) 475.

[4] G.J. Adriaenssens, S.D. Baranovskii, W. Fuhs, J. Jansen and Ö. Öktu, Phys. Rev. B **51** (1995) 9661.

[5] B. Stannowski, H. Cordes, R. Brüggemann, T. Eickhoff, S. Brocheler and H. Wagner J. Non-Cryst. Sol. **230** (1998) 1295.

Paper presented at the ICAMS 19, Nice, 2001:

J.-H. Zollondz, S. Reynolds, C. Main, V. Smirnov, I. Zrinscak,
The Influence of Defects on Response Speed of High Gain Two-Beam Photogating in a-Si: H Structures, in print.

The Influence of Defects on Response Speed of High Gain Two-Beam Photogating in a-Si:H PIN Structures

J.-H. Zollondz, S. Reynolds, C. Main, V. Smirnov and I. Zrinscak

School of Science and Engineering, University of Abertay Dundee, Dundee DD1 1HG, UK.

Corresponding Author:

Steve Reynolds,

School of Science and Engineering,

University of Abertay Dundee,

Dundee DD1 1HG, UK.

Tel: +44 1382 308258

Fax: +44 1382 308688

Email: s.reynolds@tay.ac.uk

Abstract

The dynamic characteristics of two-beam photogating in reverse biased a-Si:H pin devices have been investigated. The photogated current switch-on rise time scales approximately inversely with probe beam flux, suggesting the supply and subsequent capture of holes generated in the i-layer by the probe beam is the rate-limiting step. This interpretation leads to an estimated i-layer trap density of 4×10^{15} cm^{-3}. The switch-off decay is complex, but contains an exponential component with a time-constant of 2 s independent of probe beam flux. A mechanism involving emission and subsequent extraction or recombination of holes trapped in a narrow energy range of states some 0.7 eV deep is proposed to account for this. These findings are compared with independent data from dark current, transient photocurrent and constant photocurrent measurements.

PACS Codes: 71.55.J; 71.23.C; 73.50.P; 71.23

1. Introduction

If a reverse-biased a-Si:H pin device is illuminated with a low intensity 'probe' beam from one side and simultaneously with a higher intensity strongly absorbed 'bias' beam from the other side, the current associated with the probe beam may considerably exceed that expected from the direct generation of primary photocurrent [1,2]. Detailed computer

simulations [1,3] support the view that this amplification, or 'photogating', results from the modulation of internal fields by the space charge introduced by the probe beam, which releases charge produced by the bias beam for collection.

In order to quantify these effects, we define the *collection efficiency* (*CE*) as

$$CE = \Delta I_P / eA\Phi_P, \tag{1}$$

where $\Delta I_P = I_P(on) - I_P(off)$ is the change in photocurrent due to the probe beam with the bias beam applied, e the electron charge, A the illumination cross-section and Φ_P the probe beam flux. Photogating is thus associated with a *CE* of greater than one; in practice values approaching 100 have been observed.

Photogating is most pronounced when the bias beam is incident from the p-side and the probe beam from the n-side ('electron gating'), where an electron current is controlled by a hole-mediated space charge, although transposing the beams (to give 'hole gating') still results in a significant effect. *CE* values in excess of 50 have been measured for both electron [1] and hole [2] gating at low probe fluxes.

Computer simulations [1,3] reveal that under bias beam illumination, electrons trapped in D^- states dominate the space charge through most of the i-layer. However, close to the p-i interface, holes trapped in valence band tail states are predominant. The resulting electric field profile shows a minimum where the transition occurs. When the probe beam is applied, hole trapping reduces the D^- density, decreasing the field over part of the i-layer but *increasing* the field minimum by a large fraction and thereby promoting release of electrons from this region. The resulting electric field profiles are shown in Fig. 1. Further simulations reveal that the increase in net generation rate due to the probe beam is some 50 times greater in the vicinity of the field minimum (through a reduction in recombination rate) than that on the n-side of the i-layer. The simulation thus accounts both for the phenomenon of photogating and its magnitude.

The work presented here examines the time-dependence of electron gating on application, and removal, of probe illumination. The above model suggests that the rate-limiting step in the modulation of the internal field during switch-on is simply the supply of photogenerated holes, drifting into the i-layer from the probe beam generation region near the n-i interface, which are captured by D^- defects. Measurements of the switch-on speed versus probe flux allow us to test this hypothesis. Independent estimations of the density of states, from dark current, transient photocurrent and constant photocurrent measurements are also presented in support of the model. Finally, we examine the switch-off response and suggest possible mechanisms to account for this.

2. Experimental

Bias and probe illumination was produced using LEDs (Ledtronics Inc., 470 nm and 615 nm peak emission wavelengths respectively). Photocurrent transients were amplified using a current preamplifier (Burr-Brown OPA637) with

variable gain and offset, and recorded using a digital storage oscilloscope (Tektronix TDS3052). Data were transferred to a PC for detailed analysis.

The a-Si:H pin sample was grown using plasma-enhanced chemical vapour deposition, with p and n layers of 30 nm thickness and an i-layer thickness of 3.5 μm. TCO contacts of diameter 2.8 mm were used on both sides, masked to approximately 2 mm diameter by black plastic film to avoid inadvertent illumination of the probe side of the structure by the bias beam. The sample was degraded by exposure to AM1.5 illumination for approximately 1 min prior to measurement. The *CE* maximum was subsequently found to occur at a reverse bias voltage of 1 V, and this value was used here while measuring the photogating response.

3. Results

The normalised photogated current switch-on transient, parametric in Φ_P, is shown in Fig. 2. Plots of the 50% rise time τ_{ON} versus Φ_P, and versus *CE*, are presented in Fig. 3. It can be seen from Fig. 3 that τ_{on} decreases with increasing Φ_P as a power law, of index 1.4, and also that τ_{on} increases with increasing (steady state) *CE* as a power law, of index 1.7. Over this range of excitation *CE* is roughly inversely proportional to Φ_P, as previously reported [1]. The normalised photogated current decay, parametric in Φ_P, is shown in Fig 4. The density of states distribution obtained for this sample using a combination of post-transit time of flight [4] and constant photocurrent spectroscopies [5] is presented in Fig. 5.

4. Discussion

4.1. Switch-on response

Computer simulations show that, in the steady state, photogating results from a reduction in the density of D^- defects by capture of holes generated by the probe beam, which converts a spatially-uniform fraction f throughout the i-layer to D^0 states. Although dependent to some extent on material parameters, in particular the relative capture rates of electrons and holes by defects, f is predicted to be of order 0.01 in the mid-range of our measurements. From Fig. 3 we see that the switch-on time is roughly inversely related to probe flux, as expected if it is determined by the rate of supply of holes to the i-layer by the probe beam. A quantitative estimate of the hole trap density N_{th} may thus be made by equating the number of probe beam photons required to turn on photogating to the number of converted traps:

$$\Phi_P A \tau_{on} = f N_{th} A d \qquad (2)$$

where A is the illumination cross-section and d is the i-layer width. From Fig 3, a mid-range flux of Φ_P of 3×10^{13} cm^{-2} s^{-1} corresponds to $\tau_{on} = 5\times10^{-4}$ s, yielding $N_{th} = 4\times10^{15}$ cm^{-3}.

It is possible to estimate the trap density in the i-layer by other means, to seek to corroborate this line of reasoning. The saturation current I_0 at 300 K was found to be approximately 5 nA and largely independent of (reverse) voltage bias. Assuming this current is furnished by electron emission from deep traps of density N_{te} we have:

$$I_0 = e(Ad)N_{te}\nu\exp(-E_{te}/kT), \tag{3}$$

where ν is the attempt to escape frequency, E_{te} is the trap depth, k is Boltzmann's constant and T is the absolute temperature. A value of N_{te} of 4×10^{15} cm^{-3} would be consistent with emission from a depth of 0.75 eV, close to the Fermi energy, assuming ν = 10^{12} s^{-1}. This reasoning involves *electron*, rather than *hole* trap densities, but according to the defect pool model [3,6] charged and neutral species are expected to occur with similar densities in the central region of the i-layer, and so the comparison may be justified. The absolute value is rather lower than reported [7] for gently light-soaked material but is not unreasonable given the approximations made.

At low probe fluxes, the switch-on transient may be described empirically by

$$\Delta I_P(t) = \Delta I_P(\infty)(1-\exp(-(t/\tau)^{\beta})). \tag{4}$$

As an example, a fit to the curve taken at $\Phi_P = 10^{13}$ cm^{-2} s^{-1} is indicated in Fig. 3, with $\tau = 7.7\times10^{-3}$ s, $\beta = 0.43$. The physical significance of this 'stretched exponential' characteristic is unclear, although similar behaviour has been observed to occur in a number of physical systems, including the decay in photoconductivity in amorphous semiconductors [8], and is normally indicative of a distribution of relaxation times. In this case it may signify a broad energy distribution of hole traps.

At probe fluxes approaching the bias flux there is evidence in Fig. 3 of an overshoot in ΔI_P at short times prior to a low steady state *CE* being established, though this is masked to some extent by amplifier overload. A high transient *CE* might be anticipated to occur before the field at the p-i interface is significantly perturbed by the strong probe beam, which then destroys the conditions needed for a high *CE* to be maintained. Transient overshoots have also been reported in conventional (single beam) switch-on experiments [9] at low temperatures (150 K) due to re-emission of deeply trapped charge.

4.2. Switch-off Response

The inhomogeneous nature of both the device structure and the illumination profile foretell that the switch-off behaviour is likely to be complex. Decays taken at high probe fluxes show a very rapid drop in current, by a factor of 2 or more, in less than 1 ms. This is then followed (in all cases) by a more gradual fall between 5 and 500 ms, concluding in an exponential decay of characteristic time $\tau_{off} = 2$ s. It is tempting to associate the fast processes with the 'gating' region of the

device, the field minimum close to the p-i interface. Here the simulations show there is a high recombination rate, which *increases* on removal of the probe beam as discussed above. However, for the device to return to the steady state (bias illumination only) the additional trapped hole charge in the bulk of the i-layer must also recombine. If hole emission is the rate-limiting step, then τ_{off} corresponds to a trap depth of 0.7 eV below the valence band. However, the DOS shown in Fig. 5 suggests a local *minimum* at this energy. Further, we observe no sharp features (on a scale of kT). Thus at present we have no independent evidence in support of this mechanism.

5. Conclusions

In a two beam photogating measurement, the probe beam switch-on response time varies approximately inversely with intensity, suggesting a photogating mechanism that is limited by the supply of carriers generated by the probe beam. This interpretation is consistent with earlier work based on steady-state measurements and computer simulations, which identifies the effect as originating from the modulation of the bias-beam induced low field region at the p-i interface by hole capture in the i-layer. A trap density of order 4×10^{15} cm^{-3} is estimated from the switch-on data, consistent with an independent estimate based on the dark saturation current. We suggest the initial rapid switch-off decay originates in the low field 'gating' region near the p-i interface, with the exponential feature at longer times being linked to hole emission from a narrow band of states in the bulk i-layer some 0.7 eV below the band edge. However, our CPM measurements indicate a broad energetic distribution, with no peak observable in this range.

Further work will include a study of the temperature and voltage bias dependence of the dynamic characteristics, which will then be compared with the simulated *dynamic* response [9] of the two-beam experiment. This style of approach has previously proved invaluable in understanding the origins of the steady-state photogating effect. In this way we hope to construct the accurate models necessary to establish a quantitative method for assessment of material quality and a basis for device design.

Acknowledgments

The authors thank M. Schubert and his group at IPE Stuttgart for provision of samples used in this work.

References

[1] C. Main, J.-H. Zollondz, S.Reynolds, W. Gao, R. Brüggemann, M.J. Rose, J. Appl. Phys. 85 (1999) 296.

[2] J.-H. Zollondz, C. Main, S. Reynolds, MRS Symp. Proc. Ser. 557 Ch.135 (1999) 475.

[3] W. Gao, Ph.D. thesis, University of Abertay Dundee, UK, 1995.

[4] G.F. Seynhave, R.P. Barclay, G.J. Adriaenssens, J.M. Marshall, Phys. Rev. B 39 (1989) 10196.

[5] P. Sládek, P. St'ahel, P. Roca I Cabarrocas, P. Morin, Phil. Mag. B 77 (1998) 1049.

[6] G. Schumm, J. Non-Cryst. Sol. 164-166 (1993) 317.

[7] C. Longeaud, D. Roy, Z.T. Hangouan, Appl. Phys. Letts. 77 (2000) 3604.

[8] G.J. Adriaenssens, S.D. Baranovskii, W. Fuhs, J. Jansen, Ö. Öktu, Phys. Rev. B 51 (1995) 9661.

[9] B. Stannowski, H. Cordes, R. Brüggemann, T Eickhoff, S. Brocheler, H. Wagner, J. Non-Cryst. Sol. 230 (1998) 1295.

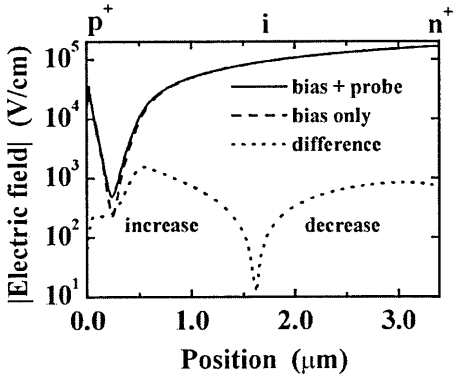

Fig. 1. Internal electric field profile simulation of pin device under electron photogating conditions.

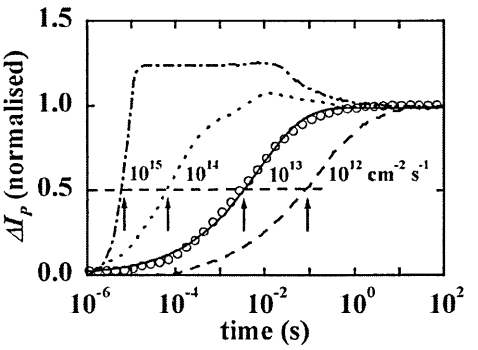

Fig. 2. Measured photogated current switch-on transient as a function of probe flux

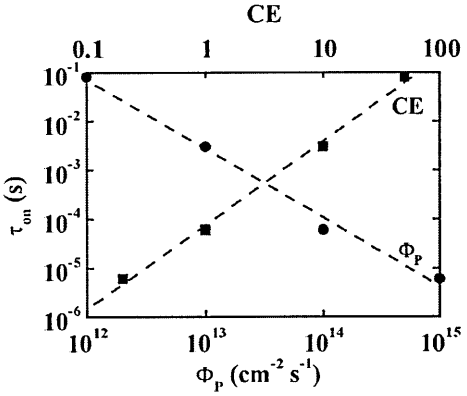

Fig. 3. 50% risetime τ_{on} versus probe flux Φ_P (lower axis) and collection efficiency *CE* (upper axis).

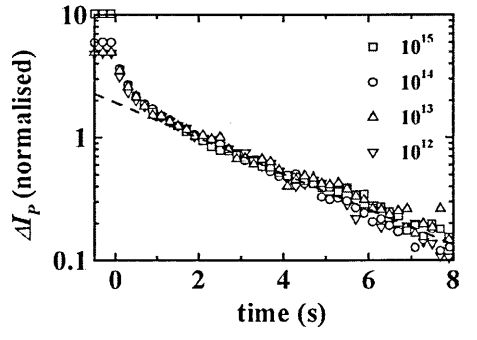

Fig. 4. Measured photogated current decay transient as a function of probe flux.

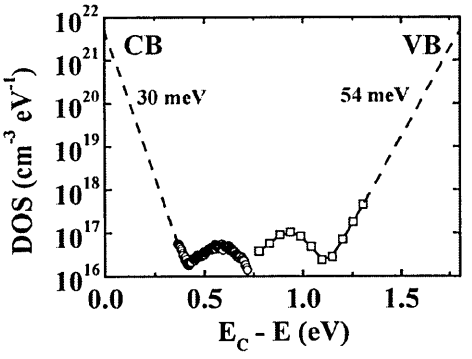

Fig. 5. Density of states versus energy for pin sample. Data have been scaled assuming a band-edge DOS of 4×10^{21} cm^{-3} eV^{-1}.